

# **Structural Characterization and Structure-property Correlation of Nanostructured Superconducting Coated Conductors and Thermoelectric Materials**

## **Dissertation**

der Mathematisch-Naturwissenschaftlichen Fakultät  
der Eberhard Karls Universität Tübingen  
zur Erlangung des Grades eines  
Doktors der Naturwissenschaften  
(Dr. rer. nat.)

vorgelegt von  
Zainul Aabdin  
aus Balrampur, Indien

Tübingen  
2013

Tag der mündlichen Qualifikation:

12.06.2013

Dekan:

Prof. Dr. Wolfgang Rosenstiel

1. Berichterstatter:

Prof. Dr. Oliver Eibl

2. Berichterstatter:

Prof. Dr. Reinhold Kleiner

## Summary

Superconductors and thermoelectric materials play a significant role in energy technology, nanostructured materials promise exciting new advances in the field of superconductivity and thermoelectricity.  $\text{YBa}_2\text{Cu}_3\text{O}_{7-x}$  and  $\text{DyBa}_2\text{Cu}_3\text{O}_{7-x}$  are the most widely used high-temperature superconducting materials, applications in energy and magnet technologies require almost single-crystalline and nano-engineered materials over kilometers of length. Bismuth telluride ( $\text{Bi}_2\text{Te}_3$ ) bulk materials are widely used Peltier materials at room temperature, because of their high figure of merit ( $ZT \sim 1$ ). The efficiency of these materials for applications are limited, nanostructured materials would allow to overcome these limitations.

Both compounds  $\text{DyBa}_2\text{Cu}_3\text{O}_{7-x}$  and  $\text{Bi}_2\text{Te}_3$  have a layered anisotropic structure. To obtain a better understanding of the structure-property correlation for such nanostructured materials, a number of modern microscopy and microanalyses methods and tools have to be employed. Among these are analytical Transmission Electron Microscopy (TEM), i.e. energy-filtered TEM (EFTEM) combined with quantitative energy-dispersive X-ray spectrometry (EDX), which have been applied in this study. For this study, more than 80 specimens were prepared in plan-view or cross-section using conventional grinding and polishing techniques followed by  $\text{Ar}^+$  ion etching and were characterized by TEM.

## Structure-property correlation of $\text{DyBa}_2\text{Cu}_3\text{O}_{7-x}$ coated conductors

The bismuth strontium calcium copper oxide (BSCCO) based high-temperature superconducting (HTS) wires, which are known as first generation (1G) wires, have been used for a number of applications, however, they are unable to operate at high temperatures and magnetic fields due to thermally activated flux flow. Therefore, there is a fast growing worldwide interest in the second generation (2G) HTS wires. The 2G HTS wires are based on thin-film technologies referred as coated conductor (CC) technology. The CC technology yields biaxially textured (almost single crystalline) superconducting layers over kilometers of length.

Inclined substrate deposition (ISD) CCs have a multilayer structure and were grown by an electron-beam evaporation technique for all deposited layers. The sequence of layers starting from the Hastelloy substrate is ISD MgO buffer layer, MgO cap layer and DyBCO layer. CCs investigated in this work were prepared by THEVA Dünnschichttechnik GmbH and were characterized for their superconducting properties within the HIGHWAY project (funded by the BMWi). Microstructural characterization of these tapes was carried out at the University of Tübingen.

The maximum critical current of CCs is still limited to about  $300\text{-}400 \text{ A cm}^{-1}$  (current per width of the tape) at 77 K and zero magnetic field. It could be enhanced by increasing the thickness of the superconducting layer. However, for ion beam assisted deposition (IBAD) or rolling assisted biaxially textured substrate (RABiTS) technologies a scale-up of the thickness is limited to only a few microns by fundamental reasons (loss of biaxial texturing) related to the thin-film growth process. In contrast, ISD technology overcomes these limitations and yields monolithic DyBCO superconducting thick-films without much degradation of the critical current densities, as will be shown in this thesis. DyBCO based ISD CCs reported here yielded a critical current of about  $1000 \text{ A cm}^{-1}$  at 77 K and zero field, which is a record value. Typical critical current densities of DyBCO films were  $2.1 \text{ MA cm}^{-2}$  at 77 K in a self-field.

Quantitative transmission electron microscopy and spectroscopy of ISD CCs is a challenging task because of the complex multilayer architecture, complex micro- and nanostructure, difficult TEM specimen preparation and the challenges in understanding the physics of the TEM methods. Combined EFTEM and EDX were applied to study the microstructure and chemistry of different layers and interfaces. EFTEM was used to produce phase maps and EDX yielded a quantitative chemical composition of phases present in different layers. CCs were studied with respect to: (1) the Hastelloy-MgO interface, (2) the MgO buffer layer, (3) the DyBCO films

and (4) DyBCO films with BaZrO<sub>3</sub> nano inclusions by applying energy-filtered bright-field, dark-field imaging and diffraction techniques.

In the columnar MgO buffer layers, columns had a typical diameter of few 100 nm and showed a biaxial-texturing irrespective of the Hastelloy texture. The MgO-DyBCO interface yielded a faceted structure, the width of the facets was 150-350 nm while the facets height was about 100 nm.

Despite the large lattice mismatch of 8.5 % between DyBCO and MgO, the DyBCO film grew epitaxially on the MgO buffer layer. DyBCO films were found to be highly biaxially textured, almost single crystalline, and contained only small-angle grain boundaries with average DyBCO grain size of about 300 nm. ISD DyBCO films retained their biaxial texture for film thicknesses up to 6  $\mu\text{m}$ . This is a unique and completely different feature of ISD CCs as compared to CCs prepared by other technologies. Therefore, ISD offers the potential for high-quality, biaxially-textured MgO buffer layers suitable for thick and long-length superconducting CCs with larger critical currents.

The electron microscopy results presented in this thesis helped to improve and optimize the microstructure of ISD grown DyBCO CCs. As a result, a record value of critical current (1000 A cm<sup>-1</sup>) for a 6  $\mu\text{m}$  thick monolithic film and a detailed understanding of the growth processes was achieved.

### Structure-property correlation of thermoelectric Bi<sub>2</sub>Te<sub>3</sub> bulk materials

According to G. Slack an optimized thermoelectric material would behave as a “phonon glass/electron crystal” (PGEC), i.e., it would have electrical properties of a crystalline material and thermal properties of an amorphous or glass-like material. Nanostructures provide a possibility to disconnect thermal and electrical transport (Wiedemann-Franz law) by enhancing phonon scattering and thereby reducing the lattice thermal conductivity without significantly affecting the electrical conductivity and, thus, increasing the figure of merit.

This thesis will present results on the structure-property correlation in Bi<sub>2</sub>Te<sub>3</sub> nanostructured bulk investigated within the DFG Priority Program “Nanostructured Thermoelectrics”. For this (i) natural nanostructures (nns) were produced by Ar<sup>+</sup> ion irradiation of bulk materials and (ii) nanostructured bulk materials were produced by spark plasma sintering (SPS). The nns is particularly interesting because of the ease and effectiveness, with which Ar<sup>+</sup> ion beam irradiation can produce nanostructured thermoelectric materials in Bi<sub>2</sub>Te<sub>3</sub>. The nns formation by the Ar<sup>+</sup> ion irradiation relates particularly to nanomaterials since ion irradiation can be applied very effectively in this case. The nns consists of a sinusoidal displacement field with an amplitude of 10 pm and a periodicity of 10 nm. For the first time, a controlled formation and removal of the nns in bulk Bi<sub>2</sub>Te<sub>3</sub> by Ar<sup>+</sup> ion irradiation was shown. Samples were repeatedly ion-etched and investigated by TEM using two-beam diffraction conditions.

By an SPS process, n-type Bi<sub>2</sub>(Te<sub>0.91</sub>Se<sub>0.09</sub>)<sub>3</sub> and p-type (Bi<sub>0.26</sub>Sb<sub>0.74</sub>)<sub>2</sub>Te<sub>3</sub> nanostructured bulk materials were prepared by ball milling of commercial precursors. Lattice thermal conductivity was successfully decreased (from 1.78 to 0.44 W m<sup>-1</sup>K<sup>-1</sup> for n-type and from 1.74 to 0.41 W m<sup>-1</sup>K<sup>-1</sup> for p-type materials) due to the fine grain sizes (50-130 nm) in sintered materials. However, the results show that thermoelectric properties are very sensitive to oxidation and require careful protection from contamination during synthesis.

With this thesis a quantitative study of the microstructure has been carried out for high-quality, device-relevant superconducting and thermoelectric materials, for which transport properties were investigated in detail. The significance of this work lies in the improved TEM specimen preparation, high-quality transmission electron microscopy, high-accuracy, quantitative spectroscopy for different classes of energy materials, which helped to establish a precise structure-property correlation and thereby enhancing the performance of these materials.

## Zusammenfassung

Supraleitende und thermoelektrische Materialien sind wichtige Materialien für die Energietechnik, man erwartet von nanostrukturierten Materialien erhebliche Verbesserungen der Eigenschaften.  $\text{YBa}_2\text{Cu}_3\text{O}_{7-x}$  und  $\text{DyBa}_2\text{Cu}_3\text{O}_{7-x}$  sind Hochtemperatur-Supraleiter (HTS)-Verbindungen, für Anwendungen in der Energie- und Magnettechnologie sind nahezu einkristalline Materialien von mehreren Kilometern Länge erforderlich.  $\text{Bi}_2\text{Te}_3$  basierte Materialien sind aufgrund ihres hohen thermoelektrischen Gütefaktors ( $ZT \sim 1$ ) weit verbreitete Peltier-Materialien für Anwendungen bei Raumtemperatur, durch Nanostrukturierung kann eine Steigerung des thermoelektrischen Gütefaktors erreicht werden.

Beide Verbindungen ( $\text{DyBa}_2\text{Cu}_3\text{O}_{7-x}$  und  $\text{Bi}_2\text{Te}_3$ ) besitzen geschichtete, anisotrope Kristallstrukturen. Eine Reihe von modernen, mikroskopischen und mikroanalytischen Methoden müssen angewandt werden, um ein besseres Verständnis der Struktur-Eigenschafts-Korrelation für diese Materialien zu erhalten. Dazu wurde im Rahmen dieser Arbeit die analytische Transmissionselektronenmikroskopie (TEM) eingesetzt, die aus einer Kombination von energiegefilterter TEM (EFTEM) und quantitativer, energiedispersiven Röntgenspektrometrie (EDX) besteht. Für diese Arbeit wurden mehr als 80 Proben unter Verwendung der herkömmlichen Schleif- und Poliertechniken und dem anschließendem  $\text{Ar}^+$  Ionenstrahlätzen hergestellt und mittels TEM untersucht.

### Struktur-Eigenschafts-Korrelation von supraleitenden $\text{DyBa}_2\text{Cu}_3\text{O}_{7-x}$ -Bandleitern

Drähte mit supraleitenden Wismut-Strontium-Kalzium-Kupfer-Oxid werden als Drähte der ersten Generation (1G) bezeichnet und sind für eine Reihe von supraleitenden Anwendungen verwendet worden. Sie können jedoch aufgrund des thermisch aktivierten Flußkriechens nicht bei höheren Temperaturen und starken Magnetfeldern betrieben werden. Daher gibt es weltweit ein schnell wachsendes Interesse an HTS-Drähten der zweiten Generation (2G). Die Herstellung der 2G-HTS-Drähte basiert auf Dünnschichttechnologien, die als Coated Conductor (CC)-Technologien bezeichnet werden. Die CC-Technologien ermöglichen, biaxial texturierte (nahezu einkristalline), supraleitende Schichten mit mehreren Kilometern Länge herzustellen.

Inclined Substrate Deposition (ISD) ist eine der CC-Technologien. Die so hergestellten CCs sind mehrschichtig aufgebaut, wobei alle Schichten mittels Elektronenstrahlverdampfung abgeschieden werden. Die Sequenz der Schichten, ausgehend vom Hastelloy-Substrat, lautet: ISD-MgO-Pufferschicht, MgO-Deckschicht und DyBCO-Film. Die hier untersuchten CCs wurden von THEVA Dünnschichttechnik GmbH hergestellt und im Rahmen des HIGHWAY-Projekts (gefördert durch das BMWi) hinsichtlich ihrer supraleitenden Eigenschaften charakterisiert. Die Mikrostrukturuntersuchungen dieser Drähte wurden an der Universität Tübingen durchgeführt.

Der maximale kritische Strom der CCs ist eine Zielgröße für die Anwendungen, er betrug zu Beginn dieser Arbeit etwa  $300\text{-}400 \text{ A cm}^{-1}$  (Strom bezogen auf die Breite des Drahtes) bei 77 K und keinem äußeren Magnetfeld. Dieser Wert könnte durch eine Erhöhung der Dicke der supraleitenden Schicht verbessert werden, jedoch erlauben die CC-Technologien basierend auf ionenstrahlunterstützter Deposition (ion beam assisted deposition IBAD) oder der Deposition auf biaxial walztexturierten Substraten (rolling assisted biaxially textured substrate, RABiTS) nur eine Filmdicke von wenigen Mikrometern ohne Verlust der biaxialen Texturierung. Die ISD-Technologie dagegen überwindet diese Barriere und ergibt dicke, supraleitende, monolithische DyBCO Filme mit nur wenig reduzierten kritischen Stromdichten, wie in dieser Arbeit gezeigt wird. Die ISD CCs dieser Arbeit ergaben einen kritischen Strom von etwa  $1000 \text{ A cm}^{-1}$  bei 77 K und Nullfeld, was einen Rekordwert darstellt. Die typischen kritischen Stromdichten dieser DyBCO-Filme betragen dabei  $2,1 \text{ MA cm}^{-2}$  bei 77 K im Eigenfeld.

Quantitative Transmissionselektronenmikroskopie und Spektroskopie an ISD CCs ist eine anspruchsvolle Aufgabe. Dies ergibt sich aus der komplexen mehrschichtigen Architektur, der komplexen Mikro- und Nanostruktur, der schwierigen TEM Probenpräparation der CCs

und dem Verständnis der anspruchsvollen physikalischen Hintergründe der TEM-Methoden. Es wurden kombinierte EFTEM und EDX-Untersuchungen zur Analyse der Mikrostruktur und Chemie der verschiedenen Schichten und Grenzflächen durchgeführt. EFTEM-Abbildungen zeigen die Verteilung der Phasen, die EDX-Untersuchungen ergaben die quantitative chemische Zusammensetzung der Phasen in den verschiedenen Schichten. Die CCs wurden mittels energiegefilterter Hellfeld- und Dunkelfeldabbildung, sowie Elektronenbeugung bezüglich folgender Merkmale untersucht: (i) die Hastelloy-MgO-Grenzfläche, (ii) die MgO-Pufferschicht, (iii) die DyBCO Filme und (iv) DyBCO Filme mit BaZrO<sub>3</sub> Nanopartikeln.

In der säulenförmigen MgO-Pufferschicht hatten die Säulen einen typischen Durchmesser von einigen 100 nm und wiesen unabhängig von der Orientierung des Hastelloysubstrates eine biaxiale Texturierung auf. Die MgO-DyBCO Grenzfläche zeigte eine facettierte Struktur mit einer Breite der Facetten von 150-350 nm und einer Höhe von etwa 100 nm. Die DyBCO Filme wuchsen trotz der großen Gitterfehlpassung von 8,5% zwischen DyBCO und MgO epitaktisch auf der MgO-Pufferschicht auf. Die DyBCO Filme erwiesen sich als stark biaxial texturiert, nahezu einkristallin und enthielten nur Kleinwinkelkorngrenzen, bei einer durchschnittlichen Korngröße von etwa 300 nm. Die ISD DyBCO Filme behielten ihre biaxiale Textur bis zu Schichtdicken von 6 µm bei, dies ist ein für die ISD CCs einzigartiges Unterscheidungsmerkmal gegenüber CCs, die mit anderen Technologien hergestellt wurden. Deshalb bietet ISD das Potenzial zur Herstellung hochwertiger, biaxial texturierter MgO-Pufferschichten, welche für dicke und lange supraleitende CCs Drähte mit höheren kritischen Strömen geeignet sind.

Die in dieser Arbeit gewonnen elektronenmikroskopischen Ergebnisse trugen zur Verbesserung und Optimierung der Mikrostruktur der mittels ISD gewachsenen DyBCO CCs bei. Die Untersuchungen förderten aber auch ein detailliertes Verständnis der Wachstumsprozesse, insbesondere das der 6 µm dicken monolithische Filme mit einem Rekordwert des kritischen Stroms (1000 A cm<sup>-1</sup>).

### **Struktur-Eigenschafts-Korrelation von thermoelektrischen Bi<sub>2</sub>Te<sub>3</sub>-Volumenmaterialien**

Nach G. Slack sollte sich ein optimiertes thermoelektrisches Material wie ein amorphes bzw. glasartiges Material bezüglich der Phononen und wie ein Kristall bezüglich der Elektronen (phonon glas/electron crystal PGEC) verhalten. Nanostrukturen bieten die Möglichkeit, die Kopplung zwischen thermischen und elektrischen Transport (Wiedemann-Franz-Gesetz) aufzuheben. Die Erhöhung des thermoelektrischen Gütefaktors gelingt, wenn die Phononenstreuung erhöht und somit die Gitterwärmeleitfähigkeit erniedrigt wird, während die elektrische Leitfähigkeit nicht signifikant abnehmen darf.

In dieser Arbeit werden die Ergebnisse der Mikrostruktur-Eigenschafts-Untersuchungen an nanostrukturierten Bi<sub>2</sub>Te<sub>3</sub>-Volumenmaterialien dargestellt, die im Rahmen des DFG-Schwerpunktprogramms "Nanostrukturierte Thermoelektrika" erforscht wurden. Zu den untersuchten Materialien gehören (i) natürliche Nanostrukturen (nns), die in Volumenmaterialien mittels Ar<sup>+</sup> Ionenbestrahlung erzeugt wurden, und (ii) nanostrukturierte Volumenmaterialien, die durch den Spark-Plasma-Sinterungsprozess (SPS) hergestellt wurden. Die nns und damit nanostrukturiertes, thermoelektrisches Material kann durch Bestrahlung mit Ar<sup>+</sup> Ionen erzeugt werden kann. Die Erzeugung der nns durch Ar<sup>+</sup> Ionenstrahlung stellt ein neues und bedeutendes nanotechnologisches Herstellungsverfahren dar. Die nns besteht aus einem sinusförmigen Verschiebungsfeld mit einer Amplitude von 10 pm und einer Wellenlänge von 10 nm. In dieser Arbeit wird zum ersten Mal eine kontrollierte Bildung und Entfernung der nns in Bi<sub>2</sub>Te<sub>3</sub> Materialien mittels Ar<sup>+</sup> Ionenbestrahlung gezeigt. Die Proben wurden wiederholt bestrahlt und mittels TEM unter Zweistrahl-Beugungsbedingungen untersucht.

Das (SPS) Herstellungsverfahren ergab elektronenleitende Bi<sub>2</sub>(Te<sub>0,91</sub>Se<sub>0,09</sub>)<sub>3</sub> und löcherleitende (Bi<sub>0,26</sub>Sb<sub>0,74</sub>)<sub>2</sub>Te<sub>3</sub> nanostrukturierte Volumenmaterialien, wobei das kommerzielle Ausgangsmaterial zuvor in einer Kugelmühle pulverisiert wurde. Die Gitterwärmeleitfähigkeit der gesinterten Proben (von 1,78 bis 0,44 W m<sup>-1</sup>K<sup>-1</sup> für n-typ und von 1,74 bis 0,41 W m<sup>-1</sup>K<sup>-1</sup> für p-

---

typ Materialien) wurde aufgrund der feinen Körnung (50-130 nm) nach dem Sintern erfolgreich reduziert. Allerdings zeigte sich, dass die thermoelektrischen Eigenschaften empfindlich durch Oxidation degradiert wurden und daher ein sorgfältiger Schutz vor Kontamination während der Synthese erforderlich ist.

In dieser Arbeit wurde eine quantitative Untersuchung der Mikrostruktur an qualitativ hochwertigen supraleitenden und thermoelektrischen Materialien durchgeführt, die für die Anwendung relevant sind. Die Transporteigenschaften dieser Materialien wurden von anderen Gruppen im Detail untersucht. Die bedeutenden Beiträge dieser Arbeit sind die Anwendung einer verbesserten TEM-Probenpräparation, sowie hochwertige transmissionselektronenmikroskopische und hochgenaue, quantitative, spektroskopische Untersuchungen. Dies ermöglichte eine genaue Struktur-Eigenschaften-Korrelation und eine Verbesserung der Leistungsfähigkeit dieser Materialien.



# Chapter Preview

This thesis is divided into three parts:

- **Part I: Electron Microscopy and Specimen Preparation** - contains two chapters (Chapter 1 and 2) and will present the methodology used for sample preparation, microscopy and spectroscopy.
- **Part II: Structure-property Correlation of DyBa<sub>2</sub>Cu<sub>3</sub>O<sub>7-x</sub> Superconductors** - contains four chapters (Chapter 3-6). Chapter 3 is an introductory chapter and will present the basics of superconductivity. Remaining chapters of this part will present the microstructure-chemistry-physical property correlation of DyBa<sub>2</sub>Cu<sub>3</sub>O<sub>7-x</sub> (DyBCO) coated conductors (CCs) grown by inclined substrate deposition (ISD) technology.
- **Part III: Structure-property Correlation of Thermoelectric Bi<sub>2</sub>Te<sub>3</sub> Bulk Materials** - contains three chapters (Chapter 7-9) and will present an introduction to thermoelectricity and results of Bi<sub>2</sub>Te<sub>3</sub> bulk and nano-structured bulk materials.

**Chapter 1** is an introduction to electron microscopy and characterization of inorganic materials. A brief explanation of kinematical- and dynamical-theory of diffraction contrast is presented from literature. This chapter will also present a brief introduction to advanced electron microscopy techniques such as energy-filtered TEM (EFTEM), high-resolution TEM (HRTEM) and scanning TEM (STEM) techniques.

**Chapter 2** is dedicated to specimen preparation techniques for TEM. We will explain here preliminary preparation techniques involved in all kind of specimen preparation. A detailed step by step recipe for the plan-view and cross-section specimen preparation using conventional techniques such cutting, grinding, polishing and/or dimpling followed by argon (Ar<sup>+</sup>) ion etching is given. Additionally a more advanced preparation technique, focused ion beam (FIB) preparation, is explained for cross-section specimen preparation. Advantages and disadvantages of each technique is discussed.

**Chapter 3** is an introduction to superconductivity and physics of high-temperature superconductors (HTS). Various aspect of HTS such as critical current, critical current density, current limiting factors, biaxial texturing, and way to reduce losses and enhancing critical currents by pinning are discussed.

CCs technology and various routes for CCs technology such as ion beam assisted deposition (IBAD), rolling assisted biaxially-textured substrate (RABiTS), and ISD are described. Structural properties of DyBCO material are discussed briefly.

**Chapter 4** presents the results of Hastelloy-MgO interface of CCs deposited by the ISD technology, particularly focusing on diffusion phenomena occurring at the interface at elevated temperatures yielding void formation and affecting adhesion property of the interface. This chapter also presents a technological solution to the diffusion problem by introducing an additional blocking layer at the interface.

**Chapter 5** summarizes the growth behavior of superconducting DyBCO thin films deposited by ISD for CCs. Biaxial texturing and the orientation of DyBCO films with respect

to ISD MgO films are discussed in details. Interface, grain boundary, and volume energies of the DyBCO film were calculated and a growth model for the DyBCO film is discussed.

**Chapter 6** is about enhancing the superconducting properties of DyBCO CCs by artificial pinning. It presents the results of barium zirconium oxide ( $\text{BaZrO}_3$ ) doped DyBCO CCs deposited by inclined substrate deposition. Effect of the ISD tilted geometry on the size and alignment of  $\text{BaZrO}_3$  precipitates will be discussed in detail.

**Chapter 7** is an introduction to thermoelectricity and physics of thermoelectric materials. Various parameters affecting the thermoelectric figure of merit will be discussed. It summarizes the important physical properties of  $\text{Bi}_2\text{Te}_3$  and  $\text{Sb}_2\text{Te}_3$  bulk thermoelectric materials.

**Chapter 8** is dedicated to the structural modulation (nns: natural nano structure) observed in bulk  $\text{Bi}_2\text{Te}_3$  and  $\text{Sb}_2\text{Te}_3$ . For the first time, a controlled formation and removal of the nns in bulk  $\text{Bi}_2\text{Te}_3$  by  $\text{Ar}^+$  ion irradiation was shown. The nns consists of a sinusoidal displacement field with amplitude of 10 pm and periodicity of 10 nm. Furthermore the influence of nns on the thermoelectric properties will be discussed.

**Chapter 9** is about enhancing the thermoelectric properties of  $\text{Bi}_2\text{Te}_3$  and  $\text{Sb}_2\text{Te}_3$  bulk materials by spark plasma sintering. Results of microstructural study of spark plasma sintered nanostructured  $\text{Bi}_2\text{Te}_3$  and  $\text{Sb}_2\text{Te}_3$  bulk materials will be presented. Effect of the sintering temperature and pressure on the microstructure and transport properties such as thermal conductivity, electrical conductivity etc. and hence on thermoelectric figure of merit will be discussed.

# Contents

<b>Summary</b>	<b>i</b>
<b>Zusammenfassung</b>	<b>iii</b>
<b>Chapter preview</b>	<b>vii</b>
<b>Contents</b>	<b>ix</b>
<b>I Electron Microscopy and Specimen Preparation</b>	<b>1</b>
<b>1 Electron Microscopy and Spectroscopy</b>	<b>3</b>
1.1 Introduction . . . . .	3
1.2 Transmission Electron Microscopy (TEM) . . . . .	3
1.2.1 Transmission electron microscope used . . . . .	3
1.2.2 Techniques and acquisition conditions used . . . . .	5
1.2.3 Conventional Transmission Electron Microscopy . . . . .	6
1.2.4 High Resolution Transmission Electron Microscopy . . . . .	10
1.2.5 Analytical Electron Microscopy . . . . .	11
<b>2 TEM Specimen Preparation</b>	<b>15</b>
2.1 Introduction . . . . .	15
2.2 Materials and Methods . . . . .	16
2.2.1 Coated conductors (CCs) . . . . .	16
2.2.2 Thermoelectric materials . . . . .	16
2.3 TEM Specimen Preparation Methods . . . . .	18
2.3.1 Conventional mechanical grinding and polishing method . . . . .	18
2.3.2 Dimpling method . . . . .	23
2.3.3 Focused Ion Beam (FIB) method . . . . .	24
2.4 Results . . . . .	25
2.5 Discussion . . . . .	26
2.5.1 Stresses and stress building-up in coated conductors . . . . .	26
2.5.2 Consequence of stresses on plan-view sample preparation . . . . .	27
2.5.3 Consequence of stresses on cross-section sample preparation . . . . .	27
2.6 Conclusions . . . . .	28
<b>II Structure-property Correlation of DyBa<sub>2</sub>Cu<sub>3</sub>O<sub>7-x</sub> Coated Conductors</b>	<b>31</b>
<b>3 Basics of Superconducting Coated Conductors</b>	<b>33</b>
3.1 Introduction . . . . .	33
3.2 Superconductivity and types of Superconductors . . . . .	34

3.3	Critical Current Density of Superconductors . . . . .	36
3.3.1	Critical current limiting mechanism . . . . .	36
3.4	Structural Properties of DyBa <sub>2</sub> Cu <sub>3</sub> O <sub>7-x</sub> . . . . .	39
3.5	Coated Conductors (CCs) . . . . .	40
3.5.1	Requirements for applications . . . . .	40
3.6	Flux-line Pinning in DyBa <sub>2</sub> Cu <sub>3</sub> O <sub>7-x</sub> based Coated Conductors . . . . .	43
3.6.1	Intrinsic pinning centers . . . . .	43
3.6.2	Artificial pinning centers . . . . .	44
<b>4</b>	<b>Hastelloy-MgO Interface and Diffusion Phenomena at Elevated Temperatures</b>	<b>45</b>
4.1	Introduction . . . . .	45
4.2	Experimental . . . . .	46
4.2.1	SEM and TEM specimen preparation . . . . .	46
4.2.2	SEM and TEM analysis . . . . .	47
4.3	Results . . . . .	48
4.3.1	Microstructure of the Hastelloy-MgO interface of fully-processed sample	48
4.3.2	Microstructure of the Hastelloy-MgO interface of semi-processed sam- ples . . . . .	49
4.3.3	Microstructure of the Hastelloy-Yttrium-MgO interface of fully-processed samples with an Yttrium (Y) buffer layer . . . . .	50
4.3.4	Microstructure of the Hastelloy-Ag-MgO interface of fully-processed samples with a Silver (Ag) buffer layer . . . . .	52
4.4	Discussion . . . . .	53
4.4.1	Cr analysis by electron energy loss spectroscopy (EELS) and energy- filtered TEM . . . . .	53
4.4.2	Metal-oxide interface thermodynamics . . . . .	55
4.4.3	Technological solution . . . . .	57
4.5	Summary . . . . .	57
<b>5</b>	<b>Growth Behavior of Superconducting DyBa<sub>2</sub>Cu<sub>3</sub>O<sub>7-x</sub> Thin Films Deposited by In- clined Substrate Deposition for Coated Conductors</b>	<b>59</b>
5.1	Introduction . . . . .	59
5.2	Experimental . . . . .	60
5.2.1	Tape fabrication process . . . . .	60
5.2.2	SEM and TEM specimen preparation . . . . .	60
5.2.3	SEM and TEM analysis . . . . .	61
5.3	Results . . . . .	61
5.4	Discussion . . . . .	64
5.4.1	Inclined substrate deposition (ISD) technology . . . . .	64
5.4.2	DyBa <sub>2</sub> Cu <sub>3</sub> O <sub>7-x</sub> film growth mechanism and origin of microstructure observed . . . . .	64
5.4.3	Considerations of relevant energies in DyBa <sub>2</sub> Cu <sub>3</sub> O <sub>7-x</sub> films . . . . .	65
5.4.4	Comparison of the microstructure of inclined substrate deposition (ISD) grown films with films grown by other technologies . . . . .	68
5.5	Conclusions . . . . .	69
<b>6</b>	<b>Microstructure of BaZrO<sub>3</sub> Doped DyBa<sub>2</sub>Cu<sub>3</sub>O<sub>7-x</sub> Coated Conductors Deposited by Inclined Substrate Deposition</b>	<b>71</b>
6.1	Introduction . . . . .	71
6.2	Experimental . . . . .	72
6.3	Results . . . . .	72
6.4	Discussion . . . . .	74

---

6.5	Conclusions . . . . .	76
<b>III Structure-property Correlation of Thermoelectric <math>\text{Bi}_2\text{Te}_3</math> Bulk Materials</b>		<b>79</b>
<b>7</b>	<b>Thermoelectricity</b>	<b>81</b>
7.1	Introduction . . . . .	81
7.2	Basic Thermoelectric Phenomena . . . . .	82
7.2.1	Seebeck and Peltier effects . . . . .	82
7.3	Definition and Description of the Figure of Merit . . . . .	83
7.4	Transport Properties and High Figure of Merit Criteria . . . . .	84
7.4.1	Seebeck coefficient or thermopower . . . . .	84
7.4.2	Electrical conductivity . . . . .	84
7.4.3	Thermal conductivity . . . . .	85
7.4.4	Criterion for High-ZT or high performance thermoelectric material . . . . .	85
7.5	Thermoelectricity in $\text{Bi}_2\text{Te}_3$ . . . . .	86
7.5.1	Crystal structure and thermoelectric properties of bulk $\text{Bi}_2\text{Te}_3$ . . . . .	86
7.5.2	Motivation of this work . . . . .	87
<b>8</b>	<b>Switching of the Natural Nanostructure in <math>\text{Bi}_2\text{Te}_3</math> Materials by Ion Irradiation</b>	<b>89</b>
8.1	Introduction . . . . .	89
8.2	Experimental . . . . .	90
8.3	Results and Discussion . . . . .	91
8.4	Conclusions . . . . .	93
<b>9</b>	<b>Spark Plasma Sintered Nanostructured <math>\text{Bi}_2\text{Te}_3</math> bulk with Low Thermal Conductivity</b>	<b>95</b>
9.1	Introduction . . . . .	95
9.2	Materials and Methods . . . . .	95
9.2.1	Material synthesis and transport properties measurements . . . . .	95
9.2.2	TEM specimen preparation and analysis . . . . .	97
9.3	Results . . . . .	97
9.3.1	Crystallite sizes and thermoelectric properties . . . . .	97
9.3.2	Nanostructure of p-type materials after spark plasma sintering . . . . .	98
9.3.3	Advanced TEM and spectroscopy of p-type materials after spark plasma sintering . . . . .	98
9.3.4	Nanostructure of n-type materials after spark plasma sintering . . . . .	100
9.3.5	Advanced TEM and spectroscopy of n-type materials after spark plasma sintering . . . . .	100
9.4	Discussion . . . . .	101
9.5	Conclusions . . . . .	103
<b>Appendix A Specimen Preparation Tools</b>		<b>105</b>
<b>Bibliography</b>		<b>109</b>
<b>List of Tables</b>		<b>119</b>
<b>List of Figures</b>		<b>121</b>
<b>List of Acronyms and Symbols</b>		<b>125</b>
<b>Acknowledgment</b>		<b>127</b>

---

<b>Eidesstattliche Versicherung</b>	<b>129</b>
<b>Declaration</b>	<b>131</b>
<b>List of Publications</b>	<b>133</b>
<b>Curriculum Vitae</b>	<b>135</b>

**Part I**

**Electron Microscopy and Specimen  
Preparation**



# Chapter 1

## Electron Microscopy and Spectroscopy

### 1.1 Introduction

In this thesis a study of two different materials has been carried out: (i) superconductors  $\text{DyBa}_2\text{Cu}_3\text{O}_{7-x}$  (DyBCO) and (ii) thermoelectric ( $\text{Bi}_2\text{Te}_3$ ). DyBCO and  $\text{Bi}_2\text{Te}_3$  both have layered structure and show isotropic behavior, i.e. physical properties depend on the micro- and nano-texturing and its orientation. Therefore, a better understanding of structure-property correlation for such nanostructure materials can only be understood by employing a number of electron microscopy and microanalyses methods and tools. Furthermore, nanostructured materials take on rich variety of properties and promise exciting new advances in the field of superconductivity and thermoelectricity. However, to get a useful benefit of nanostructured material, precise control at sub 100 nm level of nanostructuring is of crucial importance. Therefore, analytical Transmission Electron Microscopy (TEM), i.e. energy-filtered TEM (EFTEM) combined with energy-dispersive X-ray spectrometry (EDX), are methods of choice for such a study.

Today, TEM comprises a wide range of different methods that use the various signals arising from the interaction of the electron beam with the sample to obtain information about crystal structure, microstructure, chemical composition and electronic structure. The methods that are needed are determined by the question to be solved. In this thesis the following methods were applied: conventional bright-field (BF), dark-field (DF) TEM (for microstructure), high-resolution TEM (for nanostructure), electron diffraction (for texturing), EDX spectroscopy (for chemical composition), electron spectroscopic imaging (ESI) and EFTEM (for elemental mapping).

These electron microscopy methods are briefly described in this chapter and were primarily utilized to characterize and to establish a structure-property correlation for DyBCO superconducting thin films coated conductors (CCs) grown by the inclined substrate deposition (ISD) technology. However, all these methods are equally important for many other materials, as an example, in this thesis  $\text{Bi}_2\text{Te}_3$  nanostructured bulk materials were studied by utilizing the methods listed above.

### 1.2 Transmission Electron Microscopy (TEM)

#### 1.2.1 Transmission electron microscope used

##### 1.2.1.1 Zeiss EM912 omega

A Zeiss EM912 $\Omega$  TEM [1] was used with a  $\text{LaB}_6$  gun operated at 120 kV yielding a point resolution of 0.37 nm (**Fig. 1.1a**). Fig. 1.1b shows a ray diagram of the electron beam passing through the Omega energy filter. The microscope is equipped with (i) a Köhler illumination system [2], (ii) an Omega energy filter [3], (iii) a side entry EDX detector with an energy resolution of 132 eV at the  $Mn - K_{\alpha 1}$  line, (iv) a low background, liquid nitrogen cooling,

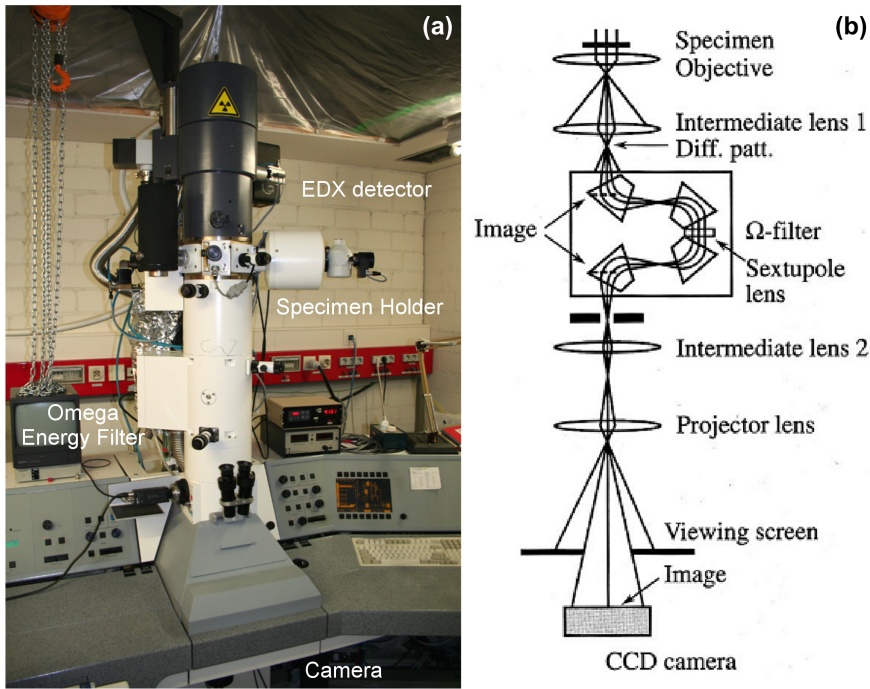


**Figure 1.1:** (a) Photograph of the Zeiss912 Omega TEM and (b) the electron-beam path and the Omega in-column energy-filter [1].

double-tilt holder with a tilting range of  $\pm 60^\circ$  for the X-axis and  $\pm 30^\circ$  for the Y-axis, and (v) a CCD camera (14 bit,  $2048 \times 2048$  pixel).

A detailed ray diagram of the Omega in-column energy filter is shown in **Fig. 1.2**. The energy filter generates in its exit image plane an achromatic 1:1 image of its entrance image plane, i.e., all electrons from one image point are focused again, but electrons of different energy losses pass this point with different angles to the optical axis. All electrons of the same energy are focused at the same point in the energy-dispersive plane of the spectrometer, which is located below the exit image plane, thus forming an electron energy loss spectrum [3]. A slit aperture of variable width is centered around the optical axis in the energy dispersive plane. Electrons which have lost a definite amount of energy in the sample are selected by this aperture and used for further imaging.

An EFTEM, therefore, offers many more modes of operation than a conventional TEM, e.g., energy-filtered bright- and dark-field imaging, electron-spectroscopic imaging (ESI), electron-

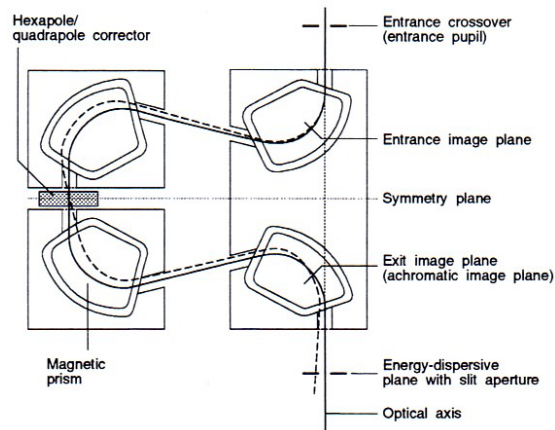


**Figure 1.2:** Schematic diagram of the Omega in-column spectrometer. Solid line shows the achromatic electron beam, whereas, dotted line shows spectrally dispersed electron beam [1].

**Table 1.1:** Acquisition conditions and parameters used for imaging and diffraction pattern for DyBCO and Bi<sub>2</sub>Te<sub>3</sub> materials.

	<b>Imaging</b>	<b>Diffraction Pattern</b>
Condenser aperture	3	3
Objective aperture	3 (3.5 mrad)	none
Width of the energy slit aperture	10 eV	10 eV
Excitation error (s) for BF	slightly > 0	-
Excitation error (s) for DF	0	-
Magnifications (kx)	10, 16, 25 31, 50, 63, 125	-
Camera length (mm)	-	293, 450, 540
Acquisition time (s)	1-5	1-10

**Table 1.2:** Acquisition conditions and parameters used for acquiring RGB images of DyBCO and Bi<sub>2</sub>Te<sub>3</sub> materials.

	<b>DyBCO</b>	<b>Hastelloy-MgO interface</b>	<b>Bi<sub>2</sub>Te<sub>3</sub></b>	<b>Sb<sub>2</sub>Te<sub>3</sub></b>
Width of the energy slit aperture	5 eV	5 eV	5 eV	5 eV
Objective aperture (mrad)	3.5	3.5	3.5	3.5
1 <sup>st</sup> window position (eV)	17		15	15
2 <sup>nd</sup> window position (eV)	26		25 (Bi-O <sub>IV,V</sub> )	31
3 <sup>rd</sup> window position (eV)	37		15	15
Magnifications (kx)	20	20	20	20
Acquisition time (s)	1-5	1-5	1-3	1-3

spectroscopic diffraction (ESD), electron energy-loss spectroscopy (EELS), element or structure contrast, plasmon loss imaging, image EELS, and many more. In addition to this, the quality of all the results obtained in conventional modes of operation of a TEM can be substantially improved by energy filtering [3].

Images and EELS spectra were acquired using a CCD camera (14 bit, 2048×2048 pixel) and processed by the iTEM software package [4]. A Si(Li) EDX detector (with an ultra thin window) was used to acquire the EDX spectra which are further processed by the INCA software package [5].

## 1.2.2 Techniques and acquisition conditions used

### 1.2.2.1 Techniques used

In this work the following techniques were utilized to characterize the DyBCO based superconducting coated conductors and the Bi<sub>2</sub>Te<sub>3</sub> thermoelectric material using Zeiss 912Ω TEM.

1. Energy-filtered bright-field (EF-BF) diffraction contrast imaging
2. Energy-filtered dark-field (EF-DF) diffraction contrast imaging
3. Energy-filtered selected area electron diffraction (SAED))
4. Low-loss and core-loss electron energy-loss spectroscopy (EELS)
5. Elemental maps by energy-filtered transmission electron microscopy (EFTEM)
6. Energy-dispersive X-ray (EDX) spectroscopy

### 1.2.2.2 Advantages and disadvantages of different techniques

In this work all images and diffraction patterns were acquired by using zero-loss energy-filtering with an energy slit aperture of 10 eV widths. Note that the zero-loss filtering removes the contribution of inelastically scattered electrons of both images and diffraction patterns. Therefore

**Table 1.3:** Acquisition conditions and parameters used for obtaining low-loss and core-loss EELS for DyBCO and Bi<sub>2</sub>Te<sub>3</sub> materials.

Spectra	Emission current ( $\mu\text{A}$ )	Spot size (nm)	Obj. Aper. (mrad)	Spectral mag. (x)	Acquisition time (ms)	Times integ.
Low-loss	< 1	10	3.5	100	50-200	50
Core-loss	3-5	50	8.1	100	1-5	-

energy filtering is more important for thicker specimens; hence, zero-loss filtering will improve the contrast and the resolution of such images considerably [6].

Further, the zero-loss filtering helps to reduce the inelastic background due to plasmon or higher energy-loss from the diffraction pattern yielding better contrast in the diffraction pattern and offers a possibility for more accurate, quantitative analysis. Note that plasmon losses are the dominating diffuse background in electron diffraction pattern [7].

EELS and EDX techniques were utilized to quantify the chemical composition of the matrix and secondary phases of the analyzed materials. Note that the EDX is quite easy to use and is particularly sensitive to heavier elements. The EELS is a little more difficult technique, however, is capable of measuring atomic composition, chemical bonding, valence and conduction band electronic properties [8]. The difference is mainly due to the difference in energy resolution between the two techniques ( $\sim 1$  eV or better for EELS and  $\sim 132$  eV for EDX). Therefore, at many instances in this work a combined (EELS and EDX) analysis were employed.

The most extensive analytical use of energy-filtered imaging is for core-loss imaging and elemental mapping. The ability of an energy filter to show a two dimensional distribution of a specific element, integrated over the specimen thickness, makes it a powerful tool for analytical studies. Though many features of the EELS (plasmon peaks, ionization edges) can be used for energy-filtered imaging, the low-loss region has particularly great potential for imaging of chemical phases and obtaining phase maps, due to high signal to noise ratio (SNR) and images can be recorded with short acquisition time. Therefore a combined, low-loss superimposed energy-filtered imaging (RGB) and EDX, analysis were employed to map and quantify the chemical composition of bulk, grain boundaries, interfaces and precipitates [6].

### 1.2.2.3 Acquisition condition used for different techniques with the Zeiss 912 $\Omega$ TEM

Same acquisition conditions and parameters were used for characterizing both the superconducting DyBa<sub>2</sub>Cu<sub>3</sub>O<sub>7-x</sub> coated conductors and Bi<sub>2</sub>Te<sub>3</sub> thermoelectric materials using Zeiss 912 $\Omega$  TEM. Acquisition conditions for diffraction contrast imaging (BF and DF), low-loss EFTEM imaging, EELS and EDX using the Zeiss 912 $\Omega$  TEM are given in Tables 1.1-1.3, respectively.

## 1.2.3 Conventional Transmission Electron Microscopy

Conventional TEM includes bright-field, dark-field imaging and selected area electron diffraction (SAED) techniques. In a conventional TEM, a thin specimen is irradiated by an electron beam, electrons interact strongly with atoms by elastic and inelastic scattering. The specimen must, therefore, be very thin, typically of the order of 5-100 nm for 120 kV electrons. In crystalline specimens, the primary beam (bright-field) or one Bragg diffracted beam on axis (dark-field) yields diffraction contrast which is important e.g. for imaging defects in crystalline materials [9].

### 1.2.3.1 Electron diffraction pattern

Information about crystal structure and orientation is provided by electron diffraction. The possibility of combining electron diffraction and the various imaging mode i.e bright-field and dark-field imaging is the most powerful feature of the TEM for the investigation of the crystal

structure and its defects in crystalline materials. Biaxial texturing and the orientation of MgO buffer layers and of high-temperature superconducting DyBCO films (see Chapter 3 for more details) were analyzed by acquiring SAED patterns of different layers. SAED patterns provide a quick determination of the microstructure, crystalline structure and texture of different layers and interfaces of CCs.

### 1.2.3.2 Energy-filtered diffraction contrast imaging

In crystalline or polycrystalline materials, the diffraction contrast imaging is a common and powerful technique to image grains, grain boundaries, precipitates, and defects [10]. To enhance the image contrast and make the interpretation of the image simpler, diffraction contrast images are usually acquired close to a two-beam condition. In a two-beam condition the sample is oriented in such a way that only the direct beam and one Bragg diffracted beam  $g_{hkl}$  are strongly excited in the diffraction pattern. Under such condition only the  $(hkl)$  planes perpendicular to the diffracting vector  $g_{hkl}$  are in or close to a Bragg diffracting condition. Such a diffraction condition yields the simplest case for interpreting the image contrast because only one set of lattice planes contributes to the image. Bright- and/or dark-field images under different two beam conditions together with their corresponding  $g_{hkl}$  diffraction vectors enable to characterize quantitatively the extended defects in a crystal [11].

Diffraction contrast images were enhanced by using elastically scattered electrons using an energy slit aperture of 5 eV and 10 eV in combination with an in-column omega energy filter to remove the inelastically scattered electrons from the final image. The inelastic scattering increases the background intensity thereby reducing the contrast in the diffraction contrast image especially in thicker regions of the specimen.

### 1.2.3.3 Kinematical theory of diffraction contrast

The physics of diffraction by a crystal can be best understood by considering the scattering from two identical atoms. The geometry of such a system introduces a path difference ( $\Delta l = -\vec{q} \cdot \vec{r}$ ) between the two scattered waves, which results in an additional phase factor  $exp(-2\pi i \vec{q} \cdot \vec{r})$  for the second atom at point  $\vec{r}$ , where  $\vec{q} = \vec{k}_0 - \vec{k}_D$  is the difference of the scattered wave vector,  $\vec{k}_D$ , and the incoming wave vector,  $\vec{k}_0$ . Using this approach for correlating the phase factor, the scattering amplitudes of many different systems can be calculated. Here we consider only a perfect crystal, i.e., a collection of unit cells. The scattering amplitude of a perfect crystal can then be written as the sum over all scattering centers at position  $(\vec{r}_j + \vec{R}_n)$ .

$$f = \sum_n \sum_j f_j e^{-2\pi i \vec{q} \cdot (\vec{r}_j + \vec{R}_n)} \quad (1.1)$$

$$f = \left( \sum_n e^{-2\pi i \vec{q} \cdot \vec{R}_n} \right) \left( \sum_j f_j e^{-2\pi i \vec{q} \cdot \vec{r}_j} \right) \quad (1.2)$$

where,  $f_j$  is the atomic scattering factor of atom  $j$  within unit cell,  $\vec{r}_j$  is the vector of the  $j$ th atom from the origin of the unit cell,  $\vec{R}_n$  is the lattice vector of the unit cell, and  $\vec{q} = \vec{k}_0 - \vec{k}_D = \vec{g} + \vec{s}$ ,  $\vec{g}$  is the reciprocal lattice vector, and  $\vec{s}$  is the excitation error [9].

In the above equation, the first factor is related to the *lattice function* and depends only on the Bravais lattice of the crystal, whereas the second factor is called *kinematical structure factor* and depends only on the position and type of atoms inside the unit cell. By considering thin slices of the specimen perpendicular to the electron beam (**Fig. 1.3**), and summing the scattering amplitude from each slice, taking into account the phase differences of the waves scattered at different depth, it can be shown that the diffracted intensity in the *two-beam approximation* is given by:

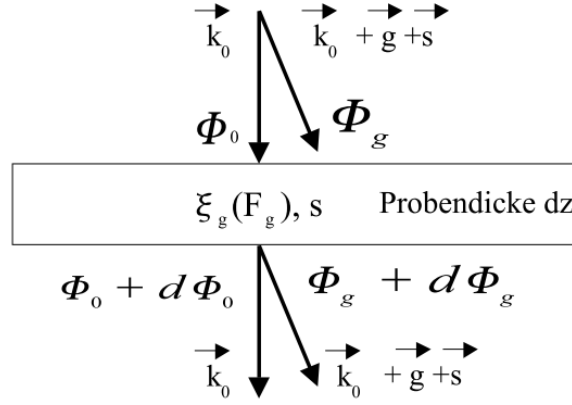


**Figure 1.3:** For the dynamic diffraction theory for the two-beam case, amplitude and phase changes in the direct and diffracted beam for a sample of thickness  $dz$  [14].

$$I_g = |\phi_g|^2 = \left(\frac{\pi}{\xi_g}\right)^2 \left(\frac{\sin(\pi t s)}{\pi s}\right)^2 \quad \text{and} \quad |\phi_0|^2 = 1 - |\phi_g|^2 \quad (1.3)$$

where,

$|\phi_0|$  = amplitude of direct beam;

$|\phi_g|$  = amplitude of diffracted beam;

$\xi_g$  = extinction length =  $\frac{\pi V \cos(\theta_B)}{\lambda F_g}$  ;

$V$  = volume of unit cell ;

$\theta_B$  = Bragg angle ;

$F_g$  = kinematical structure factor of the material at angle  $\theta_B$ ;

$\lambda = 2\pi/|\vec{k}|$  = wavelength.

This theory predicts that the diffracted intensity is periodic in the two independent quantities,  $t$  and  $s$  (see eq. 1.3) and explains the thickness fringes (occurring due to the periodicity with respect to  $t$ ) and bend contours (occurring due to variations of excitation error) in a sample. However, it can not explain the non-complementaries with respect to thickness fringes or bend contours observed in TEM bright-field and dark-field images. Furthermore, this theory is only valid for the case  $|\phi_g| \ll |\phi_0|$ , because  $\phi_g$  will diverge with increasing  $t$  for  $s \approx 0$  case. This is one of the reasons why the *dynamical theory* is needed, which takes into account the back diffraction of the diffracted beam into the direct beam and vice versa. Furthermore, the kinematical theory does not described what happened with. More details about the kinematical theory of diffraction contrast can be found in references [12, 13, 14].

#### 1.2.3.4 Dynamical theory of diffraction contrast

The theory of dynamical diffraction contrast imaging describes the rate of change of the amplitudes of both the diffracted and the direct beam when transmitting through a slice with thickness  $dz$ . The total wave function for the transmitted beam can be written as a series of sum of the direct beam and diffracted beams with an appropriate phase factor:

$$\psi^T(\vec{r}) = \phi_0 e^{2\pi i \vec{k}_0 \cdot \vec{r}} + \phi_{g_1} e^{2\pi i (\vec{k}_0 + \vec{g}_1 + \vec{s}_1) \cdot \vec{r}} + \phi_{g_2} e^{2\pi i (\vec{k}_0 + \vec{g}_2 + \vec{s}_2) \cdot \vec{r}} + \dots \quad (1.4)$$

For the *two-beam approximation*, which is the simplest case to deal but very important approximation, the above equation can be simplified as:

$$\psi^T(\vec{r}) = \phi_0 e^{2\pi i \vec{k}_0 \cdot \vec{r}} + \phi_g e^{2\pi i (\vec{k}_0 + \vec{g} + \vec{s}) \cdot \vec{r}} \quad (1.5)$$

where,  $\vec{k}_0$  and  $(\vec{k}_0 + \vec{g} + \vec{s})$  are the wave vectors of the direct and diffracted beam, respectively. As stated above the dynamical diffraction theory consider the back diffraction of the diffracted beam into direct beam as the beam travels through the sample. Therefore, if the amplitude  $\phi_g$  changes by a small increment ( $d\phi_g$ ) as the beam passes through a thin slice of material of thickness  $dz$ , we can write the expression for the changes in  $\phi_g$  and  $\phi_0$  as:

$$\frac{d\phi_g}{dz} = \frac{\pi i}{\xi_g} \phi_0 e^{2\pi i(\vec{g} + \vec{s}) \cdot \vec{r}} + \frac{\pi i}{\xi_0} \phi_g \quad (1.6)$$

$$\frac{d\phi_0}{dz} = \frac{\pi i}{\xi_0} \phi_0 + \frac{\pi i}{\xi_g} \phi_g e^{-2\pi i(\vec{g} + \vec{s}) \cdot \vec{r}} \quad (1.7)$$

where,  $\xi_0$  and  $\xi_g$  are the extinction lengths for the direct and diffracted beams, respectively, and an expression for extinction length is given in eq. 1.3. Eqs. 1.6 and 1.7 are known as *Howie-Whelan differential equation*, which is a pair of coupled linear differential equations. These equations (eqs. 1.6 and 1.7) shows that the rate of change of diffracted and direct beam amplitude are each proportional to the amplitude of the diffracted and direct beam. These equations can be written in matrix form as:

$$\frac{d}{dz} \begin{pmatrix} \phi_g(z) \\ \phi_0(z) \end{pmatrix} = i\pi \begin{pmatrix} \frac{1}{\xi_0} & \frac{1}{\xi_g} e^{-2\pi i(\vec{g} + \vec{s}) \cdot \vec{r}} \\ \frac{1}{\xi_g} e^{2\pi i(\vec{g} + \vec{s}) \cdot \vec{r}} & \frac{1}{\xi_0} \end{pmatrix} \begin{pmatrix} \phi_g(z) \\ \phi_0(z) \end{pmatrix} \quad (1.8)$$

Thus the rate of change of diffracted and direct beam amplitudes are each proportional to the amplitudes of the diffracted and direct beam.

Different to the kinematical theory these equations also consider the back diffraction of the diffracted beam to the direct beam as the beam travels through the sample. Solution of these equations give the amplitudes of the diffracted as well as of the direct beam. For the two beam case, we can write down the diffracted intensity at the bottom (exit surface) of the specimen (i.e. at  $z = t$ ) as:

$$|\phi_g|^2 = \left( \frac{\pi t}{\xi_g} \right)^2 \left( \frac{\sin(\pi t s_{eff})}{\pi t s_{eff}} \right)^2 \quad \text{and} \quad |\phi_0|^2 = 1 - |\phi_g|^2 \quad (1.9)$$

where,  $s_{eff} = \sqrt{s^2 + 1/\xi_g^2}$  is the effective excitation error. Eq. 1.9 shows that the diffracted intensity is periodic in two independent quantities,  $t$  and  $s_{eff}$ .

If we imagine the situation where  $t$  remains constant but  $s$  (and hence  $s_{eff}$ ) varies locally, then we produce bend contours. Similarly, if  $s$  remains constant while  $t$  varies, then thickness fringes will result. Therefore, the above equation could explain the thickness fringes and bending contours. Further, eq. 1.9 will never diverge with increasing thickness for the case  $s = 0$  as eq. 1.3 does.

However, solution in eq. 1.9 can not still explain the non-complementaries observed in the TEM bright-field and dark-field images, because inelastic scattering of electrons and absorption effect. Absorption effect can be considered phenomenologically, by adding an imaginary potential yielding the complex term,  $i/\xi'_0$  and  $i/\xi'_g$  to the terms  $1/\xi_0$  and  $1/\xi_g$  in the *Howie-Whelan differential equations*:

$$\frac{d}{dz} \begin{pmatrix} \phi_g(z) \\ \phi_0(z) \end{pmatrix} = i\pi \begin{pmatrix} \left( \frac{1}{\xi_0} + \frac{i}{\xi'_0} \right) & \left( \frac{1}{\xi_g} + \frac{i}{\xi'_g} \right) e^{-2\pi i(\vec{g} + \vec{s}) \cdot \vec{r}} \\ \left( \frac{1}{\xi_g} + \frac{i}{\xi'_g} \right) e^{2\pi i(\vec{g} + \vec{s}) \cdot \vec{r}} & \left( \frac{1}{\xi_0} + \frac{i}{\xi'_0} \right) \end{pmatrix} \begin{pmatrix} \phi_g(z) \\ \phi_0(z) \end{pmatrix} \quad (1.10)$$

After a suitable transformation for  $\phi_0$ ,  $\phi_g$ , the unit of length and by assuming  $\xi'_0 = \xi'_g$ , the above *Howie-Whelan* equation can be expressed as:

$$\frac{d}{dz} \begin{pmatrix} \phi_g(z) \\ \phi_0(z) \end{pmatrix} = i\pi \begin{pmatrix} (-A + 2iw) & (i - A) \\ (i - A) & (-A) \end{pmatrix} \begin{pmatrix} \phi_g(z) \\ \phi_0(z) \end{pmatrix} \quad (1.11)$$

where,  $A = \xi_g/\xi'_g$ , is called the anomalous absorption coefficient, and  $w = s\xi_g$ , is the excitation error parameter. The intensity of the direct and diffracted beam can then be determined analytically:

$$\phi_0(z) = \{ \cos^2(\beta/2)e^{-iXz} + \sin^2(\beta/2)e^{iXz} \} e^{-\pi z/\xi'_0} \quad (1.12)$$

$$\phi_g(z) = \cos(\beta/2)\sin(\beta/2) \{ e^{-iXz} - e^{iXz} \} e^{-\pi z/\xi'_0} \quad (1.13)$$

where,  $X = (\pi\sqrt{1+w^2})/\xi_g + (\pi i\sqrt{1+w^2})/\xi'_g$ .

Real crystals contain defects, e.g. dislocations, stacking faults etc. They cause local displacement  $R(\vec{r})$  of the atoms from their positions in the crystal with perfect translation symmetry. Such a displacement might destroy translational symmetry and yield bending of the lattice planes and therefore variation in local  $s$  values. The Howie-Whelan equation for such a distorted crystal, considering absorption, are written as:

$$\frac{d}{dz} \begin{pmatrix} \phi_g(z) \\ \phi_0(z) \end{pmatrix} = i\pi \begin{pmatrix} (\frac{1}{\xi_0} + \frac{i}{\xi'_0}) & (\frac{1}{\xi_g} + \frac{i}{\xi'_g})e^{-2\pi i(sz + \vec{g} \cdot \vec{R})} \\ (\frac{1}{\xi_g} + \frac{i}{\xi'_g})e^{2\pi i(sz + \vec{g} \cdot \vec{R})} & (\frac{1}{\xi_0} + \frac{i}{\xi'_0}) \end{pmatrix} \begin{pmatrix} \phi_g(z) \\ \phi_0(z) \end{pmatrix} \quad (1.14)$$

Similar to the ideal crystal, this can be modified as:

$$\frac{d}{dz} \begin{pmatrix} \phi_g(z) \\ \phi_0(z) \end{pmatrix} = i\pi \begin{pmatrix} (-A + 2i(w + \pi\vec{g} \cdot \frac{d\vec{R}}{dz})) & (i - A) \\ (i - A) & (-A) \end{pmatrix} \begin{pmatrix} \phi_g(z) \\ \phi_0(z) \end{pmatrix} \quad (1.15)$$

On comparing this equation with the defect free crystal, the effective excitation parameter for the distorted crystal is defined as:

$$w_{eff} = \left( w + \pi\vec{g} \cdot \frac{d\vec{R}}{dz} \right) \quad (1.16)$$

The above *Howie-Whelan* equation can only be solved numerically by considering the *column approximation* due to the local changes of the strain field (Eq. 1.16) [15]. For an ideal crystal, the second term will always yield zero, because of constant  $\vec{R}$ . If we ignore the absorption effect, eq. 1.15 will yield a well known equation (eq. 1.9) for the intensities, explaining thickness fringes. Further, from the above equation it is clear that if the product  $\vec{g} \cdot \frac{d\vec{R}}{dz}$  is zero (or indeed an integer) then the crystal containing defect will give contrast identical to that of perfect crystal. For example for a screw dislocation in an elastically isotropic media  $\frac{d\vec{R}}{dz}$  is directly proportional to  $\vec{b}$  (Burger vector), therefore a screw dislocation will be invisible if  $\vec{g} \cdot \vec{b}$  is zero. A more detailed description of dynamical diffraction theory can be found in references [12, 13, 14, 9].

#### 1.2.4 High Resolution Transmission Electron Microscopy

Conventional TEM diffraction contrast images yield amplitude contrast of the transmitted beam or of one diffracted beam, whereas, high-resolution TEM (HRTEM) imaging is an imaging technique where two or more beams are allowed to interfere to form an image and it yields both phase and amplitude contrast. Under favorable conditions, an HRTEM image can be directly interpreted in terms of the projected crystal structure (crystal potential) along the electron-beam

direction and the resulting HRTEM image is a two dimensional projection of the three dimensional structure, with the columns (or planes) of atoms being either dark or bright, depending on the exact specimen and imaging conditions.

The HRTEM is an imaging mode of the TEM that allows to image the crystal structure of a sample with atomic resolution. At present, the highest resolution realized is 0.5 Å with microscopes such as the aberration corrected Titan (FEI). At these small scales, individual atoms and crystalline defects can be imaged. The HRTEM technique allows the direct observation of the crystal structure and, therefore, has an advantage over other methods. However, it is not always possible to interpret the lattice images directly in terms of sample structure or composition. This is because the contrast in the images is sensitive to a number of factors: specimen thickness and orientation, objective lens defocus, spherical and chromatic aberrations. The ability to determine the positions of atoms within materials has made the HRTEM an indispensable tool for nanotechnology research and development in many fields. For more details about high resolution TEM see references [16, 17].

### 1.2.5 Analytical Electron Microscopy

The strength of the TEM is not only that it can provide high-magnification and/or high-resolution images that contain information down to 0.1-0.2 nm, but it can also operate with small electron probes in various micro-analytical modes with spatial resolution of 1-100 nm. For example a TEM equipped with an energy filter offers extraordinary advantages such as improved conventional TEM imaging (improved contrast and resolution), EELS [18] and EFTEM [6]. EELS can be utilized for specimen thickness measurement, elemental mapping etc.

#### 1.2.5.1 Electron Energy-Loss Spectroscopy (EELS)

During its propagation through a thin specimen, an electron may undergo inelastic scattering, i.e. it will lose energy. As a consequence, an energy-loss spectrum can either be recorded by a magnetic prism spectrometer behind the final image or with an imaging filter inside the column of the microscope. An EELS spectrum is considered to consist of three regions [8]. Those electrons which have lost negligible energy by inelastic scattering contribute to the *zero-loss peak*. The *low-loss* region, containing electrons which have lost up to about 50 eV, arises usually from plasmon scattering and interband transitions. The *core-loss* region, containing higher energy losses (higher than 126 eV), arises from inner shell ionization processes, which can be used for elemental analysis.

EELS in the TEM requires thin samples, significantly thinner than the mean free path, which is about 60 nm for Si for 120 kV electrons [19]. For the quantification of a specific element of interest the following has to be taken into account: (i) ionization cross-section,  $\sigma_K$ , (ii) number of atoms per unit area,  $N$ , (iii) collection angle,  $\beta$ , (iv) energy slit width,  $\Delta$ , and (v) the edge of interest, say  $K$ .

The total transmitted intensity,  $I_K$ , of an ionization edge of interest is given by [8]:

$$I_K = P_K I_T \quad (1.17)$$

where,  $P_K$  is the probability of ionization and  $I_T$  intensity of the whole spectrum. By assuming single ionization events, the probability of ionization can be given by:

$$P_K = N \sigma_K e^{-t/\lambda_K} \quad (1.18)$$

where,  $t$  is the specimen thickness and all other terms are explained in the above paragraph. The integrated intensity of the edge of interest for thin specimen having large mean free path ( $\lambda_k$ ) can be expressed as:

$$I_K \approx N\sigma_K I_T \quad (1.19)$$

or

$$N = \frac{I_K}{\sigma_K I_T} \quad (1.20)$$

Taking into account the width ( $\Delta$ ) of the energy slit and collection semi-angle ( $\beta$ ), the above equation could be expressed more precisely as:

$$N = \frac{I_K(\beta, \Delta)}{\sigma_K(\beta, \Delta) I_l(\beta, \Delta)} \quad (1.21)$$

For a ratio of two elements A and B, the low-loss intensity drops out:

$$\frac{N_A}{N_B} = \frac{\sigma_K^B(\beta, \Delta) I_K^A(\beta, \Delta)}{\sigma_K^A(\beta, \Delta) I_K^B(\beta, \Delta)} \quad (1.22)$$

Relevant ionization edges for elements analyzed in this thesis are given in **Table 1.4**. Ratio imaging technique could be utilized to make phase contrast images.

### 1.2.5.2 TEM EDX quantitative chemical analysis

EDX analysis, is an X-ray technique used to identify the elemental composition of nano sized regions in a specimen. SEM and TEM instruments equipped with EDX systems provide a unique possibility of quantitative chemical analysis. EDX in the TEM allows for specific element quantification, through point measurement and is relatively straight forward to use in comparison to EELS. We used a Zeiss 912 omega microscope equipped with a Si(Li) EDX detector from Oxford instrument provided with the INCA software [5]. For TEM EDX quantification, the Cliff-Lorimer equation holds for thin specimen if absorption and fluorescence effects are not considered [9]:

$$\frac{C_A}{C_B} = k_{AB} \frac{I_A}{I_B} \quad (1.23)$$

where,  $C_A$  and  $C_B$  are the weight percent of element A and B in the specimen,  $I_A$  and  $I_B$  are the net counts of characteristic X-ray lines, which we can measure. The term  $k_{AB}$  is termed as the *Cliff-Lorimer factor*.

Table 1.4: Ionization edges of elements relevant for this work.

Element	Z	Edges (eV)										$\theta_E$ [mrad]*							
		K	L <sub>I</sub>	L <sub>II</sub>	L <sub>III</sub>	M <sub>I</sub>	M <sub>II</sub>	M <sub>III</sub>	M <sub>IV</sub>	M <sub>V</sub>	N <sub>I</sub>	N <sub>II,III</sub>	N <sub>IV,V</sub>	O <sub>I</sub>	O <sub>II</sub>	O <sub>III</sub>	O <sub>IV</sub>	max., min.	
O	8	532	-	-	-	-	-	-	-	-	-	-	-	-	-	-	-	-	2.22, -
Mg	12	1305	89	52	52	-	-	-	-	-	-	-	-	-	-	-	-	-	5.44, 0.22
Si	14	-	149	100	99	-	-	-	-	-	-	-	-	-	-	-	-	-	0.63, 0.41
Ni	28	-	1008	872	855	112	68	68	-	-	-	-	-	-	-	-	-	-	4.20, 0.28
Cu	29	-	1096	951	931	120	74	74	-	-	-	-	-	-	-	-	-	-	4.56, 0.31
Y	39	-	-	-	-	395	313	301	160	158	46	26	-	-	-	-	-	-	1.65, 0.11
Zr	40	-	-	-	-	431	345	331	183	180	62	29	-	-	-	-	-	-	1.80, 0.12
Ag	47	-	-	-	-	717	602	571	373	367	95	62	-	-	-	-	-	-	2.99, 0.26
Ba	56	-	-	-	-	-	-	-	796	781	253	192	93	40	17	-	-	-	3.32, 0.07
Dy	66	-	-	-	-	-	-	-	-	-	416	332	154	63	26	-	-	-	1.73, 0.11
Sb	51	-	-	-	-	944	812	766	537	528	152	99	32	-	-	-	-	-	3.93, 0.13
Te	52	-	-	-	-	-	870	819	582	572	168	110	40	12	-	-	-	-	3.63, 0.05
Bi	83	-	-	-	-	-	-	-	-	-	939	806	464	160	117	93	27	-	3.91, 0.11

\*  $\theta_E = E/2E_0$ , where  $E_0 = 120 \text{ keV}$  and max. and min.  $\theta_E$  are calculated by using maximum and minimum value of energy, respectively.



## Chapter 2

# TEM Specimen Preparation

### 2.1 Introduction

Successful Transmission Electron Microscopy (TEM) in all of its manifestations depends on the quality of the specimens examined. One of the most critical requirements of a TEM sample is its thickness. The TEM specimen must be electron transparent (10-100 nm) and representative of the material to be studied. Modern ion milling [20], tripod polishing [21], and focused ion beam (FIB) [22] tools are helpful for TEM specimen preparation. However, preparation of thin specimens is more than just laboratory hardware and excellent protocols for thinning a specimen to electron transparency. Successful preparation of thin specimens requires detailed knowledge of the various methods available in the TEM and how sample thickness affects the analysis. The analytical question determines the method of sample preparation. For example, there may be several methods that could be used to produce specimens of the same material, but without a clear idea of the information required, even successfully thinned specimens may be only marginally useful. Thus, considerable thought should go into understanding the problem. In some cases, information from light microscopy and SEM will solve the problem without even making a TEM thin specimen. In other cases, such information will be helpful not only for the TEM analysis itself but also for preparing appropriate thin specimens for such analysis.

In this thesis, DyBa<sub>2</sub>Cu<sub>3</sub>O<sub>7-x</sub> (DyBCO) films with MgO buffer layers on Hastelloy substrates were studied. Films were grown by inclined substrate deposition (ISD) (explained in more details in Chapter 3) technology. The critical current density and other superconducting properties of such coated conductors (CCs) are governed by the quality of the microstructure i.e. the biaxial texture of the superconducting films. The biaxial texture of the superconducting films is itself governed by the biaxial texturing of the MgO buffer layer. Therefore, a precise study of the sample in plan-view as well as in cross-section is required to fully understand the microstructure and the biaxial texturing of the buffer layer and superconducting layer.

The thesis will also present a microstructural study of Bi<sub>2</sub>Te<sub>3</sub> Peltier bulk materials. More detailed explanation of the Bi<sub>2</sub>Te<sub>3</sub> Peltier bulk materials can be found in Chapter 7. The anisotropy of the material requires detailed study in two different perpendicular orientations. Therefore, samples were prepared and analyzed in two different perpendicular orientations. Furthermore, for such materials the lattice thermal conductivity is sensitive to structural disorder at the nano scale. Therefore, TEM analysis of such materials is of key importance and that requires thin artifact free specimen preparation.

In this chapter we discuss different TEM specimen preparation techniques with respect to their suitability, advantages and limitations for ISD CCs and for Bi<sub>2</sub>Te<sub>3</sub> thermoelectric materials. The techniques presented here are equally suitable for a wide range of other materials [23].

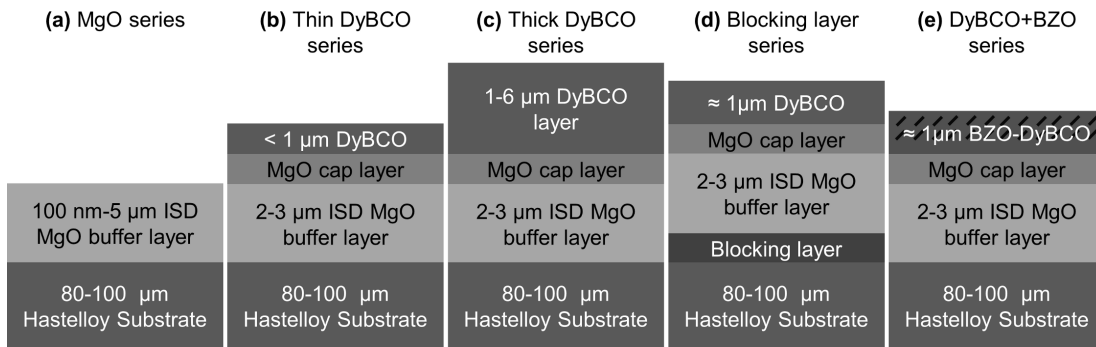


**Figure 2.1:** Schematics of the layer structure of ISD grown DyBCO CCs: (a) MgO, (b) the thin DyBCO, (c) thick DyBCO, (d) blocking layer and (e) DyBCO + BZO series. Note that the MgO series is a semi-processed sample, i.e. it does not have all the layers to study the MgO buffer layer.

## 2.2 Materials and Methods

### 2.2.1 Coated conductors (CCs)

All the superconducting tape samples studied in this thesis were grown by the ISD technology (explained in more details in Chapter 3) using thermal evaporation for all deposited films. A more detailed description of the used setup and the deposition parameters are found in Chapter 3 (Sec. 3.5.1.3) and also in references [24, 25]. To study different aspect of ISD CCs, samples with different layer structure were produced as shown in **Fig. 2.1**. For a fully processed sample, the sequence of layers starting from the Hastelloy substrate was: MgO buffer layer, MgO cap layer and DyBCO layer as shown in Fig. 2.1b. **Table 2.1** lists all the CC samples with their basic properties analyzed in this thesis.

TEM analysis of such CCs is of key importance, but at the same time specimen preparation of such CCs is challenging for the four reasons: (i) Hastelloy substrates are thin ( $\leq 100\ \mu\text{m}$ ) and, therefore, handling of the samples is difficult, particularly, in cross-section, (ii) surface roughness of the Hastelloy substrate and some time of thin films; therefore, gluing any dummy or support to Hastelloy substrate is not possible directly and gluing two samples face-to-face is also not possible, (iii) ion milling rates of the substrate (Hastelloy), buffer film (MgO), and superconducting film (DyBCO) are significantly different; the MgO buffer films are thinned faster than the Hastelloy substrates, and (iv) due to lattice mismatch (8.5%) between the buffer layer (MgO) and the superconducting thin film (DyBCO), the DyBCO films were found to be under tensile stress.

### 2.2.2 Thermoelectric materials

Thermoelectric materials analyzed in this thesis could be divided in two main categories: (i) bulk, and (ii) nano-structured bulk. Both categories had samples of n-type  $\text{Bi}_2(\text{Te}_{0.91}\text{Se}_{0.09})_3$  and p-type  $(\text{Bi}_{0.26}\text{Sb}_{0.74})_2\text{Te}_3$ . The bulk materials were synthesized by the Bridgman technique, which were obtained from commercially available Peltier devices. The nano-structured bulk materials was synthesized by ball milling yielding grain size of 10-20 nm. In a subsequent step compacted ultra-fine powder was sintered in a spark plasma sintering (SPS) apparatus, with which densities larger than 90% of the theoretical density could be achieved avoiding substantial grain growth. A more detailed description about samples and their properties are found in Chapter 7 and also in reference [26]. **Table 2.2** lists all the samples with their basic properties analyzed in this thesis.

Quantitative TEM analysis of such materials is of key importance to make structure-property-chemistry correlation. However, easy cleavage along the c-axis due to Van-der-Waals bonding turned out to be a severe obstacle for specimen preparation and hence the TEM study.

**Table 2.1:** CC samples with their basic properties investigated within the HIGHWAY project.

Series	Sample	Highway No.	Sample layer structure and thicknesses <sup>a</sup>	$J_c$ [MA cm <sup>-2</sup> ]
MgO	Sample 1	ISD100120C	HS (80 $\mu$ m) MgO BL (400 nm)	-
	Sample 2	ISD100122A	HS (80 $\mu$ m) MgO BL (5 $\mu$ m)	-
Thin DyBCO	Sample 3	Düse3120	HS (80 $\mu$ m) MgO BL (2.5 $\mu$ m) MgO CL (150 nm) DyBCO (330 nm)	2.1
	Sample 4	Düse39100	HS (80 $\mu$ m) MgO BL (2.2 $\mu$ m) MgO CL (150 nm) DyBCO (500 nm)	< 0.1
Thick DyBCO	Sample 5	DS1003090	HS (80 $\mu$ m) MgO BL (2.2 $\mu$ m) MgO CL (150 nm) DyBCO (5 $\mu$ m)	1.7
Blocking layer	Sample 6	DS1003091	HS (80 $\mu$ m) Ag MgO BL (2.2 $\mu$ m) MgO CL (150 nm) DyBCO (1 $\mu$ m)	0.8
	Sample 7	DS1003092	HS (80 $\mu$ m) Y MgO BL (2.2 $\mu$ m) MgO CL (150 nm) DyBCO (1 $\mu$ m)	0.6
	Sample 8	TUE027	HS (80 $\mu$ m) Si MgO BL (2.2 $\mu$ m) MgO CL (150 nm) DyBCO (1 $\mu$ m)	0.9
	Sample 9	TUE029	HS (80 $\mu$ m) Zr MgO BL (2.2 $\mu$ m) MgO CL (150 nm) DyBCO (1 $\mu$ m)	0.4
DyBCO+BZO	Sample 10	TUE002	HS (80 $\mu$ m) MgO BL (2.2 $\mu$ m) MgO CL (150 nm) DyBCO+3.5%BZO (1 $\mu$ m)	1.1

<sup>a</sup>HS: Hastelloy substrate; BL: Buffer layer; CL: Cap layer.

**Table 2.2:** Thermoelectric material samples with their basic properties (SPS sintering temperature  $T_{sint}$ , theoretical density  $\rho$ , thermal conductivity  $\lambda$ , thermopower  $S$  and electrical conductivity  $\sigma$ ) investigated within the DFG Priority Program “Nanostructured Thermoelectrics” (SPP1386). Transport properties were measured at room temperature ( $\sim 25$  °C).

Series	Sample	SPP1386 No.	Process	Type	$T_{sint}$ [°C]	$\rho$ [%]	$\lambda$ [W mK <sup>-1</sup> ]	$S$ [ $\mu$ V K <sup>-1</sup> ]	$\sigma$ [ $\Omega^{-1}$ cm <sup>-1</sup> ]
Bulk	Sample 1	Bi <sub>2</sub> Te <sub>3</sub> (BT06)	As cast	n-type	100	100	1.40    c	-172    c	183    c
	Sample 2	Sb <sub>2</sub> Te <sub>3</sub> (ST06)	As cast	p-type	100	100	1.21    c	203    c	269    c
Nano-structure bulk	Sample 3	n30kt-ht-122	SPS	n-type	230	90.7	0.44	-148	121
	Sample 4	p40kt-ht-370	SPS	p-type	130	92.6	0.41	121	57

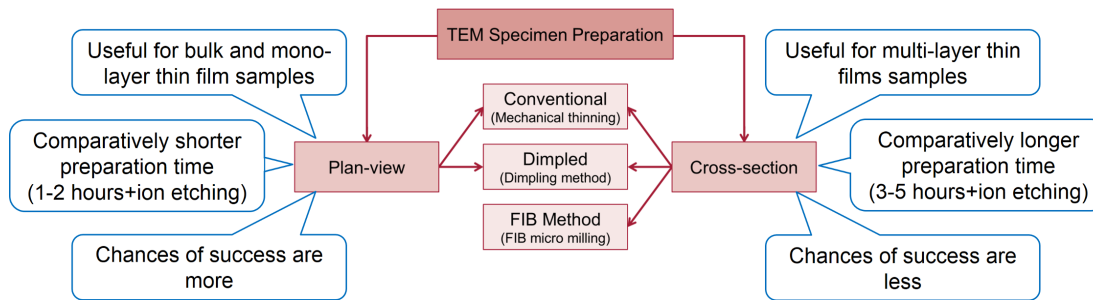


**Figure 2.2:** A flow chart of different types of TEM specimen preparation methods with their advantages and limitations.

## 2.3 TEM Specimen Preparation Methods

TEM specimen preparation can be divided into the following three main categories:

1. Mechanical grinding/polishing method
2. Dimpling method [21]
3. FIB method [22, 27]

The first two techniques are conventional methods and most frequently used methods for material science TEM sample preparation. The third method is an advanced method and requires an expensive FIB machine. In the following sections, a short description of each technique is given. Each method has its own advantages and limitations. The method of choice depends on the sample nature and information required. A flow chart of different preparation methods is shown in **Fig. 2.2**.

### 2.3.1 Conventional mechanical grinding and polishing method

Conventional mechanical grinding/polishing method is an important and frequently used techniques for TEM sample preparation. It consists of four major steps listed below:

1. Separation method of samples
2. Cross section sandwich technique
3. Mechanical grinding and polishing to less than 20  $\mu\text{m}$  thickness of samples
4. Gluing the ring and ion etching

#### 2.3.1.1 Separation method of samples

There is a long list of techniques that are employed for TEM specimen preparation in material science. Most important and frequently used techniques are described below:

**Sawing of samples:** This technique is used to make slices of bulk samples in order to reduce their dimensions and then prepare them using other preparation techniques. In most cases, slices with parallel faces of thickness 1-0.1 mm are made. This technique is used to cut practically all materials (bulk and multilayer, compact or porous) of any shape. They can be single phase or multiphase, from very hard to soft. A view graph of the sawing machine is shown in appendix A (Fig. A.4).

**Ultrasonic cutting of samples:** This technique is used to cut off a specimen using ultrasonic trepans of varying shapes (e.g. a 3 mm circular disk) on raw samples or samples that were previously reduced to small dimensions using sawing and/or polishing. These samples can then be worked on using other preparation techniques. A lubricant containing abrasive is placed

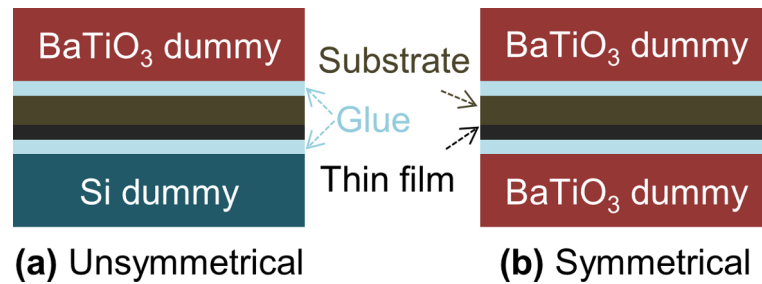


**Figure 2.3:** (a) Unsymmetrical and (b) symmetrical sandwich dummy structure.

between the tool and the specimen. The friction of the abrasive grains, which are harder than the specimen, cuts into the material with precision. This technique is used to cut bulk, thin film, single-phase, or multiphase materials. It is not suitable for ductile, very brittle, or soft materials. A view graph of the ultrasonic punching/cutting machine is shown in appendix A (Fig. A.4).

**Punching supporting rings:** This technique is used to punch out a ring of suitable material (e.g. Aluminium). The ring inner and outer diameters may vary depending on the need. These rings are used to provide a mechanical support to a finished and thin (less than 20  $\mu\text{m}$ ) TEM specimen. For a 3 mm diameter TEM holder, one can use a ring with outer diameter of 3 mm and inner diameter of 1.5 mm or 2 mm. This technique utilizes a special punching tool. A view graph of the ring punching tool is shown in appendix A (Fig. A.2).

### 2.3.1.2 Mechanical punching or cutting of samples

As discussed above, the ultrasonic cutting is not suitable for very hard (e.g. Hastelloy) or soft materials (e.g. Aluminium) metallic materials. A special punching tool is utilized to punch specimen of defined shape and size, for example a 3 mm circular disk from the specimen. This technique is used to punch thin films on thin substrate or tape, foils etc. It is not suitable for bulk, and very brittle materials. A view graph of the specimen punching tool is shown in appendix A (Fig. A.2).

Note that to retain the directional information in the punched out disks, samples were punched out by overlapping the successive punches as shown in **Fig. 2.7a**. For ISD CCs, this assured that in the cross-section samples the *c*-axis and in the longitudinal-section the [110] direction i.e. the tape direction of the DyBCO will lie in the plane of TEM specimens.

### 2.3.1.3 Cross-section sandwich technique

Sandwich technique consists of making a stack of at least two strips of the sample stuck face-to-face using a suitable glue (M-bond), helps to protect the surface layers during the thinning process. The stack also increases the size of the sample to be handled. The nature of the material or type of preparation to be performed may require a sandwich of the sample with two dummies from both the side of sample as shown in **Fig. 2.3**. Note that dummies are polished pieces of suitable material such as silicon, barium titanate etc. and of suitable size, for most of the cases we used  $3 \times 3 \text{ mm}^2$ . Then, the glued structure should be pressed between two brass piston (pressing tool) and backed in a hot oven at 120  $^{\circ}\text{C}$  for 2 hours. This will ensure a planar and close contact of the surfaces. A view graph of the pressing tool is shown in appendix A (Fig. A.3).

### 2.3.1.4 Mechanical grinding and polishing to less than 20 $\mu\text{m}$ thickness of samples

**Mechanical grinding of samples** This technique is used to grind bulk or thick specimen using: a SiC plate of different grit sizes (1000-5000) to produce smooth surfaces and thin spec-

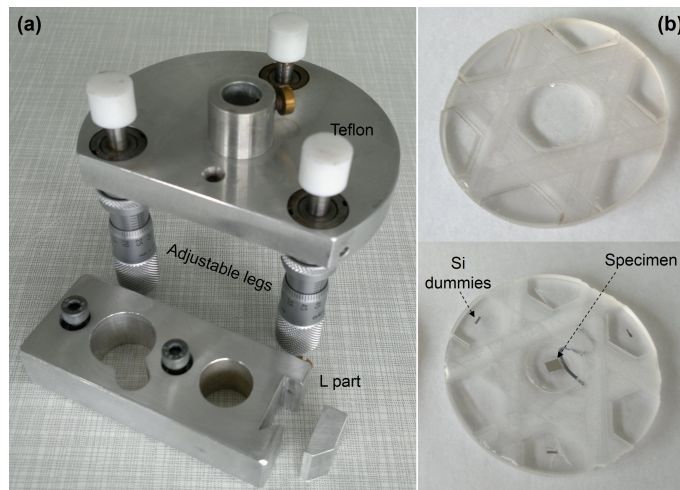


**Figure 2.4:** A view graphs of the (a) Tripod holder and (b) Star holder without and with glued dummies and specimen on the holder.

imens (less than  $300\ \mu\text{m}$ ), that can be directly used for mechanical polishing. The grinding is done by gluing the sample on a metal piece (holder) on a motorized SiC plates. For softer material one can use hand grinding, i.e. without motor. A view graph of the grinding machine with SiC plates is shown in appendix A (Fig. A.5).

**Mechanical polishing of samples:** This technique is used to produce smooth surfaces and thin specimens (less than  $20\ \mu\text{m}$ ) that have been obtained by sawing, punching, ultrasonic cutting, or grinding. This technique is also commonly used prior to dimpling method to thin the sample up to  $100\ \mu\text{m}$  thickness. In most cases, mechanical polishing is used to obtain a flat (parallel-sided slices), scratch-free surface, while reducing mechanical damage. This polishing technique employs diamond coated abrasive plates. A fluid (continuously flowing water) must be used, it serves as a lubricant, coolant and removes excess material particles. This technique can be used to polish almost all bulk, compact, and thin film materials. The materials can be multiphase materials and can contain precipitates or segregation. The materials can be of any hardness less than sapphire or diamond, with the exception of very soft materials. A view graph of the polishing disks is shown in appendix A (Fig. A.6). Generally, mechanical polishing was carried out by two kinds of holders:

1. Tripod holder
2. Star holder

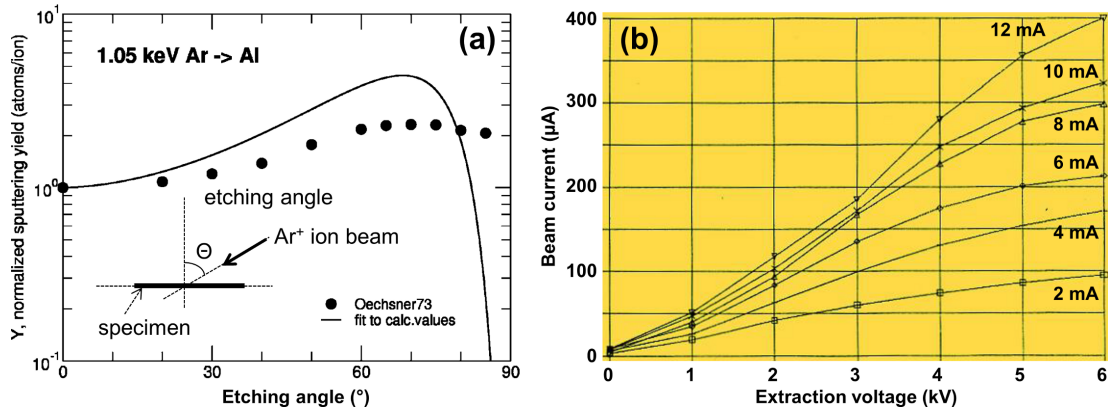
The Tripod holder shown in **Fig. 2.4a** is useful for samples having any thickness due to adjustable legs, but not suitable for thinning samples less than few tens of micron. Whereas, the Star holder polishing shown in Fig. 2.4b can only be used for samples having a thickness less than  $300\ \mu\text{m}$  because of Si dummies, which has a typical thickness of  $300\ \mu\text{m}$ . Star holder polishing consist of the following two main steps:

- Gluing three Si dummies on the alternate pads, and sample at the central pad using a suitable glue (white glue).
- Polishing the sample on diamond coated abrasive plates using the recipe given in **Table 2.3**.

More details about tripod polishing can be found in the reference [28].

**Table 2.3:** Recipe for the mechanical polishing on the diamond coated abrasive plates

Plate/Grit size [ $\mu\text{m}$ ]	Suitable for specimen thicknesses [ $\mu\text{m}$ ]
30	300-80
15	80-40
9	40-22
3	22-13
1	13-10

**Figure 2.5:** (a) Etching rate dependence on the beam incidence angle [29] and (b) the ion beam current vs. extractor voltage at different source current for the Fischione 1010 [20].

### 2.3.1.5 Gluing a ring to sample and ion etching

**Gluing a ring to sample:** This technique is used to provide mechanical stability to thin (less than 20  $\mu\text{m}$ ) and mechanically unstable samples (such as cross-section). In this technique a ring of aluminium or any other suitable material is glued on a fully processed and thin samples using a suitable glue (such as M-bond). Bake the glued sample at 100 °C for 20 minutes to make the glue harder.

**Ion etching of a finished sample:** This technique is used to thin samples down to electron transparency. It is suitable for the samples having a thickness between a few microns to maximum 20  $\mu\text{m}$ . It is generally used for final thinning of samples prepared by the star holder, tripod, or dimpling method. The thinning technique consists of sputtering the sample using ionic bombardment. A beam of  $\text{Ar}^+$  ions is generated, which is accelerated (0-8 kV for Fischione 1010) and directed towards the center of the sample. The sample can be tilted by an angle (0°-30° for Fischione 1010) with respect to the beam. The etching rate depends on the energy/dose (extraction voltage and source current), the tilt angle of the beam with respect to the specimen plane, and material to be etched. The sputtering yield depending on the etching angle is shown in **Fig. 2.5a**. Initially, the sputtering yield increases but then decreases due to increased ion implantation. **Fig. 2.5b** shows the ion beam current vs. extractor voltage at different source current for the Fischione 1010. The sample can also be rotated in its plane through a 0°-360° to make the etching process rotationally symmetric. A schematic of the etching geometry is shown in **Fig. 2.7d** and a view graph of ion etching machine (Fischione 1010) is shown in **Fig. 2.6**. Optimized etching parameters that yielded high quality samples are listed in **Table 2.4** for different materials. Using the recipes listed in **Table 2.4** almost amorphous free (only few nm) large (3-4  $\mu\text{m}$ ) and thin (few tens of nm) electron transparent samples were prepared.

In summary the conventional mechanical grinding/polishing method is most widely used technique to prepare TEM specimen from a variety of materials because of simple equipment used, works for plan-view as well as for cross-section samples. The most important steps of conventional mechanical grinding/polishing method for plan-view and cross-section are sum-



**Figure 2.6:** A view graph of Fischione 1010 low-angle ion etching machine.

**Table 2.4:** Optimized recipe for DyBCO, Bi<sub>2</sub>Te<sub>3</sub>, bulk and thin films, Si (single crystal) and Al foil ion etching using Fischione 1010 ion mill.

Steps	Energy		Rotation PV/CS [degree]	Tilt angle [degree]	Etching rate [ $\mu\text{m}/\text{hour}/\text{gun}$ ]
	V [kV]	I [mA]			
<b>DyBCO CCs</b>					
Perforation	3.5	3	$\pm 360/\pm 45$	12	2.2
Polishing	1	3	$\pm 360/\pm 45$	10	-
<b>Bi<sub>2</sub>Te<sub>3</sub>, Si, and Al</b>					
Perforation	3	3	$\pm 360/\pm 45$	12	2.1, 2.5, and 2.5
Polishing	1	3	$\pm 360/\pm 45$	10	-

marized below:

**Plan-view method:** It consists of the following main steps:

1. Punch a disk of 3 mm in diameter from sample using punching tool (Sec. 2.3.1.2) or ultrasonic cutter (Sec. 2.3.1.1).
2. Press the punched sample using pressing tool to make its surface flat (use this step only for samples cut using punching tool).
3. Clean the sample in acetone or ethanol using ultrasonic cleaner.
4. Grind the sample on SiC plates (only if sample is thicker than 300  $\mu\text{m}$ ) (Sec. 2.3.1.4).
5. Polish the sample using star holder polishing (Sec. 2.3.1.4).
6. Glue an aluminum ring on the sample for mechanical stability, if sample thickness is less than 20  $\mu\text{m}$  (Sec. 2.3.1.5).
7. Remove the polished sample from the holder by dissolving the glue in acetone.
8. Ion etch the sample as explained in Sec. 2.3.1.5.

**Conventional cross-section method:** It consists of the following main steps:

1. Repeat step 1 to 3 of the above section (Sec. 2.3.1.5).
2. Polish the substrate side for two side sandwich (ignore this step for one side sandwich).
3. Make the sandwich of the sample as explained in Sec. 2.3.1.3.
4. Cut the sandwich into two parallel slice or piece as shown in Fig. 2.7c.
5. Grind and polish the slices from both side using tripod and star holder polishing as explained in section (Sec. 2.3.1.4).

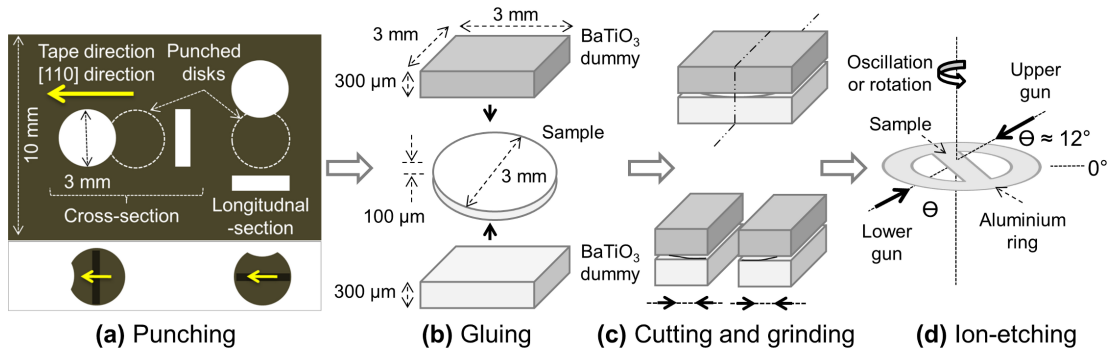


Figure 2.7: Four major steps of the conventional cross-section preparation.

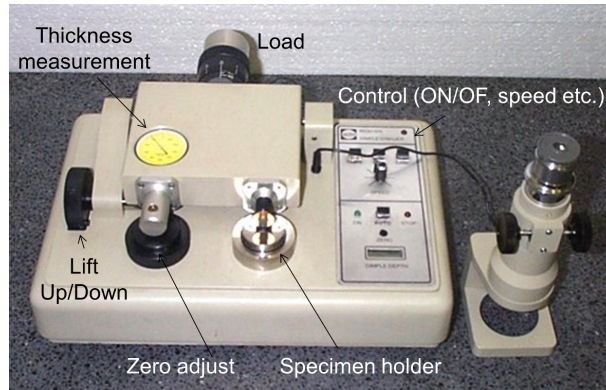


Figure 2.8: Dimpling tool or machine.

6. Repeat step 6 to 8 of the above Sec. (Sec. 2.3.1.5).

More detailed information about conventional mechanical grinding/polishing method can be found in the references [23, 30].

### 2.3.2 Dimpling method

This technique [31] is used to grind a concave impression or dimple, thinning the center of a disk. This polishing technique employs mechanical abrasion. The friction of the abrasive grains, which are harder than the specimen to be polished, is used to wear down materials. A view graph of a dimpling tool is shown in Fig. 2.8. A schematic in cross-sectional view of a dimpled sample and ion etching geometry of it are shown in Figs. 2.9a and 2.9b, respectively.

A plan-view dimpling mainly consists of the following steps:

1. Repeat the steps 1 to 5 of Sec. 2.3.1.5 and polish down the sample to less 100  $\mu\text{m}$  thickness.
2. Glue the sample on the dimpler holder (a cylindrical piece of glass).

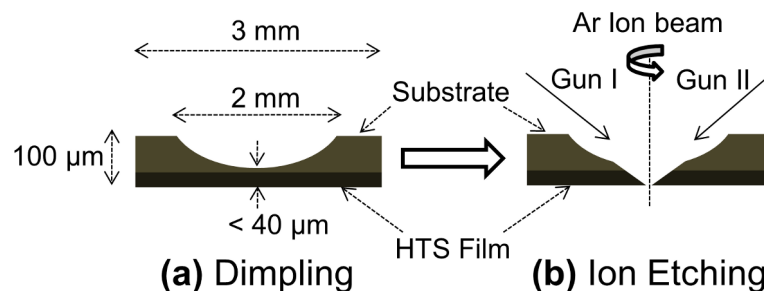


Figure 2.9: A schematic in cross-sectional view of (a) a dimpled sample and (b) its ion etching geometry.

**Table 2.5:** Optimal dimpling recipe for the ISD CCs (Hastelloy).

Specimen thickness [ $\mu\text{m}$ ]	Load [arbitrary unit]	Paste grit size [ $\mu\text{m}$ ]
120-60	35	16
60-40	30	6
40-30	30	2.5
30-24	25	2
24-20	25	0.5

3. Set the zero point with respect to the glass piece surface.
4. Turn on sample holder rotation and center the specimen with respect to the sample holder rotation i.e. at the cross-wire.
5. Set speed and load of the dimpler disk.
6. Turn on dimpler disk rotation, clean it, and apply a paste of suitable grit size (0.5-16  $\mu\text{m}$ ).
7. Gently drop the dimpler on the specimen and finish dimpling using the recipe given in **Table 2.5**
8. Remove the polished sample from the holder by dissolving the glue in acetone.
9. Ion etch the sample as explained in Sec. 2.3.1.5.

Note that the dimpling recipe given in Table 2.5 is optimal for CCs i.e. a hard material (Hastelloy substrate). The recipe will equally work well for other materials such as Si, just start with a reduced load, for example start with 25 load and accordingly reduce the load with the specimen thickness for Si.

### 2.3.3 Focused Ion Beam (FIB) method

This technique is used to machine a thin lamella (thin slice) on nano scale, in a precise direction and area of a sample. It consists of the following main steps:

1. Orient the sample in the required direction, searching for an area to be cut, and depositing either a metal layer or a carbon layer to protect the material surface during ion milling (**Fig. 2.10a**).
2. Machine two parallel trenches on both sides of the sample area to be observed (Fig. 2.10b).
3. Cut both sides of the slice to remove it and then attach it to a special TEM grid (Fig. 2.10c).
4. Attach the lamella to needle (micro-manipulator) (Fig. 2.10d).
5. Attach the lamella to the special TEM grid with the help of micro-manipulator (Fig. 2.10e).
6. Final thinning, down to a thickness of few tens of nm and then polishing (Fig. 2.10f).

The FIB method is a good technique for cross-section preparation. The FIB method is very useful for precise area and orientation selection. The FIB techniques could be used for delaminating films, for which the conventional cross-section will completely fail. A more detailed description of FIB method can be found in the references [22, 27, 23].

Since ISD CCs are composed of many layers with different etching or sputtering rates, therefore, getting FIB samples thinner than 50 nm for CCs is a challenging job. The FIB method has to be optimized for CCs with respect to the knock-on-damage and thinning parameters. Further the amorphization problem during the final FIB thinning of sample also makes it very difficult to get a FIB sample thinner than 50 nm. At present the conventional cross-section preparation yielded thinner samples for ISD CCs. Note that the FIB work was done at NMI in Reutlingen.

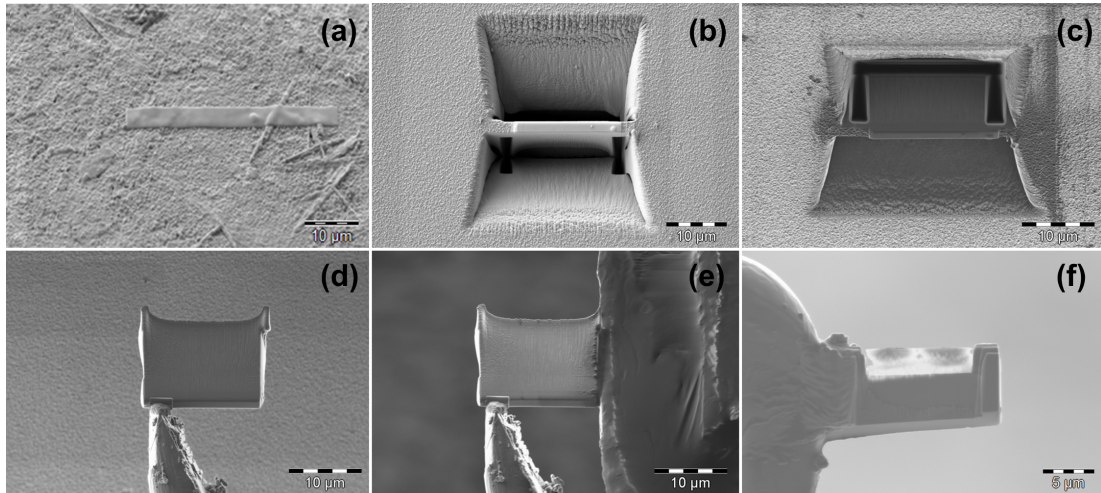


**Figure 2.10:** FIB TEM lamella preparation process: (a) Pt protection layer deposited on the area of interest on top of the DyBCO film, (b) milling parallel trenches, (c) cutting the edges of the slice or lamella for lift-out, (d) attached lamella to the needle, (e) attachment of the lamella to the special TEM grid, and (f) final thinning and polishing.

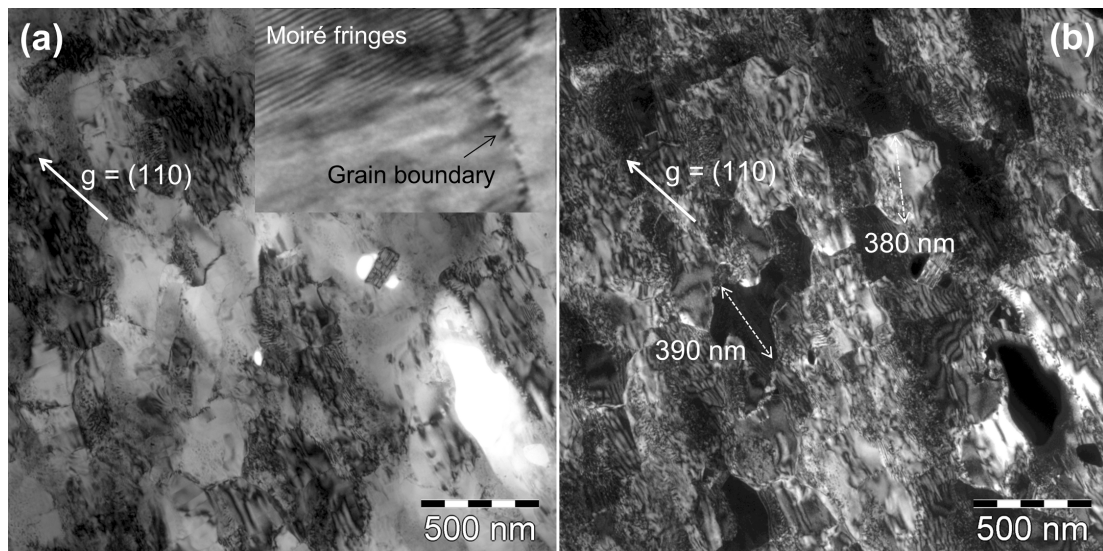


**Figure 2.11:** (a) Bright-field and (b) corresponding (110) dark-field image in plan-view of sample 3 (Table 2.1) prepared by dimpling method.

## 2.4 Results

**Figs. 2.11a** and 2.11b show an overview (low-magnification) bright-field and corresponding (110) dark-field images of a CCs (Sample 3, Table 2.1). The sample was prepared in plan-view by the dimpling method. We found large electron transparent area and were able to image individual grains, grain boundaries, dislocation, Moiré fringes due to small angle grain boundaries. DyBCO grains were found to be 200-500 nm in size. Diffraction contrast images were heavily dominated by strain contrast due to the high dislocation density. Only the dimpling method worked for CCs having tensile stresses in the DyBCO film. Note that the conventional plan-view preparation (Sec. 2.3.1.5) completely failed for such CCs due to the stresses present in the DyBCO film.

**Fig. 2.12a** shows an overview bright-field image of the same CCs (Sample 3, Table 2.1) sample in cross-section prepared by the conventional cross-section method (Sec. 2.3.1.5). **Fig. 2.12b** shows a high-resolution image at the MgO-DyBCO interface. **Figs. 2.13a** and 2.13b show an overview image and a high-resolution image of the same sample prepared by the FIB

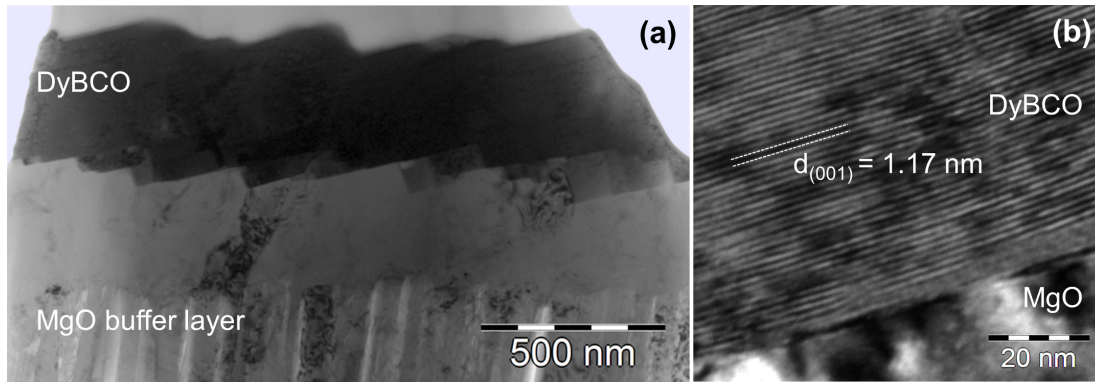


**Figure 2.12:** Conventionally prepared cross-section sample: (a) bright-field image and (b) high-resolution bright-field image of the MgO-DyBCO interface of sample 3 (Table 2.1).

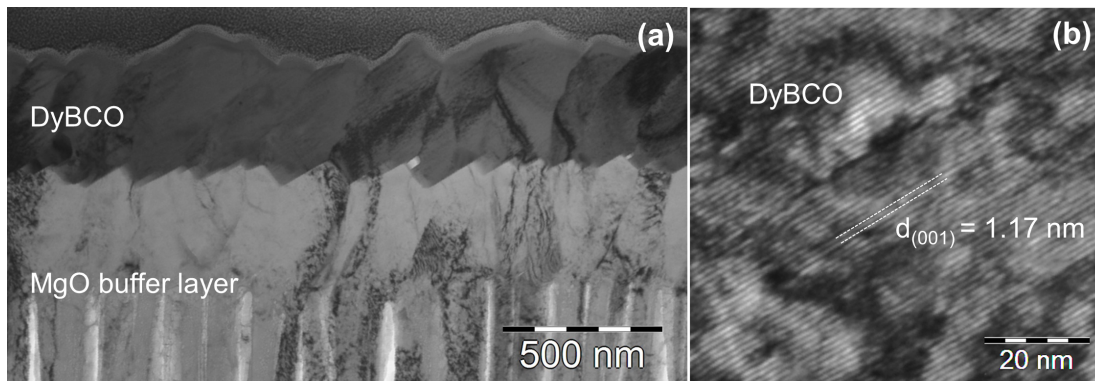


**Figure 2.13:** FIB prepared cross-section sample: (a) bright-field image and (b) high-resolution bright-field image of the DyBCO film of sample 3 (Table 2.1).

method (Sec. 2.10), respectively. Bright-field overview images show that the FIB method yields a large evenly thinned area compared to the conventional cross-section method. However, the high resolution images show  $d_{001}$  lattice fringes of DyBCO, it can be seen that conventionally prepared samples yielded a slightly better contrast and quality of the lattice fringes.

**Figs. 2.14a** shows selected area diffraction pattern of DyBCO films of conventionally prepared specimens. Fig. 2.14b is the corresponding diffraction pattern of FIB prepared specimens.

The FIB prepared samples yielded a large evenly thinned area compared to the conventional preparation. However, a ring pattern in the diffraction pattern of FIB prepared specimen can be seen, which shows that they are not as suitable for high resolution microscopy as conventionally prepared samples due to knock-on damage. The FIB method has to be further optimized with respect to the knock-on-damage and thinning parameters to yield amorphous and damage free TEM specimens.

## 2.5 Discussion

### 2.5.1 Stresses and stress building-up in coated conductors

During ion etching of conventionally prepared plan-view samples of CCs, it was found that the film starts bending towards the substrate side as it got thinned. A schematic of the bending direction is shown in **Fig. 2.15a**. Considering lattice parameters of the Hastelloy (0.361 nm), the MgO (0.4212 nm), the DyBCO (0.388-0.382 nm), and the bending direction, we concluded that either the MgO film is under compressive stress or the DyBCO film under tensile stress. Due to the bending of the DyBCO film, the incidence angle of  $\text{Ar}^+$  ions was increased and the DyBCO film was preferentially etched. As a consequence such samples did not yield electron

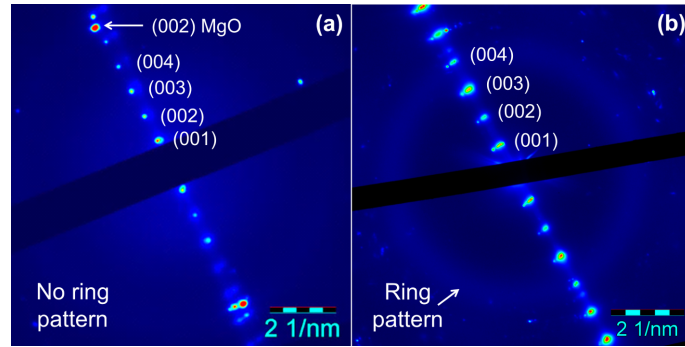


**Figure 2.14:** Selected area diffraction patterns of the DyBCO film shown in (a) Fig. 2.12 i.e. conventionally prepared and (b) Fig. 2.13 i.e. FIB prepared cross-section specimen.

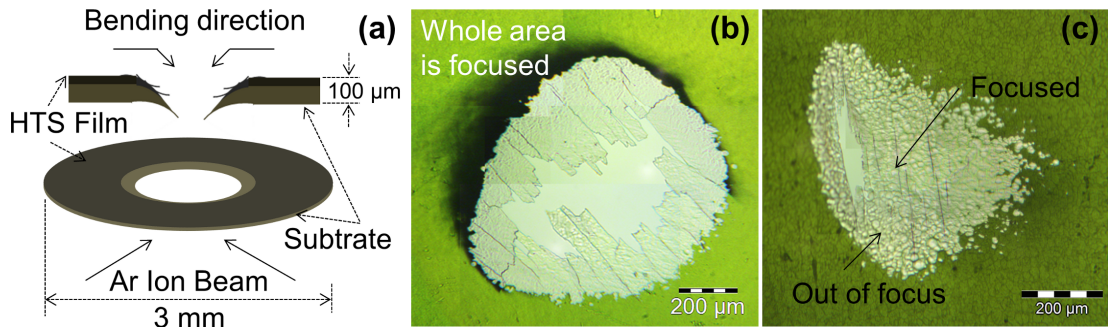


**Figure 2.15:** (a) A schematic drawing, showing bending of the ISD grown DyBCO film during ion etching due to the stresses present in the film. Light microscope images in plan-view of (b) sample 2 (semi-processed) and (c) sample 3 (fully processed) just after etching (Table 2.1).

transparent regions of DyBCO films. Bending could closely be detected in a stereo-microscope.

Fig. 2.15b and 2.15c show light microscope images of samples 2 and 3 in plan-view seen from the substrate side and acquired just after ion-etching. Sample 2 had a layer structure of Hastelloy substrate/MgO buffer layer, i.e. semi-processed, whereas sample 3 had a layer structure of Hastelloy substrate/MgO buffer layer/MgO cap layer/DyBCO, i.e. it was fully-processed (Table 2.1). The images show that no bending was observed for sample 2, whereas sample 3 shows a bending towards the substrate side and, therefore, we concluded that MgO film is stress free and only the DyBCO film is under tensile stress.

### 2.5.2 Consequence of stresses on plan-view sample preparation

Due to the stresses, the conventional plan-view preparation method [30] did not yield electron transparent regions of DyBCO films as discussed in the above section (Sec. 2.5.1). To avoid bending and hence preferential etching of DyBCO films, a mechanically more stable method such as dimpling (Sec. 2.3.2) was employed and good quality plan-view samples were prepared. The results of dimpled plan-view samples are shown in Fig. 2.11.

### 2.5.3 Consequence of stresses on cross-section sample preparation

Since the sputtering rate of Si is larger than that of BaTiO<sub>3</sub>, a sample architecture as shown in Fig. 2.3a will yield a high asymmetry after etching, i.e. the Si side will be etched away completely whereas the BaTiO<sub>3</sub> side will be still too thick, and will not be electron transparent. Therefore, the CCs cross-section TEM specimen will always have a thickness gradient, thin towards the Hastelloy substrate, thick towards the DyBCO surface. Since the Hastelloy substrate is partially etched away, the tensile stresses already evident in the plan-view specimen preparation will yield bending of the DyBCO film towards the substrate side. As a consequence, the

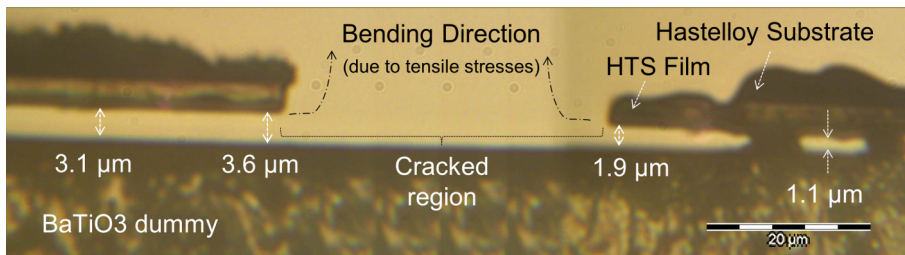


**Figure 2.16:** Light microscope image of an ion etched conventional cross-section specimen, showing delamination and cracking of the film due to tensile stresses present in the ISD grown DyBCO films.

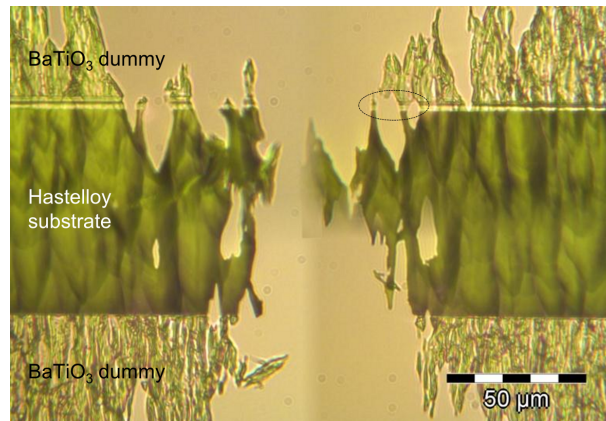


**Figure 2.17:** Light microscope image of an ion etched conventional cross-section specimen using a symmetrical dummy architecture. An electron transparent region is marked by a dotted ellipse.

cross-section will delaminate and even the layer pieces of the film will be lost due to cracking as found in our experiments and shown in **Fig. 2.16**. Thus, such samples hardly yield any electron transparent region.

To avoid preferential etching of one of the dummies, a more symmetrical architecture of the cross-section sample was chosen by replacing the Si dummy by a BaTiO<sub>3</sub> dummy as shown in Fig. 2.3b. The results of cross-section preparation using the more symmetrical dummy architecture is shown in **Fig. 2.17**. Fig. 2.17 shows a light microscope image, showing no delamination and cracking. High quality samples, i.e. containing thin electron transparent areas were observed in the TEM. The TEM results of one of the electron transparent area enclosed by dotted circle (Fig. 2.17) are shown in Fig. 2.12.

## 2.6 Conclusions

Major preparation techniques employed for TEM specimen preparation were described. Different aspects and issues of these techniques were discussed for a variety of materials, particularly, for CCs prepared by ISD technology. It was found that the DyBCO layer was under tensile stress. As a consequence, conventional plan-view and cross-section techniques failed for CCs. For plan-view TEM specimen preparation of such samples, plan-view dimpling technique is the best approach. For cross-section TEM specimen preparation, the suitable selection of dummies was found to be a key step. A more symmetrical dummy architecture was made by replacing the Si dummy by BaTiO<sub>3</sub> dummy for the cross-section preparation of such CCs. Several samples with multilayer structure were successfully prepared and etched with different etching rate for each layer. Thin and large electron transparent areas were found for all the samples.

It has been shown that, the FIB technique has some advantages over conventional cross-section such as: evenly thinned large electron transparent area of a specific region, more precise

area and direction selection etc. However, surface damage is a major challenge, which yields noticeable effects when using techniques such as high-resolution TEM, EELS. The surface damage could be minimized by optimizing FIB milling parameter, or by milling with a low energy Ar<sup>+</sup> ion beam after completion of the FIB process.

The conventional grinding and polishing method is a suitable and preferred choice of TEM specimen preparation due to short preparation time, simple equipments used, and large (over few mm) electron transparent area obtained. However, the method of choice depends on material property, information required, time, availability of equipment etc.

The techniques explained in this chapter are equally good and suitable for many other materials. For example all the Bi<sub>2</sub>Te<sub>3</sub> samples studied in this thesis were prepared by the above described techniques without any issue except that the easy cleavage along the c-axis due to Van-der-Waals bonding.



## **Part II**

# **Structure-property Correlation of DyBa<sub>2</sub>Cu<sub>3</sub>O<sub>7-x</sub> Coated Conductors**



## Chapter 3

# Basics of Superconducting Coated Conductors

### 3.1 Introduction

The discovery of superconductivity in La-Ba-Cu-O compounds with critical temperature  $T_c > 30$  K by Bednorz and Müller immediately started one of the most intense research efforts in the history of material research [32, 33]. Following this approach, in 1987, Paul Chu at University of Houston discovered superconductivity above 90 K in the Y-Ba-Cu-O system [34, 35, 36]. **Fig. 3.1** shows the rapid rise of  $T_c$  in oxide compounds. The rapid pace of discovery in high-temperature superconductivity (HTS) produced wide spread euphoria among the physics and materials science communities. Soon after, however, the euphoria was damped by the discovery of the weak-link behavior of the  $\text{YBa}_2\text{Cu}_3\text{O}_{7-x}$  (YBCO) [37]. It became clear that the major barrier to practical applications of these materials in energy and magnet technologies is not the critical temperature but their low critical current densities, especially at higher magnetic fields. On the other hand the weak-links behavior of the grain boundaries in these materials could be utilized to make superconducting quantum interference devices (SQUIDS).

There are three critical superconducting parameters that characterize a superconducting material, i.e. (i) the superconducting transition temperature or critical temperature ( $T_c$ ), (ii) the critical fields ( $B_{c1}$  and  $B_{c2}$ ) and (iii) the critical current density ( $J_c = (B, T)$ ). The third parameter,  $J_c$ , depends strongly on the microstructure of the final conductor and on the procedure to approach the final state.

Since the discovery of superconductivity, great efforts have been devoted to explain superconductivity. During the 1950s, theoretical condensed matter physicists arrived at a solid understanding, through a pair of remarkable and important theories: (i) the phenomenological Ginzburg-Landau theory (1950) and (ii) the microscopic Bardeen, Cooper and Schrieffer (BCS) theory (1957). A key conceptual element in the BCS theory is the pairing of electrons close to the Fermi level into Cooper pairs through the electron-phonon interaction. The BCS theory that has successfully described most conventional superconductors has been found insufficient on its own to explain the high values of  $T_c$  in high-temperature cuprates. A more detailed treatment of superconductivity and its theories can be found in various references [38, 39].

The behavior of superconductors in a magnetic field and the relevant superconducting properties are defined by two length scales. The first one is the London penetration depth,  $\lambda_L$ , and the second important parameter is the coherence length,  $\xi$ . The London penetration depth  $\lambda_L$ , describes the exponential decay of the magnetic field penetrating the interior of the superconductor and is given by [39]:

$$\lambda_L = \frac{m}{\mu_0 n_s e^2} \quad (3.1)$$

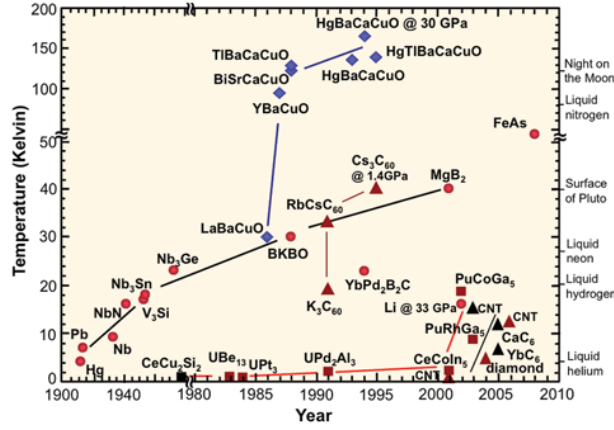


Figure 3.1: Evaluation of superconducting transition temperatures over time [38].

where  $m$  is the effective mass of electron,  $e$  is the electronic charge,  $\mu_0$  is the permeability of the vacuum,  $n_s$  is the density of superconducting electrons at zero temperature. Note that the coherence length  $\xi$  represents the length scale over which the order parameter  $\Psi$  ( $|\Psi|^2 = n_s$ ) changes at normal-superconducting interfaces and is given by [39]:

$$\xi = \frac{h\nu_F}{k_B T_c} \quad (3.2)$$

where  $v_F$  is the Fermi velocity,  $h$  is the Planck constant and  $T_c$  is the critical temperature. Both  $\lambda_L$  and  $\xi$  are temperature dependent quantities. The most relevant length scale for type-II superconductors is the coherence length of the material. Conventional superconductors (such as Nb) have coherent lengths less than 40 nm. Whereas, HTS are extreme type-II superconductors and have coherence lengths of 1-2 nm. In type-II superconductors high critical current densities can only be achieved by the presence of a high density of defects (of the order of  $2\xi$ , where  $\xi$  is the coherence length) providing pinning centers for the magnetic flux lines. On the other hand, extended defects in YBCO based superconductors such as large-angle grain boundaries form weak-links, which are a key limiting factor for the critical current densities [37].

In recent years, high quality biaxially textured YBCO thick films were manufactured using growth technologies such as ion beam assisted deposition (IBAD) [40], and rolling assisted biaxially textured substrate (RABiTS) [41] that largely eliminated weak-links in these materials. In this thesis, I will report on DyBCO films grown by the inclined substrate deposition (ISD) technology, which as a technology has many advantages over the other technologies. Due to an enhanced transition temperature ( $T_c$ ) of 90 K compared to YBCO (typical 88 K), at 77 K DyBCO films exhibit an about 20% lower surface resistance as compared to YBCO films [24]. Beyond that DyBCO films are chemically more stable under humid conditions and the long-term degradation behavior is improved.

## 3.2 Superconductivity and types of Superconductors

In 1933, Meissner and Ochsenfeld found that a metal in the superconducting state shields the magnetic field in its interior, i.e. it exhibits perfect diamagnetism, this phenomenon was called *Meissner effect*. It was discovered that the state of perfect diamagnetism is retained only if the temperature is below a *critical temperature* ( $T_c$ ) and the magnetic field is below a certain magnetic field, which is referred as *critical field* ( $B_c$ ). The value of  $B_c$  is related thermodynamically to the free-energy difference between the normal and the superconducting state.

According to the London theory of superconductivity [42], the applied magnetic field penetrates the superconductor over a mean distance  $\lambda_L$ , known as the London penetration depth. In

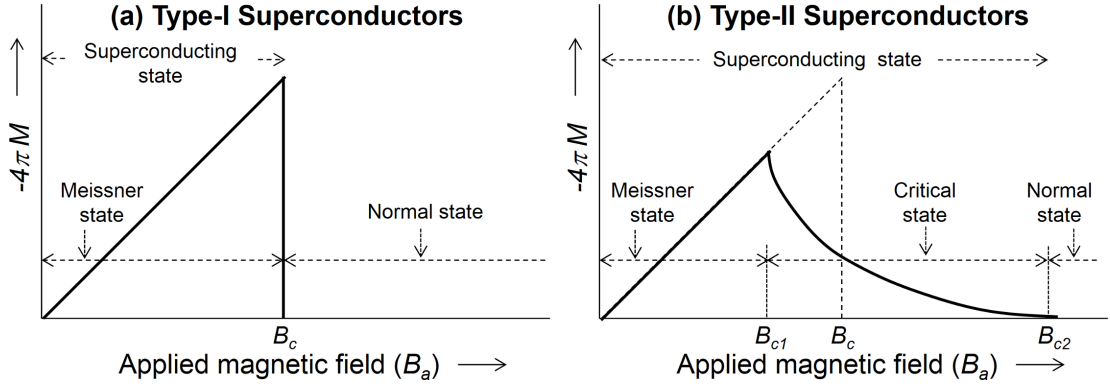


**Figure 3.2:** The magnetization curves of the two types of superconductor: (a) type-I and (b) type-II superconductors [48].

**Table 3.1:** Characteristic parameters of optimally doped YBCO superconductors [49, 50].

	Field direction	$T_c$	$B_{c1}$ [T = 0]	$B_{c2}$ [T = 0]
YBa <sub>2</sub> Cu <sub>3</sub> O <sub>7-x</sub>	$B \parallel c$ -axis	95 K ( $x = 0.11$ )	0.018 T	40 T
	$B \perp c$ -axis		0.053 T	110 T

1950, Ginzburg and Landau introduced a phenomenological theory, which described the properties of superconductors in (large) magnetic fields. *Ginzburg-Landau* theory predicts that a superconductor should have two characteristic lengths: (i) the *Ginzburg-Landau penetration depth*,  $\lambda_{GL}$ , which relates to the London penetration depth ( $\lambda_L$ ) and (ii) the *Ginzburg-Landau coherence length*,  $\xi_{GL}$ . The ratio  $\kappa = \lambda_{GL}/\xi_{GL}$  is known as Ginzburg-Landau parameter. This ratio,  $\kappa$ , distinguishes type-I superconductors, for which  $\kappa \leq 1/\sqrt{2}$ , from type-II superconductors which have higher  $\kappa$  values, i.e.  $\kappa > 1/\sqrt{2}$  [43].

For the case  $\kappa \leq 1/\sqrt{2}$ , the superconductor does not allow the magnetic flux to penetrate if the magnetic field is below the critical field ( $B_c$ ), however, at and beyond the critical field the magnetic flux will be fully penetrated i.e. the superconductor changes from the Meissner state to the normal state by a second order phase transition (**Fig. 3.2a**). Many pure metals are type-I superconductors. The critical magnetic field of type-I superconductors is low (proximately 0.1 T), therefore, such materials are not relevant in large-scale magnetic and electrical applications [44].

In contrast, for the case  $\kappa > 1/\sqrt{2}$ , superconductors exhibit a continuous increase in flux penetration starting at lower critical field ( $B_{c1}$ ) and the superconductor gets fully penetrated at upper critical field ( $B_{c2}$ ) (Fig. 3.2b), instead of showing a discontinuous disappearance of superconductivity at the thermodynamical field ( $B_c$ ) (Fig. 3.2a). The superconducting state between  $B_{c1}$  and  $B_{c2}$ , i.e. the state between the Meissner state and normal conducting state is termed as critical state (*Shubnikov phase*) and allows the coexistence of superconducting and normal conducting regions. The existence of the critical state can be explained by the negative energy between normal and superconducting regions, the appearance of normal regions will reduce the total free energy and lead to a more favorable free energy state [45].

While the class of type-I superconductors is composed entirely of metallic chemical elements, type-II superconductors may be metal alloys or even some pure metals, such as Niobium (Nb) and Vanadium (V), and also different oxide compounds (see **Table 3.1**). All metals and metal alloys have their  $T_c$  below 30 K and are referred as low-temperature superconductors (LTS), while the oxide superconductors have their  $T_c$  above 30 K and are referred as high-temperature superconductors (HTS) (page 213 of [38]). Only Type-II superconductors are relevant for applications in the energy and magnet technologies [46, 47].

**Fig. 3.3** shows a magnetization curve of a cold deformed Nb<sub>55</sub>Ta<sub>45</sub> alloy [46]. The curve a (before annealing) and b (after annealing) shows the magnetization curve of the same material,

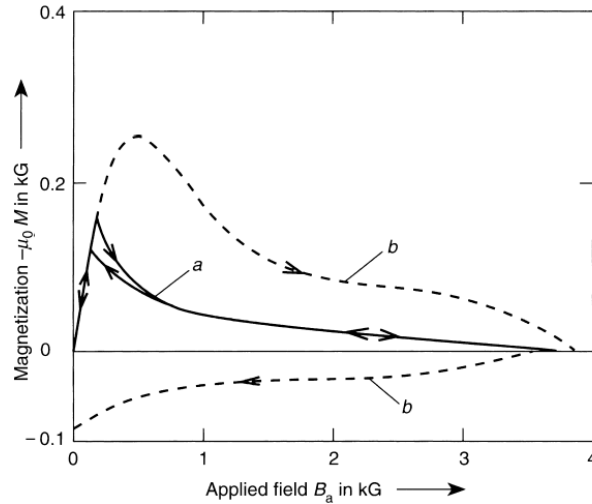


**Figure 3.3:** Magnetization curve of a cold deformation Nb<sub>55</sub>Ta<sub>45</sub> alloy: (a) after cold deformation (b) after cold deformation and annealing [46].

but they differ significantly. Structural imperfections or chemical impurities act as pinning centers for flux vortices in the crystal. After reaching  $B_{c1}$ , the magnetic flux will start to penetrate in to the interior of the material, however, magnetic flux lines are not free to move due to flux pinning. This allows the total shielding current that determines the diamagnetic behavior to be greater than in the Meissner phase. Similarly the reverse curve decreasing magnetic field can be explained and at the end of the reverse cycle, when  $B = 0$ , the value of  $B$  remains finite and positive due to the flux trapped by the superconductor.

### 3.3 Critical Current Density of Superconductors

The most important characteristic of a superconductor, from the viewpoint of practical applications, is its critical current density. The critical current density ( $J_c$ ) is reached when the current density in the superconductor yields an electrical field of  $1 \mu\text{V cm}^{-1}$  or  $10^4 \text{ V m}^{-1}$  as shown in **Fig. 3.4**.

In large scale applications such as magnets and power transmission lines, a critical current density between  $10^4 - 10^6 \text{ A cm}^{-2}$  is generally required [51]. The values of  $J_c$  for cuprate polycrystalline sintered samples typically lie in the range of  $10^2 \text{ A cm}^{-2}$  to  $10^4 \text{ A cm}^{-2}$  at 77 K (and in the range of  $10^3 \text{ A cm}^{-2}$  to  $10^5 \text{ A cm}^{-2}$  at 4.2 K) and, therefore, are inadequate for most practical purposes at 77 K. There is plenty of convincing experimental evidence indicating that the current carrying capability of polycrystalline high- $T_c$  materials is limited to a large extent by grain boundaries, which act like Josephson weak links [52, 51]. To date, for ISD based coated conductors, the  $J_c$  is in the range of  $1 \times 10^6$  to  $2 \times 10^6 \text{ A cm}^{-2}$ .

The critical current density  $J_c$  in type-II high- $T_c$  superconducting bulk materials decreases weakly with increasing temperature when  $T < T_{dp}$  (depinning temperature); when  $T < T_{dp} < T_f$  (boundary fluctuation temperature),  $J_c$  is power law decaying and when  $T > T_f$ ,  $J_c$  decays exponentially for a constant magnetic field. Whereas for a constant temperature, the critical current density  $J_c$  first decreases, then increases after reaching a maximum, and finally decreases again as the magnetic field increases [53, 54].

#### 3.3.1 Critical current limiting mechanism

Important critical current limiting mechanisms in type-II superconductors include: (i) depinning or flux-flow, (ii) thermally activated flux-flow and (iii) weak-links.

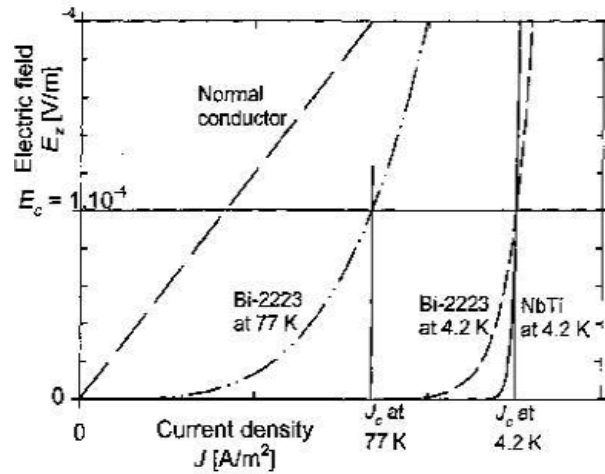


**Figure 3.4:** Critical current density definition: current density ( $J_c$ ) vs. field ( $E$ ) dependence for a superconductor [46].

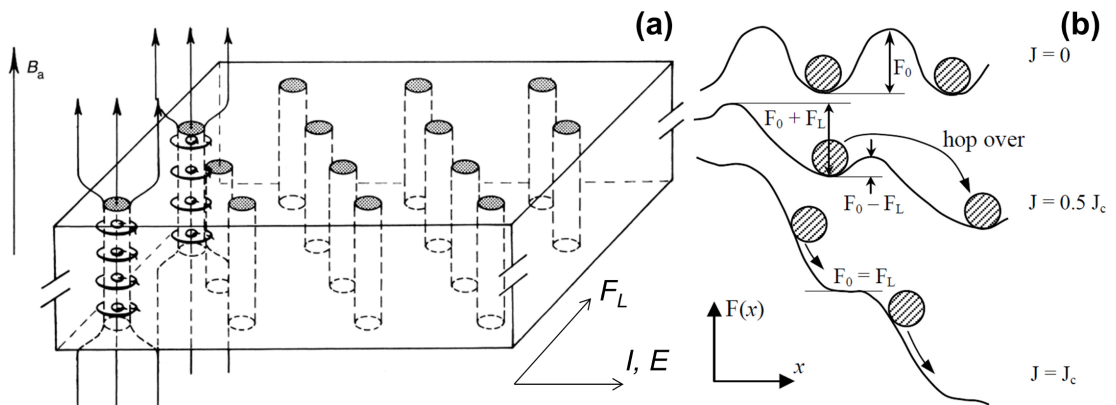


**Figure 3.5:** Schematics of: (a) the critical state of type-II superconductors with quantized vortices, and (b) mechanism of flux-flow, the presence of current in a magnetic field generates a Lorentz force, which tilts the staircase, allowing flux line to hop out of their pinning wells [46].

### 3.3.1.1 Flux-flow

Defects act as pinning centers detaining the vortices from moving under the presence of a Lorentz force (**Fig. 3.5a**). In order to free the vortices a force is needed which gives rise to the concept of *pinning force* ( $F_p$ , an energy barrier for vortices) (**Fig. 3.5b**). The current transport in a superconductor gives rise to a *Lorentz force* ( $F_L = I \vec{dl} \times \vec{B}_a$ ), where  $I$  is the transport current,  $\vec{dl}$  is the length of the current path, and  $\vec{B}_a$  the applied magnetic field. The Lorentz force acts perpendicular to the current flow and perpendicular to the magnetic field. Therefore, flux lines in the critical state could start to move (viscous-flow state) by increasing the Lorentz force beyond the depinning threshold ( $F_p$ ) close to  $J = J_c$ , where  $J_c$  is the critical current density (**Fig. 3.5b**).

Any electric field present in a superconductor is a dissipative process, giving rise to a voltage drop or electric-field ( $\vec{E} = \vec{v} \times \vec{B}_a$ , where  $\vec{v}$  is the velocity of the flux-lines) and lead to an electrical loss ( $J.E$ ). Therefore, superconductors show a small, non-zero resistance, which is referred as *flux-flow resistance*.

### 3.3.1.2 Thermally activated flux-flow

Flux-lines are usually assumed to be rigid but are elastically deformable. An extreme situation of soft flux-lines is encountered for Bi-2212 ( $\text{Bi}_2\text{Sr}_2\text{CaCu}_2\text{O}_8$ ) and Bi-2223 ( $\text{Bi}_2\text{Sr}_2\text{Ca}_2\text{Cu}_3\text{O}_x$ ). For strongly anisotropic superconductors such as Bi-2212 and Bi-2223 due to their layer struc-

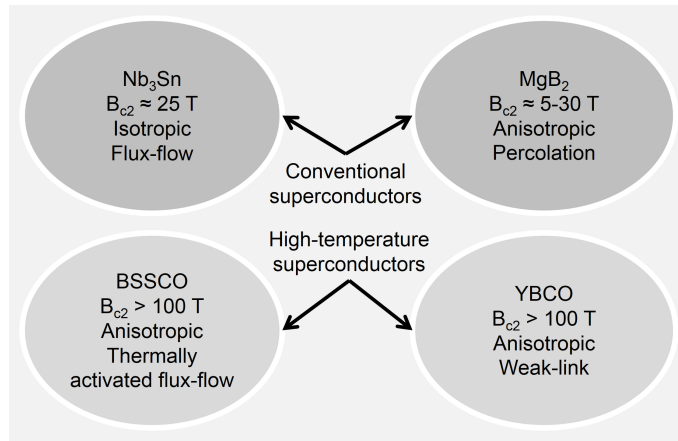


**Figure 3.6:** Schematic diagram of current limiting mechanism in different class of superconducting materials.

ture, there is a shearing of the flux-line when these are parallel to the  $c$ -axis, i.e. perpendicular to the  $\text{CuO}_2$  planes of the crystal structure. The shear modulus of the flux-lines is strongly temperature dependent and decreases with increasing temperature. The result of this low shear modulus of the flux-lines yields a dramatic decline of the critical current densities at higher temperatures, this behavior is called *thermally activated flux-flow* [57].

### 3.3.1.3 Weak-links

In some polycrystalline HTS, for example in YBCO, grain boundaries behave significantly different than the volume of material with respect to the superconducting properties. A much smaller critical current density flows across the grain boundaries than in the bulk of the material. The origin of this limitation lies in the oxygen stoichiometry of the material and of grain boundaries. In superconductivity, such a grain boundary is called *weak-links* [37].

There are several investigations in the literature on the weak-link behavior of grain boundaries such as: deviation from ideal oxygen stoichiometry [58], and strain field present at the grain boundary due to edge dislocations [59]. However, if the misorientation angle is small ( $< 6^\circ$ ), the degradation of the critical current density is small. It was reported that the critical current density across a grain boundary decreases drastically with increasing misorientation angle and the boundary behaves as a weak-links for misorientation angles greater than  $10^\circ$  (**Fig. 3.8**) [37].

Though the weak-links in superconducting materials are not desirable for high critical current application, however, weak-links could be used as superconducting quantum interference devices (SQUIDS). SQUIDS are very sensitive magnetometers that operate via the Josephson effect [60][61].

Since the current limiting mechanisms are material and microstructure dependent, different materials are subjected to different current limiting mechanisms as shown in the schematic diagram (**Fig. 3.6**). For example,  $\text{Nb}_3\text{Sn}$  and  $\text{NbTi}$  show a high critical current density of about  $10^5 \text{ A cm}^{-2}$  at 4.2 K and a field of 5 T, however, they have to be operated at low-temperatures (4.2 K).  $\text{Nb}_3\text{Sn}$  is limited to 10 T and  $\text{NbTi}$  close to 20 T applications as their  $J_c$  is limited by flux-flow mechanism (Fig. 3.7a). Note that,  $\text{Nb}_3\text{Sn}$  and  $\text{NbTi}$  are metallic superconductors which were used to make wires by the powder in tube or the multifilament method [46] (page 660 of [38]).  $\text{NbTi}$  and  $\text{Nb}_3\text{Sn}$  were being successfully used in Large Hadron Collider (LHC) and International Thermonuclear Experimental Reactor (ITER) projects, respectively.

It can be seen in **Fig. 3.7a**, that the critical current density of YBCO ceramics is about only  $5 \times 10^3 \text{ A cm}^{-2}$  at 4.2 K and zero-field. The causes of this limitation is the nature of the grain boundaries, which suppressed the current at grain boundaries and is known as weak-link [37]. In such materials grain boundaries can transport much smaller critical currents than the bulk of

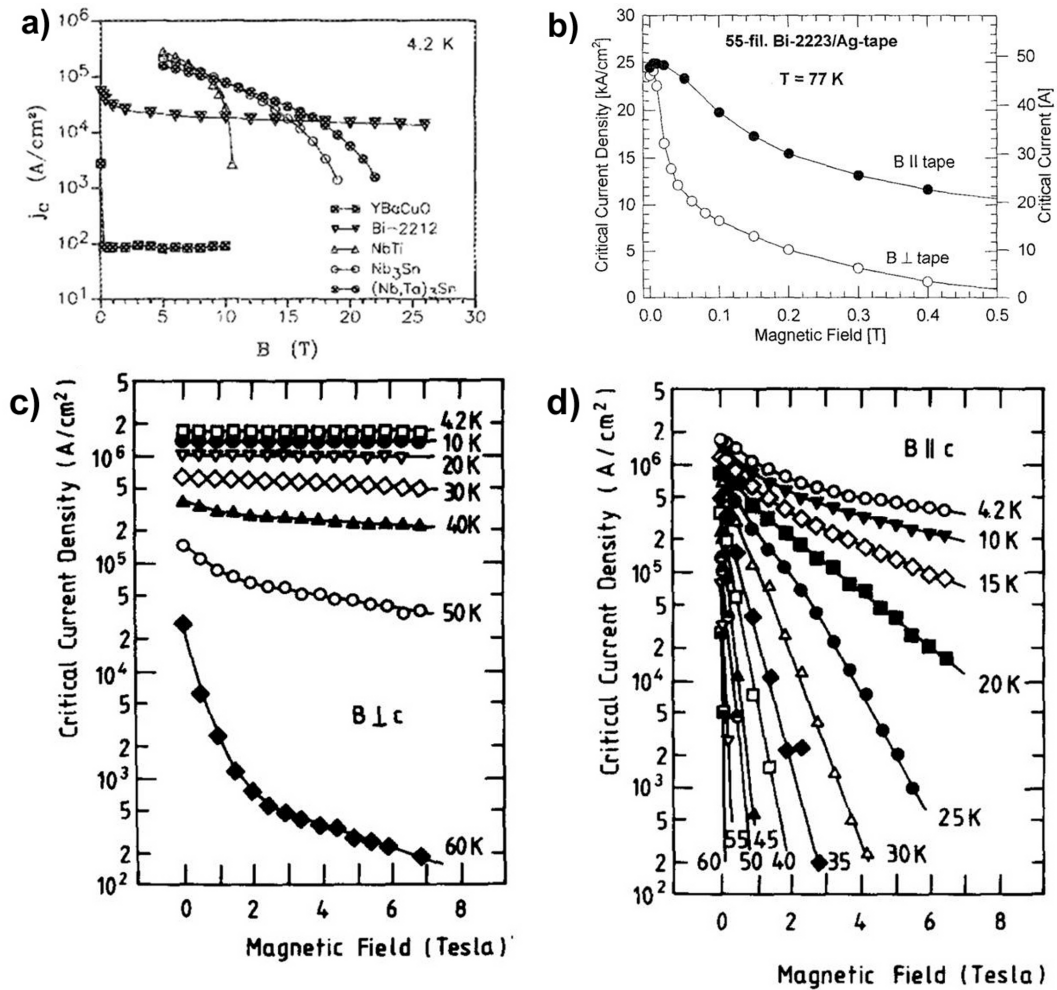


**Figure 3.7:** (a) Critical current density ( $J_c$ ) in dependence of applied magnetic field  $B$  (T) of up to 30 T at 4.2 K for various HTS materials [55]. (b)  $J_c$  and critical current (A) in dependence of  $B$  (T) applied in two perpendicular directions for a 55 filament Bi-2223/Ag tape at 77 K [56].  $J_c$  in dependence of  $B$  for (c)  $B$  perpendicular to the  $c$ -direction and (d)  $B$  parallel to the  $c$ -direction at different temperature for Bi-2223 [44].

the material itself. Furthermore, only a small magnetic field (a few 10 mT) drastically reduces the critical current density to  $100 \text{ A cm}^{-2}$  making them useless for any real power application. However, the performance could be greatly improved by growing an almost single crystalline (or only with small-angle grain boundaries) material.

Another material showed a high critical current density and stable behavior over large applied magnetic fields; Bi-2223/Ag-tapes, but were limited by *thermally activated flux-flow* [55]. These materials also show a large anisotropy and the thermally activated flux-flow problem is much more severe for the magnetic field applied parallel to the  $c$ -axis. For the field perpendicular to the  $c$ -axis and temperature up to 40 K material shows rather high critical current densities ( $3 \cdot 10^6 \text{ A cm}^{-2}$ , only a reduction of about 25% at 8 T and 40 K) as can be seen in Figs. 3.7b-d [44].

### 3.4 Structural Properties of DyBa<sub>2</sub>Cu<sub>3</sub>O<sub>7-x</sub>

The DyBa<sub>2</sub>Cu<sub>3</sub>O<sub>7-x</sub> (DyBCO) compound is an oxide with three perovskite-like cubes stacked on top of each other as shown in Fig. 3.9. The central unit cell contains a Dysprosium (Dy) cation and the other two contain Barium (Ba) atoms. Perpendicular to the  $c$ -axis CuO<sub>2</sub> planes are found adjacent to the Dy layer which are known to be responsible for superconductivity.

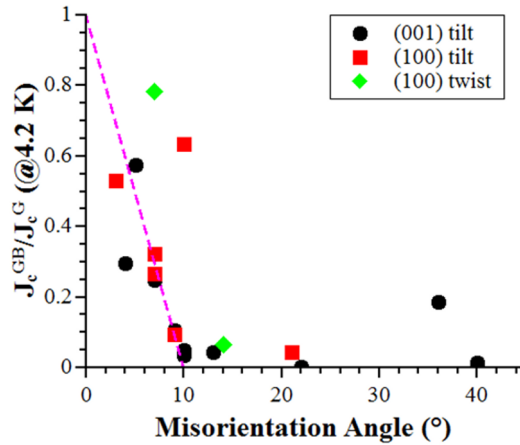


Figure 3.8: Grain boundary current in dependence on grain boundary misorientation angle [59].

The Cu-O chain layer acts as a charge carrier reservoir. The oxygen content can vary only in the CuO chain layer. The total oxygen content can vary from  $\text{DyBa}_2\text{Cu}_3\text{O}_6$  ( $x = 1$ ) to the fully oxygenated phase  $\text{DyBa}_2\text{Cu}_3\text{O}_7$  ( $x = 0$ ). For  $0 \leq x \leq 0.5$ , the compound is orthorhombic (Fig. 3.9a) and superconducting, and for  $0.5 < x \leq 1$  it is tetragonal (Fig. 3.9b) and non-metallic. The orthorhombic structure is described in space group  $Pmmm$  with the  $c$ -axis parallel to the long cell dimension. The lattice parameters of the orthorhombic phase are:  $a = 0.3889$  nm,  $b = 0.3849$  nm, and  $c = 1.1739$  nm [62].

The tetragonal DyBCO structure is structurally almost identical to the orthorhombic form. The most significant difference between the two forms occurs at the O(1) position of the insulating plane between adjacent BaO planes i.e. in the CuO chain layer. In the tetragonal structure these sites are symmetrically equivalent and must be equally occupied. In the orthorhombic structure, however, in the Cu-O chain layer oxygen atoms along the  $[100]$  direction (i.e.  $a$ -axis) are completely removed, therefore,  $a$  is slightly longer than  $b$ .

### 3.5 Coated Conductors (CCs)

Coated conductors (CCs) (page 689 of [38]) are superconducting wires or tapes designed for applications of superconductors in energy and magnet technologies. CCs consist of a metallic substrate tape, in most cases a Ni alloy, coated with one or more buffer layers, and a superconducting layer on top (Fig. 3.10). The buffer layer prevents diffusion of metal elements into the superconductor during high-temperature processing and provides the biaxial texture (i.e. in-plane and out-of-plane texture) to the HTS film. In case of a textured substrate, the buffer layer helps to transfer the biaxial texture of the substrate to the HTS film. Whereas in case of an untextured substrate, the buffer layer itself provides a biaxial textured film, such that a HTS film can be grown epitaxially on top of it. Note that the biaxial texture of the superconducting layer is necessary for obtaining high superconducting transport currents. A biaxial texture yields small-angle grain boundaries that do not show the weak-links behavior, which is a major problem of untextured cuprate HTS materials [63].

#### 3.5.1 Requirements for applications

DyBCO films can be used in high-field applications at 77 K such as (i) fault current limiters, (ii) motors, and (iii) generators. For the full utilization of the potential of HTS, however, many technological and economical aspects have to be taken into consideration.

For building superconducting coils for magnets, superconducting tapes should be mechanically flexible along with high-mechanical strength and relatively inexpensive to scale up to

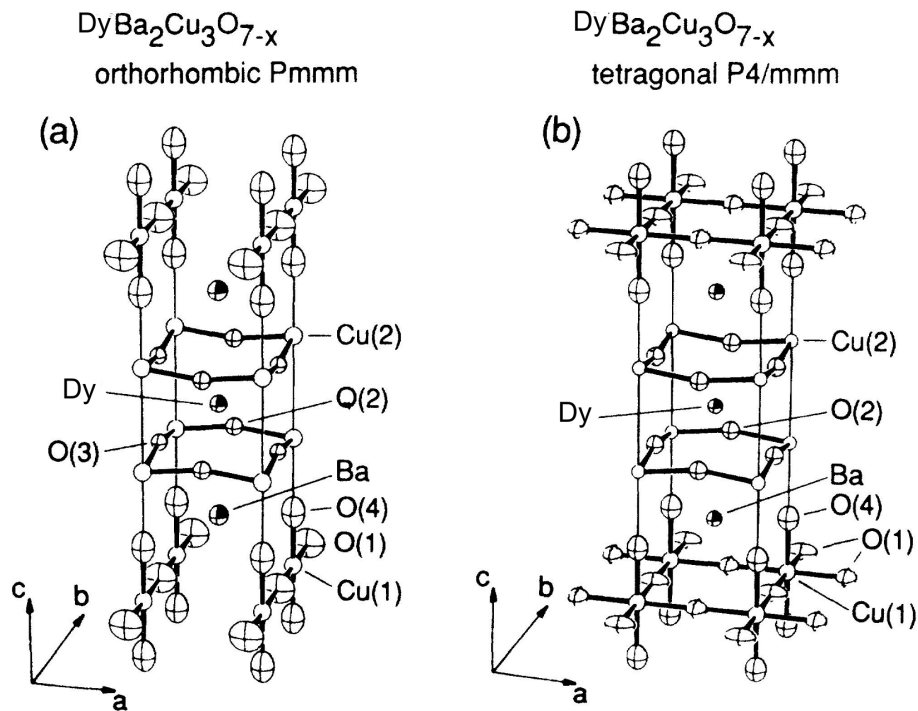


**Figure 3.9:**  $\text{DyBa}_2\text{Cu}_3\text{O}_{7-x}$  (DyBCO) crystal structure: (a) orthorhombic and (b) tetragonal phase. The O(1) site in the tetragonal phase is not fully occupied [37].

long lengths. This immediately highlights the great advantage of metallic substrates (or metal alloy) and this requires a film deposition technology which provides almost single crystalline (or biaxially-textured) superconducting films over kilometers of length. The substrate manufacturing and the film deposition technique should be cheap and easy to realize. Further different losses (AC and DC losses) should be minimized for improving the function/cost ratio. It is essential to obtain losses as low as possible, especially in AC applications, in which the magnetization losses are much higher than transport current losses due to flux flow resistance [64].

Note that if the applied magnetic field,  $B$ , exceeds the lower critical field,  $B_{c1}$ , which is usually the case particularly for the anisotropic HTS such as YBCO, an AC current can no longer be carried without loss.

A transport current in a superconductor generates a magnetic field around the conductor,

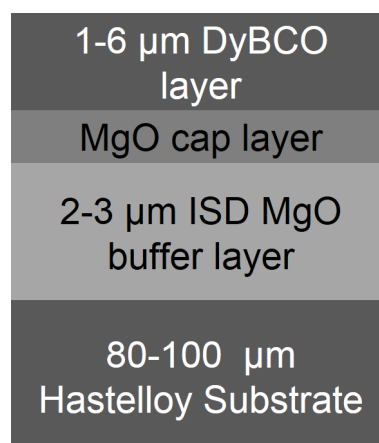


**Figure 3.10:** A schematic diagram (layer structure) of coated conductors.

which is called the self-field. With an AC transport current, the alternating self-field penetrates the superconductor during each current cycle. Even if there is no external magnetic field, the variation of the self-field inside the material causes a hysteresis loss, which is called self-field loss. The dissipated energy is converted into heat that must be removed by the cooling system. AC loss is therefore an undesirable phenomenon [65].

CCs rely on the development of low cost preparation methods, especially towards the production of long lengths (few thousand meters). Over the past years various methods have been investigated to achieve the long length CCs goals. To date 2G CCs can be formed by a variety of processes such as: (i) ion beam assisted deposition (IBAD) [40], (ii) rolling assisted biaxially textured substrate (RABiTS) [41], and (iii) inclined substrate deposition (ISD) [24]. However, in all cases, the manufacturing process comprises a series of steps. In the following sections these three important technologies are explained in more detail.

### 3.5.1.1 Ion beam assisted deposition technology (IBAD)

The ion beam assisted deposition (IBAD) technology (page 691 of [38]) is based on untextured metallic substrates and yields biaxially-textured buffer layers on an untextured substrate by simultaneous ion beam bombardment to the film surface during growth. Iijima and Fujikura in Japan developed this technology in 1991 [40]. The biaxially textured templates by IBAD solved the weak-link problem of the YBCO and yielded high critical current superconducting tapes. However, the deposition of biaxially textured buffer layers is slow, since a predominant fraction of the material deposited is removed by the impinging ions which generate the biaxial texture and ensure that unfavorable orientations in the buffer layer are sputtered away. Furthermore, scale-up of this process to long lengths is complicated, however, has been realized by SuperPower in the United State and companies in Japan [66].

### 3.5.1.2 Rolling assisted biaxially textured substrate technology (RABiTS)

The rolling assisted biaxially textured substrate (RABiTS) (page 693 of [38]) is a technology used by American Superconductors [67] a leading manufacturer for obtaining cube-texture of a Ni (or alloy) substrate tape by utilizing the recrystallization behavior of Ni. The texture is generated by conventional rolling of a Ni tape with heavy deformation ( $> 95\%$ ) to a roll texture tape, followed by an annealing step which results in a recrystallization into the desired biaxially textured cubic phase of Ni. However, superconductor science and technology imposes two challenges: (i) very pure starting material for the deformation processing, and (ii) an adequately smooth surface. To meet these conditions, a multi-layer buffer system has been utilized. However, the use of a multi-layer buffer not only introduces significant complexity to the fabrication process, but also increases the cost. Furthermore, the Ni (or alloy) substrate is a ferromagnetic material, which affect the ac losses in these tapes due to magnetic hysteric loss and has a major impact to the overall AC loss [68].

### 3.5.1.3 Inclined substrate deposition technology (ISD)

ISD technology yields biaxial texturing of the buffer layer by appropriate inclining the metal substrate with respect to the incoming flux (**Fig. 3.11**). ISD was discovered by Smith in 1959 during the evaporation of permalloy on rather large substrates. By using ISD, Fujino and Hasegawa [69] successfully textured yttrium stabilized zirconia (YSZ) templates on Ni alloy tapes by PLD. In 1999, Bauer et al. [24] grew biaxially textured MgO buffer layers on Hastelloy substrate by reactive thermal evaporation of Mg.

The ISD approach combined with thermal evaporation allows a very high deposition rate for MgO at room temperature, which yields biaxially textured buffer layers for long lengths wire technology on untextured (randomly oriented) substrate. Furthermore, ISD is independent of

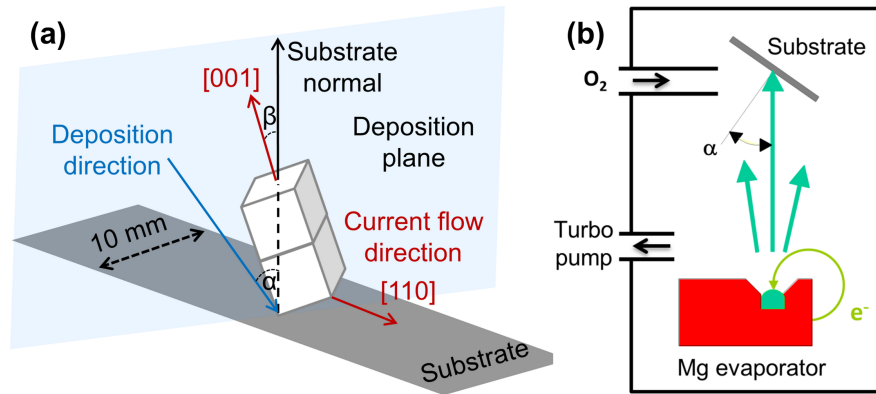


**Figure 3.11:** Schematics of (a) growth geometry and (b) growth chamber of the ISD technology [24].

recrystallization properties of the metallic substrate, therefore, untextured Hastelloy can be used as a substrate material, i.e. a high strength non-magnetic untextured material.

Many efforts have been focused on understanding the mechanism of texture formation in the ISD deposition. It is commonly accepted that the texture develops by an evolutionary shadowing process where only oriented columns survive [70]. Bauer et al. [25] reported a concept of directional diffusion along with the concept of shadowing to explain the growth mechanism and facets formation of the ISD MgO.

For thermal evaporation, the source materials are heated by some source of heat such as resistive (thermal evaporation), electron-beam, or laser beam to melt or sublime the material into the vapor state. High vacuum is required to allow the molecules to evaporate freely in the chamber, subsequent condensation on the substrate surface and to avoid condensation of atoms of the gas. Multiple sources can be used to deposit alloys and composite materials.

CCs tapes studied in this thesis were grown using reactive thermal evaporation technique by THEVA [25]. The metal species of the superconductor are evaporated in high vacuum ambient by thermal evaporation and simultaneously an oxygen flow is introduced. Since HTS require an elevated oxygen pressure for their oxide formation, the introduction of oxygen is essential. To control the chemical composition, the evaporation rate of the metal species and the flow of oxygen have to be monitored inline and controlled precisely.

### 3.6 Flux-line Pinning in DyBa<sub>2</sub>Cu<sub>3</sub>O<sub>7-x</sub> based Coated Conductors

Flux lines could be pinned to energetically favorable sites (pinning centers) such as inhomogeneities or normal conducting precipitates. However, a short coherence length ( $\xi_{ab} = 1.8 \text{ nm}$  at  $T = 0 \text{ K}$  and  $\xi = 2.7 \text{ nm}$  at  $T = 77 \text{ K}$ ) of DyBCO requires defects (pinning centers) as small as  $3.6 \text{ nm}$  to  $5.4 \text{ nm}$  ( $2\xi_{ab}$ ). Therefore, a high critical current density for wide range of magnetic fields and temperatures could be achieved for HTS materials by maximizing the homogeneity at the macroscopic level, i.e. the uniformity, alignment, and phase purity of the macroscopic building blocks (DyBCO grains), while optimizing the inhomogeneities within the building block to create flux pinning centers.

#### 3.6.1 Intrinsic pinning centers

In cuprate materials (DyBCO or YBCO), there is strong anisotropy due to their layered structure which produces noticeable pinning effects. The layered oxide materials have strong superconductivity in the CuO planes and are weakly linked in the  $c$ -direction. Hence, the structure of the superconductor itself produces intrinsic pinning [71]. If a magnetic field is applied in the  $ab$ -plane, the vortices will try to form in the layered structure. A Lorentz force in the  $c$ -direction would try to force the vortices to move from one  $ab$ -plane to the nearby  $ab$ -plane, which is much

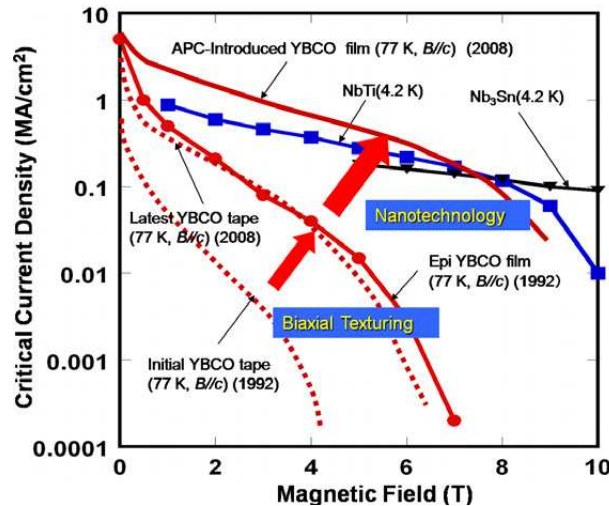


**Figure 3.12:** Development of the in-field  $J_c$  of high-temperature superconductors (HTS) at 77 K,  $B \parallel c$ , as compared to the performance of conventional superconducting wires such as Nb–Ti and Nb<sub>3</sub>Sn at 4.2 K [72].

more difficult, making the intrinsic anisotropy a powerful pinning force in cuprate materials. Due to intrinsic pinning, the critical current density is strongly anisotropic with respect to the applied magnetic field. Higher critical current densities are obtained with the magnetic field lying in the  $ab$ -plane and lower values for the magnetic field parallel to the  $c$ -axis [71].

### 3.6.2 Artificial pinning centers

Intrinsic pinning will neither improve the overall (isotropic) pinning performance nor the pinning for the magnetic field applied along the  $c$ -axis. However, practical applications require a dramatic improvement of  $J_c$  for magnetic fields along the  $c$ -direction. This can be achieved only by introducing artificial pinning centers (APCs) (page 699 of [38]). Lattice defects such as lattice strain, dislocations, stacking faults, twin boundaries, nano-precipitates, and point defects are examples of artificial pinning centers.

The introduction of APCs with controlled dimensionality and orientation is indispensable to achieve a high  $J_c$ . The APCs can be classified according to their dimension as follows: one dimensional APCs (1D-APCs) such as dislocations and columnar defects; two dimensional APCs (2D-APCs) such as small-angle grain boundaries and anti-phase boundaries; three dimensional APCs (3D-APCs) such as nano-particles, and secondary phases of the scale of  $\xi$  or more. Additionally, the defects smaller than  $\xi$ , such as vacancies, and cation disorder can be classified as zero dimensional APCs (0D-APCs). The great improvements of  $J_c$  in YBCO films were obtained by 1D-APCs, such as dislocations, BZrO<sub>3</sub> nano-rods, and by 3D-APCs, such as Y<sub>2</sub>O<sub>3</sub> nano-precipitates [73, 74].

The efficiency of the APCs is judged by the pinning performance of superconducting films. In this sense, high-quality samples (maximum pinning force  $F_{pmax} = 22 \text{ GN m}^{-3}$  at 77 K,  $B \parallel c$ ) were recently obtained by Gutierrez et al., where YBCO films with BZO nano-rods were synthesized. **Fig. 3.12** shows the progress of critical current density of the YBCO based coated conductors from the recent advances in the biaxial texturing technique and in APC technology [72]. It has already been confirmed experimentally that the critical current density of YBCO at 77 K greatly exceeds that of commercial Nb–Ti wires at 4.2 K [72].

This success in increasing critical current densities in YBCO based superconductors is due to detailed analysis of the materials by TEM and detailed analysis of anisotropic superconducting properties.

## Chapter 4

# Hastelloy-MgO Interface and Diffusion Phenomena at Elevated Temperatures

### 4.1 Introduction

The diffusion behavior of elements constituting Hastelloy-C276 (Mo, Cr, Fe, W, Co, Mn, and Ni) in MgO films was investigated using scanning electron microscope (SEM) and transmission electron microscope (TEM). The MgO films were deposited by inclined substrate deposition (ISD) technology on Hastelloy substrates for the coated conductors (CCs) tape technology.

CCs are superconducting wires and are a key component for implementing superconductivity in a large range of application requiring high critical currents in presence of magnetic fields. High critical current superconducting wires require almost single crystalline (biaxially-textured) material over kilometer of length and the CCs technology is a key technology to achieve this goal. The CCs technology consists of a flexible metal (alloy) substrate, a buffer layer, and a superconducting thin film [24]. The buffer layer plays important roles such as providing a biaxially-textured template for the superconducting layer, and blocking the diffusion of substrate elements at elevated temperatures [75]. Several technologies such as ISD [24], ion beam assisted deposition (IBAD) [40], and rolling assisted biaxially-textured substrate (RABiTS) [41] were developed with great success to achieve the biaxial texturing either in the substrate itself (RABiTS technology) or in the buffer layer (ISD and IBAD technologies). Several studies could be found in the literature on texture analysis, however, only few studies were reported on the diffusion barrier efficiency of the MgO buffer layer grown on a Hastelloy substrate [75, 76]. All the reported studies are for IBAD deposited MgO buffer layers. For IBAD technology, it was found that a thin amorphous alumina buffer layer on the Hastelloy substrate acts as an efficient barrier for the Hastelloy transition metals diffusion in the MgO buffer layer [75]. No study is available for the diffusion barrier efficiency for MgO buffer layers grown on Hastelloy substrates by the ISD technology.

It is reported that at elevated temperatures (larger than 500 °C) and in an oxygen environment, super alloys such as Hastelloy-C4 [77], Hastelloy-X [78], and Hastelloy-C276 [79] form a Cr<sub>2</sub>O<sub>3</sub> scale at the surface by thermally activated solid state reaction (SSR) or inter-diffusion reaction (*Kirkendall effect*) [80]. In ISD technology, such a SSR or *Kirkendall effect* at the Hastelloy-MgO interface may lead to a formation of voids at the interface, resulting in a poorly adhering film interface. It is also reported that deviations in stoichiometry of DyBCO (YBCO) and/or the presence of even small amount of impurities may have major effects on its superconducting properties. Therefore, a study of the Hastelloy-MgO interface is of utmost importance with respect to the microstructure and diffusion barrier efficiency for ISD CCs technology.

Hastelloy-C276 is a Ni based alloy. It has a nominal composition of 18Cr, 11Mo, 8Fe,

0.5Co, 0.5Mn, 4W, and 58Ni (at%) [78]. As discussed above, it forms a  $\text{Cr}_2\text{O}_3$  scale at elevated temperatures. The oxide scale formed at 800 °C were found crystalline with an average grain size of 0.5-1.0  $\mu\text{m}$  [79].

To understand the thermodynamics of phase formation, void formation and diffusion at the Hastelloy-MgO interface, understanding self-diffusion and inter-diffusion of the Hastelloy-MgO system is important. Therefore, a set of diffusion data relevant for the Hastelloy-MgO interface study were extracted from the references [81, 82] and presented in this study. Though, the Hastelloy contains many transition metals, it forms almost a pure  $\text{Cr}_2\text{O}_3$  scale at the surface, so understanding the Cr diffusion data is of great importance. The diffusion coefficients of  $\text{Cr}^{3+}$  ions were reported to be of the order of  $10^{-11} \text{ cm}^2\text{sec}^{-1}$ ,  $10^{-18} \text{ cm}^2\text{sec}^{-1}$ , and  $10^{-18} \text{ cm}^2\text{sec}^{-1}$  in the Ni,  $\text{Cr}_2\text{O}_3$ , and MgO matrices, respectively [82].

All the diffusion data available in the literature is for single crystalline bulk MgO materials. In ISD technology, the MgO buffer layer is a thermally grown thin film, it has small (20-30 nm) grain sizes along with porosity. Therefore, diffusion data for grain boundary and surface diffusion should be considered. In addition, diffusion data is often not available for the temperature range of interest, so extrapolation is the only choice.

Study of the Hastelloy-MgO interface revealed a diffusion layer and void formation at the interface. Void formation at the interface resulted in a poorly adhering film interface. A study of an additional layer of different materials that serves as a diffusion barrier for the Hastelloy transition metal ions at the Hastelloy-MgO interface is presented in this chapter.

## 4.2 Experimental

Six ISD CCs samples from three different series were studied in this work, namely sample 2 (MgO series), 3 (DyBCO series), and 6-9 (Blocking layer series). Analyzed samples are listed in Table 2.1 along with their layer structure and transport properties. A schematic drawing of the layer structure for the relevant series for this work are also shown in **Fig. 4.1**. A more detailed description about ISD CCs technology can be found in Chapter 3 and in references [24, 25]. For a fully-processed sample, the sequence of layers starting from the Hastelloy substrate was: the ISD MgO buffer layer, the MgO cap layer and the DyBCO layer as shown in Fig. 4.1b. All samples were grown by ISD technology using thermal evaporation for all deposited layers. Among the layers, only the MgO buffer layer was deposited at room temperature and at an inclined geometry, i.e. tilted with respect to the evaporation source. All the subsequent layers were deposited in an untitled position and at elevated temperatures. A more detailed description of the used setup and the deposition parameters are found in [24, 25].

The MgO series (sample 2) is a series of semi-processed samples and has only MgO buffer layer on the Hastelloy substrate. Since the MgO buffer layer was deposited at room temperature, samples of the MgO series were not exposed to high temperatures at all. Whereas, the DyBCO series (sample 3) is fully-processed, i.e. all layers were deposited (see above paragraph). Since the MgO cap layer and the DyBCO layer were deposited at an elevated temperature (around 700° C), samples of the DyBCO series were exposed to high temperatures during processing.

The blocking layer series (samples 6-9) are also fully-processed and were prepared in a similar way as the DyBCO series, except that it had an extra buffer layer (of Y, Ag, Si, or Zr) at the MgO-Hastelloy interface.

### 4.2.1 SEM and TEM specimen preparation

This study was intended to analyze the Hastelloy-MgO interface. Therefore, SEM and TEM analyses were done in cross-section. Two types of SEM cross-section samples were prepared by a Focused Ion Beam (FIB) workstation (Zeiss cross-beam 1540): one in a cross-section and

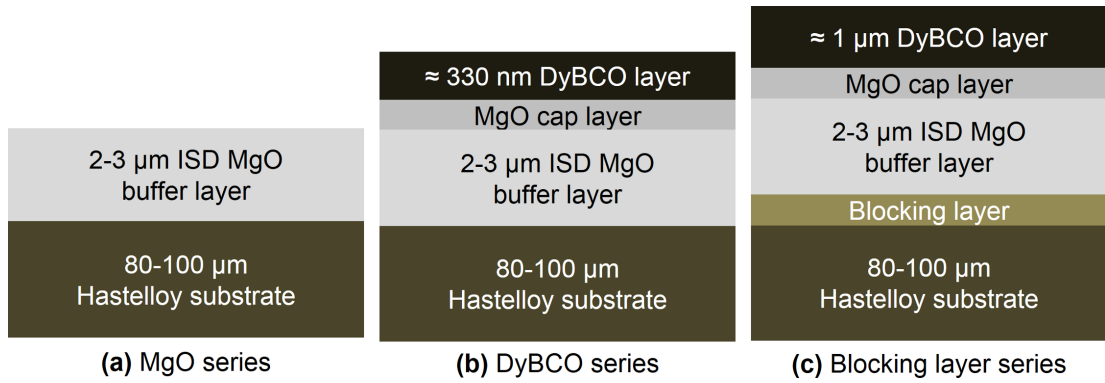


**Figure 4.1:** Schematic of the layer structure of analyzed samples: (a) the MgO series i.e. a series of semi-processed samples exposed to ambient temperature only, (b) the DyBCO series i.e. a series of fully-processed samples exposed to high temperatures and (c) the blocking layer series i.e. a series of samples having an intermediate buffer layer at the Hastelloy-MgO interface and exposed to high temperatures.

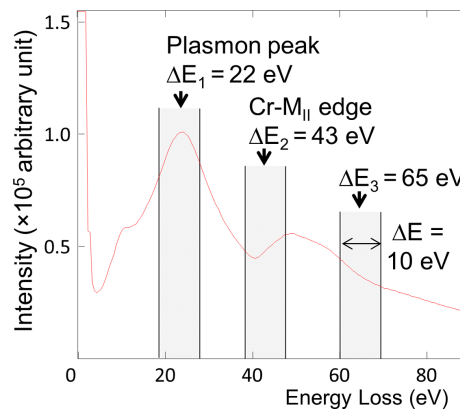


**Figure 4.2:** Low-loss EELS of Cr and positions of energy window for acquiring Cr phase map by using superimposed energy-filtered (RGB) imaging technique.

the other in a longitudinal-section. The cross-section is a section perpendicular to the direction of the tape direction and the longitudinal-section is along the tape direction (Fig. 2.7a).

TEM cross-section samples were prepared by either FIB technique (Fig. 2.10) or by conventional cross-section technique, which was first established by Eyidi et al. [30] and recently improved by Aabdin et al. [23] for ISD coated-conductors (Fig. 2.7). A more detailed descriptions about the sample preparation can be found in Chapter 2.

#### 4.2.2 SEM and TEM analysis

SEM and TEM conventional images were acquired for the study of the microstructure of the MgO-Hastelloy interface. Whereas, low-loss energy-filtered TEM (EFTEM) images were acquired for the Cr diffusion study in the MgO buffer layer at the MgO-Hastelloy interface. Low-loss EFTEM imaging were performed by acquiring three energy-filtered images. The EFTEM images were acquired at energy losses of 21 eV (Plasmon peak), 43 eV (Cr-M<sub>II</sub>, M<sub>III</sub> edge) and 65 eV (21+43 = 65 eV, considering multiple scattering effect) with an energy slit aperture of 10 eV width as shown in Fig. 4.2 and the acquired images are shown in Figs. 4.3a-4.3c. Then, the three EFTEM images were superimposed by assigning a false color to each of the EFTEM image as 21 eV (Red), 43 eV (Green), and 65 eV (Blue) (Figs. 4.3e-4.3g) to yield a superimposed energy-filtered image (Fig. 4.3h). For a detailed description of the EFTEM imaging technique, see the first section of discussion of this chapter (Sec. 4.4.1). From now we will call low-loss superimposed EFTEM images as RGB image, for simplicity.

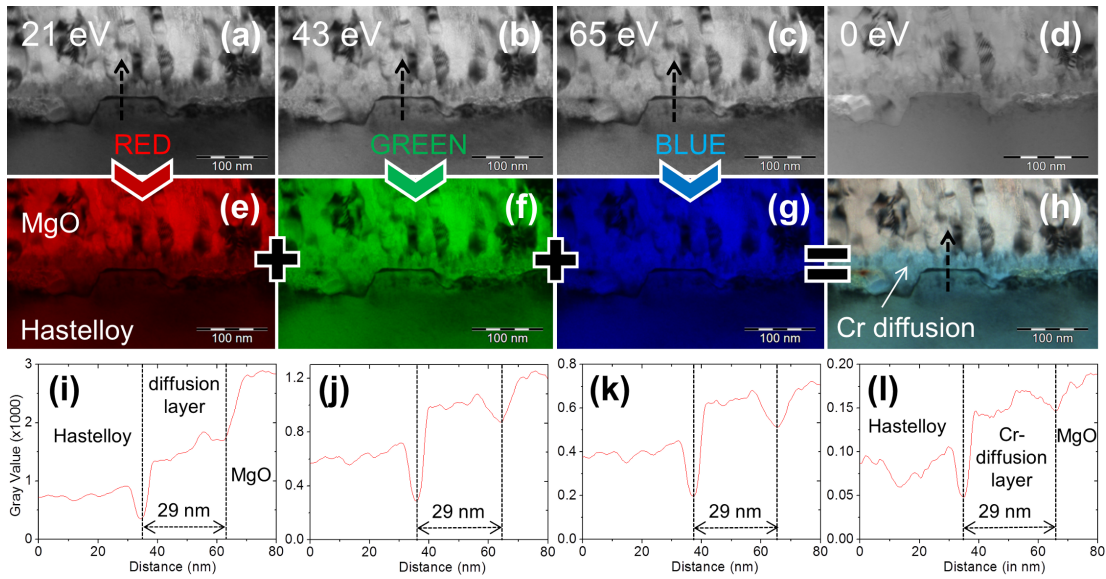


**Figure 4.3:** Energy-filtered TEM images of the Hastelloy-MgO interface acquired at energy losses (a) 21 eV, (b) 43 eV, (c) 65 eV, and (d) 0 eV with an energy slit of 10 eV width. False color coded images of EFTEM image: (e) 21 eV image as red, (f) 43 eV image as green, (g) 65 eV image as blue and (h) superimposed energy-filtered image (RGB). Line scan profiles along the substrate normal (indicated by black dotted arrow) of the Hastelloy-MgO interface for (i) 21 eV, (j) 43 eV, (k) 65 eV, and (l) RGB image.

## 4.3 Results

### 4.3.1 Microstructure of the Hastelloy-MgO interface of fully-processed sample

**Figs. 4.4a** and **4.4b** show secondary electron images of sample 3 in cross-section and in longitudinal section, respectively. Note that all samples studied in this work had several layers, here we show only the Hastelloy-MgO interface, as only this interface is relevant for this study. Secondary electron images revealed voids (see white arrows) being 50-100 nm in sizes at the Hastelloy-MgO interface. Voids formed at the end of the Hastelloy grain boundaries were about 400 nm in size (Figs. 4.4a and 4.4b). Voids had “V” shaped geometry and indented into the Hastelloy substrate. Since the “V” shaped geometry was observed in both (cross-section and longitudinal-section) two perpendicular directions, the voids had pyramidal or conical shape with the base parallel to the Hastelloy-MgO interface and the tip indented in the Hastelloy substrate.

Figs. 4.4c and 4.4d show RGB images of sample 3 of two different specimens prepared from the same tape. The specimen shown in Fig. 4.4c was prepared by the conventional cross-section technique, whereas specimen shown in Fig. 4.4d was prepared by the FIB technique. Consistent with SEM results, the “V” shaped voids were also observed in TEM images, particularly in Fig. 4.4d. A diffusion zone (bluish green colored layer indicated by black arrows in Figs. 4.4c and 4.4d) of about 20-50 nm thickness in the MgO buffer layer was observed. The diffusion zone extended further (up to 300-400 nm) into the MgO buffer layer as the voids got bigger. The core-loss EELS shown in Fig. 4.4e were acquired at the Hastelloy substrate (1), the diffusion layer (2), and the MgO buffer layer (3). The EELS reference points are marked by small circles in Fig. 4.4d. Spectrum 1 shows small chromium (Cr-L<sub>II,III</sub>) edge and no oxygen (O-K) edge, while spectrum 2 shows a large Cr-L<sub>II,III</sub> edge along with the O-K edge, indicating that the diffused zone is a Cr-rich oxide. Note that the Cr diffusion layer in Fig. 4.4c appeared as green color, whereas in Fig. 4.4d it appeared bluish green. This is due to more pronounced multiple scattering effect as the FIB prepared sample (Fig. 4.4d) was found to be thicker (80-100 nm) than the conventionally prepared sample (Fig. 4.4c), which had a thickness of about 50-60 nm.

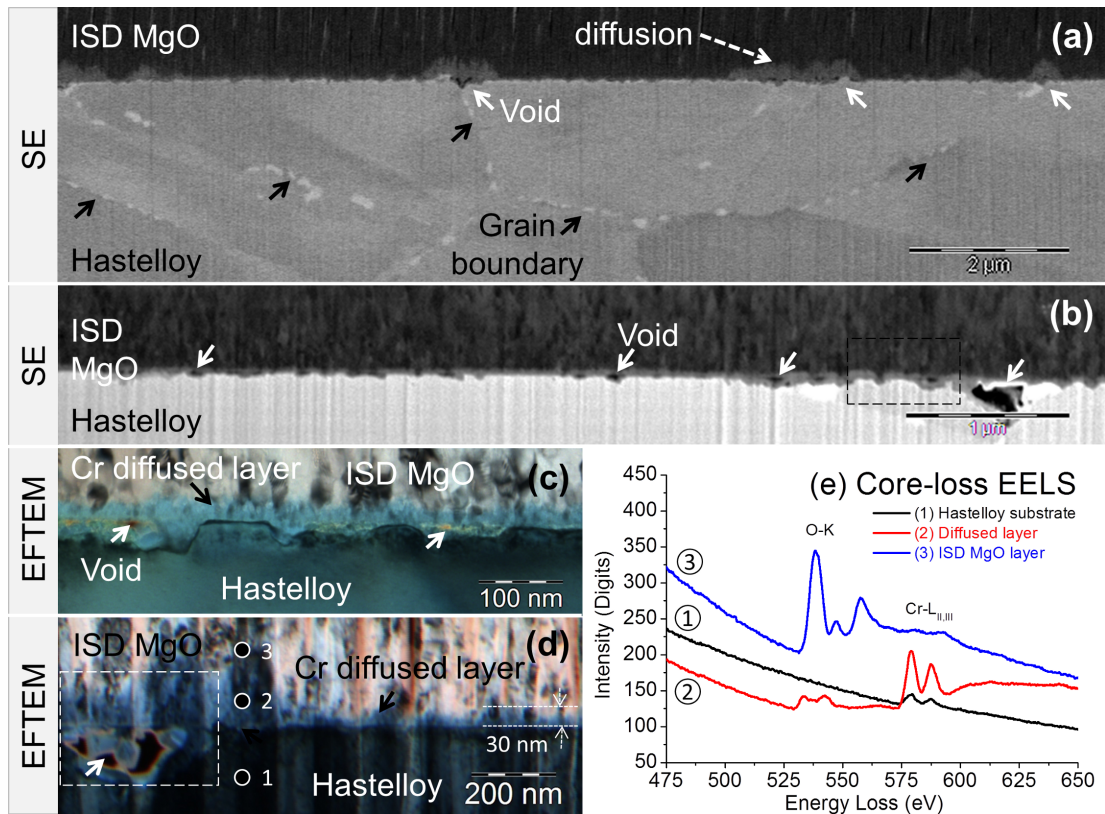


**Figure 4.4:** Secondary electron images of the Hastelloy-MgO interface of sample 1 in: (a) cross-section and (b) longitudinal-section. RGB images of the Hastelloy-MgO interface of sample 1 in cross-section prepared by (c) conventional technique and (d) FIB technique. (e) core-loss EELS of the interface layers acquired at the points indicated by small circles in (d).

### 4.3.2 Microstructure of the Hastelloy-MgO interface of semi-processed samples

**Figs. 4.5a** and 4.5b show secondary electron images of sample 2 in cross-section and in longitudinal section, respectively. In contrast to sample 3, no void formation was observed at the Hastelloy-MgO interface.

Fig. 4.5c shows a TEM bright-field image of sample 2 in cross-section and Fig. 4.5d shows a RGB image of the same area. Consistent with SEM results no voids were observed in the TEM images. The RGB image also ensured that no Cr diffusion occurred at the MgO-Hastelloy interface.

For comparison, high-magnification images of the rectangular areas at the Hastelloy-MgO interface shown in Figs. 4.4 and 4.5 are shown in **Fig. 4.6**. Figs. 4.6a and 4.6b show a secondary electron image and a RGB image of sample 3 at high magnification. The Hastelloy-MgO interface was found to be rough and a roughness of about 135 nm was measured over several microns of the interface length.

Figs. 4.6c and 4.6d show a secondary electron image and a RGB image of sample 2 at high magnification. Both images show that the interface is void free and flat. A roughness of less than 25 nm was measured over several microns of the interface length.

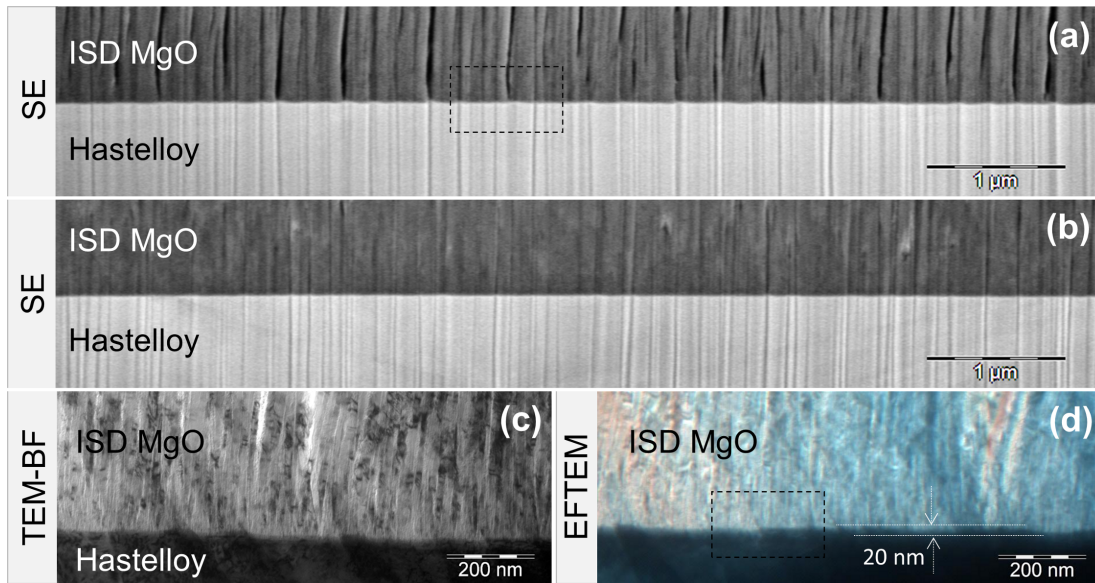


**Figure 4.5:** Secondary electron images of the Hastelloy-MgO interface of sample 2 in (a) cross-section and (b) longitudinal-section. TEM (c) bright-field and (d) RGB image of the Hastelloy-MgO interface of sample 2 in cross-section.

### 4.3.3 Microstructure of the Hastelloy-Yttrium-MgO interface of fully-processed samples with an Yttrium (Y) buffer layer

**Figs. 4.7a** and **4.7b** show a TEM bright-field image and the corresponding dark-field image of sample 7 in cross-section, respectively. Note that for sample 7 an additional layer of Yttrium (Y) was deposited at the Hastelloy substrate yielding a Hastelloy/Yttrium/MgO layer sequence. The bright-field image shows that the MgO buffer layer had a flat interface with the substrate. The interface roughness was measured to be less than 20 nm, no void was observed at the interface. An 80 nm thick Y-buffer layer (marked by white dotted lines) was observed in the dark-field image (Fig. 4.7b). The observed Y-buffer layer had a flat and sharp interface with the MgO buffer layer but a rough interface with the Hastelloy substrate. A complex phase layer of thickness around 150-200 nm was observed in between the Y-layer and the Hastelloy substrate. The complex phase at the Hastelloy interface had a wavy nature as marked by the black dotted line in Fig. 4.7b. Fig. 4.7d shows a selected area diffraction pattern (nearly two-beam condition) of the interface. Since no amorphous ring was observed in the diffraction pattern, all the layers and phases at the interface exist in crystalline phase.

Fig. 4.7c shows a RGB image of the same area shown in Fig. 4.7a. Void formation and Cr diffusion were not observed at the Y-MgO interface. On the other hand at the Hastelloy-Y interface, no void formation was observed, however, Y-diffusion and formation of Cr-rich phases in the Hastelloy near the interface were observed.

**Fig. 4.8a** shows a RGB image of another area of sample 7. Similar results as for the first area (Fig. 4.7) were observed, i.e. a complex phase formation at the Hastelloy-Yttrium interface and a flat void free interface in between the Yttrium and the MgO buffer layer.

Similar to sample 3, core-loss EELS (Fig. 4.8c) were acquired for sample 7 at the points indicated in Fig. 4.8a. Spectrum 1, which was acquired at the Hastelloy substrate, shows a small chromium (Cr-L<sub>II,III</sub>) edge but no oxygen (O-K) edge, while spectrum 2, which was acquired at the Hastelloy-Yttrium interface, shows a large Cr-L<sub>II,III</sub> edge along with the O-K edge, indicating that a complex oxide phase formation occurred near the interface in the Hastelloy substrate. Absence of Cr-L<sub>II,III</sub> edge in spectrum 3 confirmed that there is no Cr diffusion in the MgO buffer layer.

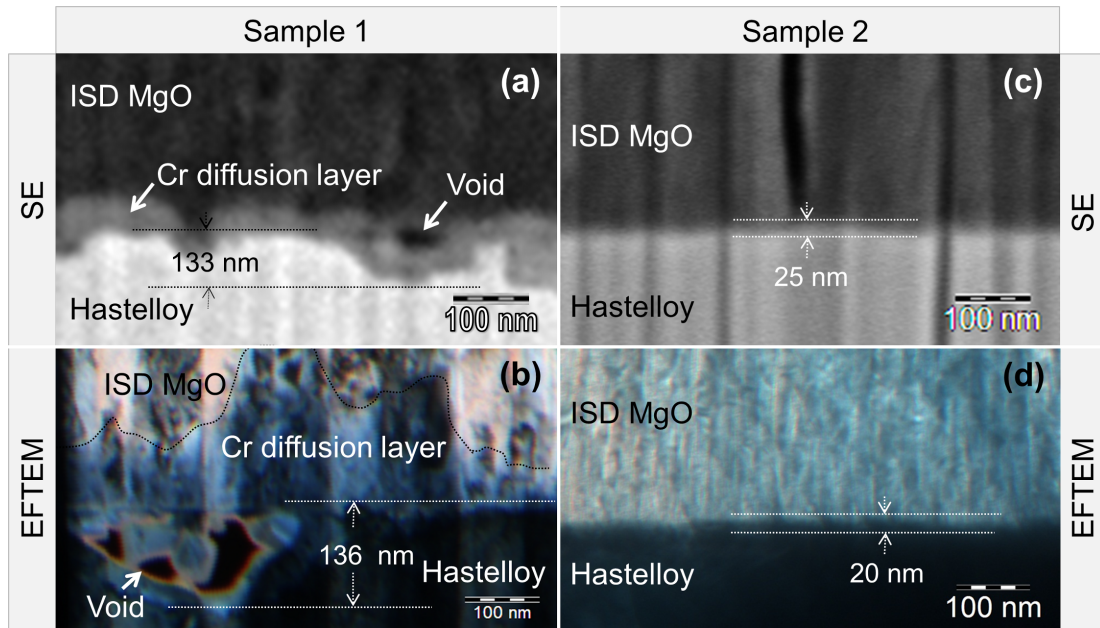


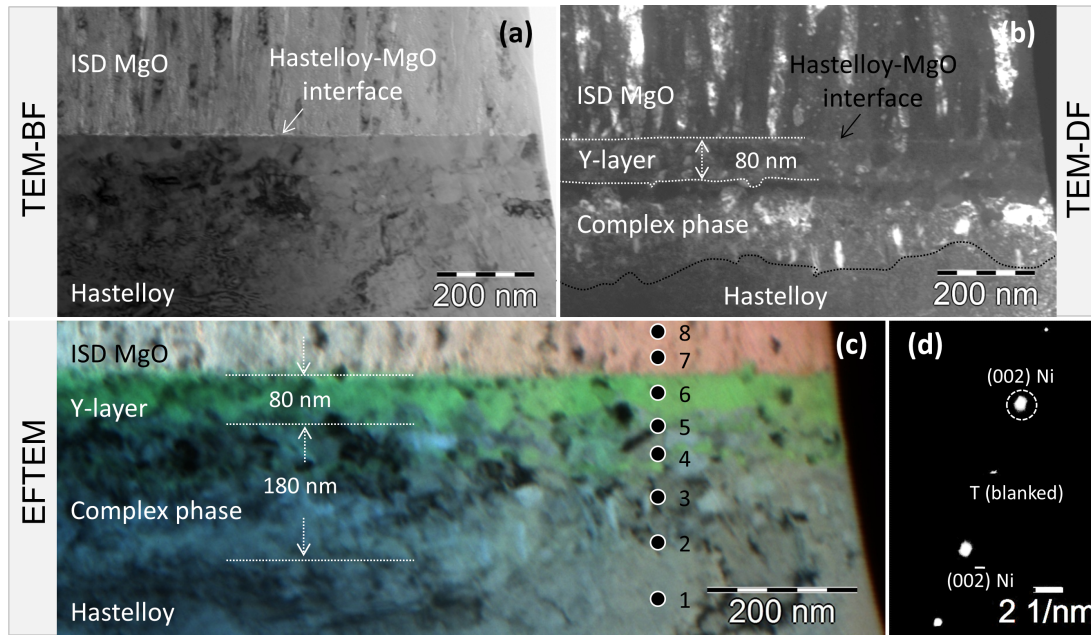
**Figure 4.6:** High-magnification images of the areas enclosed by dotted rectangles shown in Figs. 2 and 3: (a) secondary electron image, (b) RGB image of the interface of sample 1 and (c) secondary electron image, (d) RGB image of the interface of sample 2.

**Table 4.1:** TEM EDX quantitative analysis of sample 7 in cross-section. The reference points are indicated in Fig. 4.8c and some of the spectra are shown in figure 9.

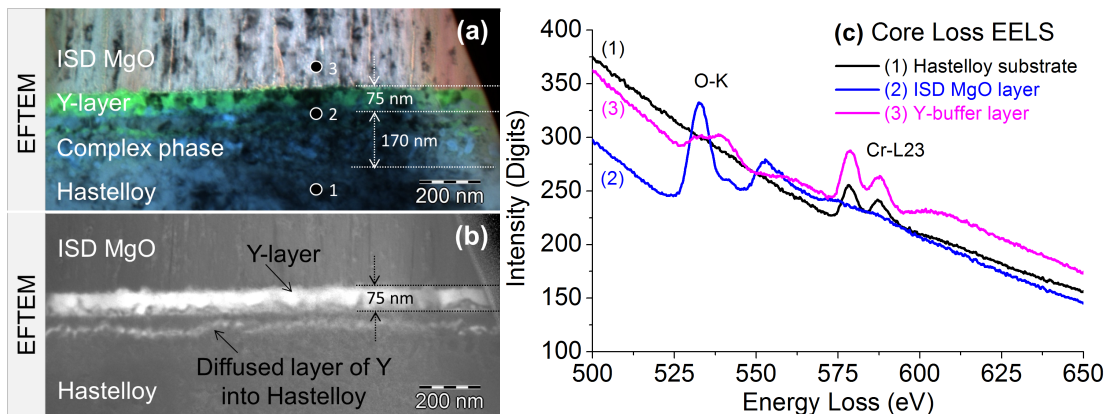
Spectrum	Ni [at.%]	Cr [at.%]	Y [at.%]	Mg [at.%]	O [at.%]
Series	Ni-K	Cr-K	Y-K	Mg-K	O-K
k-factor	1.32	1.15	2.77	1.08	1.77
Spectrum 1	58.8	17.6	0.0	0.9	22.5
Spectrum 2	63.2	17.8	0.0	0.8	18.1
Spectrum 3	5.7	30.1	15.8	0.0	48.5
Spectrum 4	8.1	10.5	5.4	1.4	74.4
Spectrum 5	5.1	26.5	13.9	0.0	54.5
Spectrum 6	1.1	0.8	40.3	0.0	57.6
Spectrum 7	0.8	0.5	0.0	42.2	55.9
Spectrum 8	0.7	0.6	0.0	42.2	56.3

Fig. 4.8b shows a ratio image of two energy-filtered images acquired at 46 eV and 24 eV energy losses with an energy slit aperture of widths 10 eV. Y-rich phases appears bright, the bright contrast down to the Y-buffer layer shows the complexity of the Hastelloy-Y interface with respect to the Y-phase.

EDX point spectra (TEM) were acquired along the perpendicular direction of the interface to quantify the chemical composition of each layer (reference points are indicated in Fig. 4.7c). A detailed quantitative analysis of the acquired spectra is summarized in **Table 4.1** and some of the spectra are shown in **Fig. 4.9**. Comparison of spectrum 2 and 3 (Fig. 4.9a and 4.9b) yielded that there is an increase in Cr-content (decrease in Ni-content) at the Y-Hastelloy interface compared to the Hastelloy substrate. Spectrum 6 (Fig. 4.9c) confirmed that the Y-layer consisted of an  $Y_2O_3$  phase. Note that Y-layer was deposited as metallic Yttrium. Spectrum 7 (Fig. 4.9d) confirmed that no Cr diffusion occurred in the MgO at the Y-MgO interface. The varying chemical composition of Ni, Cr, and Y listed in Table 4.1 shows the complexity of the Hastelloy-Y-MgO interface with respect to chemical composition. Small peaks of Al, Fe and Ti are due to re-sputtering of the aluminum ring and the  $BaTiO_3$  dummy used for cross-section preparation.



**Figure 4.7:** TEM cross-section (area 1) of sample 7: (a) bright-field image, (b) corresponding (002) dark-field image, (c) RGB image of the area shown in (a) and (d) selected area diffraction pattern of the interface. The small black circles in (c) show the EDX reference points.



**Figure 4.8:** TEM cross-section (area 2) of sample 7: (a) RGB image (b) ratio-image of two energy-filtered images, one acquired at 46 eV and the other at 24 eV with an energy slit of widths of 10 eV and (c) core-loss EELS of the interface layers acquired at the points indicated by small circles in (a).

#### 4.3.4 Microstructure of the Hastelloy-Ag-MgO interface of fully-processed samples with a Silver (Ag) buffer layer

**Fig. 4.10a** shows a low-magnification bright-field image of sample 6 in cross-section. In contrast to sample 7, the interface contained a high density of voids (white arrows in Fig. 4.10a) of size 30-200 nm. Figs. 4.10b and 4.10c show RGB images of two different areas of sample 6. In both images no layer of Ag or  $\text{AgO}_x$  was observed at the interface, instead, a  $\text{CrO}_x$  layer and a complex phase with wavy interface (black dotted line in Fig. 4.10c) were observed at the interface. A high density of voids (white arrows) and Cr diffusion (black arrows) in the MgO buffer layer at the interface were observed.

Similar to sample 7, a detailed quantitative analysis of EDX point spectra acquired at the Hastelloy-Ag-MgO interface is summarized in **Table 4.2** for sample 6. Some of the spectra are shown in **Fig. 4.11** and reference points are indicated in Figs. 4.10b and 4.10c. Spectrum 2 (Fig. 4.11a) shows an Ag containing complex phase at the interface. Spectrum 4 (Fig. 4.11b)

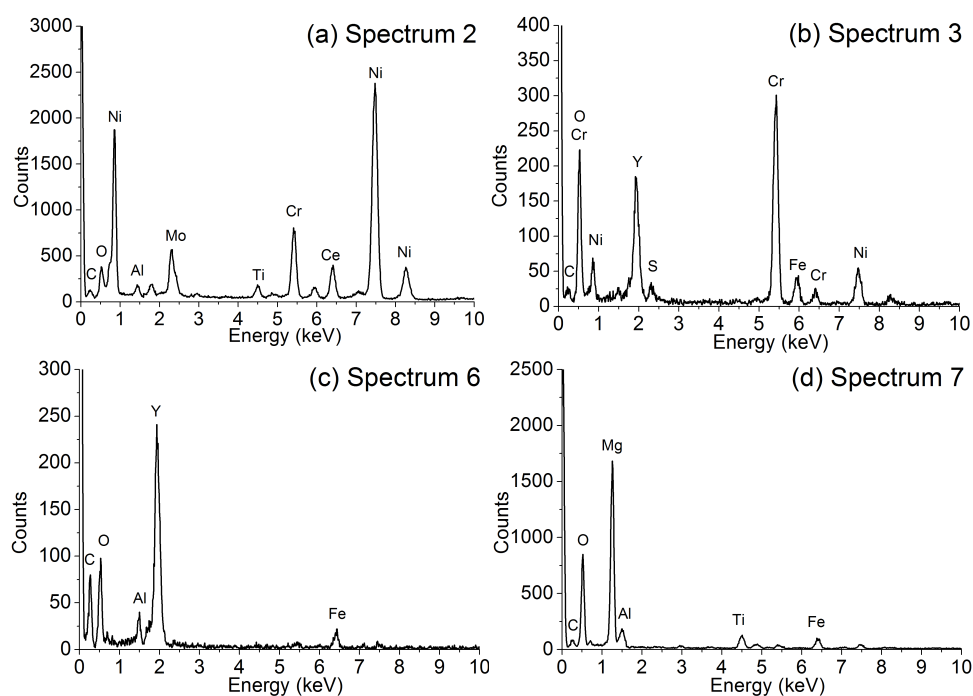


**Figure 4.9:** TEM EDX spectroscopy of sample 7: EDX spectra of (a) the Hastelloy substrate (spectrum 2), (b) the Cr-rich complex phase (spectrum 3), (c) the Y-layer (spectrum 6) and (d) the MgO buffer layer (spectrum 7). Reference points are given in Fig. 4.7c.

**Table 4.2:** TEM EDX quantitative analysis of sample 6 in cross-section. The reference points are indicated in Fig. 4.10b and 4.10c and some of the spectra are shown in Fig. 4.11.

Spectrum	Ni [at.%]	Cr [at.%]	Y [at.%]	Mg [at.%]	O [at.%]
Series	Ni-K	Cr-K	Y-K	Mg-K	O-K
k-factor	1.32	1.15	2.77	1.08	1.77
Spectrum 1	76.8	21.1	0.0	2.0	0.0
Spectrum 2	73.5	13.6	6.6	1.8	4.2
Spectrum 3	35.5	8.11	0.0	2.7	53.5
Spectrum 4	5.1	29.0	0.0	13.6	52.2
Spectrum 5	10.5	10.0	0.0	31.0	48.3
Spectrum 6	4.9	1.4	0.0	48.9	44.6
Spectrum 7	7.5	30.4	0.0	2.4	59.4

shows Cr diffusion in the MgO buffer layer at the Ag-MgO interface. The varying chemical composition of Ni, Cr, and Ag listed in Table 4.2 shows the chemical complexity of the Hastelloy-Ag-MgO interface.

## 4.4 Discussion

### 4.4.1 Cr analysis by electron energy loss spectroscopy (EELS) and energy-filtered TEM

EDX spectroscopy in the TEM is the method of choice for quantitative chemical analysis for a large class of nanomaterials because of high lateral resolution of 10 nm and detection limit of 150 ppm. Elemental distribution by EDX elemental maps, however, requires a scanning unit, which is not available in our instrument. Instead, we used EFTEM or electron spectroscopic

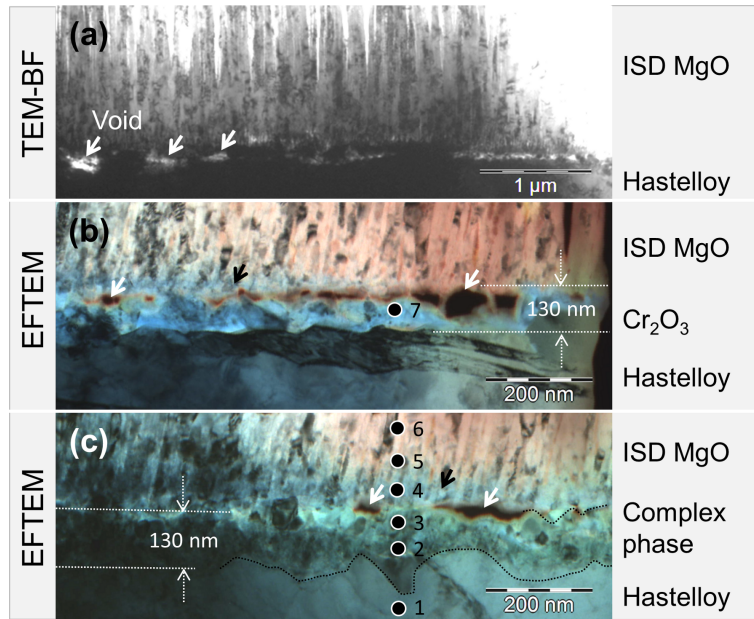


**Figure 4.10:** TEM cross-section of sample 6: (a) overview bright-field image of the Hastelloy-Ag-MgO interface, (b) and (c) RGB images of the interface of two different areas. Black arrows indicate the Cr diffusion in the MgO buffer layer and small black circles show EDX reference points.

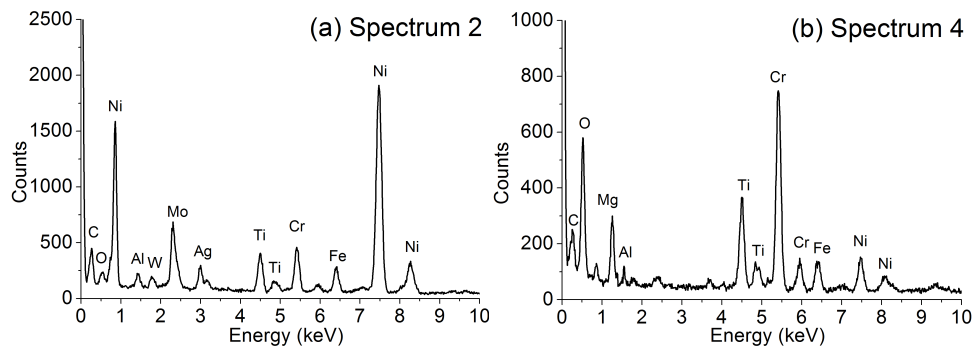


**Figure 4.11:** EDX spectroscopy (TEM) of sample 6: EDX spectra of (a) the Ag-layer (spectrum 2) and (b) Cr diffusion in the MgO buffer layer (spectrum 4). Reference points are given in Figs. 4.10b and 4.10c.

imaging (ESI) elemental maps.

The physical processes of electron energy loss spectroscopy (EELS) and ESI are same i.e. inelastic scattering of electrons. Understanding the key features of the EELS is important for optimizing acquisition of ESI/EFTEM images. Though many features of the EELS (plasmon peaks, ionization edges) can be used for energy-filtered imaging, the low-loss region has particularly great potential for imaging of chemical phases and obtaining phase maps, due to high signal-to-noise ratio and images can be recorded within a few seconds. Therefore, identifying the key features of the low-loss EELS related to the elements of interest and establishing the corresponding finger prints in the spectrum is of crucial importance for obtaining a phase map. The plasmon peak and ionization edges of Cr were identified in the low-loss spectra shown in Fig. 4.2 and found Cr-1<sup>st</sup> plasmon peak at 21 eV, Cr-M<sub>II,III</sub> edge at 43 eV and Cr-M<sub>I</sub> edge at 74 eV. A complete list of ionization edge energy for relevant elements present at the Hastelloy-MgO interface is listed in **Table 4.3**.

Since a Cr diffusion was identified by EDX spectroscopy, acquisition of Cr elemental maps by EFTEM would have been a natural choice. However, acquisition of Cr-M elemental maps by the three window method is difficult because of unfavorable peak to background signal of the Cr-M<sub>II,III</sub> ionization edge at 43 eV and the very steep background due to a plasmon peak at 21 eV. This slope of signal yields always too small number of contrast (intensity) in the final

**Table 4.3:** Key features of the low-loss EELS of the ISD MgO buffer layer, the Cr diffusion layer, the Y-layer and the Hastelloy substrate.

Phase/Layers	Ionisation peaks/edges	Peak/ionization edge position (eV)
ISD MgO buffer layer	1 <sup>st</sup> , 2 <sup>nd</sup> plasmon peaks Mg-L <sub>II,III</sub> , Mg-L <sub>I</sub> edges	11.5, 23 52, 89
Cr diffusion layer	1 <sup>st</sup> plasmon peak Cr-M <sub>II,III</sub> , Cr-M <sub>I</sub> edges	24 43, 74
Y-layer	1 <sup>st</sup> plasmon peak Y-N <sub>II,III</sub> , Y-N <sub>I</sub> edges	14 26, 46
Hastelloy substrate	1 <sup>st</sup> plasmon peak Ni-M <sub>II,III</sub> , Ni-M <sub>I</sub> edges	24 68, 112

elemental map. Therefore, we acquired three energy-filtered images at 21 eV (plasmon), 43 eV, and 65 eV and then superimposed them to yield a RGB image.

Note that this is a very fast technique (few minutes for one colored phase map). However, large area mapping by EFTEM imposes stringent requirements on sample preparation. In order to extract reliable quantitative information, specimen thickness must be smaller than a fraction of the mean free path of inelastic scattering ( $\lambda \sim$  nominally few tens of nm) and uniform over the whole area of interest.

For quantification of the acquired phase maps, a line-scan intensity (grey value) profile perpendicular to the interface was made for each EFTEM image as shown in Figs. 4.3i-4.3l. For the diffusion layer, there is a jump in the intensity in 43 eV and 65 eV EFTEM images due to Cr diffusion. The increased intensity in 43 eV EFTEM image is due to the Cr-M<sub>II,III</sub> ionization edge and confirmed that the diffused layer is rich in Cr. Note that increased intensity in 65 (21 + 43 = 64) eV EFTEM image is due to multiple scattering effect. Our results were confirmed by acquiring few EDX spectra of the Cr diffusion layer (Fig. 4.11b), in which a high peak of Cr can be seen.

#### 4.4.2 Metal-oxide interface thermodynamics

Cross-section TEM analysis of the Hastelloy-MgO interface (Figs. 4.4 and 4.6) revealed that the high temperature processing steps involved in the fabrication of thin films CCs introduced structural and chemical changes at the interface. Note that neither void formation nor Cr diffusion was observed at the interface for the samples processed at room temperature (Figs. 4.5 and 4.6). The void formation at the interface and the Cr diffusion from the Hastelloy substrate in the MgO buffer layer will be discussed by considering the *Kirkendall effect* and the *Ellingham Diagram* [83].

Certain metals have a high affinity to oxygen, i.e. a large negative enthalpy of oxide formation. At a metal-oxide (oxygen rich medium) interface, the metal species starts diffusing towards the oxide and oxygen towards the metal. Particularly at a sufficiently high temperature, an intermediate layer of metal-oxide is formed at the interface. This phenomena is called *thermally activated oxidation* of metals and may lead to *Kirkendall effect*, yielding a porous layer on the side of the more rapidly diffusing component [80].

Oxidation of alloys is much more complicated than a metal oxidation, as many different effects can occur during oxidation of the alloy. Progression of the process depends on the alloy composition, environmental conditions (temperature and pressure), free energy of oxide formation of base metal and alloying element, concentration of alloying elements, and maximum solubility of oxygen in the base metal.

The review of Wallwork [84] on the oxidation of alloys is worthwhile to discuss here to understand the complex phase formation at the Hastelloy-Y interface and the Cr diffusion in

**Table 4.4:** Free enthalpy of oxide formation of relevant elements present at the Hastelloy-MgO interface [83].

Oxidation reaction Element + O <sub>2</sub> = Oxide	Free enthalpy $\Delta H$ (in joule/mole) of oxide formation at 800 °C and P <sub>O<sub>2</sub></sub> = 1 atm. [83]
4Ag + O <sub>2</sub> = 2Ag <sub>2</sub> O	Unstable, decomposed
4/3Cr + O <sub>2</sub> = 2/3Cr <sub>2</sub> O <sub>3</sub>	5.65×10 <sup>5</sup>
Si + O <sub>2</sub> = SiO <sub>2</sub>	7.08×10 <sup>5</sup>
Zr + O <sub>2</sub> = ZrO <sub>2</sub>	9.50×10 <sup>5</sup>
2Mg + O <sub>2</sub> = 2MgO	9.90×10 <sup>5</sup>
4/3Y + O <sub>2</sub> = 2/3Y <sub>2</sub> O <sub>3</sub>	11.2×10 <sup>5</sup>

the MgO buffer layer. The author reviewed the oxidation of Ni-Cr based alloys and reported that oxidation of Ni-Cr alloys yield a full Cr<sub>2</sub>O<sub>3</sub> layer formation on the alloy surface, only if the alloy contains 15-20 wt.% Cr. The Cr<sub>2</sub>O<sub>3</sub> layer does not develop at once, initially NiO and Cr<sub>2</sub>O<sub>3</sub> both nucleates on the surface, but due to its defect state the NiO grows more rapidly and envelops the Cr<sub>2</sub>O<sub>3</sub>. This leads to rapid depletion of nickel in the surface and promotes the formation of Cr<sub>2</sub>O<sub>3</sub>. Due to relatively low negative free energy of oxide formation, NiO can react with Cr<sub>2</sub>O<sub>3</sub> and produce some NiCr<sub>2</sub>O<sub>4</sub> spinel. Therefore, presumably all diffusion phenomena occurred at the Hastelloy-MgO interface proceeds with the formation of an oxide layer of Cr (Cr<sub>2</sub>O<sub>3</sub>) at the interface.

Let us assume a thin Cr<sub>2</sub>O<sub>3</sub> layer formation at the Hastelloy-MgO interface and then consider the work reported on the MgO-Cr<sub>2</sub>O<sub>3</sub> system by Greskoich and Stubican [85]. The authors showed that at higher temperature a SSR occurred, resulting in a spinel MgCr<sub>2</sub>O<sub>4</sub> formation. The growth of the spinel occurred by a counter diffusion of Mg<sup>2+</sup> and Cr<sup>3+</sup> cations through the spinel layer i.e. the Cr<sup>3+</sup> cations of Cr<sub>2</sub>O<sub>3</sub> layer are diffusing in the MgO and the Mg<sup>2+</sup> cations of MgO in the Cr<sub>2</sub>O<sub>3</sub> through the spinel layer (MgCr<sub>2</sub>O<sub>4</sub>) and the rate defining cation is the slowly diffusing Cr<sup>3+</sup> cation.

In spite of the higher diffusion coefficient of Ni in the MgO compared to Cr (**Table 4.5**), no Ni diffusion was observed in the MgO. The reason for this might be the lower affinity of Ni to oxygen compared to Cr [83] and formation of thin Cr<sub>2</sub>O<sub>3</sub>/ MgCr<sub>2</sub>O<sub>4</sub>, which acts as a blocking layer for Ni diffusion in the MgO buffer layer.

A diffusion length of 2.4 nm for the Cr in the MgO was determined by assuming  $t = 1 h$ , whereas the observed length was 20-50 nm. By considering the general trend of surface diffusion, grain boundary diffusion and volume diffusion [86]:

$$D_{\text{surface}} > D_{\text{grain boundary}} > D_{\text{volume}}$$

and the small (10-20 nm) grain size of MgO grains in the MgO seed layer reported by Duerrschnabel et al. [87], which is a typical feature of ISD growth, the long range Cr diffusion was assigned to grain boundary diffusion in the MgO.

Furthermore, the observed big V-shaped void formation (Figs. 4.4a, 4.4b, and 4.4d) at the Hastelloy grain boundaries ending at the interface can be understood by considering the grain boundary diffusion of Cr in the Hastelloy and a Cr<sub>2</sub>O<sub>3</sub> layer formation at the interface. We showed and indicated the grain boundaries of the Hastelloy substrate in Fig. 4.4a (black arrows). The Hastelloy substrate grains were found to be 2-4 μm in size. Fast Cr diffusion along the Hastelloy grain boundaries compared to the Hastelloy bulk, accumulate Cr at the interface and at the Hastelloy grain boundaries near the interface. Therefore, the Cr diffusion in the MgO near the Hastelloy grain boundaries occurred under a constant source of Cr [88] (Fig. 4.16)]. The fast rate of diffusion of Cr in the Cr<sub>2</sub>O<sub>3</sub> compared to the oxygen, results in a *Kirkendall effect* [83], i.e. formation and accumulation of vacancies at the interface towards the fast diffusing element (Cr) i.e. Hastelloy side, resulting in a big V-shaped void formation and the Cr diffusion profile extended more deeply in the MgO as observed in Fig. 4.4d.

Loudjani et al. [89] studied the interface diffusion of Y<sub>2</sub>O<sub>3</sub> films on the Ni (30 wt.% Cr)

substrate and concluded that, the alloy substrate formed a  $\text{Cr}_2\text{O}_3$  layer at the interface. After oxidation,  $\text{Y}^{3+}$  ions from  $\text{Y}_2\text{O}_3$  layer subsequently diffused in the  $\text{Cr}_2\text{O}_3$  and finally in the alloy substrate. A similar result was observed in our Y-layer deposited samples. As shown in Fig. 4.7c a complex oxide phase with Cr-rich agglomerates was formed at the Hastelloy-Y interface after the high temperature processing. A diffuse layer of Y in the Hastelloy substrate near the interface can also be seen in Fig. 4.8b.

In contrast to Cr diffusion, no Y diffusion occurred at the Y-MgO interface, though, Berard [90] showed that both Y and Cr had comparable diffusion coefficients (Table 4.5) in MgO. This might be due to the fact that the Y-diffusion in the MgO requires  $\text{Y}_2\text{O}_3$  should decompose in metallic Y, which is energetically unfavorable process [91].

#### 4.4.3 Technological solution

CCs require biaxial texturing of the superconducting thin film over large length scale to ensure maximum critical currents. Out of many well developed techniques such as RABiTS, IBAD and ISD, only the ISD technique is independent of substrate properties i.e. the texture and recrystallization properties of the metallic substrates. It only requires that the substrate should be hard and non-magnetic. The surface of the substrate should be flat, free from voids (pits). Furthermore, during the successive processing steps, it is important to ensure that no SSR should occur between the substrate (Hastelloy) and the buffer layer (MgO) to avoid diffusion and voids at the interface. Note that any SSR or inter-diffusion reaction (*Kirkendall effect*) at the interface may lead to formation of a porous layer (voids) at the interface [80], resulting in a poorly adhering film interface as observed in the present work for sample 3. From the above discussion, it is clear that a planar layer of a passivating oxide of suitable thickness is necessary at the Hastelloy-MgO interface to avoid Cr diffusion and void formation.

Yttrium buffer layers were deposited as metallic Y on top of the Hastelloy substrate. A planar  $\text{Y}_2\text{O}_3$  layer was found at the interface after high temperature processing. The  $\text{Y}_2\text{O}_3$  layer acts as a blocking layer for Cr (Ni, Mo etc. present in the Hastelloy substrate) diffusion and thus avoids void formation at the interface. The reason for this is that  $\text{Y}_2\text{O}_3$  is an extremely stable compound:  $\text{Y}_2\text{O}_3$  has one of the highest free energies for oxide formation. No multiple valences exist, only the trivalent oxidation state is known. Structural stability is evidenced by the lack of any phase transformations [92].  $\text{Y}_2\text{O}_3$  layers were also used as diffusion barrier layers in Si-YSZ- $\text{Y}_2\text{O}_3$ -YBCO structures [93].

On the other hand, due to small negative enthalpy of oxide formation, Ag was found an inefficient buffer layer. So in principle, any other material which has a high enthalpy of oxide formation, i.e.  $\text{ZrO}_2$ ,  $\text{SiO}_2$  (Table 4.4) might act as an efficient barrier layer at the Hastelloy-MgO interface.

## 4.5 Summary

Diffusion phenomena at elevated temperatures of Hastelloy-MgO interfaces were studied by SEM and TEM using specimens prepared in cross-section. Energy-filtered imaging was demonstrated and utilized to image the Cr diffusion profile in the MgO buffer layer at the MgO-Hastelloy interface. A 20-50 nm Cr diffusion zone in the MgO buffer layer was observed for the interfaces that were exposed to high temperatures (700-800 °C) during processing. On the other hand, no diffusion of any of the Hastelloy transition metals were observed for samples that were grown at ambient temperature and were not exposed to high temperatures. Therefore, it was concluded that the diffusion phenomena was thermally activated. The diffusion phenomena yielded void formation of sizes 50-100 nm at the interface. The formation of voids was explained by considering the diffusion data of relevant elements and *Kirkendall effect*. The void formation at the interface yielded a rough and poorly adhering film interface.

**Table 4.5:** Self and inter diffusion data of the relevant elements present at the Hastelloy-MgO interface [82, 83].

Diffusing ion	Diffusion matrix	$D_0$ ( $\text{cm}^2\text{sec}^{-1}$ )	$Q$ ( $\text{kcal mole}^{-1}$ )	$T$ ( $^{\circ}\text{C}$ )	$D$ ( $\text{cm}^2\text{sec}^{-1}$ )	Diffusion length (cm)
$\text{Cr}^{+3}$	MgO	$9.80 \times 10^{-4}$	$6.80 \times 10^{+4}$	760	$3.88 \times 10^{-18}$	2.4
$\text{Ni}^{+2}$		$1.80 \times 10^{-5}$	$4.83 \times 10^{+4}$	760	$1.06 \times 10^{-15}$	39.1
$\text{Mg}^{+2}$		$2.49 \times 10^{-1}$	$7.90 \times 10^{+4}$	760	$4.61 \times 10^{-18}$	2.6
$\text{O}^{-2}$		$4.80 \times 10^{-4}$	$3.02 \times 10^{+4}$	760	$1.93 \times 10^{-10}$	$1.7 \times 10^{+4}$
$\text{Y}^{+3}$		$2.11 \times 10^{-2}$	$7.04 \times 10^{+4}$	760	$2.59 \times 10^{-17}$	6.1
$\text{Cr}^{+3}$	$\text{Cr}_2\text{O}_3$	$4.00 \times 10^{+3}$	$1.00 \times 10^{+5}$	760	$2.64 \times 10^{-18}$	2.0
$\text{O}^{-2}$		15.9	$1.01 \times 10^{+5}$	760	$7.11 \times 10^{-21}$	0.1
$\text{Y}^{+3}$		-	-	760	$8.00 \times 10^{-18}$	3.4
$\text{O}^{-2}$	$\text{Y}_2\text{O}_3$	7.24	$5.86 \times 10^{+4}$	760	$2.81 \times 10^{-12}$	$2.0 \times 10^{+3}$
$\text{Y}^{+3}$	$\text{Y}_2\text{O}_3$	$2.40 \times 10^{-4}$	$4.39 \times 10^{+4}$	760	$1.21 \times 10^{-13}$	$4.2 \times 10^{+2}$
$\text{Cr}^{+3}$	Pure Ni	$3.00 \times 10^{-2}$	$4.08 \times 10^{+4}$	760	$6.85 \times 10^{-11}$	$9.9 \times 10^{+3}$
$\text{Ni}^{+2}$		2.59	$7.01 \times 10^{+4}$	760	$3.68 \times 10^{-15}$	72.8

To suppress or block the diffusion at elevated temperatures at the interface, a thin intermediate buffer layer of different elements such as Yttrium (Y), Silver (Ag), Silicon oxide ( $\text{SiO}_2$ ), and Zirconium oxide ( $\text{ZrO}_2$ ) were deposited at the interface. In this study we reported only the two Y and Ag intermediate buffer layer. The Y buffer layer being 100 nm thick was found to be an efficient barrier layer, as no diffusion and voids were observed at the interface. The metallic Y formed an oxide at elevated temperatures, which acts as a blocking layer for the Hastelloy transition metals diffusion. On the other hand Ag was found to be an inefficient buffer layer. Therefore, on the basis of an *Ellingham diagram*, it was concluded that in principle any other material which has a high negative enthalpy of oxide formation, i.e.  $\text{SiO}_2$ ,  $\text{ZrO}_2$  would also act as an efficient barrier layer for Cr (Ni, Mo etc. present in the Hastelloy substrate) at the Hastelloy-MgO interface. It was found that the samples with Y-buffer layer yielded much better adhesion between substrate and buffer layer. Note that a few 100 nm deep diffusion in the MgO buffer layer will not affect the properties of superconducting film, therefore, almost no changes in critical current densities were observed.

## Chapter 5

# Growth Behavior of Superconducting DyBa<sub>2</sub>Cu<sub>3</sub>O<sub>7-x</sub> Thin Films Deposited by Inclined Substrate Deposition for Coated Conductors

### 5.1 Introduction

Superconducting DyBa<sub>2</sub>Cu<sub>3</sub>O<sub>7-x</sub> (DyBCO) films were grown on biaxially-textured MgO buffer layers deposited by inclined substrate deposition (ISD) on Hastelloy substrates. Despite a large lattice mismatch of 8.5% between DyBCO and MgO, the DyBCO grew epitaxially on the MgO buffer layer and the biaxial texture of the MgO was well transferred to the DyBCO. Typical critical current densities,  $J_c$ , of the DyBCO film were 2.1 MA cm<sup>-2</sup> at 77 K in a self-field. Biaxial texturing is the key for reaching the high critical current densities and was investigated by transmission electron microscopy. DyBCO grains were found to be 130–500 nm in size, with faceted grain boundaries. The c-axis of the DyBCO grains was tilted away from the substrate normal by 29° such that it was perpendicular to the MgO (002) facets. A high dislocation density of  $7.4 \times 10^{11}$  cm<sup>-2</sup> and stacking faults along the ab-planes were observed in the DyBCO film. Interface, grain boundary and volume energies of the DyBCO film were calculated and a growth model for the DyBCO film is discussed. ISD offers the potential for high-quality, biaxially textured MgO buffer layers suitable for long-length superconducting coated conductors (CCs).

ReBa<sub>2</sub>Cu<sub>3</sub>O<sub>7-x</sub> (ReBCO, Re: rare earth, i.e. Y, Dy etc.) thin films yielding high critical current densities are usually deposited as either single crystalline or biaxially textured material. CCs require biaxial texture alignment of the superconducting thin film to ensure maximum critical currents. Several techniques, including ion-beam-assisted deposition (IBAD) [40], rolling-assisted biaxially-textured substrates (RABiTS) [41] and ISD [24], were developed to deposit biaxially textured films. The ISD technique: (i) yields a highly biaxially textured MgO buffer layers at high deposition rates (20-100 Å s<sup>-1</sup>) and (ii) is independent of recrystallization properties of the metallic substrates. Therefore, Hastelloy [94], a high-strength, non-magnetic and non-textured material, can also be used. ISD is a deposition method that is simple and easy to accomplish, without the need of an assisting ion source or a complicated heat treatment.

In ReBCO CCs, the critical current density is strongly anisotropic with respect to the applied magnetic field due to intrinsic pinning produced by the layer structure. Higher critical current densities are obtained with the magnetic field lying in the ab-plane and lower values for the magnetic field parallel to the c-axis [95]. It was found that dislocations play a dominant role in the pinning, but other extended defects and point defects were also considered to be important [96]. Since small-angle grain boundaries contain dislocations, their role for flux pinning in

type-II superconductors is important. The density of small-angle grain boundaries in RABiTS and IBAD CCs is determined by the grain size of substrate (such as Ni), which is usually 40  $\mu\text{m}$ .

Of all the CC technologies, the most detailed studies of growth and microstructure have been published for the RABiTS [40] and IBAD [97] technology. For both technologies, the orientation of the c-axis is parallel to the substrate normal. Detailed comparisons of the microstructure with the critical current densities can be found in Refs. [96, 97]. Grain boundaries are considered as being weak-links in ReBCO. However, if the misorientation angle is small ( $< 6^\circ$ ), the degradation of the critical current density is small. It was reported that the critical current density across a grain boundary decreases drastically with increasing misorientation angle and the boundary behaves as a weak-link for misorientation angles greater than  $10^\circ$  [59]. The strong dependence of the critical current density on the grain boundary misorientation angle is well documented for most families of CCs and is the primary factor limiting the fabrication of high critical current density CCs. There are several investigations in the literature on the weak-link behavior of grain boundaries, such as deviation from ideal stoichiometry [58] and the presence of a strain field at the grain boundary due to edge dislocations [59].

CCs grown by the ISD technology are of great interest due to their unique growth properties: the c-axis is inclined with respect to the substrate normal [98]. Furthermore, ReBCO superconductors are highly anisotropic [95]. Therefore, ISD CCs using ReBCO superconducting film are expected to reveal a significantly different microstructure and superconducting properties compared to IBAD or RABiTS CCs.

So far, no detailed study exists for the ISD CCs. Transmission electron microscopy (TEM) analysis of ISD CCs is demanding and requires careful sample preparation. In this chapter, for the first time, we report the results of a detailed microstructural characterization and quantitative chemical analysis of DyBCO films grown by the ISD technology. We present a calculation of energies relevant for DyBCO and discuss the texture and growth mechanism of DyBCO films.

## 5.2 Experimental

### 5.2.1 Tape fabrication process

The DyBCO films studied in this work were grown by ISD technology. Critical current density was measured by the contactless self-inductance method [99] at 77 K in a self-field and found to be  $2.1 \text{ MA cm}^2$ . Samples were grown by thermal evaporation for all deposited layers. The sequence of layers starting from the Hastelloy substrate was ISD MgO buffer layer, MgO cap layer and DyBCO layer as shown in **Fig. 5.1a**. Samples had a critical temperature of 87 K.

The MgO buffer layer was deposited on a Hastelloy substrate at room temperature by tilting the substrate with respect to the evaporation source and using a deposition rate of  $20 \text{ \AA s}^{-1}$ . After depositing the buffer layer, a MgO cap layer was grown at an elevated temperature in an untilted substrate configuration and with a lower deposition rate. Subsequently, a DyBCO layer was deposited. A more detailed description of the setup used and the deposition parameters are found in Ref. [100].

### 5.2.2 SEM and TEM specimen preparation

Scanning electron microscopy (SEM) and TEM samples were prepared using either a focused ion beam (FIB) [23] workstation (Zeiss cross-beam 1540) or conventional grinding and polishing followed by ion etching (Fischione 1010). TEM cross-section samples were prepared in two different directions: one in cross-section and the other one in longitudinal section. A cross-section is a section perpendicular to the tape direction whereas a longitudinal section is along the tape direction (Fig. 5.1b).

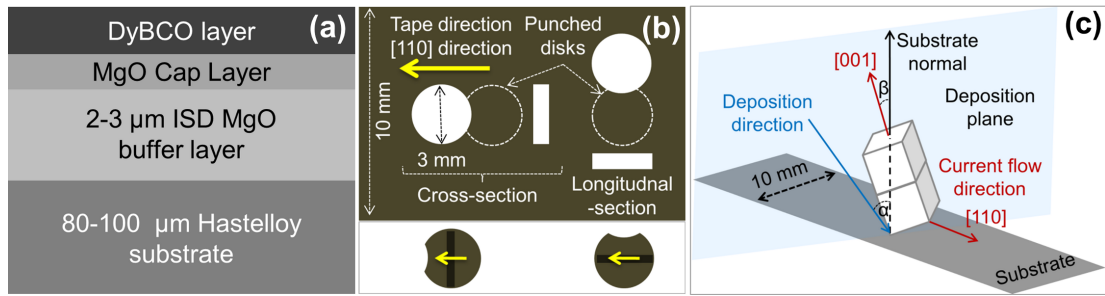


**Figure 5.1:** Schematics of (a) layer structure of the ISD CCs, (b) overlapped punching (notch formation) of CC tape to retain the direction information in the punched out circular disk for cross-section and longitudinal-section TEM specimen preparation and (c) crystallographic geometry of ISD films.

As cross-sections were prepared in two special directions, the samples were punched out by overlapping the successive punches to retain the directional information in the punched-out disks (Fig. 5.1b). This ensured that for the cross-section the  $c$ -axis and for the longitudinal section the  $[110]$  direction, i.e. the tape direction (Fig. 5.1c), of the DyBCO was lying in the plane of the TEM specimens. A more detailed description of the specimen preparation and ion etching can be found in Ref. [23].

### 5.2.3 SEM and TEM analysis

Samples were investigated using a dual beam FIB [23] equipped with a secondary electron detector and a Zeiss 912 omega TEM operating at 120 kV equipped with an in-column omega energy-filter and an energy-dispersive X-ray (EDX) detector. All images were acquired using a slit aperture of 10 eV width to increase the image contrast by eliminating the inelastically scattered electrons.

## 5.3 Results

Several CCs of varying DyBCO film thickness were grown by ISD technology. Critical current densities of DyBCO films were measured and a linear increase of the critical current with film thickness was observed up to 7.5 μm. The critical current density of DyBCO films with a thickness of 6 μm is close to that of thinner DyBCO films (DyBCO thicknesses up to 1 μm), for which critical current densities range from 1.6 to 2.6 MA cm<sup>-2</sup>. This indicates that the critical current density does not decrease significantly with increasing film thickness [101]. For ISD-DyBCO films thinner than 1 μm,  $J_c$  remained below 2.6 MA cm<sup>-2</sup> at 77 K in a self-field. Other technologies, such as RABiTS and IBAD, yield  $J_c$  values up to 4 MA cm<sup>-2</sup> [102]. In a self-field the magnetic field does not lie parallel to the  $ab$ -plane of DyBCO for ISD CCs (Figs. 5.6 and 5.7). In contrast, for CCs prepared by RABiTS or IBAD technology, the self-field is always parallel to the  $ab$ -plane, which is the favorable condition for highest  $J_c$ . We assume this to be the most relevant reason for the lower  $J_c$  of ISD CCs in a self-field. Note that monolithic thick ISD-DyBCO films yield high critical currents at 77 K in a self-field and almost no degradation in  $J_c$  with increasing film thickness was observed.

A detailed analysis of the microstructure of more than eight such CCs was carried out for understanding the growth mechanism. In this chapter we report the microstructure of thin (< 1 μm) DyBCO films; a detailed microstructural study of thick (1–6 μm) DyBCO films can be found in Ref. [101] and the references therein.

**Fig. 5.2a** and **5.2b** shows secondary electron (SE) images of an ISD CC sample in cross-section and in longitudinal section, respectively. The SE images revealed that sample had a well defined faceted MgO–DyBCO interface. The DyBCO surface was also found to be faceted and

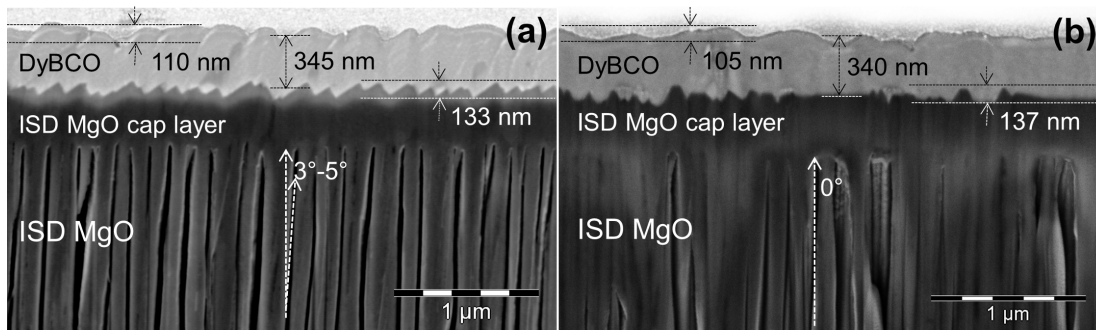


**Figure 5.2:** Secondary electron images of an ISD CC in (a) cross-section and (b) longitudinal-section. All specimens were prepared by FIB.

had a surface roughness of 110 nm. The ISD buffer layer grew in columns and the columns were found to be tilted by an angle of  $3^{\circ}$ – $5^{\circ}$  with respect to the substrate normal.

**Fig. 5.3a** shows a low-magnification bright-field TEM image of the ISD CC sample in cross-section prepared by the conventional cross-section preparation method. For image acquisition samples were tilted such that the (001) direction of DyBCO was lying in the image plane. Under such conditions all the layers from the Hastelloy substrate to the DyBCO surface were imaged; these are the Hastelloy substrate, the MgO buffer layer, the MgO cap layer and the DyBCO layer. The thickness of each layer was measured and matched well with the deposited nominal thicknesses.

Fig. 5.3b shows a bright-field image of the DyBCO film, which revealed the facets at the MgO–DyBCO interface similar to those seen in SE images (Fig. 5.2a). Compatible with SEM results, a faceted DyBCO surface was observed. Fig. 5.3c shows a high-magnification dark-field image using (001) reflection of the DyBCO. The DyBCO grain boundary is marked by white arrows and found to be faceted and tilted with respect to the substrate normal. A high-resolution image of the MgO–DyBCO interface is shown in Fig. 5.3d. In the DyBCO film, (001) lattice fringes were observed (white parallel lines in Fig. 5.3d) and it was found that (001) planes are parallel to the larger edges of facets, i.e. the *c*-axis of the DyBCO is perpendicular to the facets. The facet height was measured to be 70–130 nm and the facet wavelength was 130–350 nm. Fig. 5.3e shows a selected area electron diffraction pattern (SAED) acquired at the MgO–DyBCO interface, which revealed that the (00*l*) reflections i.e. the *c*-axis of DyBCO, is parallel to the (002) of MgO.

**Fig. 5.4a** shows a low-magnification bright-field TEM image of the ISD CC sample in cross-section prepared by FIB. The DyBCO layer was imaged over few microns and showed similar (as seen in Fig. 5.3) facets at the MgO–DyBCO interface and a faceted DyBCO top surface. Figs. 5.3 and 5.4 show similar results, proving that the microstructure of the CC is very homogeneous over the length of the CC tape. The DyBCO grains in the lower part of the film were found to be 130–350 nm in size, which is a typical size of the MgO facets. Grain boundaries of the DyBCO grains were found to be faceted and the succeeding facets at the grain boundaries had a tendency to tilt away from the substrate normal (Fig. 5.4b). The overall tilt of the grain boundaries with respect to the substrate normal was found to be  $20^{\circ}$ – $40^{\circ}$ . Fig. 5.4c shows a high-resolution dark-field image using the (001) reflection of DyBCO. Stacking faults along *ab*-planes and threading dislocations running along the *c*-axis were observed (Fig. 5.4c). The inset in Fig. 5.4c shows a SAED of the MgO–DyBCO, which shows exactly the same results as observed in Fig. 5.3e. Since the (001) direction of the DyBCO layer and (002) of the MgO were parallel as observed in the diffraction patterns (Figs. 5.3e and 5.4c inset), the biaxial texturing of the MgO buffer layer was well transferred to the DyBCO layer. Lattice fringes and the SAED in Fig. 5.4c show that the *c*-axis was tilted with respect to the substrate normal by  $29^{\circ}$ . Note that both the *c*-axis and the overall grain boundary are found to be tilted with respect to the substrate normal, the former in the left direction and the latter in the right

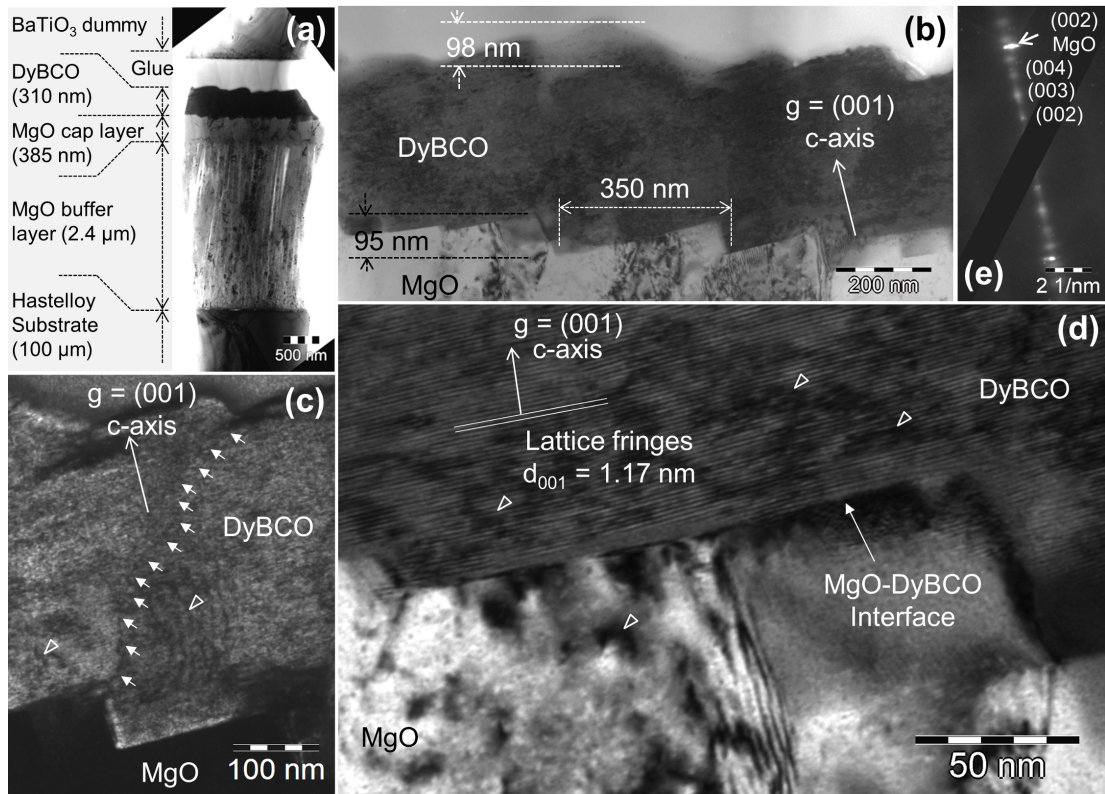


**Figure 5.3:** TEM cross-section (conventionally prepared) analysis of a high  $J_c$  ISD CC: (a) low-magnification bright-field image, (b) bright-field image of the DyBCO layer, (c)  $g = (001)$  dark-field image of a DyBCO grain boundary, (d) high-resolution bright-field image of the MgO–DyBCO interface and (e) diffraction pattern of the MgO–DyBCO interface.

direction for the present case i.e. in opposite directions. Since the diffraction pattern shows a small spread in  $(00l)$  reflections of  $3^\circ$ , DyBCO grains form small-angle grain boundaries. A high dislocation density of  $7 \times 10^{11} \text{ cm}^{-2}$  was determined in the DyBCO film in cross-section near the MgO–DyBCO interface, i.e. at the lower part of the film.

**Fig. 5.5a** shows a bright-field image of the DyBCO of the ISD CC sample in plan view. Fig. 5.5b shows a corresponding dark-field image acquired in a  $(110)$  two-beam condition. DyBCO grains and their grain boundaries could be clearly identified. DyBCO grains were found to be 130–500 nm in size. Diffraction contrast images were heavily dominated by dislocation contrast due to the high dislocation density. Fig. 5.5c shows a SAED in false color of the DyBCO film in plan view. A radial intensity plot of the diffraction pattern is shown in Fig. 5.5d. Although an overall spread of  $16^\circ$  in the  $(110)$  reflection was measured (Fig. 5.5d), the fine structure in the polar plot yielded that the adjacent DyBCO grains had a  $4^\circ$ – $6^\circ$  in-plane misalignment with each other and hence formed small-angle grain boundaries. Note that the  $[110]$  direction is the current direction within the tape. Fig. 5.5e shows a high-magnification dark-field image of the same area using a different  $(111)$  two-beam condition. Rotational Moiré fringes and dislocations at grain boundaries can be seen in the enlarged view shown in Fig. 5.5f. Rotational Moiré fringes along the  $(111)$  diffracting vector ( $\vec{g}$ ) with a fringe spacing ( $|\Delta\vec{g}|^{-1}$ ) of 2.32 nm were observed as shown in Fig. 5.5f. Since the  $\vec{g}$  vector is perpendicular to the  $\Delta\vec{g}$  vector, the observed fringes are of rotational Moiré fringe type. Therefore, using the formula  $\beta = 2 \sin^{-1}(d/2d_{rm})$  [9], where  $\beta$  is the rotation angle between grains,  $d_{rm} = |\Delta\vec{g}|^{-1}$  is the separation between Moiré fringes and  $d$  is the interplanar spacing of the DyBCO, a small-angle of rotation  $6.5^\circ$  was calculated between adjacent DyBCO grains in the  $ab$ -plane. Note that the quantitative analysis of plan-view diffraction pattern discussed in the above paragraph also revealed similar results ( $4^\circ$ – $6^\circ$ ) for in-plane grain orientations. Therefore, grain boundaries are

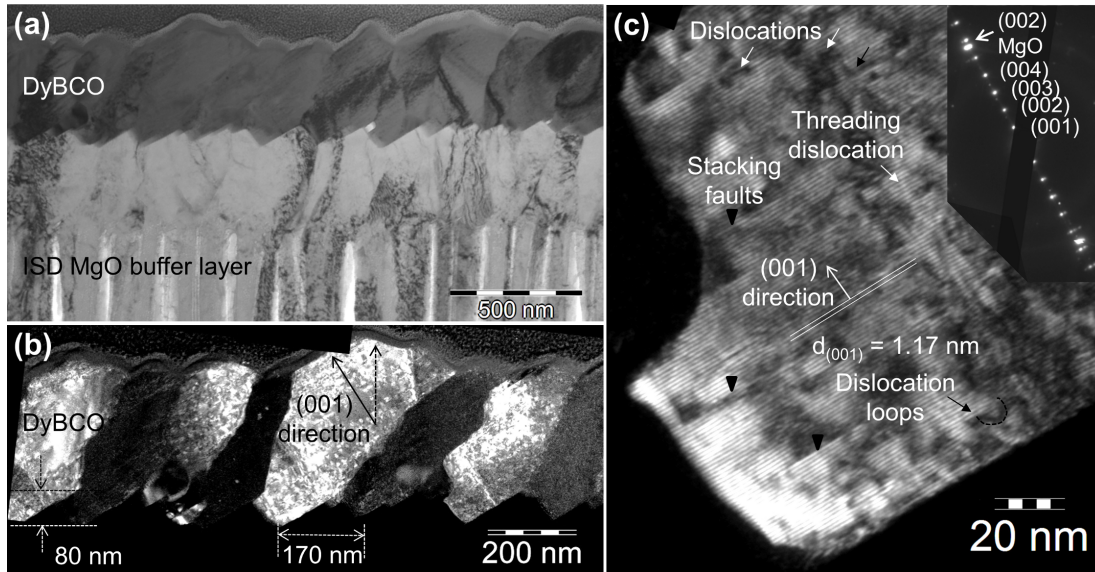


**Figure 5.4:** TEM cross-section (FIB prepared) analysis of a high  $J_c$  ISD CC: (a) low-magnification bright-field image, (b)  $g = (001)$  dark-field image of the DyBCO layer and (c) high-resolution  $g = (001)$  dark-field image of the MgO–DyBCO interface. The inset in (c) shows the diffraction pattern of the MgO–DyBCO interface. Some of the dislocation, dislocation loops and stacking faults are indicated by white, black and black (triangular) arrows, respectively.

small-angle grain boundaries. Similar to cross-section analysis, a high dislocation density ( $10^{11} \text{ cm}^{-2}$ ) was observed in plan view, i.e., at the top part of a 330 nm thick film.

## 5.4 Discussion

### 5.4.1 Inclined substrate deposition (ISD) technology

In ISD CCs a biaxial texturing is found with a tilt of the crystal axis with respect to the substrate normal [24]. Together with the anisotropy of DyBCO the critical current density of ISD CCs behaves very differently as compared to RABiTS and IBAD CCs. Keeping the magnetic field along the same crystallographic directions as in RABiTS or IBAD CCs, the critical current density dependence follows the trend of the anisotropy of the crystal structure. Besides the difference in orientation of the film with respect to the substrate normal, the grain size is significantly smaller in ISD CCs as shown by our results.

### 5.4.2 $\text{DyBa}_2\text{Cu}_3\text{O}_{7-x}$ film growth mechanism and origin of microstructure observed

In Figs. 5.3 and 5.4, we showed that the MgO–DyBCO interface is periodically faceted. The surface of the facets is parallel to the (200) plane of MgO. MgO is known as an ionic compound, the (200) planes are stoichiometric and not charged. The facets appear to be planar, even atomically flat, and the average length and height of the facets are 250 nm and 85 nm, respectively. The size of the MgO facets (i.e. facets length and height) scaled with the ISD–MgO thickness. Facets form only beyond a critical thickness of the ISD–MgO layer. The size of facets increases with MgO thickness up to a thickness of 2  $\mu\text{m}$ , and stays constant for thicker films [103].

The observed faceted surface in ISD MgO yields an increase of surface area of 1.3 in one dimension with respect to an unfaceted surface. The MgO surface energies are highly anisotropic, i.e. the ratio of the  $\{111\}$  to  $\{100\}$  surface energies is 1.29, as reported by Wander et al. [104], corresponding to the increase of surface area. Thus, we consider the driving force for the MgO

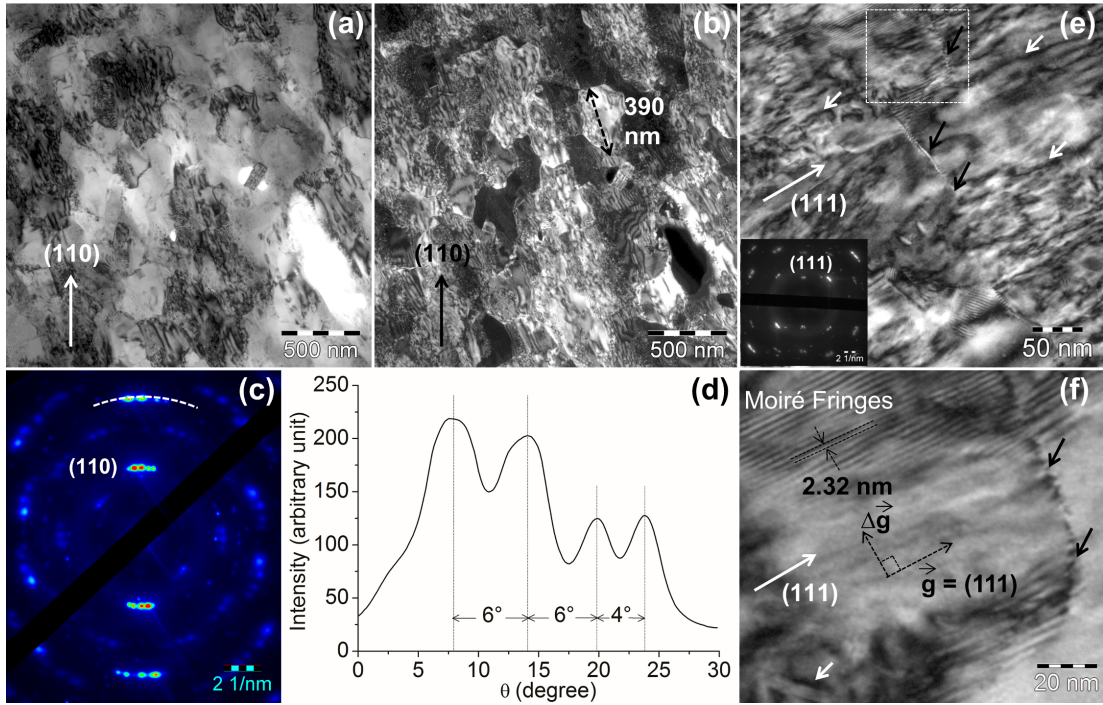


**Figure 5.5:** TEM plan view (conventionally prepared) of a high  $J_c$  ISD CC: (a) bright-field image of the DyBCO, (b) corresponding dark-field image using  $g = (110)$ , (c) diffraction pattern of the DyBCO in false color and (d) polar intensity plot along the shown white dotted arc in (c), i.e. of the (110) reflection. (e) High-magnification dark-field image using  $g = (111)$  and (f) an enlarged view of rotational Moiré fringes observed at DyBCO grain boundaries in (e).

surface faceting to be the anisotropy of the MgO surface energy together with the directional diffusion.

ReBCO thin films grown on single crystalline (002) oriented MgO showing epitaxial growth were reported in literature. It is reported that epitaxy occurs under strain due to the significant lattice mismatch (8.5%) between MgO and DyBCO. This strain is accommodated by the generation of misfit dislocations playing an important role in the growth mechanism. It was found that screw dislocations were a general feature of the epitaxial growth of c-axis ReBCO films [96]. In most of the cases the operating growth mode was suggested to be screw dislocation mediated island growth [105].

Electron diffraction revealed that the DyBCO (00 $l$ ) direction was parallel to the (002) MgO direction, both being perpendicular to the facets. In the facet plane, the ( $hk0$ ) crystallographic axes of the MgO were parallel to the ( $hk0$ ) crystallographic axes of the DyBCO. Thus, the DyBCO films grew epitaxially on facets and biaxial texturing transferred well from the MgO to the DyBCO, despite the large misfit in lattice parameters. The misfit of DyBCO with respect to MgO is 8.5%, the lattice parameters being 0.388 nm and 0.421 nm for DyBCO and MgO, respectively. It was pointed out by Aguiar et al. [106] that any misorientation of the ReBCO with respect to the MgO substrate would yield a significant increase of interface energy, larger than for SrTiO<sub>3</sub> and CeO<sub>2</sub>. Thus, MgO will strongly force DyBCO to grow at precisely the same orientation.

### 5.4.3 Considerations of relevant energies in DyBa<sub>2</sub>Cu<sub>3</sub>O<sub>7-x</sub> films

The observed microstructure in DyBCO thin films can be understood by considering surface, grain boundary and volume energies due to strain; the total energy per volume is the sum of these quantities. Since elastic strain contributes significantly to the interface, grain boundary and volume energies, elastic constants for ReBCO were used according to Ref. [107]. ReBCO

is reported to be elastically highly anisotropic: markedly different values for  $C_{11}$  (218.5 GPa) and  $C_{33}$  (61.1 GPa) were reported, and  $C_{66}$  (65.5 GPa) was about twice as large as  $C_{44}$  (32.8 GPa). The anisotropy is also seen in the off-diagonal elements  $C_{12}$  (87.6 GPa) and  $C_{13}$  (52.5 GPa). However, for simplicity the DyBCO film was still considered to be elastically isotropic and we used the shear modulus ( $\mu = 42.32 \times 10^9 \text{ N m}^{-2}$ ) and Poisson's ratio ( $\nu = 0.356$ ).

Surface energies were measured by nanoindentation for different crystallographic planes of YBCO by Miletto et al. [108] and will be used here for DyBCO. As expected, the smallest surface energy ( $\gamma_{surface} = 0.56 \text{ J m}^{-2}$ ) was found for the (001) planes. This value is small compared to other compounds, e.g. MgO, and favors the formation of faceted surfaces.

We estimated the interface energy of MgO and DyBCO assuming complete misfit relaxation by misfit dislocations at the MgO–DyBCO interface. The density per area of such dislocations was calculated using the formula (eq. 2.171 in [109]):

$$\frac{1}{D^2} = \left(\frac{f}{b}\right)^2 \quad (5.1)$$

where  $D$  is the spacing between misfit dislocations,  $b = |\vec{b}|$  is the Burgers vector and  $f$  ( $= 8.5\%$ ) is the lattice misfit between MgO and DyBCO. Thus, by assuming a Burgers vector of type [100] and excluding the energy of the dislocation core, which is usually assumed to be equal to the energy of the strain field [110], the total energy of the interface is given by (eq. 2.169 in [109]):

$$\gamma_{interface} = \frac{\mu b^2}{2\pi(1-\nu)D} \left(\ln \frac{h}{b} + 1\right) \quad (5.2)$$

where,  $h$  is the DyBCO film thickness. As a result we obtained an interface energy of  $2.8 \text{ J m}^{-2}$  (assuming  $\mu = 42.32 \times 10^9 \text{ N m}^{-2}$ ,  $b = 0.38 \text{ nm}$ ,  $\nu = 0.356$ ,  $D = 4.47 \text{ nm}$  and  $h = 500 \text{ nm}$ ). Thus, this interface energy is significantly larger than the (001) surface energy of the DyBCO, which is  $0.56 \text{ J m}^{-2}$ . The MgO–DyBCO interface energy is fairly independent of the film thickness.

The DyBCO film is strongly biaxially textured. Therefore, grain boundary energies,  $\gamma_{GB}$ , of small-angle grain boundaries are relevant and were calculated using the Read–Shockley formula [eq. 2.142, [109]]:

$$\gamma_{GB} = \sigma_0 \theta (A - \ln \theta); \quad (5.3)$$

where,

$$\sigma_0 = \frac{\mu b}{4\pi(1-\nu)} \quad (5.4)$$

and

$$A = \frac{4\pi(1-\nu)E_c}{\mu b^2} - \ln \alpha \quad (5.5)$$

where,  $\theta = b/D'$  is the tilt angle of the small-angle grain boundary,  $D'$  is the spacing between edge dislocations forming the grain boundary,  $E_c$  is the energy per unit length of the dislocation core, and  $\alpha$  is a constant of the order of unity. With these assumptions, the grain boundary energy of a  $5^\circ$  tilt grain boundary yields  $0.31 \text{ J m}^{-2}$ .

The ratio of surface energy and grain boundary energy will determine the amount of grooving, i.e. surface roughness. The observed angles can be related to the energies by the equation [111]:

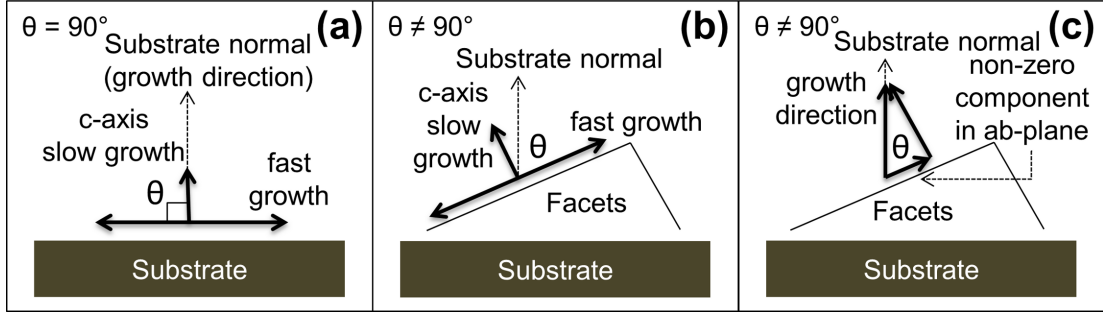


**Figure 5.6:** Schematic drawing of growth modes for (a) the IBAD and/or RABiTS and (b) the ISD. (c) A non-zero component of DyBCO growth along the ab-plane of DyBCO only exists in the ISD grown CCs.

$$\frac{\gamma_{GB}}{\sin(\theta_{S1-S2})} = \frac{\gamma_{S1}}{\sin(\theta_{S2-GB})} = \frac{\gamma_{S2}}{\sin(\theta_{S1-GB})} \quad (5.6)$$

where,  $\gamma_{S1}$  and  $\gamma_{S2}$  are surface energies,  $\theta_{S1-S2}$  is angle between the two surfaces,  $\sin(\theta_{S1-GB})$  and  $\sin(\theta_{S2-GB})$  are angles between the respective surfaces and grain boundary. Note that planar surfaces with little grooving (roughness) are expected for small-angle grain boundaries. The amount of grooving of DyBCO surface was studied by cross-section TEM and allows to estimate the energy of the grain boundaries if the surface energy was known.

The high dislocation density observed in the DyBCO films was surprising. Therefore, we calculated the volume strain energy for such configurations. A dislocation density of  $7.4 \times 10^{11} \text{ cm}^{-2}$  was determined by TEM. The line energy of the dislocations was  $1.98 \times 10^{-7} \text{ J m}^{-1}$ , resulting in a volume energy,  $E_{vol}$ , of  $2 \times 10^7 \text{ J m}^{-3}$ . These basic energies for DyBCO films are summarized in **Table 5.1**. Considering that only grain boundaries with angles less than  $10^\circ$  appear in the films, the relation hold:

*MgO-DyBCO interface energy* ( $2.8 \text{ J m}^{-2}$ ) > *DyBCO surface energy* ( $0.56 \text{ J m}^{-2}$ ) > *DyBCO small-angle grain boundary energy* ( $0.31 \text{ J m}^{-2}$ )

We calculated energies of DyBCO grains as a function of thickness to understand which of the energies, volume or interface energies (surface, interface, grain boundary), were dominant. A functional for the energy per grain,  $E_{grain}$ , as a function of the grain size,  $x$ , and film thickness,  $h$ , can be expressed as:

$$E_{grain} = Ax^2 + Bxh + Cx^2h = (\gamma_{surface} - \gamma_{interface})x^2 + 4\gamma_{GB}xh + E_{vol}x^2h \quad (5.7)$$

Thus, the energy per unit volume of the DyBCO grains can be represented as:

$$\frac{E_{grain}}{x^2h} = \frac{(\gamma_{surface} - \gamma_{interface})}{h} + \frac{4\gamma_{GB}}{x} + E_{vol} \quad (5.8)$$

In Table 5.1 energy values are listed for a grain size of 500 nm which is a typical size observed by TEM. The ratio of volume energy vs. interface energy yields unity for a film thickness of 185 nm.

The work of Aguiar et al. [106], indicates that the misorientation of YBCO with respect to MgO dramatically increases the MgO-DyBCO interface energy. As a consequence, at the MgO-DyBCO interface the DyBCO grain size was found to be equal to the MgO grain size (250 nm). Thus, the misorientation of the MgO columns is directly transferred into a misorientation of the DyBCO grains, fixing the grain size of DyBCO.

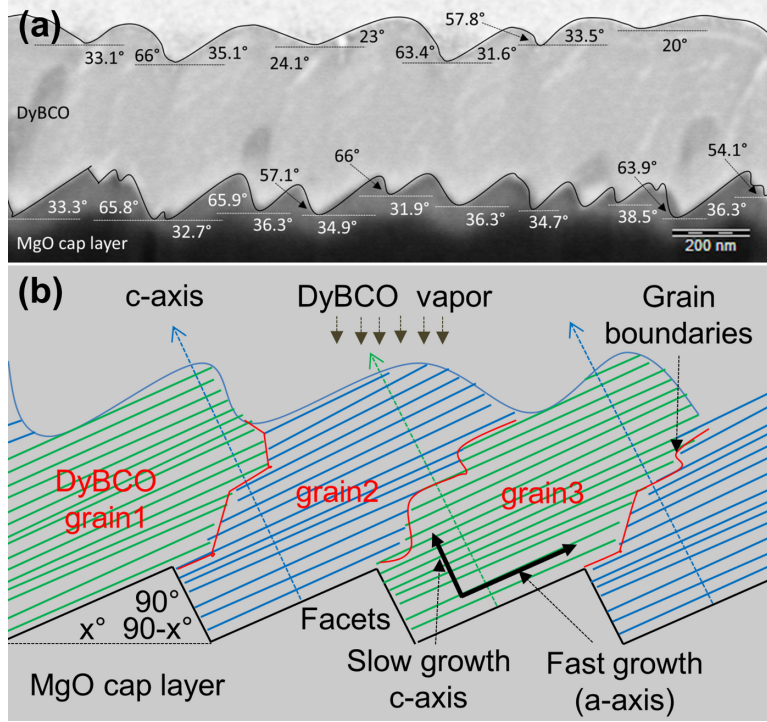


**Figure 5.7:** Growth mechanism of DyBCO films for the ISD technology: (a) secondary electron image of the DyBCO layer in cross-section with overlay schematics. The schematic shows shape and tilt of facets at the MgO–DyBCO interface and of DyBCO top surface with respect to substrate. (b) A schematic drawing of the growth mechanism of the DyBCO film on a tilted geometry (faceted MgO buffer), the tilting mechanism of the grain boundaries and the c-axis out of the substrate normal.

**Table 5.1:** Calculated energies for DyBCO films grown by the ISD technology.

	Energy	Energy/grain*
Interface energy ( $\gamma_{interface}$ )	$2.8 \text{ J m}^{-2}$	$\gamma_{interface} \cdot A = 0.7 \cdot 10^{-12} \text{ J}$
Surface energy ( $\gamma_{surface}$ )	$0.56 \text{ J m}^{-2}$	$\gamma_{surface} \cdot A = 0.14 \cdot 10^{-12} \text{ J}$
Grain boundary energy ( $\gamma_{GB}$ )	$0.31 \text{ J m}^{-2}$	$4\gamma_{GB} \cdot A = 0.31 \cdot 10^{-12} \text{ J}$
Volume energy of strain dislocations ( $E_{vol}$ )	$2.02 \cdot 10^7 \text{ J m}^{-3}$	$E_{vol} \cdot A \cdot z = 2.52 \cdot h \cdot 10^{-12} \text{ J}$

\* we assumed that the basal area of DyBCO grain ( $A$ ) =  $x \cdot y = 500 \cdot 500 \text{ nm}^2 = 0.25 \cdot 10^{-12} \text{ m}^2$  and thickness of the DyBCO film ( $z$ ) =  $500 \cdot h \text{ nm} = 0.5 \cdot h \cdot 10^{-12} \text{ m}^2$ , where  $h$  is a factor.

#### 5.4.4 Comparison of the microstructure of inclined substrate deposition (ISD) grown films with films grown by other technologies

It is well documented that both IBAD [97] and RABiTS [41] can produce high quality biaxially textured ReBCO films with an in-plane alignment better than  $10^\circ$ . However, ReBCO is highly anisotropic with respect to growth, i.e. it shows a slow growth along the c-axis and a fast growth along the ab-axes (Fig. 5.6a), which makes the growth process unstable with respect to a-axis growth for RABiTS and IBAD technologies, i.e. once a-axis grains are formed they quickly grow. Note that a-axis growth breaks the biaxial-texturing and introduces large-angle grain boundaries, which dramatically limit the critical current density in CCs [59]. On the other hand in the case of ISD, well defined MgO facets provide a tilted geometry for the DyBCO growth as shown in Fig. 5.6b. Due to the tilted geometry the growth direction has a non-zero component parallel to the ab-plane of DyBCO (Fig. 5.6c), which makes the growth process stable with respect to a-axis growth. The results presented in this chapter showed that no a-axis grains exist for DyBCO films grown on faceted MgO buffer layers.

Furthermore, due to the tilted geometry and highly anisotropic nature of DyBCO with re-

spect to growth, faceted grain boundaries appeared in ISD CCs as shown in Figs. 5.3c and 5.4b. The facets of the grain boundaries are aligned along the ab-plane of DyBCO. The nonzero component of growth along the ab-plane of DyBCO and the grain boundary facet formation tilts the grain boundary away from the substrate normal, as seen in Fig. 5.4b. The faceted structure of the substrate is not found for RABiTS or IBAD technology, for which ReBCO is deposited on planar and unfaceted surfaces [41][97]. The grain boundaries always appear roughly parallel to the substrate normal [95]. By considering the above discussion, a growth model for DyBCO is presented as shown in Fig. 5.7.

## 5.5 Conclusions

DyBCO films were grown on biaxially textured MgO buffer layers deposited by ISD technology on Hastelloy substrates and were analyzed by SEM and TEM in cross-section and plan-view. Typical critical current densities of DyBCO films were  $2.1 \text{ MA cm}^{-2}$  at 77 K in a self-field. The MgO–DyBCO interface was found to be faceted; the smooth and planar MgO facets were found to be parallel to the MgO {200} planes. Facets had an average length of 250 nm and a height of 85 nm. The c-axis of the DyBCO film was tilted away from the substrate normal by  $29^\circ$  such that it was perpendicular to the MgO facets. A maximum misalignment of  $3^\circ$  was found in the c-axis and a maximum misorientation of  $6^\circ$  was determined in the (110) direction of adjacent DyBCO grains. Therefore, the DyBCO film had a good in-plane and out-of-plane biaxial texture. In the DyBCO film grains were found to be 130–500 nm in size; no a-axis grains and only small-angle grain boundaries were observed. A high dislocation density of  $7 \times 10^{11} \text{ cm}^{-2}$  was found in the DyBCO film.

The driving force for faceting of the MgO surface is the anisotropy of MgO surface energies together with the directional diffusion due to ISD. Grain boundary, interface and volume energies of the DyBCO film were calculated. It was found that the MgO–DyBCO interface energy has the largest value amongst all calculated energies. Misorientation of DyBCO with respect to MgO dramatically increases the interface energy and favors the epitaxial c-axis growth of DyBCO on MgO facets. The lowest energy was found for surface energies, which allows faceted DyBCO surfaces.

In summary, optimized growth conditions for the MgO films yielded a well-faceted surface and a highly biaxially textured growth behavior of the DyBCO in ISD technology. This is due to the faceted structure of the MgO surface yielding a non-zero component of the DyBCO growth parallel to the ab-plane. The growth velocity is larger in the ab-plane for this compound. A growth model for DyBCO is presented.



## Chapter 6

# Microstructure of BaZrO<sub>3</sub> Doped DyBa<sub>2</sub>Cu<sub>3</sub>O<sub>7-x</sub> Coated Conductors Deposited by Inclined Substrate Deposition

### 6.1 Introduction

Microstructure engineering provides an effective way to improve the magnetic vortex pinning via addition of nano-precipitates into a superconducting matrix. Precise control of these nano-precipitates, including their dimension and alignment, is critical to obtain optimal pinning. BaZrO<sub>3</sub> nano-precipitates (BZO-NPs) in inclined substrate deposition (ISD) grown DyBa<sub>2</sub>Cu<sub>3</sub>O<sub>7-x</sub> (DyBCO) films were introduced by electron beam evaporation of DyBCO powder with 3.5 wt.% BZO addition. A critical current density ( $J_c$ ) of 1.1 MA cm<sup>-2</sup> at 77 K in self-field was measured. Alignment and size of the BZO-NPs were investigated using transmission electron microscope (TEM). The alignment of NPs was greatly affected by the tilted geometry of ISD growth.

For most of the large-scale applications of coated conductors (CCs), a high critical current ( $I_c$ ) in the presence of high magnetic fields is required. The layered structure of YBCO (or DyBCO) provides sufficiently strong natural pinning for the fields applied in the ab-plane. These natural pinning sites, however, are ineffective for the applied magnetic field along the c-axis of DyBCO. In the last few years, particularly, for the ion beam assisted deposition (IBAD) and the rolling assisted biaxially-textured substrate (RABiTS) technologies a significantly enhanced  $I_c$  for high magnetic fields applied along the c-axis was achieved by introducing columnar defects aligned along the c-axis of YBCO [112, 113]. Recently, for a 2 μm thick YBCO film grown by IBAD technology, an  $I_c$  of 1010 A cm<sup>-1</sup> at 75.6 K in self-field and a minimum  $I_c$  of 234 A cm<sup>-1</sup> at 75.6 K and at 1T field was achieved [114].

Due to the tilted geometry, ISD grown DyBCO films showed significantly different  $I_c$  dependence on the angle between applied magnetic field and substrate normal. The maxima of  $I_c$  were found for the field applied along the ab-plane, not parallel to substrate [100] as for other technologies. ISD grown DyBCO films showed reduced anisotropy in  $I_c$ , most probably due to high density of small-angle faceted grain boundaries and dislocations. It is well known that defects such as vacancies, stacking faults, twin boundaries, low angle grain boundaries, dislocations, and precipitates act as natural pinning centers. In this chapter we report the microstructure of BZO doped DyBCO films grown by the ISD technology.

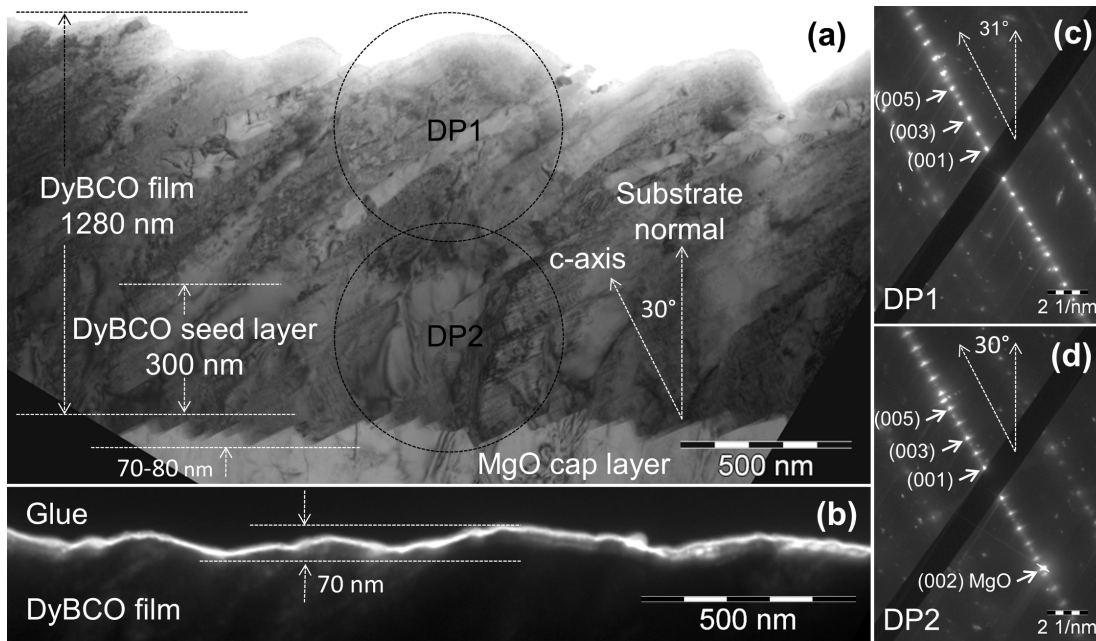


**Figure 6.1:** (a) A low-magnification bright-field image of the DyBCO film, (b) a dark-field image of the DyBCO top surface from a thick region showing the surface roughness, (c) and (d) are selected area electron diffraction patterns acquired at the top part and lower part of the DyBCO film, respectively.

## 6.2 Experimental

In this chapter the DyBCO+BZO series samples were studied (Sample 10, Table 2.1). MgO buffer layers were deposited on Hastelloy substrates at room temperature by tilting the substrates with respect to the evaporation source. Subsequently, BZO-NPs in DyBCO films were introduced by electron-beam evaporation of DyBCO powder with 3.5 wt.% BZO addition. A more detailed description of the used setup and the deposition parameters are found in reference [100]. The layer structure of the analyzed sample is listed in Table 2.1 and shown in Fig. 2.1e. A typical critical current density of  $1.1 \text{ MA cm}^{-2}$  at 77 K in self-field was measured.

TEM cross-section samples were prepared by mechanical grinding and polishing [30]. TEM plan-view samples were prepared by dimpling the sample down to  $20 \mu\text{m}$  thickness, followed by ion-milling (Fischione 1010). More detailed descriptions about the sample preparation can be found in Chapter 2.

Conventional microscopy was done at a Zeiss EM912 $\Omega$  TEM operated at 120 kV equipped with an in-column energy filter and an energy-dispersive X-ray (EDX) detector. All TEM images and diffraction patterns were acquired using a 10 eV energy slit aperture to reduce inelastically scattered electrons contributing to the image background. A more detailed description about the used microscope and acquisition conditions can be found in Chapter 1. For nanostructural information, a FEI Titan TEM with probe and Cs corrector having a resolution of 0.08 nm in scanning TEM (STEM) mode was used. High resolution high angular annular dark field (HR-HAADF) images were acquired using either a camera length of 145 mm or 70 nm.

## 6.3 Results

**Fig. 6.1a** shows a low magnification bright-field image of the DyBCO film (Sample 10). A faceted MgO-DyBCO interface was observed as reported for other series of ISD CCs in the previous chapters. On top of MgO buffer layer a 300 nm thick DyBCO seed layer (i.e. pure DyBCO film without any BZO-NPs) and a 1000 nm thick DyBCO film with BZO-NPs were observed. Fig. 6.1b shows a (001) dark-field image of the DyBCO top surface from a thick

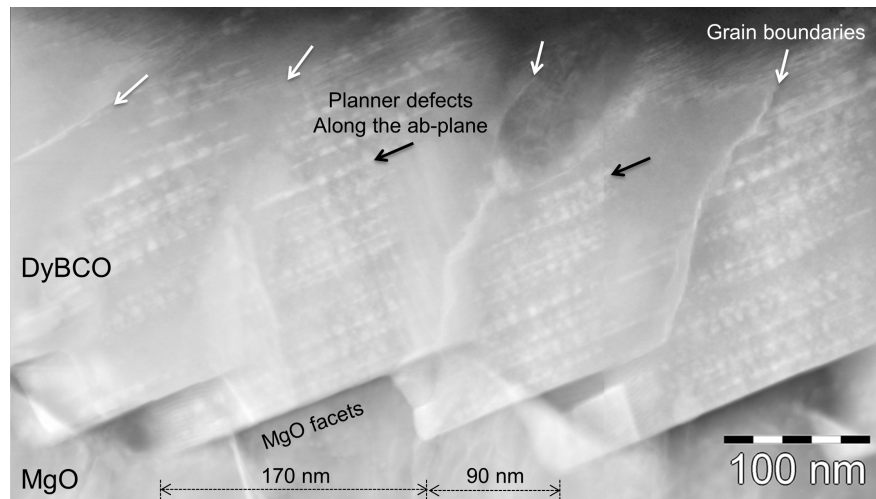


**Figure 6.2:** A STEM image of the MgO-DyBCO interface of sample 10 in cross-section acquired by a FEI Titan microscope using a camera length of 145 mm. In the image planar defects (black arrows) and grain boundaries (white arrows) are marked.

region to image the DyBCO film surface roughness as in the thin part shown in Fig. 6.1a the top surface is partially etched out. A flat DyBCO surface having a surface roughness less than 70 nm was observed. Selected area diffraction patterns (Fig. 6.1c and 6.1d) acquired from the upper and lower part of the DyBCO film showed that the DyBCO grew epitaxially on the MgO buffer layer. The c-axis of the DyBCO film enclosed an angle of  $30^\circ$  with the substrate normal and retained its orientation over the total DyBCO film thickness. We observed a spread of  $3^\circ$  in the (00 $l$ ) direction of DyBCO over several microns, i.e. the DyBCO grains form small-angle grain boundaries.

**Fig. 6.2** shows a STEM image of the lower part of the DyBCO film i.e. the seed layer of sample 10 in cross-section acquired by a FEI Titan TEM using a camera length of 145 mm. Similar to conventional bright-field and dark-field TEM images, the faceted MgO-DyBCO interface and faceted grain boundaries were observed in the STEM image. In contrast to the conventional microscopy, planar defects along the ab-plane of the DyBCO can be seen in the STEM images. **Fig. 6.3a** shows a HAADF image of the MgO-DyBCO interface, showing the (00 $l$ ) lattice fringes parallel to the facets. A magnified image of the lattice fringe is shown in the inset of Fig. 6.3a, showing some dark fringes marked by black arrows. The dark fringes/lines show the extra Cu planes along the ab-plane of DyBCO. Fig. 6.3b shows a HR-HAADF of the DyBCO grain boundary. Faceting of the DyBCO grain boundary at nano scale (5 nm) can be seen in the HR-HAADF. Inset in Fig. 6.3b shows a magnified image of one of such facets. No bending, only a slight shift (less than 0.5 nm) in the ab-plane of DyBCO was observed at grain boundary.

**Fig. 6.4** shows a high magnification bright-field image of sample 10 in cross-section. The inset shows a selected area diffraction pattern of the area shown. DyBCO grains were found to be  $1000 \times 300 \text{ nm}^2$  in size in cross-section. BZO-NPs in the DyBCO matrix were identified by the translational Moiré fringe contrast. They were aligned along the ab-plane instead of along the c-axis of DyBCO, as reported for the YBCO based CCs on a flat geometry.

**Figs. 6.5a** and **6.5b** show bright-field image and corresponding  $g = (110)$  dark-field image of the sample in plan-view, respectively. Similar to the cross-section, BZO-NPs were identified in the DyBCO matrix by the translational Moiré fringe contrast. A high magnification image of the BZO-NPs is shown in the inset in Fig. 6.5a. DyBCO grains were found to be 200-500 nm in size in plan-view. A high dislocation density of about  $2 \times 10^{11} \text{ cm}^{-2}$  was observed in the DyBCO film in plan-view.

The combined analysis, i.e. plan-view and cross-section analyses, confirmed that BZO-NPs

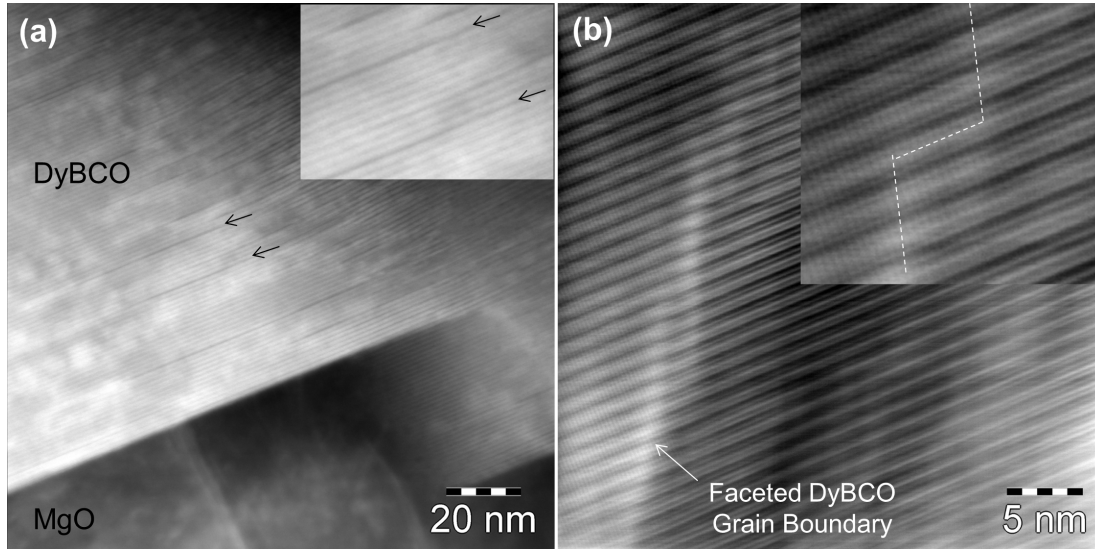


**Figure 6.3:** A HR-HAADF image of (a) the MgO-DyBCO interface and (b) a DyBCO grain boundary. Inset in (a) shows a magnified view of lattice fringes and inset in (b) shows a magnified view of the DyBCO grain boundary facets. Images were acquired by a FEI Titan microscope using a camera length of 70 mm.

**Table 6.1:** TEM EDX quantitative analysis of the DyBCO film in plan-view.

	Spectrum	Dy [at.%]	Ba [at.%]	Cu [at.%]	Zr [at.%]
	k-factor	2.304	2.050	1.457	2.967
Matrix	Spectrum 1	18.8	34.9	44.6	1.7
	Spectrum 2	19.3	34.6	44.3	1.8
	Spectrum 3	19.6	33.3	45.3	1.8
	Spectrum 4	19.8	33.6	44.9	1.7
Secondary phase	Spectrum 5	48.8	28.3	17.9	5.0

exist in form of rods of around 35 nm in length, 5-15 nm in diameter, and separated by 10-20 nm from each other.

Inset in Fig. 6.5b shows a selected area diffraction pattern of the DyBCO in plan-view. A good in-plane biaxial texturing was found in the DyBCO film, as we observed a maximum spread of  $6^\circ$  in (110) reflection in the diffraction pattern.

EDX spectra were acquired at selected points of the plan-view sample in the TEM and were quantitatively analyzed as listed in **Table 6.1**. Some of the spectra are shown in **Fig. 6.6**, a 1.7 at.% Zr was observed in the DyBCO matrix. Dy-rich and Cu-rich secondary phases were observed in form of platelets along the ab-plane and at grain boundaries. Remarkably, a significantly increased amount (5 at.%) of Zr was observed in the Dy-rich secondary phases at grain boundaries.

## 6.4 Discussion

Conventional TEM images as well as the HR-HAADF images showed a lot of planar defects along the DyBCO ab-plane. However, defects such as stacking faults are planar defects parallel to the ab-plane and are only effective if the magnetic field is applied near the ab-plane. Instead of the stacking faults itself, dislocations formed at the boundaries between the stacking faults and the DyBCO matrix act as a strong linear pinning centers parallel to the ab-plane, because the strain field surrounding a dislocation core produces a local depression in the superconducting order parameter [115]. Chisholm and Pennycook [59] investigated the origin of the  $J_c$  reduction due to tilt grain boundaries and estimated the radius of the depressed region as  $r_m = 2.9 |\vec{b}|$ ,

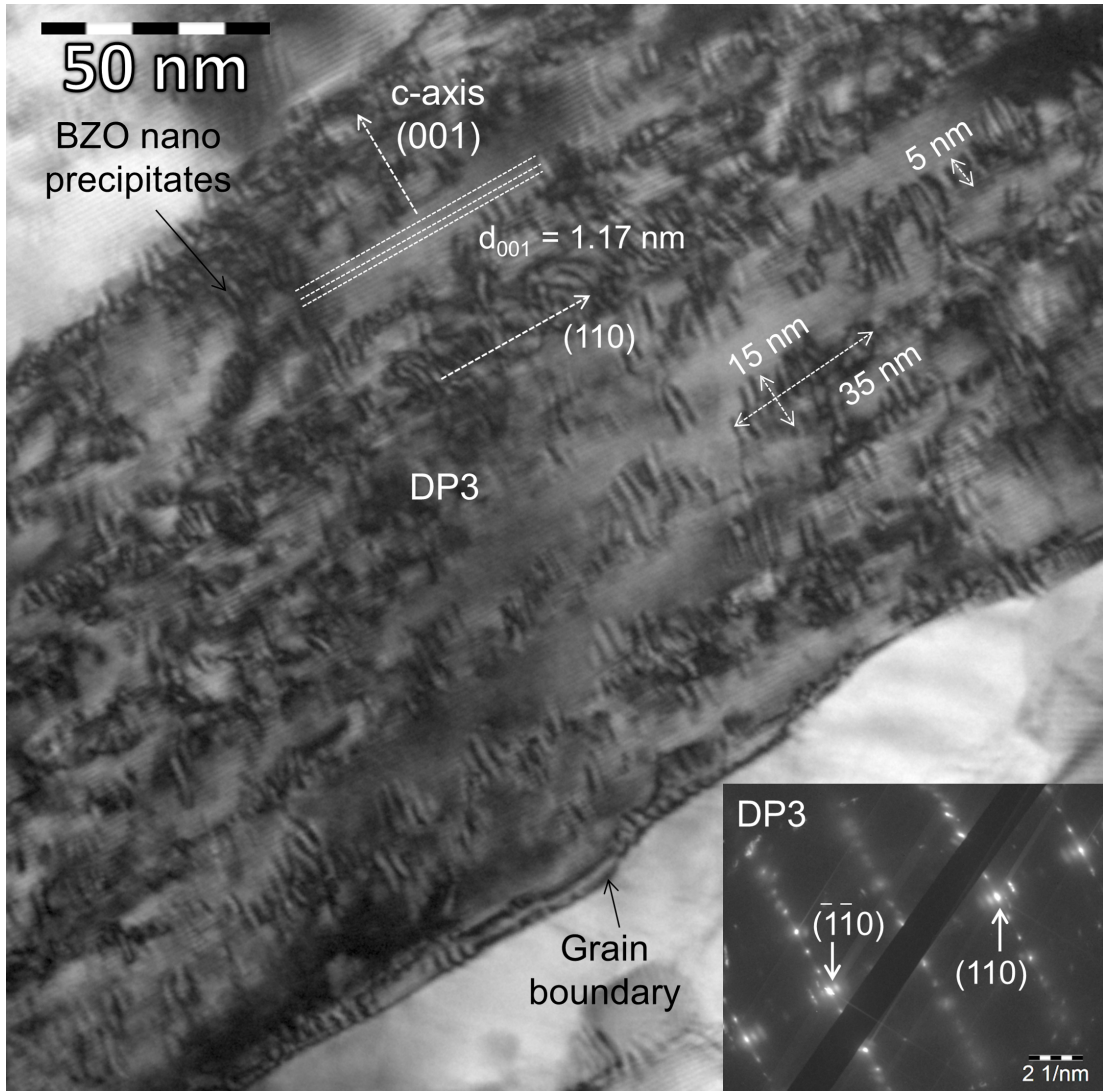


**Figure 6.4:** High-magnification bright-field image of a DyBCO grain in cross-section, showing the size and orientation of the BZO nano-precipitates. Inset is a selected area diffraction pattern of the shown DyBCO grain.

where  $|\vec{b}|$  is the Burgers vector of the dislocation. For DyBCO, this yields  $r_m \approx 0.8$  nm, i.e. the region of depressed order parameters surrounding a dislocation core is substantially larger than the thickness of a CuO chain layer. Note that, the most frequently observed stacking faults are Y124-type with double CuO chains [116, 117]. Thus, the dislocations associated with stacking faults are much stronger pinning centers than the stacking faults itself. We believe that the reduced anisotropy in the  $I_c$  of ISD DyBCO films is due to high density of defects.

We showed that BZO-NPs in ISD DyBCO were aligned along the ab-plane and not along the c-axis as seen in majority of YBCO films grown by the IBAD or the RABiTS technology [112, 113]. Therefore, these BZO-NPs will work as pinning only for the fields applied parallel to the ab-plane of DyBCO. They will not help much for the fields applied along the substrate normal or along the c-axis of DyBCO, which is required to enhance the overall  $I_c$  and reduce anisotropy in  $I_c$  with respect to the direction of applied external magnetic fields.

The growth behavior of BZO-NPs in ISD DyBCO can be understood by considering the growth mechanism of pure DyBCO grown by the ISD technology reported by Aabdin et al. [118] or Chapter 5. Due to the tilted geometry, ISD growth yields a non-zero component of DyBCO growth along the ab-plane of DyBCO. The non-zero component and highly anisotropic nature of the DyBCO yields a laminar (plane-by-plane) growth mechanism. That forced the BZO-NPs growth along the ab-plane. Note that for the IBAD or the RABiTS geometry for

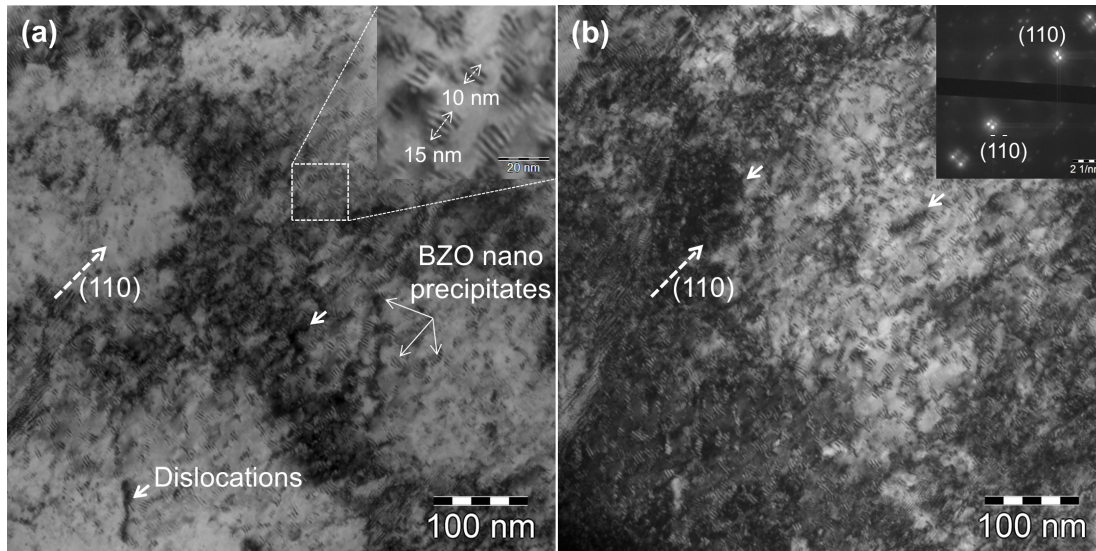


**Figure 6.5:** (a) A bright-field image and (b) the corresponding  $g = (110)$  dark-field image of the DyBCO film in plan-view. Inset in (a) is a high-magnification image of the enclosed area and in (b) is a selected area diffraction patterns of the DyBCO film. In both images the BZO-NPs could be identified by Moiré fringe contrast.

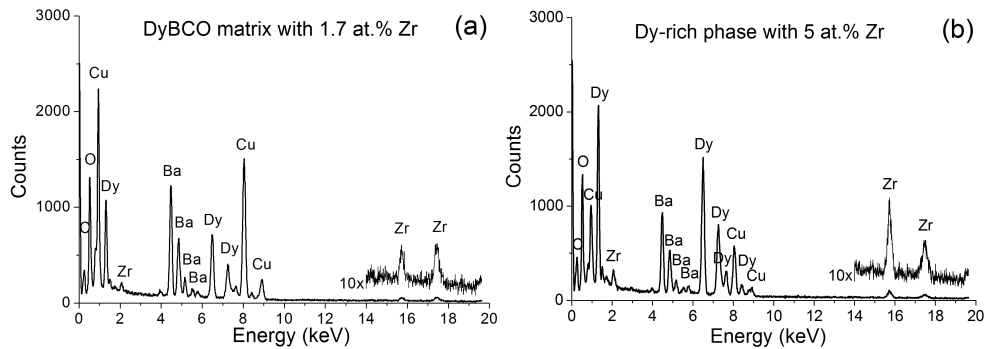


**Figure 6.6:** TEM spectroscopy results in plan-view: point EDX spectra of (a) the DyBCO matrix (spectrum 3 in table 1) and (b) Dy-rich secondary phases observed in the DyBCO matrix (spectrum 5 in Table 6.1).

which the in-plane component is zero only a component along the substrate normal exist, that forced the BZO growth along the substrate normal [119].

## 6.5 Conclusions

The microstructure of ISD grown DyBCO films doped with 3.5 wt.% BZO were studied by TEM. The BZO were found to be grown in form of rods of around 35 nm in length, 5-15 nm in diameter and separated by 10-20 nm from each other. They were identified by translational Moiré fringe contrast and found to be aligned along the  $ab$ -plane of DyBCO. They were found to be homogeneously distributed in the DyBCO matrix in form of rods. The  $ab$ -plane of the DyBCO itself was found to be tilted by  $30^\circ$  with respect to the substrate. The  $c$ -axis of DyBCO enclosed an angle of  $30^\circ$  with the substrate normal. A maximum misalignment of  $3^\circ$  in the  $(00l)$  direction of DyBCO was observed over several microns, i.e. DyBCO grains form only small-angle grain boundaries. A good in-plane biaxial texturing was observed in the DyBCO film. DyBCO grains were found to be 200-500 nm in size. A large number of dislocations, dislocation loops, extra Cu planes and planar defects along the  $ab$ -plane of DyBCO were observed improving the overall anisotropy in the  $I_c$  of ISD DyBCO films.

In summary, the BZO-NPs alignment was greatly affected by the tilted geometry of the ISD growth. The BZO-NPs observed in ISD grown DyBCO matrix are not optimum pinning centers

---

for the fields applied along the c-axis of DyBCO. Therefore, the ISD growth needs to be optimized with respect to the BZO-NPs growth, particularly, the growth direction of BZO-NPs.



## **Part III**

# **Structure-property Correlation of Thermoelectric $\text{Bi}_2\text{Te}_3$ Bulk Materials**



## Chapter 7

# Thermoelectricity

### 7.1 Introduction

In 1823 T. J. Seebeck reported that a compass needle was deflected if placed in the vicinity of a closed loop, formed from two dissimilar conductors, when one of the junction was heated (**Fig. 7.1**) [120]. After few years, Seebeck accounted that the phenomena observed was caused by an electric current flowing in the circuit and he had discovered a thermoelectric effect so called the *Seebeck Effect*.

Thermoelectric materials have many applications in the conversion of thermal to electrical energy and in solid-state cooling [121, 122]. Although, thermoelectric devices have found specialized applications where their high reliability, lack of moving parts, and ability to be scaled to small sizes provide key advantages relative to competing technologies, the energy conversion efficiencies of these devices remain generally poor. Over the past decades, there has been interest in the field of thermoelectrics to identify more efficient compounds and materials.

G. Slack et al. [123][124] suggested that the best thermoelectric material would behave as a “phonon glass/electron crystal” (PGEC); i.e. it would have the electrical properties of a crystalline material and the thermal properties of an amorphous or glass-like material.

The challenges to develop thermoelectric materials with superior performance is to tailor the interconnected thermoelectric physical parameters: electrical conductivity, Seebeck coefficient and thermal conductivity for crystalline system. Nanostructures provide a possibility to disconnect thermal and electrical transport (Wiedemann-Franz law) by enhancing phonon scattering and thereby reducing the lattice thermal conductivity without significantly affecting the electrical conductivity and, thus, increasing the figure of merit.

The PGEC approach more recently led to advanced engineering of thermoelectric nanomaterials [125, 126, 127, 128], yielding thermal conductivities less than  $1 \text{ W m}^{-1} \text{ K}^{-1}$  as shown for  $\text{AgPb}_m\text{SbTe}_{2-m}$  bulk [125].

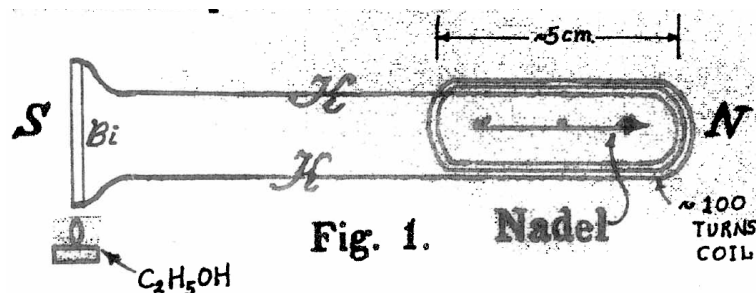


**Figure 7.1:** Thomas Johann Seebeck experiment, reproduced from Treatise of the Royal Prussian Academy of Sciences in Berlin (Abhandlung der Königlichen Preussischen Akademie der Wissenschaften zu Berlin, p265-375, 1822-1823).

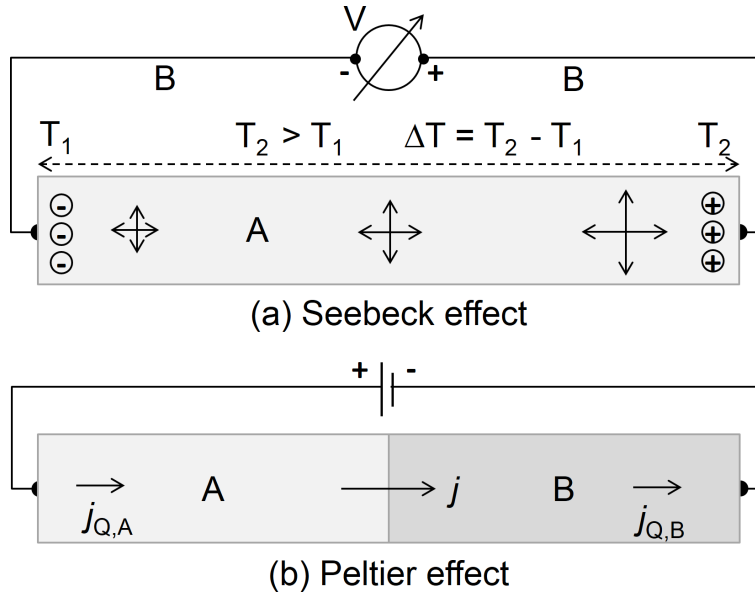


**Figure 7.2:** Schematics of thermoelectric effects: (a) the Seebeck effect and (b) the Peltier effect.

In this chapter, basics of thermoelectricity and criterion for materials with high thermoelectric figure of merit ( $ZT$ ) will be discussed. More details about the thermoelectricity can be found in references [121, 129, 130].

## 7.2 Basic Thermoelectric Phenomena

### 7.2.1 Seebeck and Peltier effects

In 1821 Thomas Johann Seebeck discovered that a circuit composed of two different metals could deflect a compass needle when a temperature gradient was applied across it (Figs. 7.1 and 7.2a). This effect termed as the *Seebeck effect*. The ratio ( $\Delta V/\Delta T$ ) of the voltage developed to a temperature difference is related to an intrinsic property of the materials called the *Seebeck coefficient* or *thermopower*,  $S$ .

$$S = \frac{dV}{dT} \quad (7.1)$$

Fig. 7.2a shows a schematic diagram of *Seebeck effect*. A larger temperature is applied to the right end ( $T_2 > T_1$ ) i.e. a temperature gradient ( $|\vec{\nabla}T| = T_2 - T_1$ ) from left to right exists. Therefore, if we assume that material is n-type (electron conducting), electron will diffuse and accumulate to the left end yielding an electric field ( $|\vec{E}|$ ) from right to left. Since,  $|\vec{\nabla}T|$  and  $|\vec{E}|$  are in opposite direction,  $S$  will be negative. On the other hand for p-type (hole conducting) material  $S$  will be positive because positive charges will accumulate at the left end and in this case both  $|\vec{\nabla}T|$  and  $|\vec{E}|$  will be in the same direction ([131], page 63).

After few year of the discovery of the Seebeck effect, a related effect, the *Peltier effect*, was discovered by J.C.A. Peltier, who observed that when an electrical current is passed through the junction of two dissimilar materials (Fig. 7.2b), heat is either absorbed or rejected at the junction, depending on the direction of the current passed through the junction. Thus heating (heat generated) or cooling (heat absorbed) of the junction area will take place. The ratio of the heat current density,  $j_Q$ , to the electrical current density,  $j$ , is defined as the *absolute Peltier coefficient*,  $\pi$ , of the material:

$$\pi = \frac{j_Q}{j} \approx \frac{E_g}{2e} \quad (7.2)$$

For semiconductors, similar to Seebeck coefficient, the sign of the Peltier coefficient depends on the type of majority charge carriers, being negative for n-type and positive for p-type semiconductors. The net Peltier heat at the junction (A-B) is given by  $\pi_{AB} = \pi_A - \pi_B$ . Peltier coefficient of the junction will be positive if heat is generated and negative if heat is absorbed at the junction when the current flows from A to B (Fig. 7.2b). This effect is largely due to the difference in Fermi energies of the two materials and the fact that with an electrical current there is always associated the transport of thermal energy. For  $\text{Bi}_2\text{Te}_3$   $\pi = 80 \text{ mV}$  assuming  $E_g = 0.16 \text{ eV}$ .

Thomson recognized that the Seebeck and Peltier coefficient are related to each other and from thermodynamic arguments, he derived the relation:

$$\pi = TS \quad (7.3)$$

however, a rigorous description of thermal influences on the electrical current and vice versa has been presented by Onsager in 1931 [132]. His theory discusses the relations of reciprocity of reversible and irreversible processes, where the coupling of the electrical and the thermal subsystems are investigated. Due to the phenomena of electron and phonon transport in conductors and semiconductors, electrical current density ( $j$ ) and heat current density ( $j_Q$ ) are, in general, coupled and linear functions of the electric field and the gradient of temperature [121], i.e.:

$$\vec{j}_Q = \sigma \vec{E} - \sigma \alpha \vec{\nabla} T \quad (7.4)$$

$$\vec{j} = \pi \vec{j}_Q - \kappa \vec{\nabla} T \quad (7.5)$$

where  $E$  and  $T$  are the electric field and temperature, respectively,  $\alpha$  is the Seebeck coefficient,  $\pi$  is the Peltier coefficient,  $\sigma$  is the electrical conductivity and  $\kappa$  is the thermal conductivity. It is clear from equations 7.4 and 7.5 that in any material which allows both electrical and heat conduction: (i) a temperature gradient causes an electric field to develop in the absence of electrical current and (ii) an electric field causes a thermal gradient to develop in the absence of thermal current.

### 7.3 Definition and Description of the Figure of Merit

The potential of materials for thermoelectric applications is determined by the figure of merit,  $ZT$  [129]:

$$ZT = \frac{S^2 \sigma}{\lambda} T = \frac{S^2 \sigma}{\lambda_{latt} + \lambda_{el}} T \quad (7.6)$$

where  $S$ ,  $\sigma$ ,  $T$  and  $\lambda$  are the Seebeck coefficient (or thermopower), electrical conductivity, absolute temperature, and total thermal conductivity, respectively. The total thermal conductivity,  $\lambda$ , is the sum of the lattice thermal conductivity,  $\lambda_{latt}$ , and the electronic thermal conductivity,  $\lambda_{el}$ . Therefore, a good thermoelectric material requires a high thermopower,  $S$ , a high electrical conductivity,  $\sigma$ , and a low thermal conductivity,  $\lambda$ .

Only a small increase in the thermoelectric figure of merit was achieved in the last decades. The reason for this is that the thermopower,  $S$ , the electrical conductivity,  $\sigma$ , and the thermal conductivity,  $\lambda$ , depend on each other and it is difficult to improve one transport coefficient without significantly changing the others as shown in **Fig. 7.3a**. However, the power factor  $S^2 \sigma$  (or  $S^2 / \rho$ , where  $\rho$  is the electrical resistivity), is typically optimized in narrow-gap semiconducting materials as a function of carrier concentration (typically  $\sim 10^{19}$  carriers/cm<sup>3</sup>), through doping, to give the highest  $ZT$ . The  $ZT$  for a single material is somewhat meaningless for device point of view, since an array of thermoelectric couples is utilized in a device or module.

A device or module can only be made by utilizing a junction concept of two types of materials, namely n-type and p-type as shown in **Fig. 7.4**.

## 7.4 Transport Properties and High Figure of Merit Criteria

The thermopower  $S$ , the electrical conductivity,  $\sigma$ , and the electronic thermal conductivity,  $\lambda_{el}$ , of crystalline solids can be determined by using the band theory of solids and the linearized Boltzmann equation [130]. Note that all these quantities are anisotropic for most of thermoelectric materials, however, only simplified equations for isotropic materials will be presented and discussed in the following sections. A more detailed explanation can be found in the Ref. [129]. A more detailed information about thermoelectric properties of anisotropic semiconductors can be found in reference [133].

### 7.4.1 Seebeck coefficient or thermopower

The thermopower or Seebeck coefficient can be thought of as the heat per carrier over temperature, or more simply, the entropy per carrier. For metals it can be approximated as:

$$|S| \approx \frac{C_{el}}{q} \approx \left( \frac{k_B}{e} \right) \frac{k_B T}{E_F} \quad (7.7)$$

where,  $C_{el}$ ,  $E_F$ ,  $k_B$ , and  $q(e)$  are the electronic specific heat, Fermi energy, Boltzmann constant, charge of carrier (of electron). The quantity  $k_B/e \approx 87 \mu V K^{-1}$  is a constant that represents the thermopower of a classical electron gas. Metals have much smaller thermopower values than  $87 \mu V K^{-1}$  (in the order of  $1 - 10 \mu V K^{-1}$ ) and it decreases with decreasing temperatures,  $E_F \gg k_B T$ .

In a semiconductor, a carrier should be first excited across an energy gap  $E_g$ . In this case, the thermopower can be approximated by using equations 7.2 and 7.3:

$$|S| \approx \frac{\pi}{T} \approx \frac{j_Q}{jT} \approx \frac{E_g/2}{eT} \quad (7.8)$$

Thus, the thermopower is higher than the characteristic value of  $87 \mu V K^{-1}$  and increases with decreasing temperature. Semiconductors can exhibit either electron conduction (negative thermopower) or hole conduction (positive thermopower). Typical thermopower values required for good thermoelectric performance are in the order of  $160 - 250 \mu V K^{-1}$  or greater [134]. For  $\text{Bi}_2\text{Te}_3$   $S = -160 \mu V K^{-1}$  assuming  $E_g = 0.16 \text{ eV}$  and  $T = 300 \text{ K}$ . A much more detailed information about Boltzmann transport and Seebeck can be found in Ref. [135].

### 7.4.2 Electrical conductivity

Metals have a large charge carrier density, typically  $n \approx 10^{22} \text{ cm}^{-3}$ . Therefore, the electrical conductivity,  $\sigma$ , is very high for metals, in the order of  $10^6 \Omega^{-1} \text{ cm}^{-1}$ . However, the Seebeck coefficient is very low for metals (Fig. 7.3). On the other hand, for intrinsic semiconductors, the carriers must be (thermally) excited across the band gap for conduction. For semiconductor, the temperature dependent behavior of electrical conductivity,  $\sigma$ , can be expressed as:

$$\sigma = \sigma_0 \exp\left(\frac{-E_g}{k_B T}\right) \text{ and, } \sigma_0 = nq\mu \quad (7.9)$$

where,  $\mu$  is the mobility of charge carrier. Therefore, there are two primary ways to achieve a high conductivity in intrinsic semiconductors, either by having a small gap to excite charge carriers across the band gap or by having very high-mobility carriers. Optimally doped ( $n \approx$

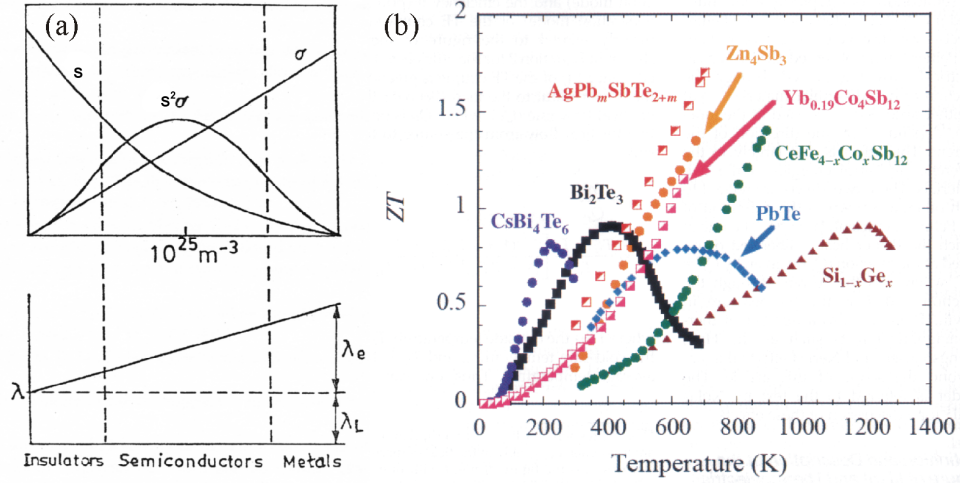


**Figure 7.3:** (a) Schematic plot of the thermopower,  $S$ , the electrical conductivity,  $\sigma$ , the power factor,  $S^2\sigma$ , the lattice thermal conductivity,  $\lambda_L$ , and the electronic thermal conductivity,  $\lambda_e$ , in dependence of the carrier density. (b) Thermoelectric figure of merit  $ZT$  in dependence of the temperature for various bulk thermoelectric materials [134].

$10^{19} \text{ cm}^{-3}$ ) extrinsic semiconductors are good candidates of high performance thermoelectric materials (Fig. 7.3). Typical values of the electrical conductivity for a good thermoelectric material are in the order of about  $10^3 \Omega^{-1} \text{ cm}^{-1}$ .

### 7.4.3 Thermal conductivity

The thermal conductivity,  $\lambda$ , is related to the transfer of heat through a material. Heat transfer can occur either by electrons (electronic thermal conductivity,  $\lambda_{el}$ ) or by phonons (lattice thermal conductivity,  $\lambda_{latt}$ ) and the total thermal conductivity is given by the sum of these two, i.e.  $\lambda = \lambda_{el} + \lambda_{latt}$ . The electronic thermal conductivity of metals and the electrical conductivity are interrelated by the Wiedemann-Franz relationship:

$$\lambda_{el} = L_0 \sigma T \quad (7.10)$$

where,  $L_0 = 2.45 \cdot 10^{-8} \text{ W } \Omega \text{ K}^{-2}$  is the Lorentz number.

The lattice thermal conductivity is given by:

$$\lambda_{latt} = \frac{1}{3} v_s C l_{ph} \quad (7.11)$$

where,  $v_s$  is the velocity of sound,  $C$  is the total specific heat, and  $l_{ph}$  is the phonon mean free path. At high temperatures ( $T \geq 300 \text{ K}$ ), the sound velocity and the heat capacity are essentially temperature-independent in typical materials. Therefore, the magnitude and the temperature-dependence of  $\lambda_{latt}$  are basically determined by the mean free path of the phonons. Slack defined the minimum thermal conductivity,  $\lambda_{min}$ , as the thermal conductivity when the mean free path is essentially limited by the interatomic distance between the atoms within the crystal [123]. Typical analysis of  $\lambda_{min}$  results in values of  $\lambda_{min} \approx 0.25 - 0.5 \text{ W m}^{-1} \text{ K}^{-1}$ . Typical thermal conductivity values for a good thermoelectric material are  $\lambda < 2 \text{ W m}^{-1} \text{ K}^{-1}$ , and typically  $\lambda_{latt} \approx \lambda_{el}$ .

### 7.4.4 Criterion for High-ZT or high performance thermoelectric material

As shown in Eq. 7.6 a high- $ZT$  value requires a high thermopower,  $S$ , a high electrical conductivity,  $\sigma$ , and a low thermal conductivity,  $\lambda$ . Due to the fact that  $S$ ,  $\sigma$ , and  $\lambda$  depend on each

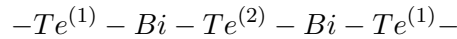
other, it is difficult to improve the overall performance of pure thermoelectric materials. However, alloying would allow to overcome these barriers. The following criteria can be derived for high performance thermoelectric materials:

1. **Charge carrier control:** Beyond a certain level of charge carriers, the thermopower,  $S$ , decreases with increasing carrier density,  $n$ , whereas the electrical conductivity increases with increasing carrier density,  $n$ . Therefore, the power factor,  $S^2\sigma$ , and hence the thermoelectric figure of merit,  $ZT$ , show a maximum for a carrier density of about  $10^9 \text{ cm}^{-3}$ . This means only heavily doped extrinsic semiconductor are suitable for high- $ZT$  materials. Note that  $S$  will be zero for intrinsic semiconductors. The electrical conductivity  $\sigma$  would be too small for insulators and the thermopower  $S$  for metals.
2. **Temperature range and Materials:** Fig. 7.3 shows the thermoelectric figure of merit,  $ZT$ , dependence on the temperature for various materials. This figure shows that a particular material is only suitable for a particular temperature range. For example  $\text{Bi}_2\text{Te}_3$  shows a maximum  $ZT$  value of about 1 at 300 K and is therefore widely used for Peltier devices at room temperature.
3. **Minimum required values for  $S$ ,  $\sigma$ , and  $\lambda$ :** For a high performance, the material should have a minimum thermopower of about  $160 \mu\text{V K}^{-1}$ , a typical electrical conductivity of about  $10^3 \Omega^{-1} \text{ cm}^{-1}$  or larger, and a thermal conductivity smaller than  $2 \text{ W m}^{-1} \text{ K}^{-1}$ .

## 7.5 Thermoelectricity in $\text{Bi}_2\text{Te}_3$

### 7.5.1 Crystal structure and thermoelectric properties of bulk $\text{Bi}_2\text{Te}_3$

$\text{Bi}_2\text{Te}_3$  has a rhombohedral unit cell with space group  $R\bar{3}m$ . This space group can also be represented by a pseudo-hexagonal unit cell, which is easier to understand. The pseudo-hexagonal cell consists of a layered structure with three five-layer-groups with the sequence:



This sequence is called a quintet and the superscripts refer to the two types of bonding. The  $Te^{(1)} - Te^{(1)}$  bonds are considered to be of Van der Waals type, whereas the  $Te^{(1)} - Bi$  and  $Bi - Te^{(2)}$  are of ionic-covalent type [136]. The lattice parameters of the pseudo-hexagonal unit cell are

$$a = 0.438 \text{ nm}, \quad c = 3.04 \text{ nm}$$

The lamellar structure of  $\text{Bi}_2\text{Te}_3$  and the weak  $Te^{(1)} - Te^{(1)}$  bonds between two quintets are responsible for the easy cleavage along the planes perpendicular to the c-axis (i.e. along the basal planes). Besides this striking mechanical anisotropy, most of the transport properties also possess a strong anisotropy. For example, the thermoelectric figure of merit is by a factor of 2 higher for a current direction parallel to the basal plane compared to a current direction parallel to the c-axis [121]. The reasons are a smaller carrier mobility and a smaller thermal conductivity in a direction parallel to the c-axis.

$\text{Bi}_2\text{Te}_3$  is known for its large thermopower,  $S \approx 200 \mu\text{V K}^{-1}$ , high electrical conductivity,  $\sigma \approx \pm 1000 \Omega^{-1} \text{ cm}^{-1}$ , low thermal conductivity,  $\lambda \approx \pm 1.5 \text{ W m K}^{-1}$ , and high thermoelectric figure of merit,  $ZT \approx 1$ , at room temperature. At higher temperatures, the thermopower and thereby the figure of merit decreases drastically due to increasing minority carrier effects (Fig. 7.3b). A more detailed about the thermoelectric properties and material parameters of  $\text{Bi}_2\text{Te}_3$  are given in the textbook of Goldsmid [129].

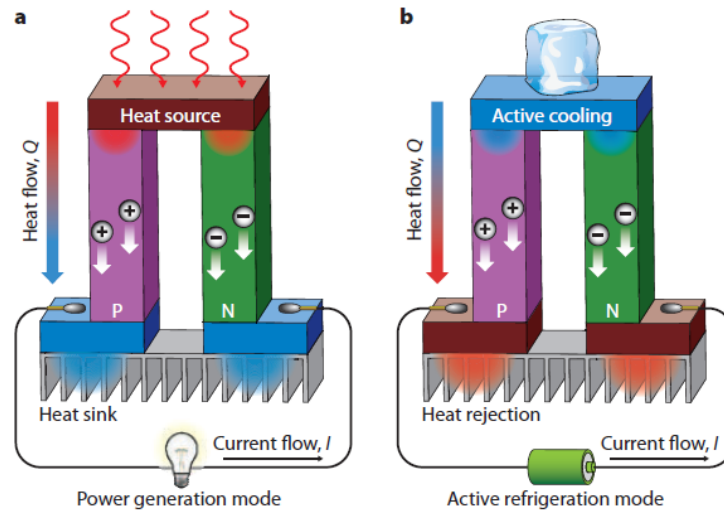


**Figure 7.4:** Schematic diagram of a single-couple thermoelectric (a) refrigerator and (b) power-generator. [137]

### 7.5.2 Motivation of this work

In the mid 1990s, research in the field of thermoelectric material experienced a revival due to theoretical predictions of L.D. Hicks and M.S. Dresselhaus [138] that the power factor and thereby thermoelectric efficiency could be greatly enhanced in nanowires and quantum well systems. This was shown once by R. Venkatasubramanian et al. [139] for  $\text{Bi}_2\text{Te}_3/\text{Sb}_2\text{Te}_3$  superlattices with period of 6 nm, yielding a spectacular  $ZT$  value of 2.4.

On the other hand, phonon scattering was also increased in these superlattices, resulting in a lattice thermal conductivity of less than  $1 \text{ W m}^{-1} \text{ K}^{-1}$ . Goldsmid and Penn [140] already proposed that phonon-grain-boundary scattering could be an effective way for  $ZT$  enhancement as one possibility. Ultrafine grains would substantially scatter low frequency phonon having long mean free path. Recently, thermal conductivity of less than  $1 \text{ W m}^{-1} \text{ K}^{-1}$  and  $ZT$  values beyond 1 were reported in a large number of nanostructured  $\text{Bi}_2\text{Te}_3$  based bulk materials [141, 142, 143, 144, 145], e.g. for samples prepared by ball milling of ternary compounds and subsequent hot pressing [145].

This work will focus on TEM investigations and microstructure-property correlation of nanostructured  $\text{Bi}_2\text{Te}_3$  materials prepared by two different routes:

1. A nanostructure with a wavelength of 10 nm was generated by  $\text{Ar}^+$  ion irradiation. This nanostructure was found to be a sinusoidal displacement field superimposed to the average structure as shown by N. Peranio [146]. It was referred to as natural nanostructure (nns). The displacement field of the nns could be successfully characterized by N. Peranio with respect to wavelength, wave vector, displacement vector, and displacement amplitude by detailed TEM investigations using two-beam diffraction contrast conditions. However, the formation of the nns remained unclear and will be in focus in this work.
2. Artificially nanostructured bulk were prepared from commercially (Peltron GmbH) available ternary compound samples by ball milling and subsequent compaction by spark plasma sintering (SPS). In the literature similar synthesis approaches were reported yielding grain sizes between 50 nm and  $1 \mu\text{m}$  and a  $ZT$  enhancement to values between 1 and 1.5 for p-type material [141, 142, 143, 144, 145] and  $ZT = 1.1$  for n-type material. In this work n-type and p-type nanostructured bulk prepared by the SPS process will be presented with grain sizes less than 100 nm. The nanostructure was characterized by TEM and results will be correlated to transport properties.



## Chapter 8

# Switching of the Natural Nanostructure in $\text{Bi}_2\text{Te}_3$ Materials by Ion Irradiation

### 8.1 Introduction

For 60 years, increasing the efficiency of thermoelectric materials has remained a major challenge in research and technology. A high thermopower  $S$  and electrical conductivity  $\sigma$ , but a low thermal conductivity  $\lambda$  are required for a high thermoelectric figure of merit  $ZT = (S^2\sigma/\lambda)T$  beyond 1. Crystalline semiconductors yield an optimum balance between high thermopower ( $200 \mu\text{V K}^{-1}$ ) and high electrical conductivity ( $1000 \Omega^{-1}\text{cm}^{-1}$ ), which are determined by the charge carrier density ( $10^{19}$ - $10^{20} \text{cm}^{-3}$ ).

The phonon-glass electron-crystal (PGEC) approach introduced by G. Slack et al. [124] was a significant step forward for the understanding of thermoelectric materials properties. It more recently led to advanced engineering of thermoelectric nanomaterials [125, 126, 127, 128], yielding enhanced phonon scattering and thermal conductivities less than  $1 \text{W m}^{-1} \text{K}^{-1}$  as shown for  $\text{AgPb}_m\text{SbTe}_{2-m}$  bulk [125].

$\text{Bi}_2\text{Te}_3$  compounds reveal the highest  $ZT$  at room temperature and its bulk alloys are intensively used in technological applications. Their transport properties fulfill the PGEC criterion, in particular, the low thermal conductivity was attributed to a high structural disorder mainly due to alloying [147]. However, another type of structural disorder was found recently in these materials, referred to as the natural nanostructure (nns) [146]. This nns was investigated in detail by transmission electron microscope (TEM) and can be understood as a sinusoidal displacement field superimposed to the average structure. It has a wavelength of 10 nm and a wave vector parallel to the  $\{1,0,10\}$  reciprocal direction, being inclined by  $39^\circ$  with respect to the crystal c-axis [146]. The amplitude of the sinusoidal displacement  $\vec{u}$  was found to be 10 pm and its direction was parallel to the  $\langle 5, -5, 1 \rangle$  direction. Note that the nns has a strong crystallographic signature that can be explored in two-beam diffraction contrast experiments by TEM. The contrast depends on the excited reflection  $\vec{g}$  and strong contrast is observed for  $\vec{g} \cdot \vec{u}$  different from zero, which is well understood from the dynamical diffraction theory. The strong diffraction contrast already implied that the nns is a volume effect rather than being restricted to the surface.

The nns was shown to be of general character for  $\text{Bi}_2\text{Te}_3$ -based materials; we found it with identical wavelengths and wave vectors in n- and p-type  $\text{Bi}_2\text{Te}_3$ -based bulk materials [146], in thin films [148, 149], and superlattices [148]. The nns competes with artificial nanostructures such as multilayers that are grown for reducing the thermal conductivity [139], since it appears on the same length scale. The nns would be an ideal structural phenomenon for realizing the PGEC concept and should scatter phonons effectively.

In our previous work, TEM samples were prepared with a Gatan Duomill ion etching machine using standard etching parameters: Ar<sup>+</sup> ion etching with an energy of 4 keV and an etching angle of 12° for obtaining a hole, and 2 keV and 8° etching angle for reducing the thickness of amorphous layers. This standard etching procedure yielded TEM samples which showed the nns and others that did not [146]. Therefore, formation of the nns could neither be controlled nor understood. However, control would be of utmost importance for technical applications since the strain field associated with the nns should significantly decrease thermal conductivity and thereby increase the thermoelectric figure of merit. The nns was also identified by other groups in bulk, thin films, and nanostructured bulk [150, 151, 145, 152, 153]; whereas some reports revealed no evidence for the nns [154, 155, 156].

More recently, we used an improved low-angle, low-energy ion etching equipment (Fischione 1010) for n- and p-type Bi<sub>2</sub>Te<sub>3</sub>-based bulk materials with energies in the range of 0.5 keV to 3 keV and etching angles between 6° to 30°. This machine is known to give artefact-free TEM samples, Müller et al. [157] used it for imaging single Sb dopant atoms in Si. Recently, Ar<sup>+</sup> ion etching in Si was investigated in detail. The thickness of amorphous surface layers introduced by the ion etching can be kept small and was less than 2 nm [158] for conditions similar as applied in this work.

We realized that the nns can be switched ON and OFF in a controlled way by ion etching, the range of etching parameters and minimum dose for switching the nns ON and OFF will be presented in this work. It is known, that low energy (100 eV) ion beam irradiation during film deposition is an effective method for modifying the grown film properties of various materials such as Ta thin films [159]. Ion irradiation would yield an elegant and effective technological route for improving thermoelectric nanomaterials on a large scale.

## 8.2 Experimental

The same specimens and the same experimental procedure were applied as in Peranio and Eibl [146], and will, therefore, not be repeated here in full detail. The samples were strongly textured n-type Bi<sub>2</sub>(Te<sub>0.91</sub>Se<sub>0.09</sub>)<sub>3</sub> and p-type (Bi<sub>0.26</sub>Sb<sub>0.74</sub>)<sub>2</sub>Te<sub>3</sub> bulk materials synthesized by the Bridgman technique into pellets. We realized that forming and removing the nns by ion irradiation depends on the orientation of the crystal c-axis (space group  $R\bar{3}m$ ) with respect to the plane of the TEM samples. In this work, only samples close to a  $\langle 1, 1, 0 \rangle$  orientation were used in which the c-axis lay in the plane of the sample (Fig. 2a). Samples were first mechanically polished to a thickness of 25 μm. Then, samples were ion etched with a Fischione 1010 ion etching machine using 3 keV Ar<sup>+</sup> ions and an ion source current of 3 mA. The samples were irradiated at a shallow angle of 12° with a continuously rotating sample holder (**Fig. 8.2a**). A hole with diameter of typically 100 μm was obtained after several hours, using two oppositely arranged ion guns (Fig. 8.2a). After this, large electron transparent regions were obtained and the samples were investigated in the TEM and re-etched at different etching conditions as explained in **Table 8.1**. Ion energies, etching angles, and ion source currents as quoted in this work were inserted at the panel of the etching machine. Beam currents as listed in Table 8.1 were measured with respect to ion source currents and ion energies [20]. The stability of the nns was briefly addressed in Peranio and Eibl [146], more detailed results will be presented elsewhere. A detailed explanation how to image the nns in the TEM was given in Peranio and Eibl [146], only the most important details will be repeated here: i) two-beam cases with one strongly excited reflection have to be established, ii) a sinusoidal strain contrast due to the nns appears with the  $\{0,1,5\}$  reflections, iii) the nns goes out of contrast with a strongly excited  $\{1,0,10\}$  reflections. Only these two reflection conditions ( $g = \{0, 1, 5\}$  and  $g = \{1, 0, 10\}$ ) need to be used to prove the presence or absence of the nns. If present, the nns contrast will be visible over large (several 100 μm) regions of the TEM sample. Altogether 6 TEM samples were investigated in detail, for each the chemical composition was measured by quantitative

**Table 8.1:** Ion etching parameters for completely forming and removing nns in n-type  $\text{Bi}_2(\text{Te}_{0.91}\text{Se}_{0.09})_3$  and p-type  $(\text{Bi}_{0.26}\text{Sb}_{0.74})_2\text{Te}_3$  bulk materials. The etching angle was  $10^\circ$ .

Ion energy [keV]	Ion source current [mA]	Beam current [ $\mu\text{A}$ ]	Etching time [min.]	Result
3.0	3	80	1	nns switched ON
2.0	3	55	2	nns switched ON
1.5	3	35	5	nns switched ON
1.0	3	25	5	nns switched OFF

energy-dispersive X-ray spectroscopy [160].

### 8.3 Results and Discussion

It was realized that ion irradiation of the samples yielded the possibility of forming (switching ON) and removing (switching OFF) the nns: A TEM specimen was prepared from p-type  $(\text{Bi}_{0.26}\text{Sb}_{0.74})_2\text{Te}_3$  bulk material with the c-axis lying in the plane of the specimen. The nns was clearly observed in the TEM after the initial etching at a ion energy of 3 keV, see experimental section for other etching parameters. After this initial etching the specimen was subjected to a re-etching series; the specimen was repeatedly etched at 1 keV and 3 keV, the other etching parameters are given in **Table 8.1**. First, the sample was re-etched at 1 keV and the image in **Fig. 8.1a** was acquired. It proves that the nns disappeared. After second re-etching at 3 keV the nns re-appeared (**Fig. 8.1b**), and a third re-etching at 1 keV removed the nns again (**Fig. 8.1c**). Finally, a fourth re-etching at 3 keV yielded the nns once again (not shown). The same ion irradiation procedure was applied on a TEM specimen obtained from n-type  $\text{Bi}_2(\text{Te}_{0.91}\text{Se}_{0.09})_3$  bulk material, yielding identical results (**Fig. 8.1d-8.1f**). Controlled formation and removal of the nns was, therefore, proved for n- and p-type TEM specimens for two cycles (ON/OFF). In more detailed experiments we could prove that ion energies as low as 1.5 keV form the nns (**Table 8.1**). We emphasize that the presence or absence of the nns could be seen both in the images and also in the diffraction patterns (insets in **Fig. 8.1**).

In switching ON the nns by ion irradiation at 3 keV we noticed that it would first be seen after etching for 30 s in thicker regions of the samples, and then it would also appear in the very thin region after prolonged etching for 1 min. Forming and removing the nns could be verified for TEM samples prepared from different batches of pellets. In total the results could be reproduced for three n-type specimens obtained from two pellets and three p-type specimens also obtained from two different pellets. Finally, the same results were obtained with a Gatan PIPS 691 ion etching equipment: i) the nns was removed for an ion energy of 1 keV, beam current of about 15-25  $\mu\text{A}$ , and an etching angle of  $10^\circ$ ; ii) it was formed for an ion energy of 5 keV, beam current of about 35-50  $\mu\text{A}$ , and an etching angle of  $10^\circ$ .

The ion etching of  $\text{Bi}_2\text{Te}_3$  at 3 keV yielded an amorphous edge with a distance of 30 nm between vacuum and the crystalline part of the specimen (**Figs. 8.1b and 8.1e**). After etching at 1 keV for several hours this edge can be reduced to 8 nm to 15 nm. Thus,  $\text{Bi}_2\text{Te}_3$  samples behave like most other crystalline compounds under ion etching. This indicates that the surface layers of the TEM samples consist of amorphous  $\text{Bi}_2\text{Te}_3$  due to the ion irradiation. Thus, the nns was not present at the surface but in the inner part of the sample as proved by the TEM images.

As a final point the effect of the etching angle was studied. One n-type sample was etched at energies between 0.5 keV to 3 keV; for each energy the etching angle was increased in steps of  $2^\circ$  to  $5^\circ$ . The results are summarized in **Fig. 8.2**, showing that with decreasing ion energy larger etching angles are required for forming the nns. As an example, the nns was removed at 1 keV and an etching angle of  $10^\circ$  as shown above, but was formed at the same energy and

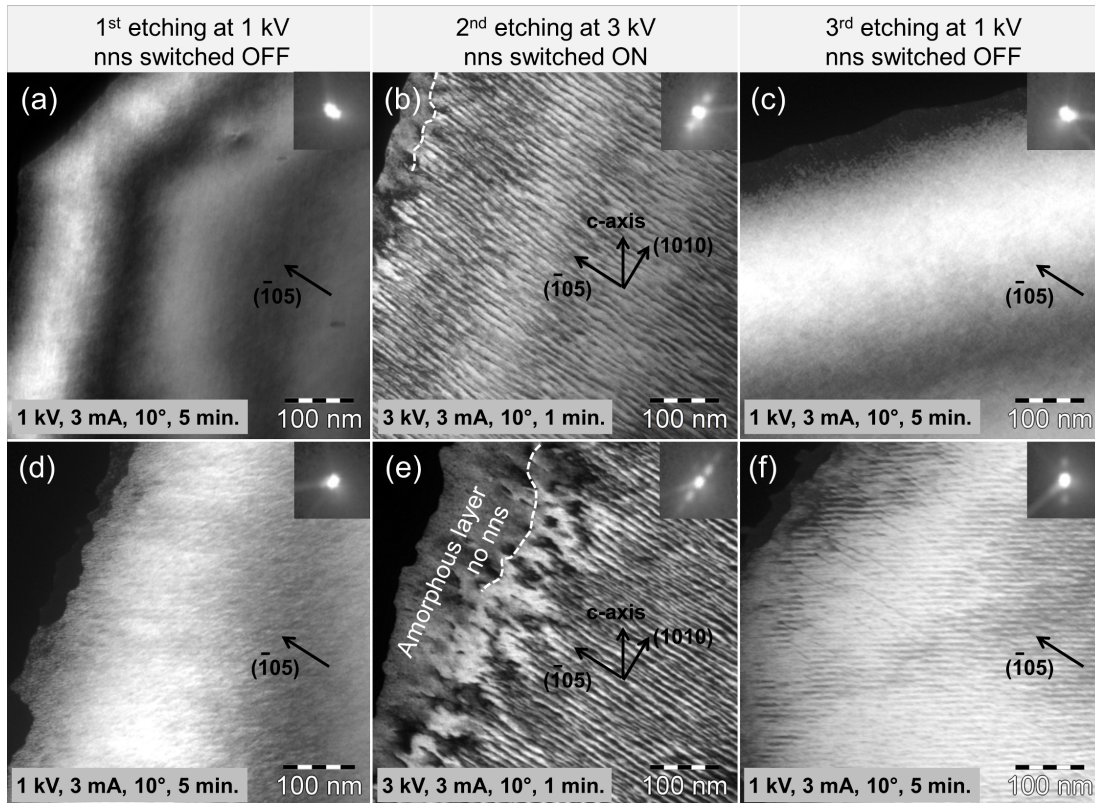


**Figure 8.1:** TEM dark-field images acquired under  $g = \{0, 1, 5\}$  two-beam conditions for imaging the nns in p-type  $(\text{Bi}_{0.26}\text{Sb}_{0.74})_2\text{Te}_3$  (a-c) and n-type  $\text{Bi}_2(\text{Te}_{0.91}\text{Se}_{0.09})_3$  bulk materials (d-f). Etching at 3 keV (b,e) revealed the nns with a wavelength of 10 nm parallel to (1,0,10) planes. After etching at 1 keV the samples did not show the nns along the (1,0,10) planes and no contrast is seen (a,c,d). Only in (f) is a residual contrast seen with fringes parallel to (001) planes. The inserts in the upper right corner show the  $\{0,1,5\}$  reflections with satellite reflection due to the nns in (b) and (e).

an etching angle of  $15^\circ$ . Hence, formation and removal of the nns can also be controlled by increasing or decreasing the etching angle, respectively.

The crystallographic nature of the nns was confirmed in this work as it was described by Peranio and Eibl [146]. Two simple experimental conditions can be set up in a TEM to verify the presence of the nns. Imaging the nns requires controlled tilting of the TEM sample and establishing well defined two-beam diffraction conditions with  $\{0,1,5\}$  and  $\{1,0,10\}$  type of reflections. The maximum tilt needed is about  $12^\circ$  out of the  $\langle 110 \rangle$  pole. These experiments prove that the nns is not a simple surface roughening effect, which might be thought to appear due to ion irradiation, but has a crystallographic nature linked to the volume properties of the  $\text{Bi}_2\text{Te}_3$  sample. Also note that the nns gives a very strong experimental answer, both in the diffraction contrast images and in the diffraction patterns.

The results show that switching ON and OFF the nns is a process on a time scale of a few minutes (Table 8.1) and sensitively depends on the energy of the ions. Ion irradiation with 1.5 keV will form the nns and ion irradiation at 1 keV will make the nns disappear (Table 8.1). Thus, only a small change in ion energy and etching time results in formation or removal of the nns. Therefore, for obtaining reproducible results an ion etching machine operating at stable conditions with respect to ion energy ( $\Delta E < 0.5$  keV) and time ( $\Delta t > 5$  min) is essential; however, in our previous report [146] an ion etching machine (Gatan Duomill) was used for which instability occurred when operated at low energies ( $\leq 2$  keV) and ion source currents (0.25 mA), yielding random formation of the nns [146]. The control of the nns by simple ion etching yields new possibilities for optimizing materials properties.

The formation or removal of the nns was achieved with a typical dose of  $10^{16}$   $\text{Ar}^+$  ions (per

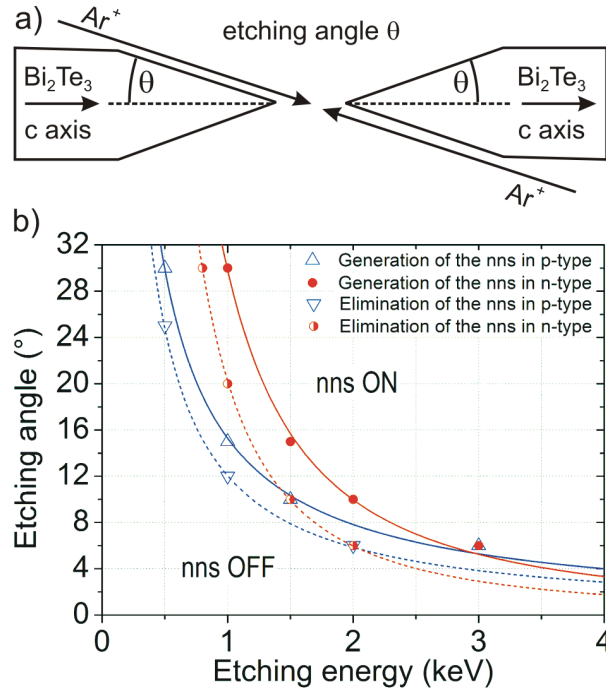


**Figure 8.2:** (a) Schematic of TEM sample orientation and etching angle applied for Ar<sup>+</sup> ion etching. (b) Dependence of formation and removal of the nns on ion energy and angle by Ar<sup>+</sup> ion irradiation for n-type Bi<sub>2</sub>(Te<sub>0.91</sub>Se<sub>0.09</sub>)<sub>3</sub> and p-type (Bi<sub>0.26</sub>Sb<sub>0.74</sub>)<sub>2</sub>Te<sub>3</sub>. The ion source current was 3 mA and the etching time was 5 min.

minute value) and a beam diameter of 1 mm was estimated. The temperature during ion etching does not seem to play an essential role for the nns formation. It is assumed that no significant temperature increase is produced in the first minutes of the ion etching.

TEM investigations clearly proved that i) the nns appeared first in thicker regions of the sample, ii) that an amorphous layer is present on the top surfaces, and iii) the nns has a crystallographic signature; i.e., it has a displacement field with defined amplitude and wave vector [146]. Diffraction contrast images probing the volume of the sample prove the presence of the nns. Therefore, it is clearly proved that the nns is a volume property of the Bi<sub>2</sub>Te<sub>3</sub> and can be switched ON and OFF by ion irradiation.

The effect of the nns on thermal conductivity was discussed in Peranio and Eibl [146]. It represents a structural modulation and should yield effective phonon scattering, reducing the thermal conductivity. Venkatasubramanian [161] summarized the phonon scattering on artificially nanostructured Bi<sub>2</sub>Te<sub>3</sub>, and similar arguments should hold for the nns. The present understanding of the thermal conductivity in Bi<sub>2</sub>Te<sub>3</sub> is poor, since the low temperature data published in the literature differed significantly: lattice thermal conductivities showed peak values of about 60 [162], 250 [163], and 6 W m<sup>-1</sup>K<sup>-1</sup>[164]. In principle, the nns could also be formed by other methods than ion irradiation and thereby give rise to the wide spread of data. The nns of Bi<sub>2</sub>Te<sub>3</sub> was previously described and would be ideal for decreasing the thermal conductivity and realizing a phonon-glass electron-crystalline material for thermoelectric applications.

## 8.4 Conclusions

The nns of Bi<sub>2</sub>Te<sub>3</sub> was previously described and would be ideal for decreasing the thermal conductivity and realizing a phonon-glass electron-crystalline material for thermoelectric applications. The nns was observed by TEM in a large number of Bi<sub>2</sub>Te<sub>3</sub> based materials containing different stoichiometry; it consists of a sinusoidal displacement field with amplitude of 10 pm and periodicity of 10 nm. Here we proved that the nns can be formed and removed by Ar<sup>+</sup> ion

irradiation in a controlled way. Its formation and removal by Ar<sup>+</sup> ion irradiation is sensitive to the ion energy and the etching angle; for example, the nns was formed at ion energies larger than 1.5 keV (switch ON) whereas it was removed at 1 keV (switch OFF), using an etching angle of 10°. Control was demonstrated by reproducing the results in six n- and p-type samples prepared from different batches, switching the nns ON and OFF twice, and verifying the results on two different ion etching machines. Controlled formation of the nns has potential for reducing the thermal conductivity and could increase the thermoelectric figure of merit in Bi<sub>2</sub>Te<sub>3</sub> materials. This relates particularly to nanomaterials since ion irradiation can be applied very effectively in this case.

## Chapter 9

# Spark Plasma Sintered Nanostructured $\text{Bi}_2\text{Te}_3$ bulk with Low Thermal Conductivity

### 9.1 Introduction

$\text{Bi}_2\text{Te}_3$  is the compound with the highest thermoelectric figure of merit  $ZT$  at room temperature, has a large number of structural and chemical degrees of freedom that affect thermoelectric properties, and requires a systematic approach in terms of materials synthesis, structural characterization, thermoelectric characterization and theory. An increase of  $ZT$  is predicted for nanomaterials with lower dimensionality [123] and was shown once for  $\text{Bi}_2\text{Te}_3/\text{Sb}_2\text{Te}_3$  superlattices [161]. After this breakthrough, fabrication of  $\text{Bi}_2\text{Te}_3$  based nanowires [125, 126, 127, 128], thin films [146, 123, 148, 149, 139] and nanostructured bulk [150, 151, 145, 152] has become a main topic of research on thermoelectric materials.

In this chapter we will present the results obtained on n-type  $\text{Bi}_2(\text{Te}_{0.91}\text{Se}_{0.09})_3$  and p-type  $(\text{Bi}_{0.26}\text{Sb}_{0.74})_2\text{Te}_3$  nanostructured bulk materials prepared by the high potential spark plasma sintering (SPS) technique. Powder X-ray diffraction investigations (XRD) were performed by partners on the as cast, ball milled and SPS samples to monitor the crystallite size. Thermoelectric properties were measured for as cast and SPS samples. The SPS samples were analyzed by energy-filtered TEM (EFTEM) combined with energy-dispersive X-ray spectroscopy (EDX) for nanostructural characterization and quantitative chemical analysis. Microscopy results will be linked to synthesis and thermoelectric characterization and  $ZT$  limiting mechanisms relevant for these nanomaterials will be discussed.

### 9.2 Materials and Methods

#### 9.2.1 Material synthesis and transport properties measurements

$\text{Bi}_2\text{Te}_3$  has a rhombohedral crystal symmetry with space group  $R\bar{3}m$ . The lattice parameters of the pseudo-hexagonal unit cell are  $a = 0.4386$  nm and  $c = 3.0497$  nm [136] resulting in a density of  $7.86$  g cm<sup>-3</sup>. The precursor samples were n-type  $\text{Bi}_2(\text{Te}_{0.91}\text{Se}_{0.09})_3$  and p-type  $(\text{Bi}_{0.26}\text{Sb}_{0.74})_2\text{Te}_3$  bulk materials synthesized by the Bridgman technique [26] with optimized chemical composition for reaching high thermoelectric figures of merit  $ZT$ . They were obtained from commercially available Peltier devices [26].

The precursor material was ground by high-energy ball-milling for about 2 h. The fine grained powder was compacted and introduced in a SPS process, the temperature was systematically varied between 130 and 400°C. Other synthesis parameters were pressure (15-25 MPa) and time (2-10 min.).

**Table 9.1:** Results for n-type Bi<sub>2</sub>(Te<sub>0.91</sub>Se<sub>0.09</sub>)<sub>3</sub> and p-type (Bi<sub>0.26</sub>Sb<sub>0.74</sub>)<sub>2</sub>Te<sub>3</sub> nanostructured bulk: SPS sintering temperature ( $T_{sint}$ ), SPS sintering force ( $F_{sint}$ ), crystallite size ( $D$ ), theoretical density as compared to as-cast material ( $\rho$ ), thermal diffusivity ( $TD$ ), heat capacity ( $C_p$ ), thermal conductivity ( $\lambda$ ), thermopower ( $S$ ), electrical conductivity ( $\sigma$ ) and thermoelectric figure of merit ( $ZT$ ). Transport properties were measured at room temperature ( $\sim 25$  °C).

<b>Samples</b>	$T_{sint}$ (°C)	$F_{sint}$ (kN)	$D$ (nm)	$\rho$ (%)	$TD$ (mm <sup>2</sup> /s)	$C_p$ (J/gK)	$\lambda$ (W/mK)	$S$ (μV/K)	$\sigma$ (1/Ωcm)	$ZT$
As cast										
n-type		100		100	1.336±c 1.054  c	0.170	1.78±c 1.40  c	-225±c -172  c	609±c 183  c	
As cast				100	1.325±c 0.913  c	0.202	1.74±c 1.21  c	240±c 203  c	627±c 269  c	
SPS treatment										
n-type	230	15	60	90.7	0.456	0.135	0.44	-148	121	0.19
SPS treatment										
p-type	130	25	24	92.6	0.455	0.142	0.41	121	57	0.062

**Table 9.2:** Phase analysis by EDX in the TEM of as-cast and SPS treated samples [160].

<b>Samples</b>	<b>n-type materials</b>				<b>p-type materials</b>			
	<b>Bi [at.%]</b>	<b>Te [at.%]</b>	<b>Se [at.%]</b>	<b>Bi [at.%]</b>	<b>Sb [at.%]</b>	<b>Te [at.%]</b>	<b>Sb [at.%]</b>	<b>Te [at.%]</b>
As cast samples								
Matrix	40.1±1.1	54.4±1.3	5.5±0.5	10.4±0.3	29.8±0.8	59.9±0.6		
Matrix	38.7±1.1	55.9±0.9	5.2±0.4	13.0±0.7	28.8±1.4	58.2±2.0		
After SPS treatment								
Grain boundary phase	45.1±1.2	50.0±1.1	4.9±0.2	7.0±2.3	62.6±15.6	30.5±13.5		

Thermal diffusivity ( $TD$ ), thermopower ( $S$ ) and electrical conductivity ( $\sigma$ ) were measured in the temperature range of 40 °C to 90 °C and listed in **Table 9.1**. Thermal diffusivity was measured in a direction parallel to the direction of pressure. Electrical conductivity and thermopower were measured with a ZEM-3 measurement device from ULVAC Technologies Inc. in a direction perpendicular to the direction of pressure. The density ( $\rho$ ) and heat capacity ( $C_p$ ) were also measured and the thermal conductivity was calculated according to  $\lambda = \rho \cdot TD \cdot C_p$ . Finally, the thermoelectric figure-of-merit was calculated as  $ZT = (S^2\sigma/\lambda) T$ . In this work only n- and p-type samples with highest  $ZT$  values were selected for the TEM analysis. All the electrical characterization and X-ray diffraction were done by the partners and microstructural characterization were done at University of Tübingen under the project DFG (SPP1386).

### 9.2.2 TEM specimen preparation and analysis

For TEM analysis, samples were conventionally prepared by grinding, polishing followed by  $\text{Ar}^+$  ion milling at 3 keV (Fischione 1010). A more detailed information about the sample preparation could be found in Chapter 2.

A Zeiss 912 $\Omega$  TEM was operated at 120 kV yielding a point resolution of 0.37 nm and an energy resolution of 1 eV. The size of crystallites was determined by TEM dark-field images acquired in two-beam diffraction conditions with strongly excited Bragg reflections.

For phase mapping, EFTEM images were acquired. Three EFTEM images were acquired at selected energy losses with a slit aperture of 5 eV width and then superimposed to make a RGB (or phase amp) image. The first and third EFTEM image were acquired at 15 eV energy loss and the second EFTEM image at 25 eV (or 31 eV) energy loss, the selected energy loss being close to the plasmon energy and the Bi-O<sub>IV,V</sub> (Sb-N<sub>IV,V</sub>) ionization edge, respectively. A more detailed explanation about low-loss ESI/EFTEM technique can be found in Chapter 4 Sec. 4.2.2.

The TEM is equipped with an EDX detector and a low-background specimen holder for chemical analysis with an energy resolution of 136 eV at the  $Mn - K_\alpha$  line and with an omega energy filter for acquisition of EELS. A high-accuracy chemical analysis data was acquired for Bi<sub>2</sub>Te<sub>3</sub> materials by EDX in the TEM by considering the following points: (i) a stray aperture was introduced to reduce hole-count artifacts by a factor of five; (ii) the Cliff Lorimer k-factors were calibrated such that the mean values of the mole fractions in Bi<sub>2</sub>Te<sub>3</sub> bulk materials measured by EDX in the TEM corresponded to those of electron probe microanalyzer (EPMA) [160]. The EDX spectra were acquired with a spot size of 32 nm and an acquisition time of 300 s. For quantitative chemical analysis, the integrated counts under the Bi-L, Sb-L, and Te-L X-ray lines were used. The integrated counts  $N$  were larger than 15000 yielding a minimum statistical error of  $\sigma_N/N = 0.8\%$  (Poisson statistics) for the determination of the local mole fractions.

## 9.3 Results

### 9.3.1 Crystallite sizes and thermoelectric properties

Nanostructured n-type Bi<sub>2</sub>(Te<sub>0.91</sub>Se<sub>0.09</sub>)<sub>3</sub> and p-type (Bi<sub>0.26</sub>Sb<sub>0.74</sub>)<sub>2</sub>Te<sub>3</sub> bulk materials were prepared using commercially available thermoelectric materials as precursors [146, 160]. Thermoelectric properties and chemical composition of these materials are presented in **Table 9.1** and **Table 9.2**. The precursor material was ground by high-energy ball-milling for about 2 h. The fine-grained powder was compacted and subjected to a SPS process with temperature varied systematically between 130°C and 400°C.

Thermoelectric properties and chemical composition of the materials after SPS sintering process are presented in the (Table 9.1 and Table 9.2) for a quick comparison with the as-cast materials. Materials yielded a density in the range of about 90% to 92% of theoretical density

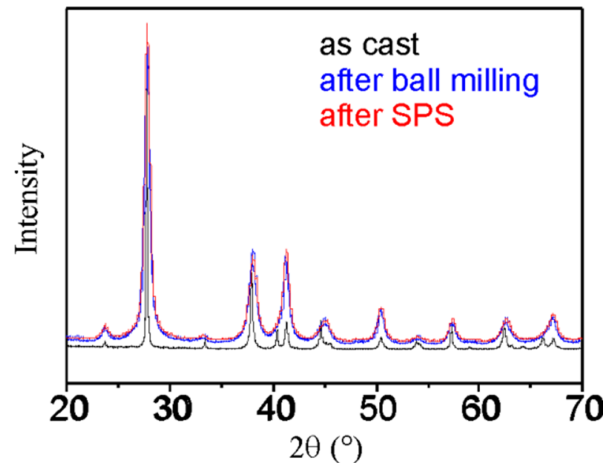


**Figure 9.1:** XRD results of Bi<sub>2</sub>(Te<sub>0.91</sub>Se<sub>0.09</sub>)<sub>3</sub> material in as-cast state (black), after ball milling (blue), and finally after SPS treatment (red). XRD analyses were done by a project partner under a DFG (SPP1386) project.

for low temperatures in the SPS treatment. Thermal diffusivities were reduced by up to 60%. Thermal conductivity was less than 0.5 W m<sup>-1</sup> K<sup>-1</sup> for 90.7% of theoretical density. Absolute thermopower was about 150 μV K<sup>-1</sup>, which is about 30% less than as cast bulk material. Electrical conductivity was more than 5 times smaller than the values of as cast bulk measured along the basal plane (Table 9.1).

**Fig. 9.1** shows a XRD pattern of Bi<sub>2</sub>(Te<sub>0.91</sub>Se<sub>0.09</sub>)<sub>3</sub> material in as-cast state, after ball milling, and after SPS treatment. The broadened X-ray diffraction peaks indicate that after the ball milling as well as after the SPS treatment the particles are of smaller size compared to as-cast material. The grain size after the ball-milling step was about 15 nm.

### 9.3.2 Nanostructure of p-type materials after spark plasma sintering

**Figs. 9.2a-9.2b** show low-magnification TEM bright-field and corresponding dark-field images using strongest reflections within the  $g = (015)$  diffraction ring (Fig. 9.2c), acquired in (Bi<sub>0.26</sub>Sb<sub>0.74</sub>)<sub>2</sub>Te<sub>3</sub> nanostructured bulk after SPS treatment. Fig. 9.2c shows selected area electron diffraction (SAED) of the area shown in Fig. 9.2a-9.2b using a selected area aperture (SAA) of 750 nm in diameter. Diffraction ring pattern can be seen in the SAED showing nano size crystallites with random orientation. Grains of sizes 50-120 nm can be clearly identified in the dark-field image as well as in the bright-field image (Figs. 9.2a-9.2b). Voids of sizes less than 50 nm were identified by comparing bright-field and dark-field images. **Fig. 9.3a** and Fig. 9.3b show high-magnification bright-field and dark-field images, respectively, of the rectangular area shown in Fig. 9.2a. Twin boundaries (TB), superstructure (S) with a spacing of about 4 nm, grain boundary dislocation (GD), and Moiré fringes (M) were observed as indicated by arrows and annotations in Fig. 9.3.

### 9.3.3 Advanced TEM and spectroscopy of p-type materials after spark plasma sintering

EFTEM imaging was applied to image the nano-sized secondary phases at grain boundaries. **Fig. 9.4a** shows a TEM bright-field image and Fig. 9.4b shows a superimposed energy-filtered image (RGB image) of the same area acquired with an energy slit aperture of width 5 eV at 15 eV (Red, first plasmon peak), 31 eV (Green, Sb N<sub>4,5</sub> ionization edge), and 15 eV (Blue)

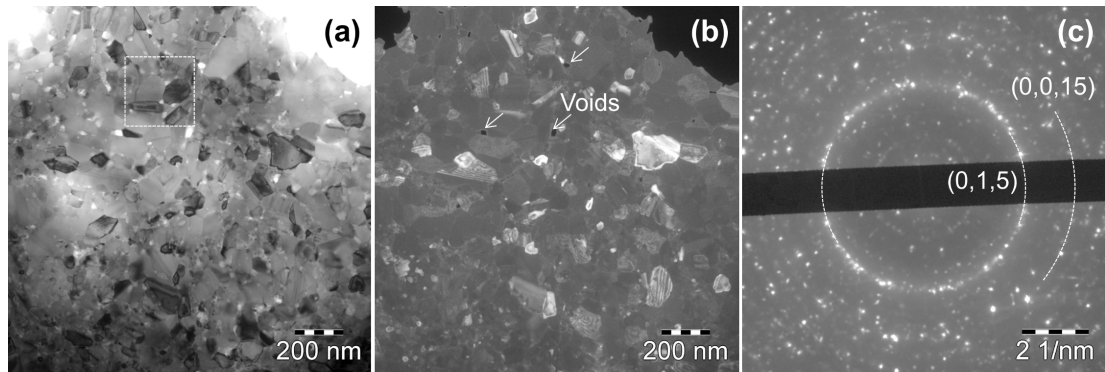


**Figure 9.2:** (a) A low-magnification bright-field image, (b) the corresponding  $g = (105)$  dark-field image and (c) a selected area electron diffraction pattern of  $(\text{Bi}_{0.26}\text{Sb}_{0.74})_2\text{Te}_3$  nanostructure bulk after SPS treatment.

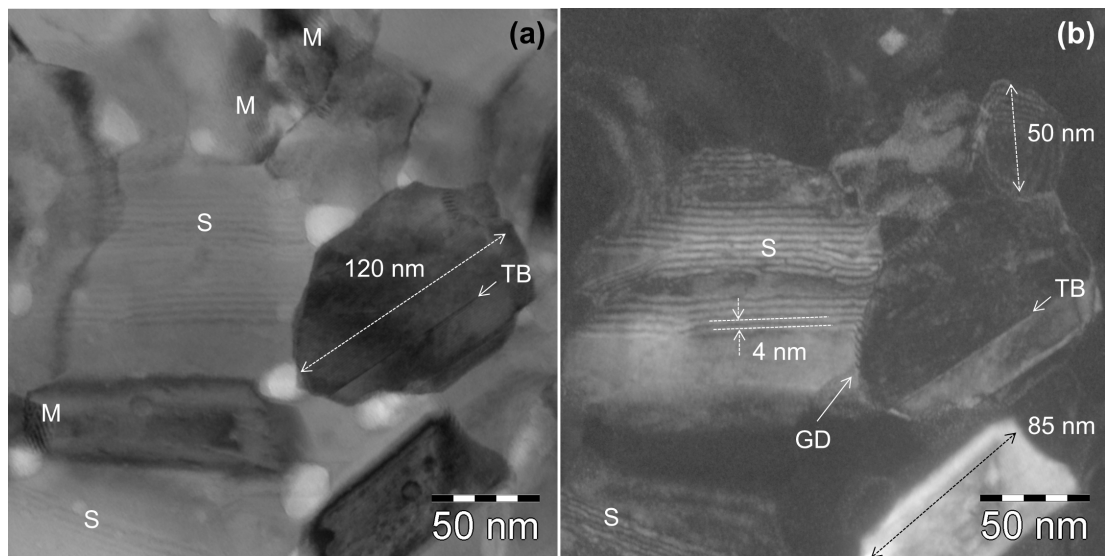


**Figure 9.3:** (a) A high-magnification bright-field image and (b) the corresponding  $g = (105)$  dark-field image of  $(\text{Bi}_{0.26}\text{Sb}_{0.74})_2\text{Te}_3$  nanostructure bulk after SPS treatment. Superstructure (S), Moiré fringes (M), twin boundaries (TB) and grain boundary dislocations (GD) are indicated by arrows and annotations.

energy losses. Ionization edges of  $\text{Bi-O}_{4,5}$  (25 eV),  $\text{Sb-N}_{4,5}$  (31 eV), and  $\text{Te-N}_{4,5}$  (40 eV) are particularly well suited to image secondary phases with high lateral resolution by EFTEM. For the present case using a 31 eV energy loss, Sb-rich phases were imaged in the  $(\text{Bi}_{0.26}\text{Sb}_{0.74})_2\text{Te}_3$  matrix. RGB image revealed grain boundary secondary phases (green phases in Fig. 9.4b) of few tenth of nm in width, which might act as insulating layers severely reducing the charge carrier mobilities and thus electrical conductivity and  $ZT$  (Table 9.1).

High-accuracy EDX analysis in TEM [146] was carried out to determine the chemical composition of nanostructured bulk matrix and of the secondary phases observed at grain boundaries (Table 9.2). The as-cast material revealed a mean chemical composition of 10.2 at.% Bi, 30.2 at.% Sb and 59.6 at.% Te with a standard deviation of 0.8 at.% (Table 2) [160]. After the SPS treatment, the matrix revealed a mean chemical composition of 13.0 at.% Bi, 28.8 at.% Sb and 58.2 at.% Te with a standard deviation of 2.0 at.%. The grain boundary secondary phases were found to be oxidized and revealed a mean chemical composition of 7.0 at.% Bi, 62.6 at.% Sb and 30.5 at.% Te with a standard deviation of 15.6 at.%. **Fig. 9.5** shows EDX spectra of the matrix and grain boundary secondary phase in linear scale and also in logarithmic scale. In contrast to the matrix, the grain boundary secondary phase clearly yielded enhanced peaks of  $\text{Sb-L}_{\alpha 1}$  at 3.6 keV and of  $\text{O-K}_{\alpha 1}$  at 0.52 keV (Figs. 9.5a and 9.5c).

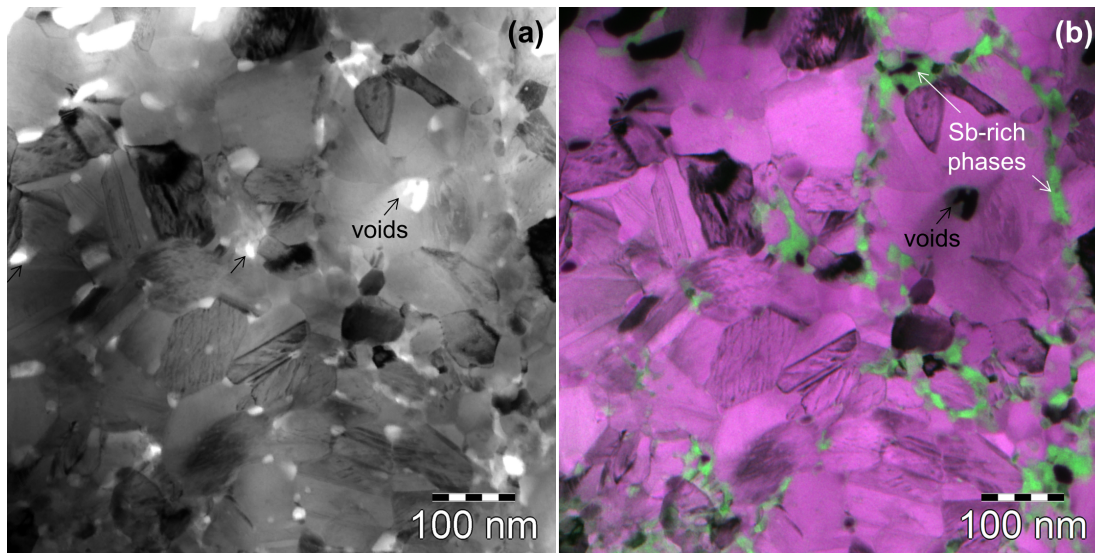


**Figure 9.4:** Energy-filtered TEM of  $(\text{Bi}_{0.26}\text{Sb}_{0.74})_2\text{Te}_3$  nanostructure bulk after SPS treatment: (a) a bright-field image and (b) a RGB image of the same area acquired using a 5 eV energy slit aperture at 15, 31, and 15 eV energy window.

### 9.3.4 Nanostructure of n-type materials after spark plasma sintering

**Figs. 9.6a-9.6b** show low-magnification bright-field and corresponding dark-field image using strongest reflections within the  $g = (015)$  diffraction ring (Fig. 9.6c), acquired in  $\text{Bi}_2(\text{Te}_{0.91}\text{Se}_{0.09})_3$  nanostructure bulk after SPS treatment. Fig. 9.6c shows SAED of the area shown in Fig. 9.6a-9.6b using a selected area aperture (SAA) of 750 nm in diameter. Similar to p-type sample, a diffraction ring pattern with bright spots can be seen in the SAED showing nano size crystallites with random orientation. Grains of sizes 50-130 nm, i.e. exactly the same size as observed in case of p-type sample, can be clearly identified in the dark-field image as well as in the bright field image. In contrast to p-type sample, in n-type sample less number of voids were found. **Fig. 9.3a** and Fig. 9.3b show high-magnification bright-field and dark-field images of the rectangular area shown in Fig. 9.6a. Dislocation (D) and Moiré fringes (M) were observed as indicated by arrows and annotations in Fig. 9.3. However no twin-boundary or superstructure were observed.

### 9.3.5 Advanced TEM and spectroscopy of n-type materials after spark plasma sintering

EFTEM images were also acquired for the n-type sample. **Fig. 9.8a** shows a bright-field image and Fig. 9.8b shows a RGB image of the same area acquired with a energy slit aperture of width 5 eV at 15 eV (Red), 25 eV (Green), and 15 eV (Blue) energy losses. In this case we used 25 eV ( $\text{Bi-O}_{4.5}$ ) energy loss instead of 31 eV to image secondary phases rich in Bi-composition. Almost same kind of grain boundary secondary phases rich in Bi (green phases in Fig. 9.8b) were observed in the RGB image, but the secondary phase is not uniformly distributed over grain boundaries as in case of p-type sample. Note that grain boundary secondary phases might act as insulating layers, severely reducing the charge carrier mobilities and thus electrical conductivity and  $ZT$ .

High-accuracy EDX analysis in TEM of as cast sample revealed a mean chemical composition of 40.7 at.% Bi, 4.8 at.% Se and 54.6 at.% Te with a standard deviation of 0.8 at.% (Table 9.2). After the SPS treatment, the matrix revealed a mean chemical composition of 38.7 at.% Bi, 5.2 at.% Se and 55.9 at.% Te with a standard deviation of 1.1 at.%. The grain boundary

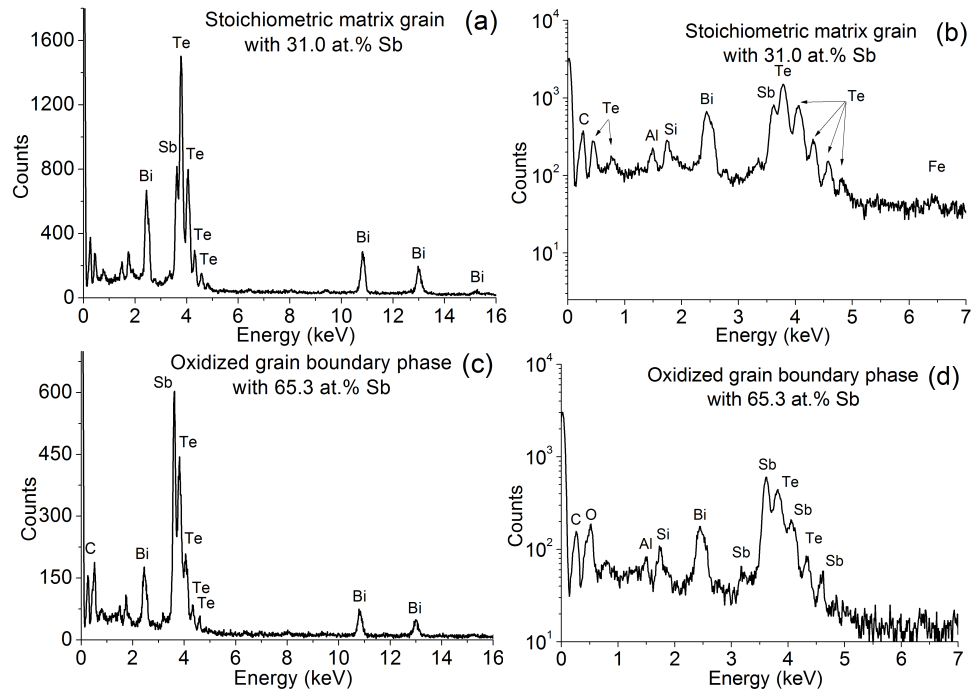


**Figure 9.5:** EDX spectroscopy (TEM) of  $(\text{Bi}_{0.26}\text{Sb}_{0.74})_2\text{Te}_3$  nanostructure bulk after SPS treatment: (a) and (b) EDX spectra of the stoichiometric matrix (pink areas in Fig. 9.4b) with 31.0 at.% Sb in linear scale and in logarithmic scale, respectively. (c) and (d) EDX spectra of the oxidized grain boundary phase (green areas in Fig. 9.4b) with 65.3 at.% Sb in linear scale and in logarithmic scale, respectively.

secondary phases were found to be oxidized and revealed a mean chemical composition of 45.1 at.% Bi, 4.9 at.% Se and 50.0 at.% Te with a standard deviation of 1.2 at.%. **Fig. 9.9** shows EDX spectra of the matrix and grain boundary secondary phase in linear scale and also in logarithmic scale. Similar to p-type, the oxygen peak  $\text{O-K}_{\alpha 1}$  at 0.52 keV observed in Fig. 9.9d confirmed that the grain boundary secondary phases exists in oxidized form.

## 9.4 Discussion

Nanostructured thermoelectric materials can be a cost-effective and scalable alternative to the custom nano-engineered systems, such as superlattices or quantum dots, in order to achieve high  $ZT$  material. However, a number of different issues have to be fulfilled in order to overcome

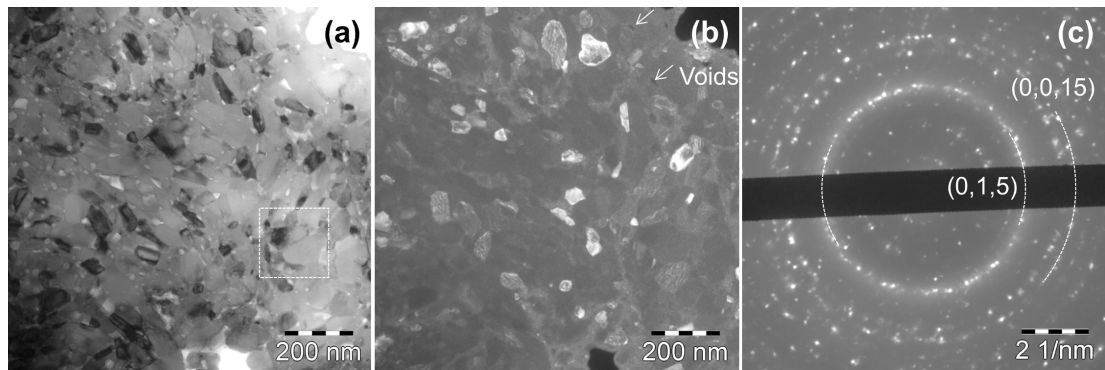


**Figure 9.6:** (a) A low-magnification bright-field image, (b) the corresponding  $g = (105)$  dark-field image and (c) a selected area electron diffraction pattern of  $\text{Bi}_2(\text{Te}_{0.91}\text{Se}_{0.09})_3$  nanostructure bulk after SPS treatment.

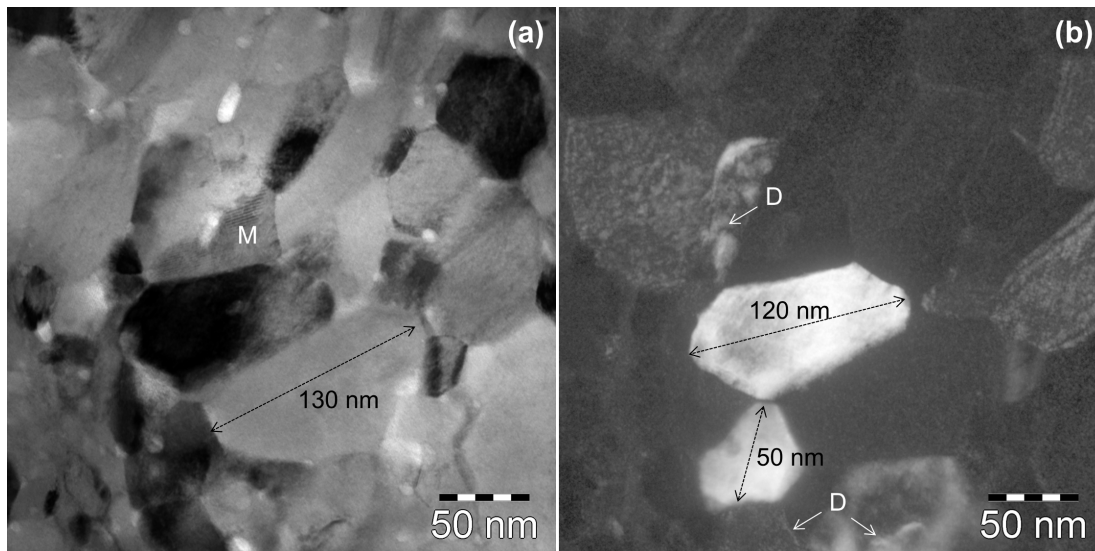


**Figure 9.7:** (a) A high-magnification bright-field image and (b) the corresponding  $g = (105)$  dark-field image of  $(\text{Bi}_{0.26}\text{Sb}_{0.74})_2\text{Te}_3$  nanostructure bulk after SPS treatment. Moiré fringes (M) and dislocations (D) are indicated by arrows and annotations.

the  $ZT$ -limiting mechanisms and to achieve benefits of nanostructured materials: (i) control of grain size; (ii) stoichiometry, antisite defects, and optimum doping; and (iii) avoiding grain boundary blocking layers.

A major result of this work is a significantly reduced thermal conductivity of about  $0.5 \text{ W m}^{-1} \text{ K}^{-1}$ , being a factor of 2-3 less than in standard bulk materials (**Table 9.1**). Our microscopic investigations of SPS materials yielded ultra-fine crystallites of 50-130 nm in size. Such nano-crystallites will give rise to increased phonon scattering and reduced lattice thermal conductivity. The sintering temperature, pressure and time as applied here were essential for obtaining densities  $> 90\%$  of the theoretical densities while simultaneously avoiding substantial grain growth during sintering process.

**Table 9.2** lists the results of quantitative chemical analysis of as cast materials and nanostructured bulk material after SPS. Note that the chemical composition of the as cast materials are optimized for high- $ZT$ . A slight change in the chemical composition was observed in the chemical composition of the matrix after SPS process. A Bi deficiency of about 1 at.% was observed in n-type materials after SPS. For  $\text{Bi}_2\text{Te}_3$  materials it is known that slight deviations from stoichiometry yields strong changes in the charge carrier density and thereby thermopower: Bi-Te bulk materials with a Te content of 60 at.% revealed p-type character and a thermopower of  $227 \mu\text{V K}^{-1}$ , whereas n-type conduction and a thermopower of  $-224 \mu\text{V K}^{-1}$  was observed for 63.5 at.% Te [165]. The Bi deficiency will result in formation  $\text{Te}_{\text{Bi}}$  antisite defects [166], acting as donors, and will increase charge carrier density and might explain the reduced thermopower after SPS. A Te deficiency of about 1.7 at.% was observed in the p-type materials after SPS. The Te deficiency will result in formation  $\text{Bi}_{\text{Te}}$  antisite defects [166], acting as acceptor; and will increase charge carrier density and might explain the reduced thermopower after SPS. Note that we have a larger deviation (1.7 at.%) from stoichiometry in p-type material than in n-type (1.4 at.%), which yielded a larger reduction of thermopower in case of p-type (50%) compared to n-type (34%) material as seen in Table 1.

TEM revealed oxidized Bi-rich or Sb-rich secondary phases at grain boundaries, which are assumed to severely reduce charge carrier mobility [167, 168]. Similar results i.e. reduced carrier mobility due to oxidized secondary phases at grain boundaries were observed by Horio and Inoue [167] in hot pressed Bi-Te materials and in  $\text{Bi}_2\text{Te}_3$  thin films grown by molecular beam epitaxy (MBE) [168]. Oxygen is known to turn p-type  $\text{Bi}_2\text{Te}_3$  into n-type bulk materials [169], however, no detailed explanation was given, why this would be the case.

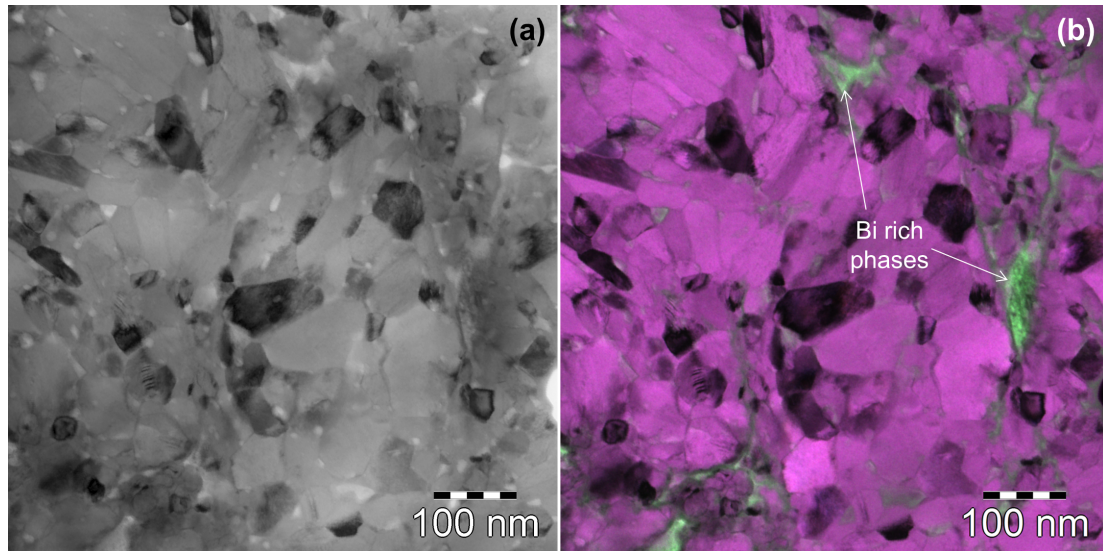


**Figure 9.8:** Energy-filtered TEM of  $\text{Bi}_2(\text{Te}_{0.91}\text{Se}_{0.09})_3$  nanostructure bulk after SPS treatment: (a) a bright-field image and (b) a RGB image of the same area acquired using a 5 eV slit aperture at 15, 25 and 15 eV energy window.

Thermoelectric properties were measured systematically depending on the amount of oxygen contamination in n-type  $\text{Bi}_2\text{Te}_{2.7}\text{Se}_{0.3}$  nanobulk material [170, 171]. As solidified material yielded 0.04 at.% oxygen and a thermopower  $-232 \mu\text{V K}^{-1}$ . As-sintered material yielded 1.8 at.% oxygen and a significantly reduced thermopower of  $-135 \mu\text{V K}^{-1}$ . Subsequent reduction of the sintered material by hydrogen yielded 0.25 at.% oxygen and a thermopower of  $-215 \mu\text{V K}^{-1}$  was recovered.

Also by alloying with other group 6 elements electrical properties of  $\text{Bi}_2\text{Te}_3$  are sensitively affected.  $\text{Bi}_2(\text{Te}_{1-x}\text{Se}_x)_3$  and  $\text{Bi}_2(\text{Te}_{1-x}\text{S}_x)_3$  mixed crystal are known to switch from p-type and n-type for 13.8 at.% Se and 7.2 at.% S, respectively. According to Horak [172] the hole concentration decreases with increasing mole fraction of Se and S in the anion sublattice, which increases the anion vacancy concentration ( $V_A^{-2}$  donors). This increase was explained by a reduced vacancy energy due to the smaller effective radius of the anions. Therefore,  $\text{Bi}_2(\text{Te}_{1-x}\text{S}_x)_3$  yielded higher anion vacancy concentrations and a transition from p- to n-type occurs at smaller  $x$  than for  $\text{Bi}_2(\text{Te}_{1-x}\text{Se}_x)_3$  mixed crystals. Similar arguments could hold for  $\text{Bi}_2(\text{Te}_{1-x}\text{O}_x)_3$ , explaining why transport properties change so drastically [135].

In summary, these results show that thermoelectric properties are sensitive to oxidation and require careful protection from contamination during synthesis and an accurate chemical analysis for understanding thermoelectric properties. The  $ZT$  values could not be improved due to the reduced charge carrier mobility despite the strong reduction of lattice thermal conductivity. Optimization for the annealing and sintering temperatures might help to get rid of the grain boundary phase and hence the low electrical conductivity problem.

## 9.5 Conclusions

In this chapter, we reported the XRD and microscopic results of n-type  $\text{Bi}_2(\text{Te}_{0.91}\text{Se}_{0.09})_3$  and p-type  $(\text{Bi}_{0.26}\text{Sb}_{0.74})_2\text{Te}_3$  nanostructured bulk materials prepared from as cast materials by ball milling followed by SPS process. The nanostructured bulk are cost-effective and scalable alternative to the custom nano-engineered systems, such as superlattices or quantum dots to achieve high- $ZT$  materials. A combination of XRD, EFTEM, and high precision EDX spectroscopy in TEM were applied to understand the nanostructure and its correlation with the observed transport properties. Peak broadening in XRD were observed after high energy ball milling and also after SPS treatment, indicating smaller grain size. Crystallites of sizes 15-23 nm were found in

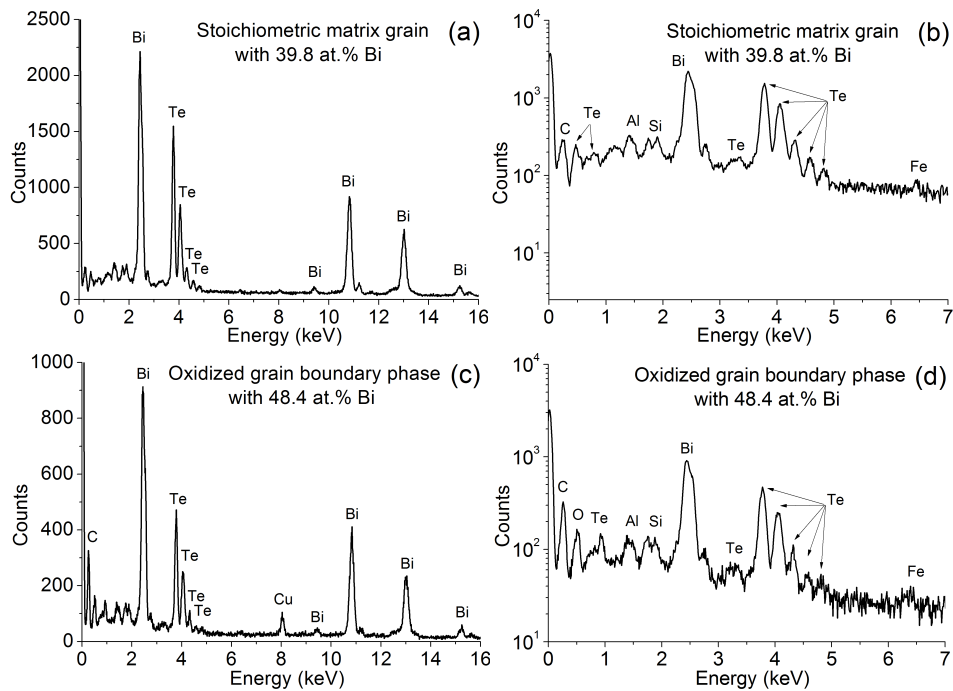


**Figure 9.9:** EDX spectroscopy (TEM) of Bi<sub>2</sub>(Te<sub>0.91</sub>Se<sub>0.09</sub>)<sub>3</sub> nanostructure bulk after SPS treatment: (a) and (b) EDX spectra of the stoichiometric matrix (pink areas in Fig. 9.8b) with 39.8 at.% Bi in linear scale and in logarithmic scale, respectively. (c) and (d) EDX spectra of the oxidized grain boundary phase (green areas in Fig. 9.8b) with 48.4 at.% Bi in linear scale and in logarithmic scale, respectively.

the ball milled powder. After the SPS treatment, highly dense nanostructured bulk materials, yielding very low thermal conductivities, were found. A thermal conductivity as low as 0.44 W m<sup>-1</sup>K<sup>-1</sup> was found at room temperature for both n- and p-type materials, which is required for high-*ZT*. The grain sizes were about 50-130 nm as determined by TEM and thermal diffusivity were reduced by 60%. Few tenth of nm thick Bi-rich (for n-type) and Sb-rich (for p-type) oxidized phase were observed at the grain boundaries. These oxidized phase at grain boundaries could reduce charge carrier mobility and hence electrical conductivities, yielding a reduced *ZT*.

In summary SPS sintered materials, yielded a good thermal conductivity but a poor electrical conductivity as a *ZT* limiting factor. An optimization of the sintering and annealing temperature is required to get rid of the grain boundary secondary phases to achieve a good electrical conductivity and thereby high-*ZT* materials.

## Appendix A

# Specimen Preparation Tools

In this appendix, you will find pictures (view graph) of specimen preparation tools, that are not shown in Chapter 2. Many tools were made at the Institute of Applied Physics departmental work shop.



**Figure A.1:** A view graph of the Ar<sup>+</sup> ion etching machine (Fischione 1010).

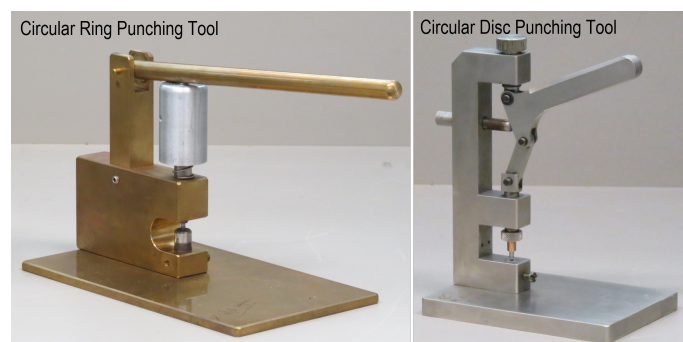


**Figure A.2:** A view graph of the circular ring and circular specimen punching tools.

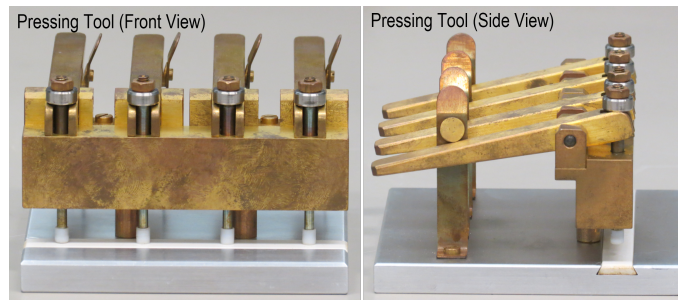


**Figure A.3:** A view graph of the pressing tool (Piano), front view and side view.

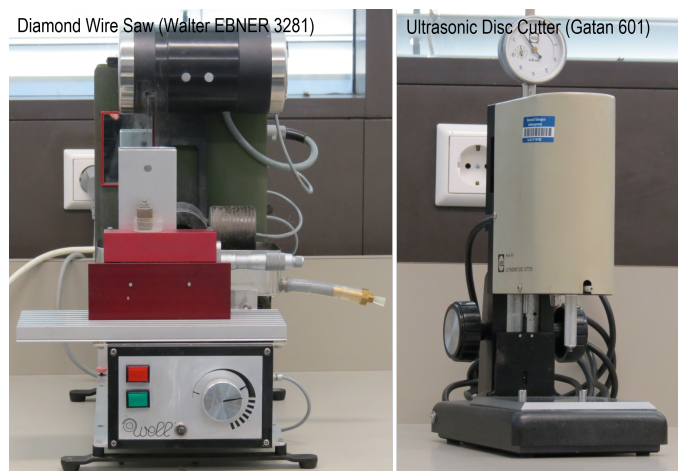


**Figure A.4:** A view graph of the diamond wire saw machine (Walter EBNER 3281) and ultrasonic circular disc cutting machine (Gatan 601).



**Figure A.5:** A view graph of the grinding machine (KNUTH-ROTOR), with two SiC plates of different grit size.

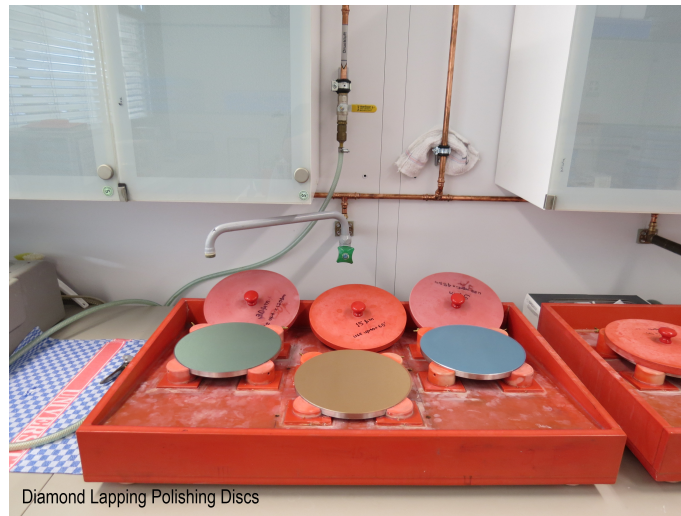


**Figure A.6:** A view graph of the diamond lapping polishing discs with different grit sizes (30  $\mu\text{m}$ , 15  $\mu\text{m}$ , 9  $\mu\text{m}$ , 3  $\mu\text{m}$ , 1  $\mu\text{m}$  and 0.5  $\mu\text{m}$ ).

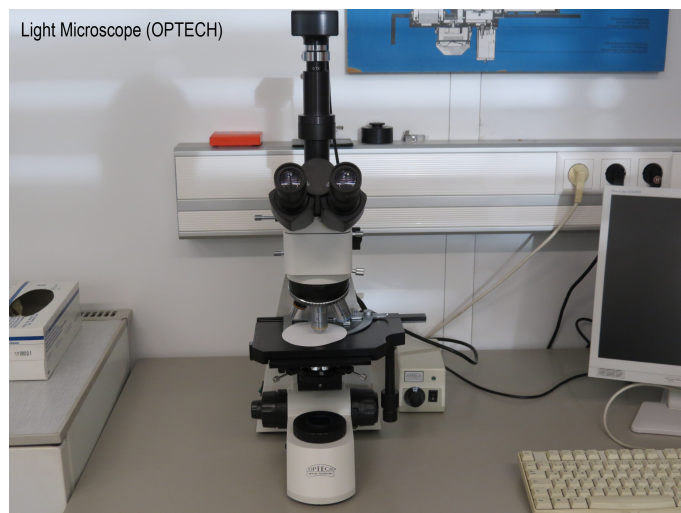


**Figure A.7:** A view graph of the light microscope (OPTECH).



# Bibliography

- [1] Transmission Electron Microscope - LEO 912 Omega manual. URL: <https://mywebspace.wisc.edu/jatikals/web/MSColdwebsite/manuals/LE0912/english/complete/MAN912E.PDF>. 1.2.1.1, 1.1, 1.2, 9.5
- [2] G. Benner and W. Probst. Köhler illumination in the TEM: fundamentals and advantages. *Journal of Microscopy*, 174(3):133–142, 1994. doi:10.1111/j.1365-2818.1994.tb03461.x. 1.2.1.1
- [3] Probst, G. Benner, J. Bihr, and E. Weimer. An “omega” energy filtering TEM - principles and applications. *Advanced Materials*, 5(4):297–300, 1993. doi:10.1002/adma.19930050417. 1.2.1.1, 1.2.1.1
- [4] iTEM manual. URL: [http://www.soft-imaging.net/en/eu/eng/2343\\_5832.htm](http://www.soft-imaging.net/en/eu/eng/2343_5832.htm). 1.2.1.1
- [5] INCA manual. URL: [http://www.cnst.nist.gov/nanofab/pdf/INCA\\_Manual.pdf](http://www.cnst.nist.gov/nanofab/pdf/INCA_Manual.pdf). 1.2.1.1, 1.2.5.2
- [6] W. Grogger, M. Varela, R. Ristau, B. Schaffer, F. Hofer, and K. M. Krishnan. Energy-filtering transmission electron microscopy on the nanometer length scale. *Journal of Electron Spectroscopy and Related Phenomena*, 143(2-3):139–147, May 2005. doi:10.1016/j.elspec.2004.09.028. 1.2.2.2, 1.2.5
- [7] J. M. Zuo, J. Pacaud, R. Hoier, and J. C. H. Spence. Experimental measurement of electron diffuse scattering in magnetite using energy-filter and imaging plates. *Micron*, 31(5):527–532, 2000. 1.2.2.2
- [8] R. F. Egerton. *Electron Energy-Loss Spectroscopy in the Electron Microscope*. Springer, 1996. URL: <http://bioimaging.dbi.udel.edu/sites/bioimaging.dbi.udel.edu/files/manuals/EELSBookbyEgerton.pdf>. 1.2.2.2, 1.2.5.1
- [9] David B. Williams and C. Barry Carter. *Transmission Electron Microscopy A Textbook for Materials Science*. Springer, New York, 2009. doi:10.1007/978-0-387-76501-3. 1.2.3, 1.2.3.3, 1.2.3.4, 1.2.5.2, 5.3
- [10] R. C. McDonald and A. J. Ardell. On diffraction contrast effects at extrinsic grain boundary dislocations. *Physica Status Solidi (A)*, 18(1):407–417, 1973. doi:10.1002/pssa.2210180141. 1.2.3.2
- [11] S. S. Ruvimov and K. Scheerschmidt. Burgers vector determination in TEM by using the dislocation parity analysis. *Physica Status Solidi (A)*, 141(2):269–284, 1994. doi:10.1002/pssa.2211410204. 1.2.3.2
- [12] P. B. Hirsch. *Electron microscopy of thin crystals*. Butterworths, 1965. 1.2.3.3, 1.2.3.4
- [13] B. Fultz and J. M. Howe. *Transmission Electron Microscopy and Diffractometry of Materials*. Springer, 2008. 1.2.3.3, 1.2.3.4
- [14] Oliver Eibl. Electron microscopy manuscript. 1.3, 1.2.3.3, 1.2.3.4, 9.5
- [15] A. Howie and M. J. Whelan. Diffraction contrast of electron microscope images of crystal lattice defects. II. The development of a dynamical theory. *Proceedings of the Royal Society of London. Series A. Mathematical and Physical Sciences*, 263(1313):217–237, September 1961. doi:10.1098/rspa.1961.0157. 1.2.3.4
- [16] Peter W. Hawkes. *Advances in Imaging and Electron Physics*. Academic Press, September 2006. URL: <http://store.elsevier.com/Advances-in-Imaging-and-Electron-Physics/isbn-9780124077010/>. 1.2.4
- [17] S. Amelinckx. *Diffraction and Imaging Techniques in Material Science*. Elsevier Science Ltd, 2nd edition, December 1978. 1.2.4
- [18] R. F. Egerton. Electron energy-loss spectroscopy in the TEM. *Reports on Progress in Physics*, 72(1):016502, January 2009. doi:10.1088/0034-4885/72/1/016502. 1.2.5

- [19] T. M. Chou and M. Libera. Mean free paths for inelastic electron scattering in silicon and poly(styrene) nanospheres. *Ultramicroscopy*, 94(1):31–35, January 2003. doi:10.1016/S0304-3991(02)00192-4. 1.2.5.1
- [20] A. Robbins. Fischione 1010 manual and private communication with Fischione. URL: <http://www.labmet.c1/Documentos/Manuales/Manual-IONMILLMODEL1010.pdf>. 2.1, 2.5, 8.2, 9.5
- [21] E. Eberg, A. F. Monsen, T. Tybell, A. T. J. van Helvoort, and R. Holmestad. Comparison of TEM specimen preparation of perovskite thin films by tripod polishing and conventional ion milling. *Journal of electron microscopy*, 57(6):175–179, December 2008. doi:10.1093/jmicro/dfn018. 2.1, 2
- [22] L. A. Giannuzzi and F. A. Stevie. A review of focused ion beam milling techniques for TEM specimen preparation. *Micron*, 30(3):197–204, June 1999. doi:10.1016/S0968-4328(99)00005-0. 2.1, 3, 2.3.3
- [23] Z. Aabdin, M. Dürschnabel, T. Rudolf, W. Dreher, and O. Eibl. TEM specimen preparation for superconducting coated conductors grown by inclined substrate deposition. In *Physics Procedia*, Keil, 2012. 2.1, 2.3.1.5, 2.3.3, 4.2.1, 5.2.2, 5.2.3
- [24] M. Bauer, R. Semerad, and H. Kinder. YBCO films on metal substrates with biaxially aligned MgO buffer layers. *IEEE Transactions on Applied Superconductivity*, 9(2):1502–1505, 1999. doi:10.1109/77.784678. 2.2.1, 3.1, 3.5.1, 3.5.1.3, 3.11, 4.1, 4.2, 5.1, 5.4.1, 9.5
- [25] M. Bauer, R. Metzger, R. Semerad, P. Berberich, and H. Kinder. Inclined substrate deposition by evaporation of magnesium oxide for coated conductors. *MRS Online Proceedings Library*, 585, 1999. doi:10.1557/PROC-585-35. 2.2.1, 3.5.1.3, 4.2
- [26] Peltron GmbH Peltier-Technik. URL: <http://www.peltier.de/index.htm>. 2.2.2, 9.2.1
- [27] J. Mayer, L. A. Giannuzzi, T. Kamino, and J. Michael. TEM sample preparation and FIB-Induced damage. *MRS Bulletin*, 32, 2007. URL: <http://info.omniprobe.com/Blog/bid/30190/FIB-Sample-Preparation-Strategies-for-TEM>. 3, 2.3.3
- [28] J. P. Benedict, R. M. Anderson, and S. J. Klepeis. Preparation of tem plan view sections on specific devices using the tripod polisher. *MRS Online Proceedings Library*, 523, 1998. doi:10.1557/PROC-523-19. 2.3.1.4
- [29] H. Oechsner. Untersuchungen zur festkörperperzestäubung bei schiefwinkligem ionenbeschuß polykristalliner metalloberflächen im energiebereich um 1 keV. *Zeitschrift für Physik A Hadrons and Nuclei*, 261(1):37–58, 1973. doi:10.1007/BF01402280. 2.5, 9.5
- [30] D. Eyidi and O. Eibl. A simple, quick and reliable method for TEM cross-section preparation of ceramic oxide films on thin metal substrates. *Micron*, 33(5):499–505, 2002. doi:10.1016/S0968-4328(02)00018-5. 2.3.1.5, 2.5.2, 4.2.1, 6.2
- [31] Model 656 Dimple Grinder. URL: <http://www.gatan.com/specimenprep/656dimplegrinder.php>. 2.3.2
- [32] J. G. Bednorz and K. A. Müller. Possible  $high - T_c$  superconductivity in the Ba-La-Cu-O system. *Zeitschrift für Physik B Condensed Matter*, 64(2):189–193, 1986. doi:10.1007/BF01303701. 3.1
- [33] J. G. Bednorz, M. Takashige, and K. A. Müller. Susceptibility measurements support  $High - T_c$  superconductivity in the Ba-La-Cu-O system. *Europhysics Letters (EPL)*, 3(3):379–386, February 1987. doi:10.1209/0295-5075/3/3/021. 3.1
- [34] M. K. Wu, J. R. Ashburn, C. J. Torng, P. H. Hor, R. L. Meng, L. Gao, Z. J. Huang, Y. Q. Wang, and C. W. Chu. Superconductivity at 93 K in a new mixed-phase Y-Ba-Cu-O compound system at ambient pressure. *Physical Review Letters*, 58(9):908–910, March 1987. doi:10.1103/PhysRevLett.58.908. 3.1
- [35] Z. Xianyu, R. J. Li, Q. H. Zhao, L. Q. Liu, Q. T. Wang, Y. F. He, Z. M. Xiu, D. X. Li, Z. B. Shao, T. G. Chen, R. P. Gao, Y. Tu, Y. Li, H. Y. Jin, D. J. Li, J. E. Hong, F. Liu, Z. J. Liu, Y. Q. Jia, and J. Q. Sun. Superconductivity in Y-Ba-Cu(Cr)-O system. *International Journal of Modern Physics B*, 01(02):281–284, June 1987. doi:10.1142/S0217979287000335. 3.1
- [36] R. J. Cava, B. Batlogg, R. B. van Dover, D. W. Murphy, S. Sunshine, T. Siegrist, J. P. Remeika, E. A. Rietman, S. Zahurak, and G. P. Espinosa. Bulk superconductivity at 91 K in single-phase oxygen-deficient perovskite  $Ba_2YCu_3O_{9-x}$ . *Physical Review Letters*, 58(16):1676–1679, April 1987. doi:10.1103/PhysRevLett.58.1676. 3.1

- [37] D. Dimos, P. Chaudhari, J. Mannhart, and F. K. LeGoues. Orientation dependence of grain-boundary critical currents in YBCO bicrystals. *Physical Review Letters*, 61(2):219, July 1988. doi:10.1103/PhysRevLett.61.219. 3.1, 3.1, 3.3.1.3, 3.3.1.3, 3.9, 9.5
- [38] Horst Rogalla, editor. *100 Years of Superconductivity*. Taylor & Francis, 1 edition, November 2011. 3.1, 3.1, 3.2, 3.3.1.3, 3.5, 3.5.1.1, 3.5.1.2, 3.6.2, 9.5
- [39] Michael Tinkham. *Introduction to Superconductivity*. Dover Publications, 1996. 3.1, 3.1
- [40] Y. Iijima, N. Tanabe, O. Kohno, and Y. Ikeno. Inplane aligned  $YBa_2Cu_3O_{7-x}$  thin-films deposited on polycrystalline metallic substrates. *Applied Physics Letters*, 60(6):769–771, February 1992. doi:10.1063/1.106514. 3.1, 3.5.1, 3.5.1.1, 4.1, 5.1
- [41] A. Goyal, D. P. Norton, J. D. Budai, M. Paranthaman, E. D. Specht, D. M. Kroeger, D. K. Christen, Q. He, B. Saffian, F. A. List, D. F. Lee, P. M. Martin, C. E. Klabunde, E. Hartfield, and V. K. Sikka. High critical current density superconducting tapes by epitaxial deposition of  $YBa_2Cu_3O_{7-x}$  thick films on biaxially textured metals. *Applied Physics Letters*, 69(12):1795, 1996. doi:10.1063/1.117489. 3.1, 3.5.1, 4.1, 5.1, 5.4.4
- [42] F. London and H. London. *Proc. Roy. Soc.*, A149:71, 1971. doi:10.1098/rspa.1935.0048. 3.2
- [43] A. Abrikosov. *Zh. Eksp. Teor. Fiz.*, 32:1174, 1957. URL: <http://www.mn.uio.no/fysikk/english/research/groups/amks/superconductivity/vortex/1957.html>. 3.2
- [44] P. Schmitt, L. Schultz, and G. Saemann-Ischenko. Electrical properties of  $Bi_2Sr_2CaCu_2O_x$  thin films prepared in situ by pulsed laser deposition. *Physica C: Superconductivity*, 168(5–6):475–478, July 1990. doi:10.1016/0921-4534(90)90064-L. 3.2, 3.7, 3.3.1.3, 9.5
- [45] Alistair Christopher Rose-Innes and E. H. Rhoderick. *Introduction to superconductivity*. Number v. 6 in Pergamon international library of science, technology, engineering, and social studies. Pergamon Press, Oxford ; New York, 2d ed edition, 1978. 3.2
- [46] W. Buckel and R. Kleiner. *Supraleitung: Grundlagen und Anwendungen*. 6th ed. Wiley-VCH, May 2008. 3.2, 3.2, 3.3, 3.4, 3.5, 3.3.1.3, 9.5
- [47] K. Kopitzki and P. Herzog. *Einfuehrung in die Festkoerperphysik*. 3rd ed. Teubner Verlag, July 2001. URL: <http://www.springer.com/materials/book/978-3-8351-0144-9>. 3.2
- [48] Zhi-Xiong Cai and Yimei Zhu. *Microstructures and Structural Defects in High-Temperature Superconductors*. World Scientific Pub. Co. Inc., March 1998. URL: <http://www.worldscientific.com/worldscibooks/10.1142/3614>. 3.2, 9.5
- [49] L. Krusin-Elbaum, A. P. Malozemoff, Y. Yeshurun, D. C. Cronmeyer, and F. Holtzberg. Temperature dependence of lower critical fields in Y-Ba-Cu-O crystals. *Physical Review B*, 39(4):2936–2939, February 1989. doi:10.1103/PhysRevB.39.2936. 3.1, 9.5
- [50] K. Nakao, N. Miura, K. Tatsuhara, H. Takeya, and H. Takei. Magnetic hysteresis of  $YBa_2Cu_3O_{7-x}$  single crystals in very high magnetic fields above 100 T. *Physical Review Letters*, 63(1):97–100, July 1989. doi:10.1103/PhysRevLett.63.97. 3.1, 9.5
- [51] J. Mannhart and C. C. Tsuei. Limits of the critical current density of polycrystalline high-temperature superconductors based on the current transport properties of single grain boundaries. *Zeitschrift für Physik B Condensed Matter*, 77(1):53–59, February 1989. doi:10.1007/BF01313619. 3.3
- [52] Peterson and Ekin. Josephson-junction model of critical current in granular  $YBa_2Cu_3O_{7-x}$  delta superconductors. *Physical Review B, Condensed matter*, 37(16):9848–9851, June 1988. URL: [http://journals.ohiolink.edu/ejc/article.cgi?issn=01631829&issue=v37i0016&article=9848\\_jmoccigyds](http://journals.ohiolink.edu/ejc/article.cgi?issn=01631829&issue=v37i0016&article=9848_jmoccigyds). 3.3
- [53] E. J. Kramer. Scaling laws for flux pinning in hard superconductors. *Journal of Applied Physics*, 44(3):1360–1370, March 1973. doi:10.1063/1.1662353. 3.3
- [54] M. Ju Chou and W. Y. Chen. The critical current density in type-II superconducting bulk materials. *arXiv:1204.3252*, April 2012. URL: <http://arxiv.org/abs/1204.3252>. 3.3
- [55] K. Heine, J. Tenbrink, and M. Thöner. High-field critical current densities in  $Bi_2Sr_2Ca_1Cu_2O_{8+x}/Ag$  wires. *Applied Physics Letters*, 55(23):2441–2443, December 1989. doi:10.1063/1.102295. 3.7, 3.3.1.3, 9.5

- [56] Th. Schuster, H. Kuhn, A. Weißhardt, H. Kronmüller, B. Roas, O. Eibl, M. Leghissa, and H. W. Neumüller. Current capability of filaments depending on their position in  $(Bi, Pb)_2Sr_2Ca_2Cu_3O_{10+x}$ -multifilament tapes. *Applied Physics Letters*, 69(13):1954–1956, September 1996. doi:10.1063/1.117633. 3.7, 9.5
- [57] W. Gerhauser, G. Ries, Hw. Neumuller, W. Schmidt, O. Eibl, G. Saemannschenko, and S. Klaumunzer. Flux-line pinning in  $Bi_2Sr_2CaCu_2O_x$  crystals - interplay of intrinsic 2d behavior and irradiation-induced columnar defects. *Physical Review Letters*, 68(6):879–882, February 1992. doi:10.1103/PhysRevLett.68.879. 3.3.1.2
- [58] S. E. Babcock and D. C. Larbalestier. Evidence for local composition variations within  $YBa_2Cu_3O_{7-x}$  grain boundaries. *Applied Physics Letters*, 55(4):393, 1989. doi:10.1063/1.102422. 3.3.1.3, 5.1
- [59] M. F. Chisholm and S. J. Pennycook. Structural origin of reduced critical currents at  $YBa_2Cu_3O_{7-x}$  grain boundaries. *Nature*, 351(6321):47–49, May 1991. doi:10.1038/351047a0. 3.3.1.3, 3.8, 5.1, 5.4.4, 6.4, 9.5
- [60] S. T. Keenan, J. Du, E. E. Mitchell, S. K. H. Lam, J. C. Macfarlane, C. J. Lewis, K. E. Leslie, and C. P. Foley. High- $T_c$  superconducting electronic devices based on YBCO step-edge grain boundary junctions. *IEICE Transaction on electronics*, E96-C(3):298–306, March 2013. URL: [http://search.ieice.org/bin/summary.php?id=e96-c\\_3\\_298&category=C&year=2013&lang=E&abst=](http://search.ieice.org/bin/summary.php?id=e96-c_3_298&category=C&year=2013&lang=E&abst=). 3.3.1.3
- [61] J. Clarke and A. I. Braginski. *The SQUID Handbook. SET: The SQUID Handbook: Volume I: Fundamentals and Technology of SQUIDS and SQUID Systems: 1*. Wiley-VCH Verlag GmbH & Co. KGaA, 1. auflage edition, May 2004. URL: [122.129.75.35/articles/3527402292.pdf](http://www.wiley-vch.de/doi/10.1002/9783527402292.pdf). 3.3.1.3
- [62] C. Ning, G. Weiyan, Z. Jiaqi, and C. Xichen. The magnetic and superconducting properties of  $DyBa_2Cu_3O_{7-x}$ . *Solid State Communications*, 65(5):333–337, February 1988. doi:10.1016/0038-1098(88)90709-0. 3.4
- [63] J. L. MacManus-Driscoll. Recent developments in conductor processing of high irreversibility field superconductors. *Annual Review of Materials Science*, 28(1):421–462, 1998. doi:10.1146/annurev.matsci.28.1.421. 3.5
- [64] I. Hlasnik. Review on AC losses in superconductors. *IEEE Transactions on Magnetics*, 17(5):2261–2269, 1981. doi:10.1109/TMAG.1981.1061318. 3.5.1
- [65] W. T. Norris. Calculation of hysteresis losses in hard superconductors carrying ac: isolated conductors and edges of thin sheets. *Journal of Physics D: Applied Physics*, 3(4):489, 2002. doi:10.1088/0022-3727/3/4/308. 3.5.1
- [66] Ho. Song, P. Brownsey, Y. Zhang, J. Waterman, T. Fukushima, and D. Hazelton. 2G HTS coil technology development at SuperPower. *IEEE Transactions on Applied Superconductivity*, 23(3), June 2013. doi:10.1109/TASC.2012.2233837. 3.5.1.1
- [67] M. W. Rupich, X. Li, S. Sathiyamurthy, C. L. H. Thieme, K. DeMoranville, J. Gannon, and S. Fleshler. Second generation wire development at AMSC. *Ieee Transactions on Applied Superconductivity*, 23(3), June 2013. doi:10.1109/TASC.2012.2235495. 3.5.1.2
- [68] J. H. Claassen and C. L. H. Thieme. Magnetic properties of Ni-based substrates for HTS tape. *Superconductor Science and Technology*, 21(10):105003, October 2008. doi:10.1088/0953-2048/21/10/105003. 3.5.1.2
- [69] K. Hasegawa, K. Fujino, H. Mukai, M. Konishi, K. Hayashi, K. Sato, S. Honjo, Y. Sato, H. Ishii, and Y. Iwata. Biaxially aligned YBCO film tapes fabricated by all pulsed laser deposition. *Applied Superconductivity*, 4(10-11):487–493, October 1996. doi:10.1016/S0964-1807(97)00035-5. 3.5.1.3
- [70] D. O. Smith, M. S. Cohen, and G. P. Weiss. Oblique-Incidence anisotropy in evaporated permalloy films. *Journal of Applied Physics*, 31(10):1755–1762, October 1960. doi:10.1063/1.1735441. 3.5.1.3
- [71] R. A. Doyle, A. M. Campbell, and R. E. Somekh. Direct observation of intrinsic pinning in YBCO thin films. *Physical Review Letters*, 71(25):4241–4244, December 1993. doi:10.1103/PhysRevLett.71.4241. 3.6.1
- [72] K. Matsumoto and P. Mele. Artificial pinning center technology to enhance vortex pinning in YBCO coated conductors. *Superconductor Science and Technology*, 23:014001, 2010. doi:10.1088/0953-2048/23/1/014001. 3.12, 3.6.2, 9.5

- [73] V. Pan, Y. Cherpak, V. Komashko, S. Pozigun, C. Tretiatchenko, A. Semenov, E. Pashitskii, and A. V. Pan. Supercurrent transport in  $YBa_2Cu_3O_{7-x}$  epitaxial thin films in a dc magnetic field. *Physical Review B*, 73(5):054508, February 2006. doi:10.1103/PhysRevB.73.054508. 3.6.2
- [74] L. Civale. Vortex pinning and creep in high-temperature superconductors with columnar defects. *Superconductor Science and Technology*, 10(7A):A11–A28, July 1997. doi:10.1088/0953-2048/10/7A/003. 3.6.2
- [75] J. Chung, C. J. Kim, S. M. Choi, S. I. Yoo, and K. M. Shin. TEM analysis of the interfacial defects in the superconducting  $GdBa_2Cu_3O_{7-x}$  tapes synthesized by IBAD-PLD. *Physica C: Superconductivity*, 463-465:722–726, October 2007. doi:10.1016/j.physc.2007.04.327. 4.1
- [76] P. N. Arendt, S. R. Foltyn, L. Civale, R. F. DePaula, P. C. Dowden, J. R. Groves, T. G. Holesinger, Q. X. Jia, S. Kreiskott, L. Stan, I. Usov, H. Wang, and J. Y. Coulter. High critical current YBCO coated conductors based on IBAD MgO. *Physica C: Superconductivity*, 412-414(Part 2):795–800, October 2004. doi:10.1016/j.physc.2003.12.074. 4.1
- [77] N. Hussain, K. A. Shahid, I. H. Khan, and S. Rahman. Oxidation of high-temperature alloys (super-alloys) at elevated temperatures in air: I. *Oxidation of Metals*, 41(3-4):251–269, April 1994. doi:10.1007/BF01080783. 4.1
- [78] Y. Katsumata, T. Yoshioka, K. Z. Thosin, T. Nishimoto, T. Izumi, S. Hayashi, and T. Narita. Formation and oxidation behavior of a diffusion-barrier-coating system on a Ni–Mo base alloy at 1,373 k in air. *Oxidation of Metals*, 68(5-6):331–342, October 2007. doi:10.1007/s11085-007-9078-6. 4.1
- [79] J. H. Park, L. Chen, K. C. Goretta, R. E. Koritala, and U. Balachandran. Oxidation of Hastelloy C276. *AIP Conference Proceedings*, 614(1):495–502, May 2002. doi:10.1063/1.1472578. 4.1
- [80] A. Zolotaryov, S. Goetze, R. Zierold, D. Novikov, B. Birajdar, D. Hesse, and K. Nielsch. Temperature-Dependent Solid-State reactions with and without kirkendall effect in  $Al_2O_3/ZnO$ ,  $Fe_2O_3/ZnO$ , and  $Co_xO_y/ZnO$  oxide thin film systems. *Advanced Engineering Materials*, 12(6):509–516, June 2010. doi:10.1002/adem.201000043. 4.1, 4.4.2, 4.4.3
- [81] P. Kofstad. *Nonstoichiometry, diffusion, and electrical conductivity in binary metal oxides*. R.E. Krieger Pub. Co., Malabar Fla., 1983. doi:10.1002/maco.19740251027. 4.1
- [82] J. Askill. *Tracer diffusion data for metals, alloys, and simple oxides*. IFI/Plenum, New York, 1970. URL: <http://tiny.cc/xtsaww>. 4.1, 4.5, 9.5
- [83] Alan Cottrell and Alan Howard Cottrell (Sir.). *An introduction to metallurgy*. Edward Arnold, 1975. URL: <http://www.ebooks.com/677899/an-introduction-to-metallurgy/cottrell-alan/>. 4.4.2, 4.4, 4.4.2, 4.5, 9.5
- [84] G. R. Wallwork. The oxidation of alloys. *Reports on Progress in Physics*, 39(5):401–485, May 1976. doi:10.1088/0034-4885/39/5/001. 4.4.2
- [85] C. Greskovich and V. S. Stubican. Interdiffusion studies in the system  $MgO - Cr_2O_3$ . *Journal of Physics and Chemistry of Solids*, 30(4):909–910, IN1–IN2, 911–917, April 1969. doi:10.1016/0022-3697(69)90288-1. 4.4.2
- [86] J. C. Fisher. Calculation of diffusion penetration curves for surface and grain boundary diffusion. *Journal of Applied Physics*, 22(1):74, 1951. doi:10.1063/1.1699825. 4.4.2
- [87] M. Dürrschnabel, Z. Aabdin, V. Große, M. Bauer, G. Sigl, W. Prusseit, and O. Eibl. Growth of biaxially-textured MgO buffer layers by inclined substrate deposition. *Physics Procedia*, (0):1546–1551, 2012. doi:10.1016/j.phpro.2012.06.208. 4.4.2
- [88] S. K. Ghandhi. *Semiconductor power devices: physics of operation and fabrication technology*. Wiley, 1977. 4.4.2
- [89] J. Li, M. K. Loudjani, B. Lesage, and A. M. Huntz. Yttrium diffusion in a chromia scale grown on a Ni-30 wt% cr alloy. *Philosophical Magazine A*, 76(4):857, 1997. doi:10.1080/01418619708214214. 4.4.2
- [90] M. F. Berard. Yttrium impurity diffusion in MgO single crystals. *Journal of the American Ceramic Society*, 54(1):58–58, January 1971. doi:10.1111/j.1151-2916.1971.tb12173.x. 4.4.2
- [91] Ellingham diagram. URL: <http://web.deu.edu.tr/metalurjimalzeme/pdf/MMM2003MetalurjiTermodinamigi/EllinghamKaynak2.pdf>. 4.4.2

- [92] H. J. Borchardt. On the oxidation of yttrium. *Journal of Inorganic and Nuclear Chemistry*, 26(5):711–714, IN1–IN3, 715–719, May 1964. doi:10.1016/0022-1902(64)80314-6. 4.4.3
- [93] A. Bardal, M. Zwerger, O. Eibl, J. Wecker, and Th. Matthée.  $YBa_2Cu_3O_{7-x}$  films on si with Y-stabilized  $ZrO_2$  and  $Y_2O_3$  buffer layers: High-resolution electron microscopy of the interfaces. *Applied Physics Letters*, 61(10):1243, 1992. doi:10.1063/1.107608. 4.4.3
- [94] J. Lu, E. S. Choi, and H. D. Zhou. Physical properties of Hastelloy® C-276™ at cryogenic temperatures. *Journal of Applied Physics*, 103(6):064908, 2008. doi:10.1063/1.2899058. 5.1
- [95] T. G. Holesinger, L. Civale, B. Maiorov, D. M. Feldmann, J. Y. Coulter, D. J. Miller, V. A. Maroni, Z. Chen, D. C. Larbalestier, R. Feenstra, X. Li, Y. Huang, T. Kodenkandath, W. Zhang, M. W. Rupich, and A. P. Malozemoff. Progress in nanoengineered microstructures for tunable high-current, high-temperature superconducting wires. *Advanced Materials*, 20(3):391–407, February 2008. doi:10.1002/adma.200700919. 5.1, 5.4.4
- [96] C. Gerber, D. Anselmetti, J. G. Bednorz, J. Mannhart, and D. G. Schlom. Screw dislocations in  $High - T_c$  films. *Nature*, 350(6316):279–280, March 1991. doi:10.1038/350279a0. 5.1, 5.4.2
- [97] P. N. Arendt and S. R. Foltyn. Biaxially textured IBAD-MgO templates for YBCO-coated conductors. *MRS Bulletin*, 29(8):543–550, August 2004. doi:10.1557/mrs2004.160. 5.1, 5.4.4
- [98] U. Balachandran, B. Ma, M. Li, B. L. Fisher, R. E. Koritala, D. J. Miller, and S. E. Dorris. Development of coated conductors by inclined substrate deposition. *Physica C: Superconductivity*, 392-396(Part 2):806–814, October 2003. doi:10.1016/S0921-4534(03)00790-1. 5.1
- [99] J. H. Claassen, M. E. Reeves, and R. J. Soulen. A contactless method for measurement of the critical current density and critical temperature of superconducting films. *Review of Scientific Instruments*, 62(4):996, 1991. doi:10.1063/1.1141991. 5.2.1
- [100] W. Prusseit, C. Hoffmann, R. Nemetschek, G. Sigl, J. Handke, A. Lümke, and H. Kinder. Long length coated conductor fabrication by inclined substrate deposition and evaporation. *Journal of Physics: Conference Series*, 43:215–218, June 2006. doi:10.1088/1742-6596/43/1/054. 5.2.1, 6.1, 6.2
- [101] M. Dürrschnabel, Z. Aabdin, M. Bauer, R. Semerad, W. Prusseit, and O. Eibl.  $DyBa_2Cu_3O_{7-x}$  superconducting coated conductors with critical currents exceeding  $1000 A cm^{-1}$ . *Superconductor Science and Technology*, 25(10):105007, October 2012. doi:10.1088/0953-2048/25/10/105007. 5.3
- [102] V. Selvamanickam, Y. Chen, I. Kesgin, A. Guevara, T. Shi, Y. Yao, Y. Qiao, Y. Zhang, Y. Zhang, G. Majkic, G. Carota, A. Rar, Y. Xie, J. Dackow, B. Maiorov, L. Civale, V. Braccini, J. Jaroszynski, A. Xu, D. Larbalestier, and R. Bhattacharya. Progress in performance improvement and new research areas for cost reduction of 2G HTS wires. *IEEE Transactions on Applied Superconductivity*, 21(3):3049–3054, June 2011. doi:10.1109/TASC.2011.2107310. 5.3
- [103] W. Prusseit, M. Bauer, V. Große, R. Semerad, G. Sigl, Z. Aabdin, M. Dürrschnabel, and O. Eibl. Working around HTS thickness limitations – towards  $1000+ A cm^{-1}$  class coated conductors. *Physics Procedia*, 2012. 5.4.2
- [104] A. Wander, I. J. Bush, and N. M. Harrison. Stability of rocksalt polar surfaces: An ab initio study of MgO(111) and NiO(111). *Physical Review B*, 68(23):233405, December 2003. doi:10.1103/PhysRevB.68.233405. 5.4.2
- [105] D. G. Schlom, D. Anselmetti, J. G. Bednorz, R. F. Broom, A. Catana, T. Frey, C. Gerber, H. J. Güntherodt, H. P. Lang, and J. Mannhart. Screw dislocation mediated growth of sputtered and laser-ablated  $YBa_2Cu_3O_{7-x}$  films. *Z. Physik B - Condens. Matter*, 86(2):163–175. 5.4.2
- [106] R. Aguiar, F. Sánchez, C. Ferrater, M. Aguiló, and M. Varela. Simulation of epitaxial growth of  $CeO_2$  on YSZ(100) and  $SrTiO_3$  on MgO(100) for  $YBa_2Cu_3O_{7-x}$  deposition. *Thin Solid Films*, 317(1-2):81–84, April 1998. doi:10.1016/S0040-6090(97)00664-0. 5.4.2, 5.4.3
- [107] E. Biagi, E. Borchì, S. D. Gennaro, and L. Masi. Elastic constants and moduli of polycrystalline  $YBa_2Cu_3O_{7-x}$  and  $La_2CuO_4$ . *Journal of Physics D: Applied Physics*, 25:901, 1992. doi:10.1088/0022-3727/25/5/025. 5.4.3
- [108] F. Mileto Granzio and U. Scotti di Uccio. Gibbs energy and growth habits of YBCO. *Journal of Alloys and Compounds*, 251(1-2):56–64, April 1997. doi:10.1016/S0925-8388(96)02769-7. 5.4.3

- [109] A. P. Sutton and R. W. Balluffi. *Interfaces in Crystalline Materials*. Oxford University Press, USA, August 1995. 5.4.3, 5.4.3, 5.4.3
- [110] G. Schoeck. The core energy of dislocations. *Acta Metallurgica et Materialia*, 43(10):3679–3684, October 1995. doi:10.1016/0956-7151(95)90151-5. 5.4.3
- [111] David Porter. *Phase Transformation in Metals and Alloys*. Van Nostrand Reinhold, August 1981. 5.4.3
- [112] A. Goyal, S. Kang, K. J. Leonard, P. M. Martin, A. A. Gapud, M. Varela, M. Paranthaman, A. O. Ijaduola, E. D. Specht, J. R. Thompson, D. K. Christen, S. J. Pennycook, and F. A. List. Irradiation-free, columnar defects comprised of self-assembled nanodots and nanorods resulting in strongly enhanced flux-pinning in YBCO films. *Superconductor Science and Technology*, 18(11):1533–1538, November 2005. doi:10.1088/0953-2048/18/11/021. 6.1, 6.4
- [113] S. Kang, K. J. Leonard, P. M. Martin, J. Li, and A. Goyal. Strong enhancement of flux pinning in YBCO multilayers with columnar defects comprised of self-assembled  $BaZrO_3$  nanodots. *Superconductor Science and Technology*, 20(1):11–15, January 2007. doi:10.1088/0953-2048/20/1/003. 6.1, 6.4
- [114] D. M. Feldmann, T. G. Holesinger, B. Maiorov, H. Zhou, S. R. Foltyn, J. Y. Coulter, and I. Apodoca.  $1000 A cm^{-1}$  in a  $2 \mu m$  thick  $YBa_2Cu_3O_{7-x}$  film with  $BaZrO_3$  and  $Y_2O_3$  additions. *Superconductor Science and Technology*, 23(11):115016, November 2010. doi:10.1088/0953-2048/23/11/115016. 6.1
- [115] V. Galluzzi, A. Augieri, T. Petrisor, L. Ciontea, G. Celentano, A. Mancini, A. Vannozzi, A.A. Angrisani, and A. Rufoloni. Deposition and characterization of YBCO films with BZO inclusions on single crystal substrate. *Physica C: Superconductivity*, 470(Supplement 1):S142–S144, December 2010. doi:10.1016/j.physc.2010.01.034. 6.4
- [116] E. D. Specht, A. Goyal, J. Li, P. M. Martin, X. Li, and M. W. Rupich. Stacking faults in  $YBa_2Cu_3O_{7-x}$ : Measurement using X-ray diffraction and effects on critical current. *Applied Physics Letters*, 89(16):162510, 2006. doi:10.1063/1.2364185. 6.4
- [117] J. Gutiérrez, B. Maiorov, T. Puig, J. Gázquez, N. Romà, H. Wang, F. Sandiumenge, and X. Obradors. The role of stacking faults in the critical current density of MOD films through a thickness dependence study. *Superconductor Science and Technology*, 22(1):015022, January 2009. doi:10.1088/0953-2048/22/1/015022. 6.4
- [118] Z. Aabdin, M. Dürrschnabel, M. Bauer, R. Semerad, W. Prusseit, and O. Eibl. Growth behavior of superconducting  $DyBa_2Cu_3O_{7-x}$  thin films deposited by inclined substrate deposition for coated conductors. *Acta Materialia*, 60(19):6592–6600, November 2012. doi:10.1016/j.actamat.2012.08.025. 6.4
- [119] A. Augieri, G. Celentano, V. Galluzzi, A. Mancini, A. Rufoloni, A. Vannozzi, A. Angrisani Armenio, T. Petrisor, L. Ciontea, S. Rubanov, E. Silva, and N. Pompeo. Pinning analyses on epitaxial  $YBa_2Cu_3O_{7-x}$  films with  $BaZrO_3$  inclusions. *Journal of Applied Physics*, 108(6):063906, 2010. doi:10.1063/1.3477451. 6.4
- [120] Abram Fedorovich Ioffe. *Semiconductor thermoelements, and Thermoelectric cooling*. Infosearch, ltd., 1957. URL: <http://tiny.cc/q8rww>. 7.1
- [121] D. M. Rowe. *Thermoelectrics Handbook: Macro to Nano*. CRC Press, 2006. 7.1, 7.2.1, 7.5.1
- [122] Lon E Bell. Cooling, heating, generating power, and recovering waste heat with thermoelectric systems. *Science (New York, N.Y.)*, 321(5895):1457–1461, September 2008. doi:10.1126/science.1158899. 7.1
- [123] C. M. Bhandari, H. Scherrer, S. Scherrer, and G. A. Slack. In *CRC Handbook of Thermoelectrics*, (Ed. D.M. Rowe), CRC, Boca Raton,., Ch. 6, 19:34, 1995. doi:10.1201/9781420049718.ch6. 7.1, 7.4.3, 9.1
- [124] G. S. Nolas, J. L. Cohn, G. A. Slack, and S. B. Schujman. Semiconducting Ge clathrates: Promising candidates for thermoelectric applications. *Applied Physics Letters*, 73(2):178–180, July 1998. doi:10.1063/1.121747. 7.1, 8.1
- [125] K. F. Hsu, S. Loo, F. Guo, W. Chen, J. S. Dyck, C. Uher, T. Hogan, E. K. Polychroniadis, and M. G. Kanatzidis. Cubic  $AgPb_mSbTe_{2+m}$ : Bulk thermoelectric materials with high figure of merit. *Science*, 303(5659):818–821, February 2004. doi:10.1126/science.1092963. 7.1, 8.1, 9.1
- [126] M. S. Dresselhaus, G. Chen, M. Y. Tang, R. G. Yang, H. Lee, D. Z. Wang, Z. F. Ren, J. P. Fleurial, and P. Gogna. New directions for low-dimensional thermoelectric materials. *Advanced Materials*, 19(8):1043–1053, 2007. doi:10.1002/adma.200600527. 7.1, 8.1, 9.1

- [127] D. L. Medlin and G. J. Snyder. Interfaces in bulk thermoelectric materials: A review for current opinion in colloid and interface science. *Current Opinion in Colloid & Interface Science*, 14(4):226–235, August 2009. doi:10.1016/j.cocis.2009.05.001. 7.1, 8.1, 9.1
- [128] G. Jeffrey Snyder and Eric S. Toberer. Complex thermoelectric materials. *Nature Materials*, 7(2):105–114, 2008. doi:10.1038/nmat2090. 7.1, 8.1, 9.1
- [129] H. Julian Goldsmid. *Introduction to Thermoelectricity*. Springer, 2009 edition, October 2009. URL: <http://www.springer.com/materials/book/978-3-642-00715-6>. 7.1, 7.3, 7.4, 7.5.1
- [130] J. M. Ziman. *Electrons and Phonons: The Theory of Transport Phenomena in Solids*. Oxford University Press, February 2001. URL: <http://tiny.cc/jtvaww>. 7.1, 7.4
- [131] F. Seitz, H. Ehrenreich, and D. Turnbull. *Solid State Physics*. Academic Press, October 1972. 7.2.1
- [132] L. Onsager. Reciprocal relations in irreversible processes. I. *Physical Review*, 37(4):405–426, February 1931. doi:10.1103/PhysRev.37.405. 7.2.1
- [133] W. Bies, R. Radtke, H. Ehrenreich, and E. Runge. Thermoelectric properties of anisotropic semiconductors. *Physical Review B*, 65(8), February 2002. doi:10.1103/PhysRevB.65.085208. 7.4
- [134] Terry M. Tritt and M. A. Subramanian. Thermoelectric materials, phenomena, and applications: A bird’s eye view. *MRS Bulletin*, 31(03):188–198, 2006. doi:10.1557/mrs2006.44. 7.4.1, 7.3, 9.5
- [135] N. Peranio, M. Winkler, M. Dürrschnabel, J. König, and O. Eibl. Assessing antisite defect and impurity concentrations in  $Bi_2Te_3$  based thin films by high-accuracy chemical analysis. *Advanced Functional Materials*, 2013. doi:10.1002/adfm.201300606. 7.4.1, 9.4
- [136] S. Scherrer and H. Scherrer. Bismuth telluride, antimony telluride, and their solid solutions. In D. Rowe, editor, *CRC Handbook of Thermoelectrics*. CRC Press, July 1995. 7.5.1, 9.2.1
- [137] Jing-Feng Li, Wei-Shu Liu, Li-Dong Zhao, and Min Zhou. High-performance nanostructured thermoelectric materials. *NPG Asia Materials*, 2(4):152–158, October 2010. doi:10.1038/asiamat.2010.138. 7.4, 9.5
- [138] L. D. Hicks and M. S. Dresselhaus. Effect of quantum-well structures on the thermoelectric figure of merit. *Physical Review B*, 47(19):12727–12731, May 1993. doi:10.1103/PhysRevB.47.12727. 7.5.2
- [139] R. Venkatasubramanian, E. Siivola, T. Colpitts, and B. O’Quinn. Thin-film thermoelectric devices with high room-temperature figures of merit. *Nature*, 413(6856):597–602, October 2001. doi:10.1038/35098012. 7.5.2, 8.1, 9.1
- [140] H. J. Goldsmid and A. W. Penn. Boundary scattering of phonons in solid solutions. *Physics Letters A*, 27(8):523–524, September 1968. doi:10.1016/0375-9601(68)90898-0. 7.5.2
- [141] Y. Q. Cao, X. B. Zhao, T. J. Zhu, X. B. Zhang, and J. P. Tu. Syntheses and thermoelectric properties of  $Bi_2Te_3/Sb_2Te_3$  bulk nanocomposites with laminated nanostructure. *Applied Physics Letters*, 92(14):143106–143106–3, April 2008. doi:10.1063/1.2900960. 7.5.2, 2
- [142] W. Xie, J. He, H. Jung Kang, X. Tang, S. Zhu, M. Laver, S. Wang, J. R. D. Copley, C. M. Brown, Q. Zhang, and T. M. Tritt. Identifying the specific nanostructures responsible for the high thermoelectric performance of  $(Bi, Sb)_2Te_3$  nanocomposites. *Nano Letters*, 10(9):3283–3289, September 2010. doi:10.1021/nl100804a. 7.5.2, 2
- [143] D. G. Ebling, A. Jacquot, H. Böttner, L. Kirste, J. Schmidt, and M. Aguirre. Influence of group IV-Te alloying on nanocomposite structure and thermoelectric properties of  $Bi_2Te_3$  compounds. *Journal of Electronic Materials*, 38(7):1450–1455, July 2009. doi:10.1007/s11664-009-0832-1. 7.5.2, 2
- [144] X. Tang, W. Xie, H. Li, W. Zhao, Q. Zhang, and M. Niino. Preparation and thermoelectric transport properties of high-performance p-type  $Bi_2Te_3$  with layered nanostructure. *Applied Physics Letters*, 90(1):012102–012102–3, January 2007. doi:10.1063/1.2425007. 7.5.2, 2
- [145] Y. Lan, B. Poudel, Yi Ma, D. Wang, M. S. Dresselhaus, G. Chen, and Z. Ren. Structure study of bulk nanograined thermoelectric bismuth antimony telluride. *Nano Letters*, 9(4):1419–1422, April 2009. doi:10.1021/nl803235n. 7.5.2, 2, 8.1, 9.1
- [146] N. Peranio and O. Eibl. Structural modulations in  $Bi_2Te_3$ . *Journal of Applied Physics*, 103(2):024314–024314–9, January 2008. doi:doi:10.1063/1.2837043. 1, 8.1, 8.2, 8.3, 9.1, 9.3.1, 9.3.3

- [147] *CRC Handbook of Thermoelectrics - CRC Press Book*. URL: <http://www.crcpress.com/product/isbn/9780849301469>. 8.1
- [148] N. Peranio, O. Eibl, and J. Nurnus. Structural and thermoelectric properties of epitaxially grown  $Bi_2Te_3$  thin films and superlattices. *Journal of Applied Physics*, 100(11):114306–114306–10, December 2006. doi: [10.1063/1.2375016](https://doi.org/10.1063/1.2375016). 8.1, 9.1
- [149] Z. Aabdin, N. Peranio, M. Winkler, D. Bessas, J. König, R. Hermann, H. Böttner, and O. Eibl.  $Sb_2Te_3$  and  $Bi_2Te_3$  thin films grown by room-temperature MBE. *Journal of Electronic Materials*, 41(6):1493–1497, 2012. doi: [10.1007/s11664-011-1870-z](https://doi.org/10.1007/s11664-011-1870-z). 8.1, 9.1
- [150] Z. C. Chen, K. Suzuki, S. Miura, K. Nishimura, and K. Ikeda. Microstructural features and deformation-induced lattice defects in hot-extruded  $Bi_2Te_3$  thermoelectric compound. *Materials Science and Engineering: A*, 500(1–2):70–78, January 2009. doi: [10.1016/j.msea.2008.09.030](https://doi.org/10.1016/j.msea.2008.09.030). 8.1, 9.1
- [151] A. Jacquot, T. Jürgen, J. Schumann, M. Jäggle, H. Böttner, T. Gemming, J. Schmidt, and D. Ebling.  $(Bi, Sb)_2Te_3 - PbTe$  chalcogenide alloys: Impact of the cooling rate and sintering parameters on the microstructures and thermoelectric performances. *Journal of Materials Research*, 26(15):1773–1784, 2011. doi: [10.1557/jmr.2011.78](https://doi.org/10.1557/jmr.2011.78). 8.1, 9.1
- [152] K. H. Lee, S. J. Hong, Y. S. Lee, and B. S. Chun. Formation of 7 layer structure in n-type  $Bi_2(Te_{0.95}Se_{0.05})_3$  thermoelectric compound fabricated by gas atomizing and hot extrusion process. *Materials Letters*, 60(23):2799–2802, October 2006. doi: [10.1016/j.matlet.2006.01.092](https://doi.org/10.1016/j.matlet.2006.01.092). 8.1, 9.1
- [153] R. J. Mehta, Y. Zhang, C. Karthik, B. Singh, R. W. Siegel, T. Borca-Tasciuc, and G. Ramanath. A new class of doped nanobulk high-figure-of-merit thermoelectrics by scalable bottom-up assembly. *Nature Materials*, 11(3):233–240, 2012. doi: [10.1038/nmat3213](https://doi.org/10.1038/nmat3213). 8.1
- [154] C. L. Ciobanu, A. Pring, N. J. Cook, P. Self, D. Jefferson, G. I. Dima, and V. Melnikov. Chemical-structural modularity in the tetradymite group: A HRTEM study. *American Mineralogist*, 94(4):517–534, April 2009. doi: [10.2138/am.2009.2906](https://doi.org/10.2138/am.2009.2906). 8.1
- [155] J. W. G. Bos, H. W. Zandbergen, M. H. Lee, N. P. Ong, and R. J. Cava. Structures and thermoelectric properties of the infinitely adaptive series  $(Bi_2)_m(Bi_2Te_3)_n$ . *Physical Review B*, 75(19):195203, May 2007. doi: [10.1103/PhysRevB.75.195203](https://doi.org/10.1103/PhysRevB.75.195203). 8.1
- [156] D. L. Medlin, Q. M. Ramasse, C. D. Spataru, and N. Y. C. Yang. Structure of the (0001) basal twin boundary in  $Bi_2Te_3$ . *Journal of Applied Physics*, 108(4):043517–043517–6, August 2010. doi: [10.1063/1.3457902](https://doi.org/10.1063/1.3457902). 8.1
- [157] P. M. Voyles, D. A. Muller, J. L. Grazul, P. H. Citrin, and H. J. L. Gossmann. Atomic-scale imaging of individual dopant atoms and clusters in highly n-type bulk Si. *Nature*, 416(6883):826–829, April 2002. doi: [10.1038/416826a](https://doi.org/10.1038/416826a). 8.1
- [158] M. J. Süess, E. Mueller, and R. Wepf. Minimization of amorphous layer in  $Ar^+$  ion milling for UHR-EM. *Ultramicroscopy*, 111(8):1224–1232, July 2011. doi: [10.1016/j.ultramic.2011.03.004](https://doi.org/10.1016/j.ultramic.2011.03.004). 8.1
- [159] K. Ino, T. Shinohara, T. Ushiki, and T. Ohmi. Ion energy, ion flux, and ion species effects on crystallographic and electrical properties of sputter-deposited ta thin films. *Journal of Vacuum Science Technology*, 15:2627–2635, September 1997. URL: <http://adsabs.harvard.edu/abs/1997JVST...15.2627I>. 8.1
- [160] N. Peranio and O. Eibl. Quantitative EDX microanalysis of  $Bi_2Te_3$  in the TEM. *Physica Status Solidi (A)*, 204(10):3243–3255, 2007. doi: [10.1002/pssa.200622579](https://doi.org/10.1002/pssa.200622579). 8.2, 9.2, 9.2.2, 9.3.1, 9.3.3, 9.5
- [161] R. Venkatasubramanian. Lattice thermal conductivity reduction and phonon localizationlike behavior in superlattice structures. *Physical Review B*, 61(4):3091–3097, January 2000. doi: [10.1103/PhysRevB.61.3091](https://doi.org/10.1103/PhysRevB.61.3091). 8.3, 9.1
- [162] D. K. C. Macdonald, E. Mooser, W. B. Pearson, I. M. Templeton, and S. B. Woods. On the possibility of thermoelectric refrigeration at very low temperatures. *Philosophical Magazine*, 4(40):433–446, 1959. doi: [10.1080/14786435908233413](https://doi.org/10.1080/14786435908233413). 8.3
- [163] A. D. Goletskaya, V. V. Sologub, and S. S. Shalyt. *Sov. Phys. Semicond.*, 5:416, 1971. URL: <http://tiny.cc/iqraww>. 8.3
- [164] P. A. Sharma, A. L. Lima Sharma, D. L. Medlin, A. M. Morales, N. Yang, M. Barney, J. He, F. Drymiotis, J. Turner, and T. M. Tritt. Low phonon thermal conductivity of layered  $(Bi_2)_m(Bi_2Te_3)_n$  thermoelectric alloys. *Physical Review B*, 83(23):235209, June 2011. doi: [10.1103/PhysRevB.83.235209](https://doi.org/10.1103/PhysRevB.83.235209). 8.3

- [165] D. M. Rowe. *CRC handbook of thermoelectrics*. CRC Press, Boca Raton, FL, 1995. URL: <http://www.crcnetbase.com/isbn/9781420049718>. 9.4
- [166] G. R. Miller and Che Yu Li. Evidence for the existence of antistructure defects in bismuth telluride by density measurements. *Journal of Physics and Chemistry of Solids*, 26(1):173–177, January 1965. doi:10.1016/0022-3697(65)90084-3. 9.4
- [167] Y. Horio and A. Inoue. Effect of oxygen content on thermoelectric properties of n-type  $(Bi, Sb)_2(Te, Se)_3$  alloys prepared by rapid solidification and hot-pressing techniques. *Materials Transactions*, 47(5):1412–1416, 2006. URL: <http://sciencelinks.jp/j-east/article/200612/000020061206A0385461.php>. 9.4
- [168] N. Peranio, M. Winkler, D. Bessas, Z. Aabdin, J. König, H. Böttner, R.P. Hermann, and O. Eibl. Room-temperature MBE deposition, thermoelectric properties, and advanced structural characterization of binary  $Bi_2Te_3$  and  $Sb_2Te_3$  thin films. *Journal of Alloys and Compounds*, 521:163–173, April 2012. doi:10.1016/j.jallcom.2012.01.108. 9.4
- [169] J. M. Schultz, J. P. McHugh, and W. A. Tiller. Effects of heavy deformation and annealing on the electrical properties of  $Bi_2Te_3$ . *Journal of Applied Physics*, 33(8):2443–2450, August 1962. doi:10.1063/1.1728990. 9.4
- [170] D. C. Cho, C. H. Lim, D. M. Lee, S. Y. Shin, and C. H. Lee. Effect of oxygen content on thermoelectric properties of sintered Bi-Te based compounds. In S. G. Kang and T. Kobayashi, editors, *Designing, Processing and Properties of Advanced Engineering Materials, Pts 1 and 2*, volume 449-4, pages 905–908. Trans Tech Publications Ltd, Zurich-Uetikon, 2004. doi:10.4028/www.scientific.net/MSF.449-452.905. 9.4
- [171] C. H. Lim, D. C. Cho, Y. S. Lee, C. H. Lee, K. T. Kim, and D. M. Lee. Effects of hydrogen reduction on the thermoelectric properties of spark-plasma-sintered  $Bi_2Te_3$  - based compounds. *Journal of the Korean Physical Society*, 46(4):995–1000, April 2005. doi:10.3938/jkps.46.995. 9.4
- [172] J. Horak, Z. Stry, and J. Votinsky. Point-defects in the mixed chalcogenides  $Bi_2Te_{3-x}X_x$  ( $X = S, Se$ ). *Philosophical Magazine B-Physics of Condensed Matter Statistical Mechanics Electronic Optical and Magnetic Properties*, 69(1):31–38, January 1994. doi:10.1080/13642819408236876. 9.4

# List of Tables

1.1	Acquisition conditions and parameters used for imaging and diffraction pattern for DyBCO and $\text{Bi}_2\text{Te}_3$ materials. . . . .	5
1.2	Acquisition conditions and parameters used for acquiring RGB images of DyBCO and $\text{Bi}_2\text{Te}_3$ materials. . . . .	5
1.3	Acquisition conditions and parameters used for obtaining low-loss and core-loss EELS for DyBCO and $\text{Bi}_2\text{Te}_3$ materials. . . . .	6
1.4	Ionization edges of elements relevant for this work. . . . .	13
2.1	CC samples with their basic properties investigated within the HIGHWAY project. . . . .	17
2.2	Thermoelectric material samples with their basic properties (SPS sintering temperature $T_{sint}$ , theoretical density $\rho$ , thermal conductivity $\lambda$ , thermopower $S$ and electrical conductivity $\sigma$ ) investigated within the DFG Priority Program “Nanostructured Thermoelectrics” (SPP1386). Transport properties were measured at room temperature ( $\sim 25$ °C). . . . .	17
2.3	Recipe for the mechanical polishing on the diamond coated abrasive plates . . . . .	21
2.4	Optimized recipe for DyBCO, $\text{Bi}_2\text{Te}_3$ , bulk and thin films, Si (single crystal) and Al foil ion etching using Fischione 1010 ion mill. . . . .	22
2.5	Optimal dimpling recipe for the ISD CCs (Hastelloy). . . . .	24
3.1	Characteristic parameters of optimally doped YBCO superconductors [49, 50]. . . . .	35
4.1	TEM EDX quantitative analysis of sample 7 in cross-section. The reference points are indicated in Fig. 4.8c and some of the spectra are shown in figure 9. . . . .	51
4.2	TEM EDX quantitative analysis of sample 6 in cross-section. The reference points are indicated in Fig. 4.10b and 4.10c and some of the spectra are shown in Fig. 4.11. . . . .	53
4.3	Key features of the low-loss EELS of the ISD MgO buffer layer, the Cr diffusion layer, the Y-layer and the Hastelloy substrate. . . . .	55
4.4	Free enthalpy of oxide formation of relevant elements present at the Hastelloy-MgO interface [83].	56
4.5	Self and inter diffusion data of the relevant elements present at the Hastelloy-MgO interface [82, 83].	58
5.1	Calculated energies for DyBCO films grown by the ISD technology. . . . .	68
6.1	TEM EDX quantitative analysis of the DyBCO film in plan-view. . . . .	74
8.1	Ion etching parameters for completely forming and removing nns in n-type $\text{Bi}_2(\text{Te}_{0.91}\text{Se}_{0.09})_3$ and p-type $(\text{Bi}_{0.26}\text{Sb}_{0.74})_2\text{Te}_3$ bulk materials. The etching angle was $10^\circ$ . . . . .	91
9.1	Results for n-type $\text{Bi}_2(\text{Te}_{0.91}\text{Se}_{0.09})_3$ and p-type $(\text{Bi}_{0.26}\text{Sb}_{0.74})_2\text{Te}_3$ nanostructured bulk: SPS sintering temperature ( $T_{sint}$ ), SPS sintering force ( $F_{sint}$ ), crystallite size ( $D$ ), theoretical density as compared to as-cast material ( $\rho$ ), thermal diffusivity ( $TD$ ), heat capacity ( $C_p$ ), thermal conductivity ( $\lambda$ ), thermopower ( $S$ ), electrical conductivity ( $\sigma$ ) and thermoelectric figure of merit ( $ZT$ ). Transport properties were measured at room temperature ( $\sim 25$ °C). . . . .	96
9.2	Phase analysis by EDX in the TEM of as-cast and SPS treated samples [160]. . . . .	96



# List of Figures

1.1	(a) Photograph of the Zeiss912 Omega TEM and (b) the electron-beam path and the Omega in-column energy-filter [1]. . . . .	4
1.2	Schematic diagram of the Omega in-column spectrometer. Solid line shows the achromatic electron beam, whereas, dotted line shows spectrally dispersed electron beam [1]. . . . .	4
1.3	For the dynamic diffraction theory for the two-beam case, amplitude and phase changes in the direct and diffracted beam for a sample of thickness $dz$ [14]. . . . .	8
2.1	Schematics of the layer structure of ISD grown DyBCO CCs: (a) MgO, (b) the thin DyBCO, (c) thick DyBCO, (d) blocking layer and (e) DyBCO + BZO series. Note that the MgO series is a semi-processed sample, i.e. it does not have all the layers to study the MgO buffer layer. . . . .	16
2.2	A flow chart of different types of TEM specimen preparation methods with their advantages and limitations. . . . .	18
2.3	(a) Unsymmetrical and (b) symmetrical sandwich dummy structure. . . . .	19
2.4	A view graphs of the (a) Tripod holder and (b) Star holder without and with glued dummies and specimen on the holder. . . . .	20
2.5	(a) Etching rate dependence on the beam incidence angle [29] and (b) the ion beam current vs. extractor voltage at different source current for the Fischione 1010 [20]. . . . .	21
2.6	A view graph of Fischione 1010 low-angle ion etching machine. . . . .	22
2.7	Four major steps of the conventional cross-section preparation. . . . .	23
2.8	Dimpling tool or machine. . . . .	23
2.9	A schematic in cross-sectional view of (a) a dimpled sample and (b) its ion etching geometry. . . . .	23
2.10	FIB TEM lamella preparation process: (a) Pt protection layer deposited on the area of interest on top of the DyBCO film, (b) milling parallel trenches, (c) cutting the edges of the slice or lamella for lift-out, (d) attached lamella to the needle, (e) attachment of the lamella to the special TEM grid, and (f) final thinning and polishing. . . . .	25
2.11	(a) Bright-field and (b) corresponding (110) dark-field image in plan-view of sample 3 (Table 2.1) prepared by dimpling method. . . . .	25
2.12	Conventionally prepared cross-section sample: (a) bright-field image and (b) high-resolution bright-field image of the MgO-DyBCO interface of sample 3 (Table 2.1). . . . .	26
2.13	FIB prepared cross-section sample: (a) bright-field image and (b) high-resolution bright-field image of the DyBCO film of sample 3 (Table 2.1). . . . .	26
2.14	Selected area diffraction patterns of the DyBCO film shown in (a) Fig. 2.12 i.e. conventionally prepared and (b) Fig. 2.13 i.e. FIB prepared cross-section specimen. . . . .	27
2.15	(a) A schematic drawing, showing bending of the ISD grown DyBCO film during ion etching due to the stresses present in the film. Light microscope images in plan-view of (b) sample 2 (semi-processed) and (c) sample 3 (fully processed) just after etching (Table 2.1). . . . .	27
2.16	Light microscope image of an ion etched conventional cross-section specimen, showing delamination and cracking of the film due to tensile stresses present in the ISD grown DyBCO films. . . . .	28
2.17	Light microscope image of an ion etched conventional cross-section specimen using a symmetrical dummy architecture. An electron transparent region is marked by a dotted ellipse. . . . .	28
3.1	Evaluation of superconducting transition temperatures over time [38]. . . . .	34
3.2	The magnetization curves of the two types of superconductor: (a) type-I and (b) type-II superconductors [48]. . . . .	35
3.3	Magnetization curve of a cold deformation $Nb_{55}Ta_{45}$ alloy: (a) after cold deformation (b) after cold deformation and annealing [46]. . . . .	36
3.4	Critical current density definition: current density ( $J_c$ ) vs. field ( $E$ ) dependence for a superconductor [46]. . . . .	37
3.5	Schematics of: (a) the critical state of type-II superconductors with quantized vortices, and (b) mechanism of flux-flow, the presence of current in a magnetic field generates a Lorentz force, which tilts the staircase, allowing flux line to hop out of their pinning wells [46]. . . . .	37

3.6	Schematic diagram of current limiting mechanism in different class of superconducting materials.	38
3.7	(a) Critical current density ( $J_c$ ) in dependence of applied magnetic field $B(T)$ of up to 30 T at 4.2 K for various HTS materials [55]. (b) $J_c$ and critical current ( $I$ ) in dependence of $B(T)$ applied in two perpendicular directions for a 55 filament Bi-2223/Ag tape at 77 K [56]. $J_c$ in dependence of $B$ for (c) $B$ perpendicular to the $c$ -direction and (d) $B$ parallel to the $c$ -direction at different temperature for Bi-2223 [44].	39
3.8	Grain boundary current in dependence on grain boundary misorientation angle [59].	40
3.9	DyBa <sub>2</sub> Cu <sub>3</sub> O <sub>7-x</sub> (DyBCO) crystal structure: (a) orthorhombic and (b) tetragonal phase. The O(1) site in the tetragonal phase is not fully occupied [37].	41
3.10	A schematic diagram (layer structure) of coated conductors.	41
3.11	Schematics of (a) growth geometry and (b) growth chamber of the ISD technology [24].	43
3.12	Development of the in-field $J_c$ of high-temperature superconductors (HTS) at 77 K, $B \parallel c$ , as compared to the performance of conventional superconducting wires such as Nb-Ti and Nb <sub>3</sub> Sn at 4.2 K [72].	44
4.1	Schematic of the layer structure of analyzed samples: (a) the MgO series i.e. a series of semi-processed samples exposed to ambient temperature only, (b) the DyBCO series i.e. a series of fully-processed samples exposed to high temperatures and (c) the blocking layer series i.e. a series of samples having an intermediate buffer layer at the Hastelloy-MgO interface and exposed to high temperatures.	47
4.2	Low-loss EELS of Cr and positions of energy window for acquiring Cr phase map by using super-imposed energy-filtered (RGB) imaging technique.	47
4.3	Energy-filtered TEM images of the Hastelloy-MgO interface acquired at energy losses (a) 21 eV, (b) 43 eV, (c) 65 eV, and (d) 0 eV with an energy slit of 10 eV width. False color coded images of EFTEM image: (e) 21 eV image as red, (f) 43 eV image as green, (g) 65 eV image as blue and (h) superimposed energy-filtered image (RGB). Line scan profiles along the substrate normal (indicated by black dotted arrow) of the Hastelloy-MgO interface for (i) 21 eV, (j) 43 eV, (k) 65 eV, and (l) RGB image.	48
4.4	Secondary electron images of the Hastelloy-MgO interface of sample 1 in: (a) cross-section and (b) longitudinal-section. RGB images of the Hastelloy-MgO interface of sample 1 in cross-section prepared by (c) conventional technique and (d) FIB technique. (e) core-loss EELS of the interface layers acquired at the points indicated by small circles in (d).	49
4.5	Secondary electron images of the Hastelloy-MgO interface of sample 2 in (a) cross-section and (b) longitudinal-section. TEM (c) bright-field and (d) RGB image of the Hastelloy-MgO interface of sample 2 in cross-section.	50
4.6	High-magnification images of the areas enclosed by dotted rectangles shown in Figs. 2 and 3: (a) secondary electron image, (b) RGB image of the interface of sample 1 and (c) secondary electron image, (d) RGB image of the interface of sample 2.	51
4.7	TEM cross-section (area 1) of sample 7: (a) bright-field image, (b) corresponding (002) dark-field image, (c) RGB image of the area shown in (a) and (d) selected area diffraction pattern of the interface. The small black circles in (c) show the EDX reference points.	52
4.8	TEM cross-section (area 2) of sample 7: (a) RGB image (b) ratio-image of two energy-filtered images, one acquired at 46 eV and the other at 24 eV with an energy slit of widths of 10 eV and (c) core-loss EELS of the interface layers acquired at the points indicated by small circles in (a).	52
4.9	TEM EDX spectroscopy of sample 7: EDX spectra of (a) the Hastelloy substrate (spectrum 2), (b) the Cr-rich complex phase (spectrum 3), (c) the Y-layer (spectrum 6) and (d) the MgO buffer layer (spectrum 7). Reference points are given in Fig. 4.7c.	53
4.10	TEM cross-section of sample 6: (a) overview bright-field image of the Hastelloy-Ag-MgO interface, (b) and (c) RGB images of the interface of two different areas. Black arrows indicate the Cr diffusion in the MgO buffer layer and small black circles show EDX reference points.	54
4.11	EDX spectroscopy (TEM) of sample 6: EDX spectra of (a) the Ag-layer (spectrum 2) and (b) Cr diffusion in the MgO buffer layer (spectrum 4). Reference points are given in Figs. 4.10b and 4.10c.	54
5.1	Schematics of (a) layer structure of the ISD CCs, (b) overlapped punching (notch formation) of CC tape to retain the direction information in the punched out circular disk for cross-section and longitudinal-section TEM specimen preparation and (c) crystallographic geometry of ISD films.	61
5.2	Secondary electron images of an ISD CC in (a) cross-section and (b) longitudinal-section. All specimens were prepared by FIB.	62
5.3	TEM cross-section (conventionally prepared) analysis of a high $J_c$ ISD CC: (a) low-magnification bright-field image, (b) bright-field image of the DyBCO layer, (c) $g = (001)$ dark-field image of a DyBCO grain boundary, (d) high-resolution bright-field image of the MgO-DyBCO interface and (e) diffraction pattern of the MgO-DyBCO interface.	63

5.4	TEM cross-section (FIB prepared) analysis of a high $J_c$ ISD CC: (a) low-magnification bright-field image, (b) $g = (001)$ dark-field image of the DyBCO layer and (c) high-resolution $g = (001)$ dark-field image of the MgO–DyBCO interface. The inset in (c) shows the diffraction pattern of the MgO–DyBCO interface. Some of the dislocation, dislocation loops and stacking faults are indicated by white, black and black (triangular) arrows, respectively. . . . .	64
5.5	TEM plan view (conventionally prepared) of a high $J_c$ ISD CC: (a) bright-field image of the DyBCO, (b) corresponding dark-field image using $g = (110)$ , (c) diffraction pattern of the DyBCO in false color and (d) polar intensity plot along the shown white dotted arc in (c), i.e. of the (110) reflection. (e) High-magnification dark-field image using $g = (111)$ and (f) an enlarged view of rotational Moiré fringes observed at DyBCO grain boundaries in (e). . . . .	65
5.6	Schematic drawing of growth modes for (a) the IBAD and/or RABiTS and (b) the ISD. (c) A non-zero component of DyBCO growth along the ab-plane of DyBCO only exists in the ISD grown CCs. . . . .	67
5.7	Growth mechanism of DyBCO films for the ISD technology: (a) secondary electron image of the DyBCO layer in cross-section with overlay schematics. The schematic shows shape and tilt of facets at the MgO–DyBCO interface and of DyBCO top surface with respect to substrate. (b) A schematic drawing of the growth mechanism of the DyBCO film on a tilted geometry (faceted MgO buffer), the tilting mechanism of the grain boundaries and the c-axis out of the substrate normal. . . . .	68
6.1	(a) A low-magnification bright-field image of the DyBCO film, (b) a dark-field image of the DyBCO top surface from a thick region showing the surface roughness, (c) and (d) are selected area electron diffraction patterns acquired at the top part and lower part of the DyBCO film, respectively. . . . .	72
6.2	A STEM image of the MgO–DyBCO interface of sample 10 in cross-section acquired by a FEI Titan microscope using a camera length of 145 mm. In the image planar defects (black arrows) and grain boundaries (white arrows) are marked. . . . .	73
6.3	A HR-HAADF image of (a) the MgO–DyBCO interface and (b) a DyBCO grain boundary. Inset in (a) shows a magnified view of lattice fringes and inset in (b) shows a magnified view of the DyBCO grain boundary facets. Images were acquired by a FEI Titan microscope using a camera length of 70 mm. . . . .	74
6.4	High-magnification bright-field image of a DyBCO grain in cross-section, showing the size and orientation of the BZO nano-precipitates. Inset is a selected area diffraction pattern of the shown DyBCO grain. . . . .	75
6.5	(a) A bright-field image and (b) the corresponding $g = (110)$ dark-field image of the DyBCO film in plan-view. Inset in (a) is a high-magnification image of the enclosed area and in (b) is a selected area diffraction patterns of the DyBCO film. In both images the BZO-NPs could be identified by Moiré fringe contrast. . . . .	76
6.6	TEM spectroscopy results in plan-view: point EDX spectra of (a) the DyBCO matrix (spectrum 3 in table 1) and (b) Dy-rich secondary phases observed in the DyBCO matrix (spectrum 5 in Table 6.1). . . . .	76
7.1	Thomas Johann Seebeck experiment, reproduced from Treatise of the Royal Prussian Academy of Sciences in Berlin (Abhandlung der Königlichen Preussischen Akademie der Wissenschaften zu Berlin, p265-375, 1822-1823). . . . .	81
7.2	Schematics of thermoelectric effects: (a) the Seebeck effect and (b) the Peltier effect. . . . .	82
7.3	(a) Schematic plot of the thermopower, $S$ , the electrical conductivity, $\sigma$ , the power factor, $S^2\sigma$ , the lattice thermal conductivity, $\lambda_L$ , and the electronic thermal conductivity, $\lambda_e$ , in dependence of the carrier density. (b) Thermoelectric figure of merit $ZT$ in dependence of the temperature for various bulk thermoelectric materials [134]. . . . .	85
7.4	Schematic diagram of a single-couple thermoelectric (a) refrigerator and (b) power-generator. [137]	87
8.1	TEM dark-field images acquired under $g = \{0, 1, 5\}$ two-beam conditions for imaging the nns in p-type $(\text{Bi}_{0.26}\text{Sb}_{0.74})_2\text{Te}_3$ (a-c) and n-type $\text{Bi}_2(\text{Te}_{0.91}\text{Se}_{0.09})_3$ bulk materials (d-f). Etching at 3 keV (b,e) revealed the nns with a wavelength of 10 nm parallel to (1,0,10) planes. After etching at 1 keV the samples did not show the nns along the (1,0,10) planes and no contrast is seen (a,c,d). Only in (f) is a residual contrast seen with fringes parallel to (001) planes. The inserts in the upper right corner show the $\{0,1,5\}$ reflections with satellite reflection due to the nns in (b) and (e). . . . .	92
8.2	(a) Schematic of TEM sample orientation and etching angle applied for $\text{Ar}^+$ ion etching. (b) Dependence of formation and removal of the nns on ion energy and angle by $\text{Ar}^+$ ion irradiation for n-type $\text{Bi}_2(\text{Te}_{0.91}\text{Se}_{0.09})_3$ and p-type $(\text{Bi}_{0.26}\text{Sb}_{0.74})_2\text{Te}_3$ . The ion source current was 3 mA and the etching time was 5 min. . . . .	93
9.1	XRD results of $\text{Bi}_2(\text{Te}_{0.91}\text{Se}_{0.09})_3$ material in as-cast state (black), after ball milling (blue), and finally after SPS treatment (red). XRD analyses were done by a project partner under a DFG (SPP1386) project. . . . .	98

9.2	(a) A low-magnification bright-field image, (b) the corresponding $g = (105)$ dark-field image and (c) a selected area electron diffraction pattern of $(\text{Bi}_{0.26}\text{Sb}_{0.74})_2\text{Te}_3$ nanostructure bulk after SPS treatment.	99
9.3	(a) A high-magnification bright-field image and (b) the corresponding $g = (105)$ dark-field image of $(\text{Bi}_{0.26}\text{Sb}_{0.74})_2\text{Te}_3$ nanostructure bulk after SPS treatment. Superstructure (S), Moiré fringes (M), twin boundaries (TB) and grain boundary dislocations (GD) are indicated by arrows and annotations.	99
9.4	Energy-filtered TEM of $(\text{Bi}_{0.26}\text{Sb}_{0.74})_2\text{Te}_3$ nanostructure bulk after SPS treatment: (a) a bright-field image and (b) a RGB image of the same area acquired using a 5 eV energy slit aperture at 15, 31, and 15 eV energy window.	100
9.5	EDX spectroscopy (TEM) of $(\text{Bi}_{0.26}\text{Sb}_{0.74})_2\text{Te}_3$ nanostructure bulk after SPS treatment: (a) and (b) EDX spectra of the stoichiometric matrix (pink areas in Fig. 9.4b) with 31.0 at.% Sb in linear scale and in logarithmic scale, respectively. (c) and (d) EDX spectra of the oxidized grain boundary phase (green areas in Fig. 9.4b) with 65.3 at.% Sb in linear scale and in logarithmic scale, respectively.	101
9.6	(a) A low-magnification bright-field image, (b) the corresponding $g = (105)$ dark-field image and (c) a selected area electron diffraction pattern of $\text{Bi}_2(\text{Te}_{0.91}\text{Se}_{0.09})_3$ nanostructure bulk after SPS treatment.	101
9.7	(a) A high-magnification bright-field image and (b) the corresponding $g = (105)$ dark-field image of $(\text{Bi}_{0.26}\text{Sb}_{0.74})_2\text{Te}_3$ nanostructure bulk after SPS treatment. Moiré fringes (M) and dislocations (D) are indicated by arrows and annotations.	102
9.8	Energy-filtered TEM of $\text{Bi}_2(\text{Te}_{0.91}\text{Se}_{0.09})_3$ nanostructure bulk after SPS treatment: (a) a bright-field image and (b) a RGB image of the same area acquired using a 5 eV slit aperture at 15, 25 and 15 eV energy window.	103
9.9	EDX spectroscopy (TEM) of $\text{Bi}_2(\text{Te}_{0.91}\text{Se}_{0.09})_3$ nanostructure bulk after SPS treatment: (a) and (b) EDX spectra of the stoichiometric matrix (pink areas in Fig. 9.8b) with 39.8 at.% Bi in linear scale and in logarithmic scale, respectively. (c) and (d) EDX spectra of the oxidized grain boundary phase (green areas in Fig. 9.8b) with 48.4 at.% Bi in linear scale and in logarithmic scale, respectively.	104
A.1	A view graph of the $\text{Ar}^+$ ion etching machine (Fischione 1010).	105
A.2	A view graph of the circular ring and circular specimen punching tools.	105
A.3	A view graph of the pressing tool (Piano), front view and side view.	106
A.4	A view graph of the diamond wire saw machine (Walter EBNER 3281) and ultrasonic circular disc cutting machine (Gatan 601).	106
A.5	A view graph of the grinding machine (KNUTH-ROTOR), with two SiC plates of different grit size.	106
A.6	A view graph of the diamond lapping polishing discs with different grit sizes (30 $\mu\text{m}$ , 15 $\mu\text{m}$ , 9 $\mu\text{m}$ , 3 $\mu\text{m}$ , 1 $\mu\text{m}$ and 0.5 $\mu\text{m}$ ).	107
A.7	A view graph of the light microscope (OPTECH).	107

# List of Acronyms and Symbols

## Acronyms

<i>BF</i>	Bright-field
<i>CCs</i>	Coated Conductors
<i>CS</i>	Cross-Section
<i>DF</i>	Dark-field
<i>DyBCO</i>	Dysprosium Barium Copper Oxide ( $DyBa_2Cu_3O_{7-x}$ , x denotes deviation from stoichiometry)
<i>EDX</i>	Energy Dispersive X-ray Microanalysis
<i>EELS</i>	Electron Energy-Loss Spectroscopy
<i>EFTEM</i>	Energy-Filtered Transmission Electron Microscopy
<i>ESI</i>	Electron Spectroscopic Imaging
<i>FIB</i>	Focused Ion Beam
<i>HRTEM</i>	High-Resolution Transmission Electron Microscopy
<i>HTS</i>	High Temperature Superconductor
<i>IBAD</i>	Ion Beam Assisted Deposition
<i>ISD</i>	Inclined Substrate Deposition
<i>LM</i>	Light Microscopy
<i>nns</i>	Natural Nanostructure
<i>PV</i>	Plan-View
<i>RABiTS</i>	Rolling Assisted Biaxially Textured Substrate
<i>RGB</i>	Red Gree Blue (Term used for ESI images)
<i>SAED</i>	Selected Area Electron Diffraction
<i>SE</i>	Secondary Electron
<i>SEM</i>	Scanning Electron Microscopy
<i>SPS</i>	Spark Plasma Sintering
<i>STEM</i>	Scanning Transmission Electron Microscopy
<i>TEM</i>	Transmission Electron Microscopy
<i>XRD</i>	X-ray Diffraction
<i>YBCO</i>	Yttrium Barium Copper Oxide



# *Acknowledgment*

All praises to Almighty Allah who bestowed me with everything and always helped me at every step of my life.

I would like to thank my supervisor Prof. Dr. Oliver Eibl for giving me the opportunity to work towards my PhD. in his group, for the excellent guidance during all stages, for the high level training in transmission electron microscopy applied to materials science and materials physics, for teaching me how to overcome problems and showing me the importance of good planning, things that are not only useful in science, but are also important for life in general, thank you very much. It is a great honor for me to have been a part of his team at University of Tübingen, the successful completion of the work has been only possible due to his excellent guidance, meticulous observation and critical analysis.

Many thanks to Prof. Dr. Reinhold Kleiner who kindly accepted to take part in the thesis evaluation committee. I would like to thank Prof. Dr. Dieter P. Kern and Prof. Dr. Martin Oettel for accepting my request to take part in my PhD defense as an examiner. I would also like to express my great thanks to Prof. Dr. Dieter Kölle, Prof. Dr. Nils Schopohl, Prof. Dr. Reinhold Kleiner and Prof. Dr. Frank Schreiber for lecture courses and exams.

During my stay in Tübingen I had the opportunity to attend several conferences and work within three exciting research projects as an electron microscopist in three different fields: superconductivity, thermoelectricity and solar cell. I would like to thank all the colleagues with whom I collaborated within these projects, especially Dr. M. Bauer, Dr. W. Prusseit, Mr. T. Rudol, Mr. R. Semarad and Mr. V. Große from THEVA GmbH. Dr. V. Pacheco from Fraunhofer Institute for Manufacturing and Advanced Materials and Dr. F. Clement and Mr. R. Hönig from ISE Fraunhofer for providing samples and also for their supports. I would like to thank NMI Reutlingen for providing FIB cut samples

I would also like to thank my colleagues at the Institute of Applied Physics at the University of Tübingen for the great working atmosphere and support during my stay at the Institute, especially Dr. N. Peranio, Mr. M. Dürrschnabel, Mr. J. Elia, Ms. E. Lohman, Dipl. Ing. B. Dögel, Dr. A. Bisemeier, Dr. M. Kühnle and Mr. M. Weiler.

The years spent in Tübingen would not have been as wonderful without my Indian friends, including Dr. Dharam, Mr. Anil, Dr. Monika, Mr. Vinod, Dr. Manoj, Mrs. Sunita, Dr. Khallel, Dr. Nazneen, Mrs. Ankita and some friend from other countries including Ms. K. Stauber, Dr. Ahmed, and Mrs. Sara.

I would like to thank all the friends I have made over the years for their moral support, they have made me feel at home and gave helpful suggestions, discussion and feedback. List is very long, in no particular order Dr. Vijay Raj Singh, Dr. Brijdar Balaji, Dr. Yogendra Kumar Mishra and Dr. Gautam Singh. Sorry if I miss someone's name, who made my days at University of Tübingen (Tübingen) enjoyable and cheerful. I still have to thank the rest of my friends, whom I can not name all, but I am sure I owe them a lot for all the good times together.

Thank also to my family, specially my mother Wahida Husaini and grand mother Mrs. Hafiza Khatoon for their love, support, and constant guidance and care throughout my life, my brothers (Minhaj and Zafar) and my sisters (Nikhat, Talat, Farhat and Nujhat), who have always supported me and loved me. Thanks to my father Late Mr. Tafazzul Husain, whose memory has only increased after so many years of his death, for his valuable advices that he gave me in the

early age of my carrier to shape my career in the right direction. Thanks to my grand father Late Mr. Karmullah for his love and supports that he provided us after my father death. Thanks also to my brothers-in-law (Mr. Akhlaq, Mr. Shafiuddin and Irfan), siter-in-law Tasneem Amina and mother-in-law Zahida Begum for their supports and inspiration.

Last but not least, a big thanks to my wife Tabssum Fatima. Without her I would be a very different person today, and it would have been certainly much harder to stay in Germany and finish the PhD. Still today, learning to love her and to receive her love makes me a better person. Special thanks to her also for teaching me many programming languages and databases. This dissertation is dedicated to my family. Without my family help I would have never reached this stage.

This thesis has been supported by the Ministry of Economics and Technology (BMW) under the project HIGHWAY (FK 0327489C). Their support is gratefully acknowledged.

# Eidesstattliche Versicherung

Ich erkläre hiermit, dass ich die zur Promotion eingereichte Arbeit mit dem Titel “**Structural Characterization and Structure-property Correlation of Nanostructured Superconducting Coated Conductors and Thermoelectric Materials**” selbständig verfasst, nur die angegebenen Quellen und Hilfsmittel benutzt und wörtlich oder inhaltlich übernommene Stellen als solche gekennzeichnet habe. Ich versichere an Eides statt, dass diese Angaben wahr sind und dass ich nichts verschwiegen habe. Mir ist bekannt, dass die falsche Abgabe einer Versicherung an Eides statt mit Freiheitsstrafen bis zu drei Jahren oder mit Geldstrafe bestraft wird.

Weiterhin erkläre ich, dass bisher kein Promotionsversuch unternommen wurde.

Tübingen, den \_\_\_\_\_



# Declaration

I hereby declare that I alone wrote the doctoral work submitted here under the title “**Structural Characterization and Structure-property Correlation of Nanostructured Superconducting Coated Conductors and Thermoelectric Materials**”, that I only used the sources and materials cited in the work, and that all citations, whether word for word or paraphrased are given as such. I declare that I adhered to the guidelines set forth by the University of Tübingen to guarantee proper academic scholarship. I declare that these statements are true and that I am concealing nothing. I understand that any false statements can be punished with a jail term of up to three years or a financial penalty.

Furthermore, I declare that so far no attempt has been made promotion.

Tübingen \_\_\_\_\_



# List of Publications

## Publications during the Ph. D.

### Peer-reviewed journal papers

1. **Z. Aabdin**, M. Dürrschnabel, M. Bauer, R. Semerad, W. Prusseit, and O. Eibl, "Growth behavior of superconducting DyBa<sub>2</sub>Cu<sub>3</sub>O<sub>7-x</sub> thin films deposited by inclined substrate deposition for coated conductors," *Acta Mater*, 60 (19), (2012) pp. 6592–6600. doi: [10.1016/j.actamat.2012.08.025](https://doi.org/10.1016/j.actamat.2012.08.025)
2. M. Dürrschnabel, **Z. Aabdin**, M. Bauer, R. Semerad, W. Prusseit, O. Eibl, "DyBa<sub>2</sub>Cu<sub>3</sub>O<sub>7-x</sub> superconducting coated conductors with critical currents exceeding 1000 A cm<sup>-1</sup>," *Superconductor Science and Technology*, 25, (2012) pp. 105007. doi: [10.1088/0953-2048/25/10/105007](https://doi.org/10.1088/0953-2048/25/10/105007)
3. **Z. Aabdin**, N. Peranio, and O. Eibl, "Switching of the Natural Nanostructure in Bi<sub>2</sub>Te<sub>3</sub> Materials by Ion Irradiation," *Advanced Materials*, 24, (2012) pp. 4605-4608. DOI: [10.1002/adma.201201079](https://doi.org/10.1002/adma.201201079). doi: [10.1002/adma.201201079](https://doi.org/10.1002/adma.201201079)
4. G. Rogl, **Z. Aabdin**, E. Schafler, J. Horky, D. Setman, M. Zehetbauer, M. Kriegisch, O. Eibl, A. Grytsiv, E. Bauer, M. Reinecker, W. Schranz, P. Rogl, "Effect of HPT processing on the structure, thermoelectric and mechanical properties of Sr<sub>0.07</sub>Ba<sub>0.07</sub>Yb<sub>0.07</sub>Co<sub>4</sub>Sb<sub>12</sub>," *Journal of Alloys and Compounds*, 537 (2012) pp. 183-189. doi: [10.1016/j.jallcom.2012.05.011](https://doi.org/10.1016/j.jallcom.2012.05.011)
5. N. Peranio, M. Winkler, D. Bessas, **Z. Aabdin**, J. König, H. Böttner, R. Hermann, and O. Eibl, "Room-temperature MBE deposition, thermoelectric properties, and advanced structural characterization of binary Bi<sub>2</sub>Te<sub>3</sub> and Sb<sub>2</sub>Te<sub>3</sub> thin films," *Journal of Alloys and Compounds*, 521, (2012) pp. 163. doi: [10.1016/j.jallcom.2012.01.108](https://doi.org/10.1016/j.jallcom.2012.01.108)
6. N. Peranio, M. Winkler, **Z. Aabdin**, J. König, H. Böttner, and O. Eibl, "Room temperature MBE deposition of Bi<sub>2</sub>Te<sub>3</sub> and Sb<sub>2</sub>Te<sub>3</sub> thin films with low charge carrier densities," *Physica Status Solidi A*, 209(2), (2012) pp. 289–293. doi: [10.1002/pssa.201127440](https://doi.org/10.1002/pssa.201127440)
7. **Z. Aabdin**, N. Peranio, O. Eibl, W. Töllner, K. Neilsche, D. Bessas, R. P. Hermann, M. Winkler, J. König, H. Böttner, V. Pacheco, J. Schmidt, A. Hashibon, and C. Elsässer, "Nanostructure, excitations, and thermoelectric properties of Bi<sub>2</sub>Te<sub>3</sub> based nanomaterials," *Journal of Electronic Materials*, 41(6), (2012) pp. 1792-1798. doi: [10.1007/s11664-012-1997-6](https://doi.org/10.1007/s11664-012-1997-6)
8. **Z. Aabdin**, N. Peranio, M. Winkler, D. Bessas, J. König, R. P. Hermann, H. Böttner, and O. Eibl, "Sb<sub>2</sub>Te<sub>3</sub> and Bi<sub>2</sub>Te<sub>3</sub> and thin films grown by Room-Temperature MBE," *Journal of Electronic Materials*, 41(6), (2012) pp. 1493-1497. doi: [10.1007/s11664-011-1870-z](https://doi.org/10.1007/s11664-011-1870-z)

### Peer-reviewed conference paper

1. **Z. Aabdin**, M. Dürrschnabel, M. Bauer, R. Semerad, W. Prusseit, and O. Eibl, "Growth behavior of DyBa<sub>2</sub>Cu<sub>3</sub>O<sub>7-x</sub> thin films deposited by inclined substrate deposition for coated

- conductors,” *Physics Procedia*, 36 (2012) 1445-1449. doi: [10.1016/j.phpro.2012.06.240](https://doi.org/10.1016/j.phpro.2012.06.240)
2. **Z. Aabdin**, M. Dürrschnabel, M. Bauer, V. Große, R. Semerad, and O. Eibl, “Microstructure of BaZrO<sub>3</sub>-doped DyBa<sub>2</sub>Cu<sub>3</sub>O<sub>7-x</sub> coated conductors deposited by inclined substrate deposition,” *Physics Procedia*, 36 (2012) 1655-1660. doi: [10.1016/j.phpro.2012.06.324](https://doi.org/10.1016/j.phpro.2012.06.324)
  3. M. Dürrschnabel, **Z. Aabdin**, M. Bauer, T. Rudol, R. Semerad, W. Prusseit, O. Eibl, “DyBa<sub>2</sub>Cu<sub>3</sub>O<sub>7-x</sub> thick films deposited on coated conductors with I<sub>c</sub> exceeding 1000 A cm<sup>-1</sup>,” *Physics Procedia*, 36 (2012) 1649-1654. doi: [10.1016/j.phpro.2012.06.323](https://doi.org/10.1016/j.phpro.2012.06.323)
  4. M. Dürrschnabel, **Z. Aabdin**, M. Bauer, V. Große, G. Sigl, O. Eibl, “Growth of biaxially-textured MgO buffer layers by inclined substrate deposition,” *Physics Procedia*, 36 (2012) 1546-1551. doi: [10.1016/j.phpro.2012.06.208](https://doi.org/10.1016/j.phpro.2012.06.208)
  5. W. Prusseit, M. Bauer, V. Große, R. Semerad, G. Sigl, **Z. Aabdin**, M. Dürrschnabel, O. Eibl, “Working around HTS thickness limitations – towards 1000+ A cm<sup>-1</sup> class coated conductors,” *Physics Procedia*, 36 (2012) 1417-1422. doi: [10.1016/j.phpro.2012.06.146](https://doi.org/10.1016/j.phpro.2012.06.146)
  6. **Z. Aabdin**, M. Winkler, D. Bessas, J. König, N. Peranio, O. Eibl, R. Hermann, and H. Böttner, “Sb<sub>2</sub>Te<sub>3</sub> and Bi<sub>2</sub>Te<sub>3</sub> thin films grown by molecular beam epitaxy at room temperature,” *MRS Proceedings*, 1329, August 2011. doi: [10.1557/opl.2011.1251](https://doi.org/10.1557/opl.2011.1251)
  7. N. Peranio, **Z. Aabdin**, W. Töllner, M. Winkler, J. König, O. Eibl, K. Nielsch, and H. Böttner, “Low loss EELS and EFTEM study of Bi<sub>2</sub>Te<sub>3</sub> based bulk and nanomaterials,” *MRS Proceedings*, 1329, August 2011. doi: [10.1557/opl.2011.1238](https://doi.org/10.1557/opl.2011.1238)

### Conference abstracts

1. **Z. Aabdin**, M. Dürrschnabel, O. Eibl, “Microstructure of DyBa<sub>2</sub>Cu<sub>3</sub>O<sub>7-x</sub> coated conductors deposited by inclined substrate deposition,” *MC Proceedings*, M4.P571 (ISBN: 978-3-00-033910-3), August 2011.
2. **Z. Aabdin**, M. Dürrschnabel, T. Rudolf, W. Dreher, O. Eibl, “TEM specimen preparation for superconducting coated conductors grown by inclined substrate deposition,” *MC Proceedings*, IM7.P189 (ISBN: 978-3-00-033910-3), August 2011.
3. M. Dürrschnabel, **Z. Aabdin**, O. Eibl, “Biaxial texture and nanostructure of MgO buffer layers grown by inclined substrate deposition for superconducting coated conductors,” *MC Proceedings*, M4.P570 (ISBN: 978-3-00-033910-3), August 2011.
4. N. Peranio, **Z. Aabdin**, O. Eibl, 2011. Analytical energy-filtered TEM of Bi<sub>2</sub>Te<sub>3</sub> based nanomaterials,” *MC Proceedings*, M1.P503 (ISBN: 978-3-00-033910-3), August 2011.

# Curriculum Vitae

## Personal data

---

<b>Name</b>	Mr. Zainul Aabdin
<b>Date and place of birth</b>	01, July, 1981, Balrampur (India)
<b>Nationality</b>	Indian
<b>Email</b>	<a href="mailto:zainul.aabdin@gmail.com">zainul.aabdin@gmail.com</a>

## School

---

<b>Primary schooling</b> (1986-1991)	Jamia Anwarul Uloom, Naudihwa
<b>Higher primary schooling</b> (1991-1994)	Haji Ismail Inter College, Sadullah Nagar
<b>Secondary schooling</b> (1986-1991, U. P. Board)	Haji Ismail Inter College, Sadullah Nagar
<b>Higher secondary schooling</b> (1986-1991, U. P. Board)	Mohd. Yusuf Usmani. Inter College, Utraula

## University

---

<b>Bachelor of Science (B.Sc.)</b> (1998-2001, PCM)	Ewing Christian College, Allahabad
<b>Master of Science (M.Sc.)</b> (2001-2004, Physics)	University of Allahabad, Allahabad (Prof. V. K. Jaiswal)
<b>Master of Technology (M.Tech.)</b> (2005-2008, Material Science)	Indian Institute of Technology Kanpur (Prof. Y. N. Mohapatra and Prof. V. N. Kulkarni)

## Doctor of Natural Sciences (Dr. rer. nat.)

---

<b>Pre-Ph. D. test and courses</b> (2009-2010)	Institute of Applied Physics, University of Tübingen (Prof. O. Eibl, Prof. N. Schopohl, Prof. D. Kölle, Prof. R. Kleiner, Prof. F. Schreiber)
<b>Ph. D. thesis</b> (March, 2009- June, 2013)	Institute of Applied Physics, University of Tübingen (Eberhard Karls Universität Tübingen) (Prof. Dr. Oliver Eibl)

Tübingen

---

